UNIVERSITAT POLITÈCNICA DE VALÈNCIA

Departamento de Máquinas y Motores Térmicos

DOCTORAL THESIS:

"Assessment of highly turbocharged oxygen production cycles coupled with power generation systems"

Presented by: D. FABIO ALBERTO GUTIÉRREZ CASTRO
Supervised by: DR. D. LUIS MIGUEL GARCÍA-CUEVAS GONZÁLEZ

in fulfillment of the requisites for the degree of

Doctor of Philosophy

Valencia, September 2023

Assessment of highly turbocharged oxygen production cycles coupled with power generation systems working under oxycombustion

Fabio Alberto Gutiérrez Castro

Abstract

This thesis assesses oxygen production cycles based on membranes in three industrial situations, emphasizing power production operating under oxycombustion. The primary motivation is the reduction of pollutant emissions while not affecting the system's thermal efficiency.

Current emission standards require alternatives to mitigate the effect of human activities on the environment. Oxycombustion is a promising option that addresses the formation of pollutant substances, especially NOx, facilitating carbon capture and easy integration within existing facilities. It requires a high-purity oxygen stream mixed with recycling gases to control the combustion temperature.

This oxygen production needs an air separation system with reasonable energy consumption that does not affect the system's performance. Hence, membrane air separation is an alternative with low energy consumption and costs, requiring high temperature and pressure ratios for optimum operation.

Thus, a thermoeconomic analysis of a membrane-based oxygen production cycle is performed to assess the viability of these facilities in the context of a ceramic plant. The cycle is driven by recycling gases within the plant and uses turbochargers and heat exchangers to compress and heat the air for oxygen obtention.

Two configurations were studied, whose differences come from adding a heat source and the vacuum generation method. An optimum oxygen production cost of $31\,€\,t^{-1}$ was found, being competitive when compared with an average wholesale market price of $50\,€\,t^{-1}$. Compared with other oxygen production methods, this cycle exhibits a competitive behavior regarding oxygen purity, production, and energy consumption.

The promising results of this analysis motivate the study of similar configurations working in two oxycombustion contexts: a power plant and a spark-ignition engine.

Two oxygen production methods operating with a 400 MW power production plant are compared in the first context. The power plant is the Graz cycle, which uses cryogenic air separation as its oxygen source, the baseline in this analysis.

Therefore, two membrane configurations are considered: three-end and four-end membranes. A medium-temperature stream within the power production cycle is the energy source to drive the membrane cycles. Both cases are compared with the baseline Graz cycle operation.

The three-end membrane-based cycle improves the baseline efficiency by 0.61 % and the four-end by 2.30 %. The oxygen production requires less power consumption in the membrane cases than in the baseline, increasing the net power output. Thus, membrane-based cases display a promising performance, with possible integration within an oxycombustion power plant.

In the second context, the membrane-based cycle is coupled within an oxycombustion spark-ignition engine, where different operation conditions

are evaluated regarding fuel consumption and energy availability for oxygen production. The energy source to drive the membrane-based cycle is the exhaust gases stream.

As a first step, different oxygen concentrations and engine compression ratios are studied at medium speed, comparing the performance with the engine's conventional operation. Medium oxygen concentration (30 %) was found to be optimum. This concentration allows the operation at a high engine compression ratio.

Secondly, a full-load study in a wide range of engine speeds is made. The oxycombustion engine achieves a sustainable operation at the studied speeds, reaching the reference full-load power values. Similar fuel consumptions regarding the most efficient conventional case are achieved when the engine compression ratio is elevated under oxycombustion.

Thirdly, operative limits regarding part-load and altitude operation are found. The fuel consumption behavior of the oxycombustion case is similar to a conventional turbocharged engine at part-load while improving a naturally aspirated engine operation. The minimum achievable load is between 40 to 50 % of the maximum load, depending on the engine compression ratio. The membrane cycle operation is affected at lower loads. On the other hand, the system shows a suitable performance up to 4,000 m.

Thus, it can be concluded that the membrane-based oxygen production cycle exhibits flexibility to work in a wide range of available energy, displaying a suitable performance according to the requirements. Additionally, possible advantages in energy consumption and operative costs could be found when a careful design is performed.

Resumen

Esta tesis evalúa ciclos de producción de oxígeno basados en el uso de membranas en tres contextos industriales, enfatizando en la producción de potencia operando bajo oxicombustión. La principal motivación es reducir las emisiones contaminantes sin afectar el desempeño del sistema.

Los estándares de emisiones actuales demandan alternativas para mitigar el efecto de las actividades humanas en el ambiente. La oxicombustión es una opción prometedora que aborda directamente la formación de sustancias contaminantes, especialmente la formación de NOx, facilitando la captura de dióxido de carbono y con una fácil integración en instalaciones existentes. Esta requiere un flujo de oxígeno de alta pureza mezclada con gases reciclados de proceso para controlar la temperatura de combustión.

Este flujo de oxígeno necesita de un sistema de separación de aire para ser producido, con un consumo energético razonable que no afecte el funcionamiento del sistema. En este sentido, la separación de aire con membranas es una alternativa con bajo consumo energético y bajos costos que requiere altas temperaturas y gradientes de presión para una operación óptima.

Siguiendo esta idea, se ha realizado un análisis termoeconómico de un ciclo de producción de oxígeno basado en membranas para evaluar la viabilidad de este tipo de instalaciones en el contexto de una planta de cerámica. El ciclo es alimentado por gases reciclados dentro de la planta y usa turbogrupos e intercambiadores de calor para comprimir y calentar el aire con el fin de obtener el oxígeno.

Dos configuraciones de este ciclo han sido estudiadas, diferenciadas de acuerdo con la presencia de una fuente de calor adicional y el método para la generación de vacío. Se ha encontrado un costo óptimo de producción de oxígeno de $31 €\,t^{-1}$, el cual es competitivo cuando se considera un precio promedio de mercado de $50 €\,t^{-1}$. Además, comparado con otros métodos de producción de oxígeno, este ciclo muestra un comportamiento competitivo en lo que respecta a la pureza del oxígeno, la producción y el consumo energético.

Los anteriores resultados motivaron el estudio de configuraciones similares operando en dos contextos distintos de generación de potencia que operan con oxicombustión: una planta de generación eléctrica y un motor de encendido provocado.

En el primer contexto, se compara el desempeño de dos métodos de producción de oxígeno distintos, operando en una planta de generación eléctrica de 400 MW. La planta seleccionada es el ciclo Graz, que usa separación criogénica de aire como fuente de oxígeno, siendo el caso base del análisis. En este sentido, se consideran dos configuraciones de membrana: de tres entradas y de cuatro entradas. La fuente de energía que impulsa ambas configuraciones es un flujo de temperatura media que se encuentra dentro del ciclo de potencia. Ambos casos se han comparado con el caso base del ciclo.

La configuración con una membrana de tres entradas mejora la eficiencia del caso base en un 0.61 %, y la de cuatro entradas en un 2.3 %. La producción de oxígeno requiere un menor consumo energético que en el caso base en las configuraciones de membrana, aumentando la salida de potencia neta del caso base. Por tanto, la producción de oxígeno con membranas muestra un desempeño prometedor, con una posible integración con una planta de producción de potencia que trabaja con oxicombustión.

En el segundo contexto, el ciclo basado en membranas se acopla a un motor de encendido provocado que funciona con oxicombustión, donde diferentes condiciones de operación son evaluadas en términos del consumo de combustible y disponibilidad de energía para la producción de oxígeno. La fuente primaria de energía del ciclo de membrana es el flujo de gases de escape del motor. Primeramente, diferentes concentraciones de oxígeno y relaciones de compresión del motor son estudiadas a un régimen medio, comparando el desempeño con la operación convencional del motor. Una concentración media (30 %) fue hallada como óptima en el estudio. En estas, las condiciones de operación permiten un aumento considerable de la relación de compresión del motor.

En segundo lugar, se realiza un estudio de plena carga del motor en un rango amplio de regímenes de giro del motor. El motor de oxicombustión alcanza una operación sostenible en los regímenes estudiados, alcanzando los valores de referencia de plena carga. Se han obtenido consumos de combustible similares al caso de operación convencional más eficiente cuando la relación de compresión es elevada en el caso de oxicombustión.

En tercer lugar, se han encontrado límites operativos referentes a la operación a cargas parciales y altitud. La tendencia de consumo de combustible del caso con oxicombustión es similar a un motor convencional sobrealimentado a cargas parciales, mientras que se mejora el desempeño de un motor de aspiración natural. La menor carga alcanzable está entre 40 %-50 % de la máxima carga, dependiendo de la relación de compresión del motor. La operación del ciclo de membrana es afectada a cargas más bajas. Por otro lado, el sistema muestra un desempeño adecuado hasta los 4,000 mde altitud.

Por tanto, se concluye que el ciclo de producción de oxígeno basado en membranas de separación de aire muestra flexibilidad para operar en un amplio rango de energía disponible, mostrando un desempeño adecuado de acuerdo con los requerimientos del sistema. Adicionalmente, se pueden encontrar posibles ventajas en cuanto al consumo de energía y costos operativos realizando un diseño cuidadoso del sistema.

Resum

Aquesta tesi avalua cicles de producció d'oxigen basats en l'ús de membranes en tres contexts industrials diferents, emfatitzant en la producció de potència operant amb oxicombustió. La principal motivació és reduir les emissions contaminants sense afectar el funcionament del sistema.

Els estàndards d'emissions actuals demanden alternatives per a mitigar l'efecte de les activitats humanes en l'ambient. L'oxicombustió apareix com una opció prometedora que aborda directament els mecanismes de formació de les substàncies contaminants, especialment la formació de NOx, facilitant la captura de diòxid de carboni i amb una fàcil integració en instal·lacions existents. Aquesta requerix un flux d'oxigen d'alta puresa mesclat amb gasos reciclats del procés per controlar la temperatura de combustió.

Aquest flux d'oxigen necessita un sistema de separació d'aire per a ser produït, amb un consum energètic raonable que no afecte al funcionament del sistema. En aquest sentit, la separació d'aire amb membranes és una alternativa amb baix consum energètic i amb baixos costs que requerixen altes temperatures i gradients de pressió per a una operació òptima.

Seguint aquesta idea, s'ha realitzat una anàlisi termoeconòmic d'un cicle de producció d'oxigen basat en membranes per a avaluar la viabilitat d'aquest tipus d'instal·lacions en el context d'una planta de ceràmica. El cicle és alimentat per gasos reciclats dins de la planta i usa turbogrups i intercanviadors de calor per a comprimir i calfar l'aire amb la finalitat de separar l'oxigen.

Dues configuracions d'aquest cicle han sigut estudiades, diferenciades d'acord amb la presència d'una font de calor addicional i pel mètode per a la generació de buit. S'ha trobat un cost òptim de producció d'oxigen de $31\,€\,t^{-1}$, que és competitiu quan es considera un preu de mercat de $50\,€\,t^{-1}$. A més, comparat amb altres mètodes de producció d'oxigen, aquest cicle mostra un comportament competitiu pel que fa a puresa d'oxigen, producció i consum energètic.

Els anteriors resultats motivaren l'estudi de configuracions similars operant en dos contexts diferents de generació de potència que operen amb oxicombustió: una planta de generació elèctrica i un motor d'encesa provocada.

En el primer context, s'ha comparat el funcionament de dos mètodes de producció d'oxigen diferents, operant amb una planta de generació elèctrica de 400 MW. La planta seleccionada és el cicle Graz, que usa separació criogènica d'aire com a font d'oxigen, sent el cas base de l'anàlisi. En aquest sentit, s'han considerat dues configuracions de membrana: de tres i quatre entrades respectivament. La font d'energia que impulsa ambdós configuracions és un flux de temperatura mitjana que es troba dins del cicle de potència. Ambdós casos s'han comparat amb el cas base del cicle.

La configuració amb una membrana de tres entrades millora l'eficiència del cas base amb un 0.61 %, mentre que la de quatre entrades comporta una millora d'un 2.3 %. La producció d'oxigen requerix menys consum

energètic que en el cas base en les dues configuracions de membrana, augmentant l'eixida de potència neta del cas base. Per tant, la producció d'oxigen amb membranes mostra un funcionament prometedor, amb una possible integració amb una planta de producció de potència que treballa amb oxicombustió.

En el segon context, s'ha estudiat el cicle basat amb membranes acoblat dins d'un motor d'encesa provocada funcionant amb oxicombustió. Diferents condicions d'operació han sigut avaluades en termes de consum de combustible i disponibilitat d'energia per a la producció d'oxigen. La font primària d'energia per a la producció d'oxigen és el flux de gasos d'escapament del motor.

Primerament, diferents concentracions d'oxigen i relacions de compressió del motor han sigut estudiades a un règim mitjà, comparant el funcionament amb el d'un motor convencional. Una concentració mitjana (30 %) s'ha trobat com l'òptima en aquest estudi. Les condicions d'operació en aquest cas permeten un augment considerable de la relació de compressió del motor.

En segon lloc, s'ha realitzat un estudi a plena càrrega del motor en un rang ampli de règims de gir del motor. El motor d'oxicombustió aconseguix una operació sostenible en els règims estudiats, aplegant als valors de referència a plena càrrega. S'han obtingut consums de combustible similars al cas d'operació convencional més eficient quan la relació de compressió és elevada en el cas d'oxicombustió.

En tercer lloc, s'han trobat límits operatius referents a l'operació a càrregues parcials i altitud. La tendència de consum de combustible del cas amb oxicombustió és similar a la d'un motor convencional sobrealimentat a càrregues parcials, mentre que millora el funcionament d'un motor d'aspiració natural. La menor càrrega assolible està entre 40 %-50 % de la màxima càrrega, depenent de la relació de compressió del motor. L'operació del cicle amb membrana es veu afectat a càrregues més baixes. Per una altra banda, el sistema mostra un funcionament adequat fins als 4,000 m d'altitud.

Per tant, es pot dir que el cicle de producció d'oxigen basat en membranes de separació d'aire mostra flexibilitat per a operar en un rang ampli d'energia disponible, mostrant un funcionament adequat d'acord amb els requeriments del sistema. Addicionalment, es poden trobar posibles avantatges en consum d'energia i costs operatius realitzant un disseny cuidadós del sistema.

List of publications

The papers presented here are the basis of this thesis:

- "Adapting an internal combustion engine to oxy-fuel combustion with in-situ oxygen production", in *ASME 2021 Internal Combustion Engine Division Fall Technical Conference (ICEF 2021)* (2021) by Arnau, Novella, García-Cuevas and Gutiérrez [1].
- "Thermo-economic analysis of an oxygen production plant powered by an innovative energy recovery system", in *Energy* (2022) by Serrano, Arnau, García-Cuevas and Gutiérrez [2].
- "Comparison of cryogenic and membrane oxygen production implemented in the Graz Cycle", in *Energy Conversion and Management* (2022) by Gutiérrez, García-Cuevas and Sanz [3].
- "Coupling an oxygen generation cycle with an oxy-fuel combustion spark ignition engine for zero NOx emissions and carbon capture: a feasibility study", in *Energy Conversion and Management* (2023) by Serrano, Arnau, García-Cuevas and Gutiérrez [4].

Division of work between authors

The aforementioned publications have been succesfully accomplished through collaboration with other researchers of CMT-Motores Térmicos. In addition, for the third cited publication, which was developed in the doctoral stay of the thesis author, there was a collaboration with Dr. Wolfgang Sanz, researcher of the Institute of Thermal Turbomachinery and Machine Dynamics of TU Graz. The author carried out 0D-1D simulations in the in-house software VEMOD as well as in the software IPSE-Pro from TU-Graz. The post-processing of results and their discussion have also been perfomed by the thesis author, in collaboration with the rest of co-authors, especially his supervisor, Prof. García-Cuevas.

Funding acknowledgements

The author would like to acknowledge the financial support received through contract ACIF/2020/246 of the Conselleria d'Innovació, Universitats, Ciència i Societat Digital.

Acknowledgements

Me gustaría agradecer al Dr. Luis Miguel García-Cuevas por estos años de trabajo conmigo los últimos años. Su apoyo incalculable ha sido importantísimo para llegar al final de este viaje. También me gustaría agradecer a todo el equipo de oxicombustión, cuyo trabajo ha sido crucial para poder completar este proceso. Quisiera mencionar especialmente al Dr. José Ramón Serrano, por sus consejos durante las reuniones de equipo, que enriquecieron los resultados del trabajo que he realizado. Así mismo, quisiera expresar gratitud con CMT-Motores Térmicos por permitirme completar este reto.

También me gustaría agradecer al Dr. Wolfgang Sanz por recibirme en TU Graz durante mi estancia doctoral en Austria. Fue una experiencia excelente, en la que pude intercambiar muchas ideas que han sido importantes para completar la segunda mitad de mis estudios doctorales.

Me gustaría también extender un agradecimiento especial a mis compañeros Alberto, Pau, Juan David, Miguel Ángel, Lucas y Elkin. He disfrutado mucho el tiempo que hemos compartido estos años, las discusiones de cada tema que se nos ocurriese, los almuerzos, las comidas y demás momentos compartidos. También me gustaría agradecer de manera especial a Nicolás, quien durante el primer año fue fundamental para que todo este proceso fuese completado y a quien le voy a estar siempre agradecido por su apoyo.

Gracias a todos mis amigos y hermanos de mi iglesia, Vida Cristiana. Sin ustedes, este camino hubiese sido más difícil de lo que ha sido. Gracias a todos por sus oraciones, su apoyo en los momentos más complicados, y su presencia en los momentos de alegría. Gracias a porque he sentido el apoyo de Dios a través de ustedes. No me gustaría dejarme algún nombre, pero tengo claro que no puedo dejar de mencionar a Ary, a Sara, a Sil, a Gen y a Karen por su invaluable amistad y apoyo. Gracias porque, cada una a su manera, me han mostrado que siempre han estado ahí para mí. Gracias a Juanjo y a Ana por brindarme su apoyo desde el inicio. Gracias a Jorge y a Karolin, por abrirme las puertas de su casa desde el primer minuto y por siempre estar atentos a mí.

Diana, gracias por la compañía durante los últimos ocho años de amistad, aun desde la distancia. Gracias por las horas de conversaciones, de consejos, de debates, de todo. Gracias por estar ahí. A mis amigos Julián y Daniel, por ser casi como hermanos. Gracias por todo.

Gracias a mi familia. A mi mamá y a mi papá por todo su apoyo estos años, no solo durante la tesis, sino durante mis 28 años de vida, en los que no he podido más que sentir un inmenso amor de su parte. Mi agradecimiento hacia ustedes es eterno. Gracias a ti también Rochy, hermanita mía. Gracias por siempre tu confianza absoluta y por demostrarme que siempre estás ahí para mí.

Y gracias a ti, amor mío. Tu compañía estos años ha sido el regalo más

grande que he tenido en todo este tiempo. Gracias por todo el cariño, la atención y la paciencia. Gracias por ayudarme a levantar cuando me he caído. Espero que este sea uno de los muchos logros que podamos compartir juntos.

Y finalmente, y lo más importante, gracias a Ti. Porque por ti existe lo que vemos y lo que no vemos. Porque llamas lo que no es como si fuese. Porque me has traído hasta aquí y me has acompañado, en lo más alto y en lo más bajo. Gracias por todas las personas aquí mencionadas. Gracias Dios mío.

Contents

List of Figures

List of Tables

Nomenclature

Abbreviations

ATDC After top dead center

BSCF Membrane material

BSFC Brake-specific fuel consumption

BTDC Before top dead center

CA50 Combustion phasing

CA90-10 Combustion duration

CAD Crank angle degree

CAS Cryogenic air separation

MIEC Mixed ionic-electronic conducting

CFD Computational fluid dynamics

CI Compression-ignition

CLAS Chemical looping air separation

CO_2 Carbon dioxide

CO Carbon monoxide

DOC Diesel oxidation catalyst

DPF Diesel particulate filters

EGR Exhaust gas recirculation

EPA Environmental protection agency

EU European Union

FMEP Friction mean effective pressure

GPF Gasoline particulate filters

ICE Internal combustion engines

IMEP Indicated mean effective pressure

ITM Ion transport membrane

MUSCL Monotonic Upstream-centered Scheme for Conservation Laws

NEDC New European Driving Cycle

NMOG Non-methane organic gases

NO_x Nitrogen oxides

PMEP Pumping mean effective pressure

PM Particulate matter

PSA Pressure swing adsorption

SCR Selective catalytic reduction catalysts

SI Spark-ignition

SOC Start of combustion

TSA Temperature swing adsorption

TWC Three-way catalysts

UHC Unburned hydrocarbons

VEMOD Virtual engine model

VGT Variable geometry turbine

Greek Symbols

α Combustion delay

β^* Turbulent model coefficient

Δh Enthalpy difference

$\Delta\alpha$ Combustion duration

η Efficiency

ω Speed

γ Heat capacities ratio

λ Air-fuel equivalence ratio

π Pressure ratio

Roman symbols

A Area

C Membrane material constant, unitary cost

C0 Oxygen-line compressor

C1 Compressor 1

C2 Compressor 2

C3 Compressor 3

CC Combustion chamber

C_p Specific heat capacity at constant pressure

CR Compression ratio

CS1 Non-stoichiometric conventional combustion

CS2 Stoichiometric conventional combustion

D Diameter

E Oxygen production per consumed energy

AEP Average electricity price

ANP Average natural gas price

CF Conversion factor for natural gas

EV Evaporator

$\dot{H}$ Rate enthalpy flow

CR Heat exchange network

HPEC High-pressure electric compressor

HPT High-pressure turbine

HR Heat released

HRSG Heat recovery steam generator

HTT High-temperature turbine

I Engine indicator

K Membrane material constant

L Membrane thickness

LPT	Low-pressure turbine
MAPO	Maximum amplitude of pressure oscillations
$\dot{m}$	Mass flow rate
$\dot{m}$	Mass flow
$\hat{m}$	Non-dimensional mass flow
$\hat{N}$	Non-dimensional rotational speed
m	Combustion shape form
MPT	Medium-pressure turbine
MW	Molecular weight
N	Rotational speed
OLEC	Oxygen-line electric compressor
P	Power
p	Pressure
PH1	Preheater 1
SH1	Superheater 1
PH2	Preheater 2
SH2	Superheater 2
$\dot{Q}$	Heat
R	Gas constant, hydrocarbon radical
R	Gas constant, radius
RFG	Recycled flue gases
ST	Spark timing
T	Temperature
T0	Oxygen-line turbine
T1	Turbine 1
T2	Turbine 2
T3	Turbine 3
V_t	Engine displacement
$\dot{W}$	Power
X	Molar fraction

Subscripts and superscripts

$0, 1, \ldots$	Stations, coefficient number
air	Air
ASU	Air supply unit
aux	Auxiliar
$\dot{m}^*_{O_2}$	Oxygen production in a cycle
I^*_1	Indicator 1*
I^*_2	Indicator 2*
C1+2	Recycled flue compressors
C-1	Compression intercooling
C3+4	Carbon capture compressors
CPU	Compression and purification unit
cyl	Cylinder
eng	Engine
feed	Feed side
gen	Generator

HE-2 outlet Second heat exchanger outlet

HE-3 Third heat exchanger

h heater

HP comp High-pressure compressor

HP turb High-pressure turbine

in Inlet

exh Exhaust

int Intake

LP comp Low-pressure compressor

LP turb Low-pressure turbine

memb Membrane

m Mechanical

NG Natural gas

O_2 Oxygen

out Outlet

perm Permeate side

PS inlet Permeate side inlet

red Reduced

spec Specific

total Global

tr Transformer

T Turbines

t Total state

CHAPTER 1

Introduction

Contents

1.1 Background

OXYCOMBUSTION is a promising technology to reduce polluting gas production in the current industry. Instead of atmospheric air, it uses a mixture of high-purity oxygen with a thermal buffer (usually recycled gases that primarily are CO_2/H_2O), which is used to regulate the combustor temperature [5].

According to Huang et al. [5] and Koohestanian et al. [6], the benefits of oxycombustion are the reduction of heat losses (if correct combustor re-design is performed), its high potential to be integrated within industrial facilities, the NOx emissions avoidance due to the elimination of N_2 from the combustion process, and the possibility to separate CO_2 from water vapor in the flue gases, due to the different condensation temperatures of these components.

On the other hand, air separation is required to generate a high-purity oxygen stream. The most extended oxygen production method is cryogenic air separation (CAS). This method consists of the fractional distillation of air, considering the different boiling temperatures of its components. Cryogenic plants producing more than 150 tons of oxygen with a purity of 99.5% are reported, which can recover around 98% of the oxygen in the used air [7]. However, running this separation method could represent the expense of considerable gross power output in a plant, being a highly energy-intensive process [7].

Considering the above, the research of alternative methods for oxygen production is being performed to avoid the penalties in energy consumption that come with CAS usage. One of these alternative methods is membrane separation. The membranes for this application are usually fabricated using dense ceramic compounds called mixed oxygen ionic and electronic (MIEC) materials [8]. It has been found that implementing oxygen production cycles based on MIEC membranes reduces the energy penalty due to CAS use [9, 10, 11]. In this sense, using oxygen production cycles with MIEC membranes for air separation is an alternative in industrial applications such as ceramic facilities, power plants, or the automotive industry, where the possibility of reducing pollutant emissions and improving thermal efficiency can be considered.

This thesis has been developed at CMT-Motores Termicos, which has started researching this topic in recent years, publishing promising results in this area. Several works have been performed regarding applying oxycombustion in spark-ignition (SI) and compression-ignition (CI) engines. There is research about SI engines on the experimental and computational fluid dynamics (CFD) evaluation of the combustion process in oxyfuel conditions, considering operative constraints [12, 13]. These results have been considered to study the coupling of an oxygen production system that uses membranes with an oxyfuel SI engine [1]. Additionally, regarding CI engines, the researchers have followed a similar approach. First, CFD was used to study the oxyfuel combustion characteristics under CI engines [14]. Then these results have been used to study the coupling

of an oxygen production system that uses membranes with an oxyfuel CI engine working at full and part-load [15, 16]. The results found by the researchers are promising, and an initial prototype of a multi-cylinder engine coupled with an oxygen production cycle is under construction.

1.2 Motivation

The increasing emission of pollutants and greenhouse gases generated by the industry has led to stricter emission standards by the different authorities such as the European Union (EU), where the reduction of these emissions, the improvement of energy efficiency, and an increase in the share of renewable energies are the goals to achieve in the following years.

In this frame, the development of technologies that allow the use of residual energy sources such as exhaust gases in automobiles implies the increase of energy efficiency in the automotive industry, which is responsible for a considerable part of the pollutant and greenhouse emissions.

In this sense, using the energy in exhaust or residual gases to power a method of oxygen production is considered. This approach permits the implementation of oxycombustion during the operation of power production systems, being an alternative to accomplish the proposed objective by the EU.

In this sense, using the energy in exhaust or residual gases to power a method of oxygen production that permits the implementation of oxycombustion during the operation of power production systems is shown as an alternative to accomplish the proposed objective by the EU.

However, even if there are different studies where oxycombustion has been implemented in internal combustion engines, oxygen obtention is carried out from external sources or is not considered strictly in the analysis. At the same time, oxycombustion has been examined with in situ oxygen production in different industrial applications, where the most extended methods for oxygen production are applied. These methods have a highly-extensive energy consumption, penalizing the whole system performance.

1.3 Objectives

The main objective of this research is the assessment of an oxygen production cycle based on a MIEC membrane working in different industrial scenarios for oxycombustion purposes, emphasizing its integration within a spark ignition engine operation context. In this sense, three specific objectives are established, with a growing level of complexity.

Firstly, the design of an oxygen production cycle in the context of a ceramic plant that takes advantage of the waste heat found in the process. An initial

configuration of the cycle is shown where a set of turbochargers and a heat exchanger network is implemented to take advantage of the thermal energy in a waste stream of the process to achieve optimal conditions for air separation. This is performed to demonstrate the feasibility of this type of process in terms of energy and economic costs.

Second, the evaluation of the coupling of the oxygen production cycle and a continuous flow system: a power production plant (Graz Cycle). A stream that belongs within the process is deviated to take advantage of its high enthalpy to achieve air separation. The energy integration between both cycles is studied to establish differences between the operation with the base case. This case pushes further the limits of the oxygen production cycle, as the recovered heat is of lower quality.

Third, the assessment of the mentioned oxygen production cycle working with a pulsating flow system: a spark ignition engine. The engine operation working under oxycombustion is evaluated in different operation conditions, evaluating its performance in terms of fuel consumption and energy feasibility for oxygen production. In this case, the complexity of the analysis increases due to the presence of pulsating flow and the different levels of recoverable energy because of the different studied conditions. Additionally, there is a higher degree of coupling of the power cycle with oxygen production than the previous objective.

1.4 Contents

The presented work keeps the following order:

Chapter 2 presents a literature review, beginning with the main pollutant emissions in the automotive industry, the different normative that regulate them, and the most important strategies for emission reductions in spark ignition engines, such as EGR, turbocharging, three-way catalysts, or filters. In this sense, the concept of oxycombustion is shown, where its main advantages are exposed, considering different industrial applications of this concept. As oxycombustion typically requires air separation to extract oxygen from the atmospheric air, the most extended methods for air separation are presented, emphasizing mixed-ionic electronic membranes used during this work.

The working methodology is presented in Chapter 3, where the in-house software VEMOD is presented as the primary tool used to obtain this work's results. Also, the software IPSE-Pro is used when the Graz cycle study (Chapter 5) is performed. Additionally, the main models to perform calculations are presented. First, the model to calculate the operation of MIEC membranes and its limitations are presented. On the other hand, the methodology to model combustion under oxycombustion in spark ignition engines is shown, which is

based principally on experimental work performed in CMT facilities, from which different correlations for the main variables are determined, as well as operational limits. In addition, turbocharging modeling and the scaling process of off-the-shelf turbochargers for their selection are presented. The carbon capture model is presented, where its main assumptions are established. Finally, the methods used to calculate components such as heat exchangers, coolers, or pipes are presented.

The first assessment of the oxygen production cycle using MIEC membranes is presented in Chapter 4. This oxygen production cycle works in the context of a ceramic plant, where oxygen is required in the furnaces for its product elaboration. A high-temperature recycled stream drives the cycle, whereas a set of turbochargers and a heat exchange network are considered to take advantage of energy flows in the cycle. Two operation scenarios are considered, and their energy consumption and oxygen production differences are discussed.

In Chapter 5, the oxygen production cycle is coupled with the operation of a continuous flow power production cycle, the Graz Cycle. Two different membrane configurations are evaluated, implying differences in the system distribution. Additionally, their performances are compared with the base case operation, studying their primary differences considering thermal efficiency and specific oxygen energy cost, which are explained in terms of the energy integration of the different scenarios.

The integration of the oxygen production cycle in a pulsating flow system as a spark-ignition engine is studied in Chapter 6. This coupling is first evaluated under different working conditions, and then its performance is compared with the engine's operation working under conventional combustion conditions. Then, the system is assessed under part-load operation to mainly determine operative limits and in different altitude conditions to study the system's response under different atmospheric scenarios.

The last chapter, Chapter 7, summarizes the results obtained in this work and the main findings. Additionally, possible future works are proposed to improve the obtained results presented in the document.

1.5 References

[1] F. Arnau, R. Novella, L. M. García-Cuevas, and F. Gutiérrez. "Adapting an Internal Combustion Engine to Oxy-Fuel Combustion With In-Situ Oxygen Production". In: *ASME 2021 Internal Combustion Engine Division Fall Technical Conference*. American Society of Mechanical Engineers, Oct. 2021. DOI: 10.1115/icef2021-67707 (cit. on pp. vii, 2).

[5] X. Huang, J. Guo, Z. Liu, and C. Zheng. "Opportunities and Challenges of Oxy-fuel Combustion". In: *Oxy-Fuel Combustion*. Elsevier, 2018, pp. 1–12. DOI: 10.1016/b978-0-12-812145-0.00001-3 (cit. on pp. 2, 31, 32).

[6] E. Koohestanian and F. Shahraki. "Review on principles, recent progress, and future challenges for oxy-fuel combustion CO2 capture using compression and purification unit". In: *Journal of Environmental Chemical Engineering* 9.4 (Aug. 2021), p. 105777. DOI: 10.1016/j.jece.2021.105777 (cit. on pp. 2, 32).

[7] F. Wu, M. D. Argyle, P. A. Dellenback, and M. Fan. "Progress in O2 separation for oxy-fuel combustion–A promising way for cost-effective CO2 capture: A review". In: *Progress in Energy and Combustion Science* 67 (July 2018), pp. 188–205. DOI: 10.1016/j.pecs.2018.01.004 (cit. on pp. 2, 35–38).

[8] X. Zhu and W. Yang. "Introduction to Mixed Ionic–Electronic Conducting Membranes". In: *Green Chemistry and Sustainable Technology*. Springer Berlin Heidelberg, Nov. 2016, pp. 1–10. DOI: 10.1007/978-3-662-53534-9_1 (cit. on pp. 2, 35, 38, 39, 112, 135, 140).

[9] R. Castillo. "Thermodynamic analysis of a hard coal oxyfuel power plant with high temperature three-end membrane for air separation". In: *Applied Energy* 88.5 (May 2011), pp. 1480–1493. DOI: 10.1016/j.apenergy.2010.10.044 (cit. on pp. 2, 39, 141).

[10] A. Skorek-Osikowska, Ł. Bartela, and J. Kotowicz. "A comparative thermodynamic, economic and risk analysis concerning implementation of oxy-combustion power plants integrated with cryogenic and hybrid air separation units". In: *Energy Conversion and Management* 92 (Mar. 2015), pp. 421–430. DOI: 10.1016/j.enconman.2014.12.079 (cit. on pp. 2, 39).

[11] E. Portillo, L. M. G. Fernández, F. Vega, B. Alonso-Fariñas, and B. Navarrete. "Oxygen transport membrane unit applied to oxy-combustion coal power plants: A thermodynamic assessment". In: *Journal of Environmental Chemical Engineering* 9.4 (Aug. 2021), p. 105266. DOI: 10.1016/j.jece.2021.105266 (cit. on pp. 2, 38, 39, 141).

[12] J. Serrano, J. Martín, J. Gomez-Soriano, and R. Raggi. "Theoretical and experimental evaluation of the spark-ignition premixed oxy-fuel combustion concept for future CO2 captive powerplants". In: *Energy Conversion and Management* 244 (Sept. 2021), p. 114498. DOI: 10.1016/j.enconman.2021.114498 (cit. on pp. 2, 59, 151, 156, 161).

[13] J. R. Serrano, J. M. Díaz, J. Gomez-Soriano, and R. Raggi. "Exploring the Oxy-Fuel Combustion in Spark-Ignition Engines for Future Clean Powerplants". In: *ASME 2022 ICE Forward Conference*. American Society of Mechanical Engineers, Oct. 2022. DOI: 10.1115/icef2022-89167 (cit. on pp. 2, 33, 34, 42, 58, 59, 61, 62, 151, 156, 161).

[14] J. R. Serrano, G. Bracho, J. Gomez-Soriano, and C. Fernandes. "Development of an Oxy-Fuel Combustion System in a Compression-Ignition Engine for Ultra-Low Emissions Powerplants Using CFD and Evolutionary Algorithms". In: *Applied Sciences* 12.14 (July 2022), p. 7104. DOI: 10.3390/app12147104 (cit. on p. 2).

[15] J. Serrano, F. Arnau, L. García-Cuevas, and V. Farias. "Oxy-fuel combustion feasibility of compression ignition engines using oxygen separation membranes for enabling carbon dioxide capture". In: *Energy Conversion and Management* 247 (Nov. 2021), p. 114732. DOI: 10.1016/j.enconman.2021.114732 (cit. on pp. 3, 56, 152, 153).

[16] F. Arnau, G. Bracho, L. García-Cuevas, and V. Farias. "A strategy to extend load operation map range in oxy-fuel compression ignition engines with oxygen separation membranes". In: *Applied Thermal Engineering* 226 (May 2023), p. 120268. DOI: 10.1016/j.applthermaleng.2023.120268 (cit. on pp. 3, 202).

CHAPTER 2

Literature review

Contents

2.1 Introduction

THE previous chapter introduces the main objectives that shape the present work. This research explores technologies such as oxycombustion and air separation for oxygen production, considering their application in power plants.

Integrating these technologies with existing power plants can reduce fuel consumption and emission of pollutant gases, widely fitting in global emission standards, which are becoming stricter. For example, implementing oxycombustion can lead to a cleaner combustion, as nitrogen-based pollutants are eliminated due to the nitrogen removal from the process. This improvement could allow the fulfillment of the current regulations, also reducing the activity of reduction strategies as three-way catalysts or filters.

Oxycombustion is only possible if a high-purity oxygen stream can be obtained. In systems such as engines that work in transportation, it is essential to rely on oxygen production that occupies as little space as possible and brings less likely weight to the system. Additionally, the energy demand for oxygen production is essential during the system's operation.

On the other hand, considering that the exhaust gases in an oxycombustion process consist mainly of carbon dioxide and water vapor, the possibility of carbon capture is open, which is currently being researched as a promising alternative to generate zero-emission systems.

In this sense, this chapter elaborates on the main concepts treated in this thesis. First, emissions are considered: the formation mechanisms of the primary pollutant substances such as NOx, CO, or unburned hydrocarbons (UHC), the current emissions standards, especially their evolution and present limits, and the developed strategies used to reduce the pollutant emissions. Second, the concept of oxycombustion, its advantages, and its application in industrial contexts such as the cement industry, power plants, and engines.

Finally, the air separation methods for oxygen production are presented. Cryogenic air separation is initially presented, considering it is the most extended method. Then, alternative methods, such as adsorption and chemical looping, are briefly explained, finishing this part with the concept of air separation using membranes, which is the implemented air separation method in this thesis.

2.2 Emissions

Since the mid-20th century, pollution mainly caused by the effects of mass transportation has notoriously increased. In Los Angeles, phenomena such as smog started in the 1940s [17, 18], which is formed due to the presence of unburned hydrocarbons (UHC) and nitrogen oxides (NOx) that react with

atmospheric gases in the presence of sunlight [19]. Smog irritates the eyes and the respiratory tract of humans, which started to concern Californian authorities [19]. On the other hand, in Europe, the concern about carbon monoxide emissions started in the 1960s due to its direct harm to humans, as well as an increased interest in the appearance of acid rain started in the 1970s, correlating these events with a high concentration of pollutant gases [17].

These events were responded to by introducing exhaust emission thresholds, starting with the US in 1961, Japan in 1966, and Europe in 1970 [17], and drastic restrictions on specific substances as nitrogen oxides and hydrocarbon emissions began in US, Japan, and Central Europe in the 1980s [17, 18].

By the beginning of the 1990s, it was recognized that other exhaust emissions that were not directly harmful to humans affected the global equilibrium of the atmosphere [17]. In this context, the current emissions policies have been developed, where a deep understanding of pollutant gases formation in the combustion process leads to the creation of new technologies that reduce their final emission to the environment.

This section briefly explains the fundamentals of the leading pollutant gas formation, considering state-of-the-art studies on this topic. Then, the current standards in emissions of the leading developed countries (US and EU) and the standards of the principal emerging economies such as China and India, the most populated countries with several pollution problems, are exposed. Finally, the most used technologies to reduce emissions in the automotive industries' exhaust gases, such as exhaust gases recirculation (EGR) or three-way catalysts (TWC), are presented, as well as their functioning mechanisms and effects on the engine performance.

2.2.1 Formation mechanisms

This section deals with the formation mechanisms of the most critical pollutant substances that are found in the exhaust gases of an automobile: carbon monoxide (CO), nitrogen oxides (NOx), particulate matter (PM), and unburned hydrocarbons (UHC). It is also briefly considered carbon dioxide, mainly dependent on the engine performance [19]. Sulfur-based compounds formation are not considered, as they are mainly dependent on the fuel quality [19], a topic that is not contemplated in this research.

Carbon monoxide

CO appears as a fundamental, intermediate step in the oxidation process of a hydrocarbon, and usually, its formation comes under a lack of oxygen in the combustion process [17, 19]. Locally, rich-mixture conditions appear in engines, diminishing the oxygen concentration and promoting CO formation

[19]. The latter can occur in spark-ignition engines that generally operate using stoichiometric or rich mixtures, or in compression-ignition engines, which run under lean mixtures but present a heterogenous fuel concentration through the combustion chamber [19].

In spark-ignition engines, the formation of CO comes from dissociating carbon dioxide molecules at temperatures higher than 2,000 K, where the amount of CO depends on formation and oxidation processes, which are fast and slow reactions, respectively [19]. Initially, in the hydrocarbon combustion mechanism, CO formation is one of the main steps in the reaction, which is summarized in Equation 2.1, where R stands for the hydrocarbon radical.

$$\mathrm{RH} \longrightarrow \mathrm{R} \longrightarrow \mathrm{RO_2} \longrightarrow \mathrm{RCHO} \longrightarrow \mathrm{RCO} \longrightarrow \mathrm{CO} \tag{2.1}$$

Then, this CO is mainly oxidized in a slow reaction to form CO_2, whose primary oxidation reaction is shown in Equation 2.2.

$$\mathrm{CO + OH} \longleftrightarrow \mathrm{CO_2 + H} \tag{2.2}$$

At peak cycle temperatures and pressures, this reaction is in equilibrium. However, during the expansion process, the equilibrium is altered due to the decrease of cylinder temperature, leading to high values of CO at the exhaust gases [20]. In addition, it is known that CO is normally independent of other operating parameters such as compression ratio, load, spark ignition timing, or fuel injection mechanism [17], as it is highly independent when the engine operation is performed under excess air combustion [17, 18, 19, 20].

Zhao et al. [21] studied different emissions in a spark-ignition engine with direct injection, modifying the ignition timing and the EGR levels at two different speeds in a 1.8 L engine with a compression ratio of 9.6. Regarding CO, they found that ignition timing has an insignificant effect on its emission. On the other hand, high EGR rates reduce the oxygen concentration, increasing CO formation, while low EGR rate has a beneficial result, as the relative CO_2/CO ratio increases, cutting down the carbon dioxide decomposition.

Saw and Mallikarjuna [22] studied the effect of spark plug and fuel injector location on the mixture of a gasoline direct injection engine, where four cases were examined. The results have shown that the case with the best mixture stratification, which led to a better combustion process, exhibited the lowest CO emissions.

Jiang et al. [23] examined the combustion of different fuels and its effects on pollutant gas generation, changing spark timing and fuel-air ratio. It was found that changing the spark timing has no significant effect on CO emissions for all the examined fuels while increasing the amount of fuel in the combustion chamber leads to an increment in its emission.

In the same line of thought, Deng et al. [24] assessed lean and rich combustion in a motorcycle engine, exploring the emissions of CO and NOx. Regarding CO, it is seen that its emission drops by about four times when the air-fuel equivalence ratio changes from 0.85 to 1.1. Additionally, it was found that engine load and speed have no significant effect on CO emission, where high temperatures are still found to oxidize CO into CO_2 as the load is decreased and the temperature increase due to the increment of engine speed is compensated with the decrease in the reaction time.

Duronio et al. [25] found in different studies that an increase in the injection pressure induces a better mixture formation process, which leads to avoiding fuel-enriched zones in the cylinder, reducing CO formation.

On the other hand, CO formation in spark-ignition engines could increase at transient conditions such as acceleration, deceleration, or cold starting, as control of fuel metering has to be improved [20]. This phenomenon is studied by Zhu et al. [26], where a spark-ignition engine is assessed under a European driving cycle (NEDC). The study shows that CO formation is highly dependent on the oxygen concentration in the combustion chamber, which varies as the vehicle changes its speed.

The CO formation for diesel engines is less critical than in gasoline engines, as these engines mainly operate at lean mixture conditions, increasing the oxygen concentration [20, 27]. However, as diesel combustion and mixture formation are not homogeneous, fuel-enriched zones in the combustion chamber lead to CO formation [17, 19]. Otherwise, a lean mixture in some parts of the cylinder does not handle fast combustion as flame propagation is not possible, locally reducing the temperature and affecting the CO oxidation into CO_2 [19].

Pan et al. [28] tested a compression ignition engine with different types of fuel blends, including regular diesel, to examine the effect of intake temperature on the emissions performance. It was found that increasing the intake temperature leads to a higher level of cylinder gas temperature, accelerating the CO oxidation. When using regular diesel as fuel, CO emissions are under 1 g/kWh.

Considering different load levels, both studies from Hasan et al. [29] and Selvan et al. [30] conclude that, even for different fuel blends (including regular diesel), CO emissions are promoted at low loads, due to the low temperatures that retard the CO oxidation into CO_2.

Nitrogen oxides

NOx is a generic term to name the nitrogen oxides, mainly NO and NO_2, that are the most representative of these oxides [17, 18, 19, 20]. However, other nitrogen oxides are produced in the combustion, such as N_2O, NO_3, and N_2O_3 [17, 19]. N_2O has been gaining significant importance due to its notable impact as a greenhouse gas.

The predominant nitrogen oxide in exhaust gases is NO, produced due to the oxidation of atmospheric nitrogen in the combustion chamber [17, 19, 18]. The reaction of N_2 and O_2 demands breaking a robust triple bond of the molecular nitrogen. Oxygen cannot break this molecule even at high temperatures, as the reaction is too slow [19].

In this sense, the primary mechanism of NO production is a thermal mechanism known as the expanded Zeldovich mechanism, presented in the following reactions of Equation 2.3, Equation 2.4, and Equation 2.5.

$$N_2 + O \longleftrightarrow NO + N \tag{2.3}$$

$$N + O_2 \longleftrightarrow NO + O \tag{2.4}$$

$$N + OH \longleftrightarrow NO + H \tag{2.5}$$

The oxygen molecules are disintegrated at high temperatures, forming free oxygen atoms responsible for the latter reactions [19]. In addition, due to the high activation energy of the reaction, the thermal mechanism for NO production is less important at temperatures lower than 1,800 to 2,000 K [19], where its maximum formation occurs at 2,200 to 2,400 K [17].

Being that said, it could be stated that the NO formation due to this mechanism is highly influenced by the oxygen concentration, which depends on the air-fuel ratio in the reaction zone, the reaction temperature that affects the molecular oxygen dissociation, and the reaction itself, as well as the residence time of the gases in the reaction zone at a maximum temperature [18]. Thus, NOx formation occurs where the in-cylinder temperature and oxygen concentration are high, a situation that finds its maximum near-stoichiometric combustion with oxygen excess (λ around 1.1) [19].

On the other hand, it also must be mentioned the prompt mechanism in NO formation, which gain particular significance in fuel-enriched zones that involves hydrocarbon species that comes from the fuel decomposition. These species react with molecular nitrogen, forming intermedium nitrogen-based compounds that finally release NO [18, 19].

In addition to NO formation, it must be considered the formation of NO_2 and N_2O, which gain importance in compression ignition engines due to their formation at lean mixtures and low temperatures [17, 19]. In these engines, NO_2 could represent 10 to 30 % of the total oxide nitrogens, while for spark ignition engines, its exhaust concentration is negligible [17, 19, 20]. The formation of NO_2 occurs following the reaction expressed in Equation 2.6, Equation 2.7, and Equation 2.8.

$$NO + HO_2 \longleftrightarrow NO_2 + OH \tag{2.6}$$

$$NO_2 + H \leftrightarrow NO + OH \tag{2.7}$$

$$NO_2 + O \leftrightarrow NO + O_2 \tag{2.8}$$

NO formed in the flame zone is converted to NO_2 when it is transported to low-temperature zones, which is rich in HO_2 [19, 20]. Normally, the NO_2 reacts with H and O ions, rapidly converting NO_2 into NO. However, as the flame is propagated, it mixes with cooler fluid inside the cylinder, quenching its propagation, reducing the temperature, and promoting NO_2 formation [20]. The latter explained the increment of NO_2/NO ratio at low loads in compression ignition engines, where low temperatures and air excess promote NO_2 formation [20]. Regarding N_2O, it appears in formation processes of NO at low temperatures and lean mixtures.

Its consideration gains importance as reduction strategies of NOx emissions that imply the reduction of temperatures (as EGR) in the cylinder limits the formation of NO but promotes the generation of N_2O [19]. In addition, N_2O can also be formed in reactions that involve volatile compounds that are nitrogen-based (mainly NH_3 and HCN) [19].

On spark-ignition engines, Zhao et al. [21] study the effect of EGR and spark timing in NOx emissions in a 1.8 L engine with a compression ratio of 9.6. A low EGR rate has no significant effect in NOx formation, having a considerable impact at EGR rates greater than 7.1 %. Emissions lower than 100 ppm are found at retarded ignition timings (5° before top dead center (BTDC)) and high EGR rates (13.5 %). Delaying the ignition timing helps to reduce the maximum cylinder temperature, reducing the time at high temperatures, while EGR reduces the peak temperature and oxygen concentration. The effect of both strategies helps control NOx emissions.

Lattimore et al. [31] study the effect of EGR in the combustion and emissions of a direct injection spark-ignition engine of 0.56 L and a compression ratio of 11.5. They implemented three different load levels at a constant speed. At the minimum load (0.55 MPa of indicated mean effective pressure (IMEP)), there is a remarked reduction in NOx of 64.3 % when a EGR rate of 13 % is implemented, as the in-cylinder temperature and oxygen concentration are reduced.

Similarly to Zhao et al. [21], Polat et al. [32] assessed the effect of EGR and ignition timing in a spark ignition engine. Using gasoline as fuel, they numerically examined an engine with 0.6 L displacement and a compression ratio of 10. Higher levels of EGR reduce the oxygen concentration as expected. For all the studied ignition timings, EGR has a positive effect in NOx reduction, while advancing the ignition increases the NOx formation.

Saw and Mallikarjuna [22] studied the effect of the location of the spark plug and fuel injector on the mixture in a spark ignition direct injection engine

and the impact on engine performance and emissions. They performed CFD calculations in a single-cylinder engine of 0.4 L and a compression ratio of 10.6 over four different configurations. Regarding NOx, the configuration with the best performance exhibits the highest emissions. As it has better combustion efficiency, the cylinder temperature has a higher peak, promoting the reactions that form NOx.

Jiang et al. [23] examined the effect of ignition timing and fuel-air ratio in a 1.5 L spark ignition engine using different gasoline surrogates as fuels. The authors found that delaying the ignition in 6ºCA decreases the emission of NOx by 50 % for gasoline, obtaining similar effects for the other fuels. On the other hand, increasing the fuel-air ratio from 0.9 to 1.1 helps decrease emissions by almost 75 % due to the diminished oxygen concentration.

The same trend regarding oxygen concentration is found for smaller engines that are also spark-ignited. A study by Deng et al. [24] in a 0.65 L single-cylinder engine with a compressor ratio of 10.5 used in a motorcycle shows that decreasing the fuel-air ratio from 1.1 to 0.85 at full load leads to an increment of NOx emissions of about 2.4 times. Regarding engine load, low loads lead to a decrement in NOx generation as the in-cylinder temperature is reduced. Additionally, increasing engine speed reduces the reaction times for NOx formation, reducing emissions.

Regarding compression ignition engines, the study by Pan et al. [28] uses a six-cylinder engine where the effect of intake temperature and methanol substitution rate is examined. The engine has a total displacement of 9.7 L and a compression ratio of 17, producing a maximum power of 247 kW. In this case, NO_2 is considered, as it acquires importance in these engines. As the intake temperature increases, the in-cylinder temperature also tends to increase, leading to an increment in NOx formation. For a reduction of 60 °C in the intake temperature using pure-diesel combustion, NOx emissions decrease around 25 %. On the other hand, as the intake temperature increases, the emission of NO_2 is reduced, as its production is performed at relatively low temperatures, representing 20 % of the total NOx emissions at the highest intake temperature.

Similarly, Rakopoulos et al. [33] numerically assessed a compression ignition engine with direct injection to examine the effect of EGR rate and temperature on engine performance and emissions. The engine has a 0.4 L displacement and a compression ratio of 19.8. An EGR rate of 30 % at a relatively low temperature reduces NOx generation by 64.78%. At the same time, a high-temperature EGR leads to a lower reduction of 57.09% for the same rate, as its higher temperature leads to higher in-cylinder temperatures.

Sindhu et al. [34] studied the effect of split injections in a compression ignition engine with a displacement of 0.55 L engine with a compression ratio of 16.5. The split injection with a small amount injected in the first pulse (25 %) reduces the in-cylinder temperature, diminishing NOx emissions by around

57 %.

Hasan et al. [29] studies a 3 L compression ignition engine with direct injection. Different methanol concentrations in a diesel-based fuel are examined, operating the engine at five load conditions to assess its power production, thermal efficiency, and emissions performance. Regarding NOx emission, the increment of load leads to increase emissions, while the presence of oxygen in methanol promotes NOx formation. Similar results are found by Selvan et al. [30] in a 0.7 L engine at different loads.

Regarding NOx emissions on transient conditions, Zhu et al. [26] studied a turbocharged spark ignition engine with direct injection with a 0.35 L displacement and a compression ratio of 10. The authors studied a driving cycle (NEDC) and its effect on combustion and emissions performance at cold start conditions. It was found that acceleration zones of the cycle, where load and speed increases, lead to an increment of in-cylinder temperature, producing NOx concentrations. On the other hand, deceleration conditions lead to the opposite situation, where reduction of NOx is achieved.

Unburned hydrocarbons

The presence of unburned hydrocarbons (UHC) in the exhaust gases results from incomplete combustion of the hydrocarbon fuel [17, 19, 20]. Typically, unburned hydrocarbons in the exhaust gases represent from 1 to 2 % of the total fuel in spark ignition engines, a value much less on compression ignition engines [20]. Several reasons lead to incomplete combustion: flame quenching at the cylinder walls, insufficient fuel evaporation, fuel leakage, short fresh air, and fuel circuit, trapped fuel in cylinder crevices, or local fuel-enriched zones, among others [19].

For lightly lean mixtures, there is an excess of oxygen and high temperatures in the cylinder, which induces a reduced appearance of hydrocarbons in the exhaust gases due to its oxidation in the exhaust manifold (forming CO) [19]. In this sense, it is seen that the excess fuel in the cylinder leads to incomplete combustion as the lack of oxygen does not allow the fuel to oxidize correctly, and, on the other hand, a high excess of oxygen leads to difficulties in the flame propagation, which causes that some parts of the mixture are not burned [17, 19].

The most important phenomenon that causes unburned hydrocarbon emissions is the flame quenching or misfiring in the walls of the engine combustion chambers. The air-fuel mixture near the cylinder head, liner, or piston transfers heat to these surfaces, reducing its temperature and affecting the flame propagation, which leaves unburned fuel in the cylinder [17, 19, 20].

It is important to remark that some of the hydrocarbons found in the exhaust gases are not presented in the original composition of the fuel, indicating that

different reactions as pyrolysis and synthesis, are performed inside the cylinder during the combustion process [20]. The composition of hydrocarbon fuels in the exhaust gases varies depending on the fuel composition and combustion type. In spark ignition engines, heavy compounds (with more than twelve carbons in their structure) only represent 5 % of the total unburned hydrocarbons, while for compression ignition engines, this number is between 65 to 82 % [19]. The latter acquires importance as the different hydrocarbons have different toxicity and reactivity with atmosphere components, demanding that future regulations specify the various hydrocarbons emitted.

For spark ignition engines, the application of direct injection has reduced UHC emissions, as the fuel is injected in the compression stage of the cycle, avoiding fuel losses due to short circuit in the valve crossing time [19]. However, there are still present misfiring and partial burns in the cylinder walls, too lean zones in the cylinder that limit the flame propagation or too rich zones that react too slowly to burn completely, as well as trapped fuel in small volumes of the cylinder, as it is shown by Drake et al. [35] working with experimentally with a 0.5 L engine with a compression ratio of 6.5.

Zhao et al. [21] reported that advancing the ignition timing increases the emissions remarkably, and reducing the oxygen concentration using EGR has the same effect. For a constant spark timing, the change of the EGR rate from 0 to 15 % can double the emissions while advancing the combustion by 20° of crank angle degree (CAD) with a constant EGR rate (from 5° to 25° before top dead center (BTDC)), increases around 1.5 times the UHC emissions. EGR decreases the oxygen concentration, affecting the combustion processes and the fuel that reacts. On the other hand, advancing the ignition timing leads to a higher density at the end of combustion, which affects the mass that is finally contained in the small crevices of the in-cylinder geometry [19] as well as reduces the exhaust temperature affecting the oxidation of hydrocarbons in the exhaust tailpipe that reduces the emissions [27, 36].

Lattimore et al. [31] found that increasing the load in their studied engine leads to an increment in the in-cylinder temperature, thus, promoting better combustion and reducing the UHC emissions. On contrary, reducing the oxygen concentration promotes UHC emissions, increasing 48.3 % in the lower assessed load (0.55 MPa of IMEP) across the EGR range examined.

Jiang et al. [23] observed no significant increase in the UHC emissions while changing the ignition timing of their experiments. They examined a narrow range of ignition timings (from 3° BTDC to 3° ATDC) where the effects of reducing the fuel-air mixing time before the combustion start and its subsequent accumulation in the cylinder crevices are compensated with the increasing temperature that promotes the combustion completeness—on the other hand, increasing the fuel-air ratio from 0.9 to 1.1 leads to an increase of more than 40 % in UHC emissions.

Different operation cases were examined by Zhang et al. [36] with different injection pressures, excess air ratio, or EGR. In their experimental facilities, they found that increasing the injection pressure from 7 to 8.5 MPa improves the mixing process in the cylinder, leading to better combustion. Higher increases are not recommended as fuel impingement could be produced, deteriorating combustion. A small increment from 1 to 1.13 in the excess air ratio, where the oxidation process of hydrocarbons is facilitated, helps reduce UHC in the exhaust gases. On the other hand, the presence of 20 % of EGR reduces flame propagation speed, combustion rate, and the in-cylinder temperature, promoting UHC emissions. Finally, the more advanced spark timing (45° BTDC) leads to higher UHC emissions.

In their numerical analysis, it was found that the decrease in oxygen concentration via EGR has the most decisive influence on the UHC emissions at stoichiometric combustion (over 55 % of importance), while using an excess air ratio of 1.2 has its most important variable (over 40 % of importance) in the injection pressure, that ensures a good mixing in the cylinder.

Similar trends are found in the literature for compression ignition engines, although lower levels of UHC emissions are generally presented in these engines due to the regular working of these engines under lean conditions [27]. Pan et al. [28] found that the increase in intake temperature led to an increase in the cylinder gas temperature, reducing flame quenching and finally controlling the UHC emissions.

Hasan et al. [29] found that increasing the load in the engine operation reduces UHC emissions. Increasing the power production from 20 kW to 45 kW reduces the UHC concentration by around 50 % when using regular diesel. Besides decreasing in-cylinder and exhaust temperatures as the load goes down, lower loads operate with a rich equivalence ratio during the combustion diffusion stage, promoting even more UHC emissions. However, when a low-load and poor-performance engine increases, the load leads to poor fuel distribution, which causes a slight increase in the UHC emissions, according to Selvan et al. [30].

For transient conditions, Zhu et al. [26] concluded that idling conditions increase the UHC emissions, as well as the deceleration of the engine due to a decrease in the oxygen concentration in the cylinder. The authors found that stages at very low loads, low temperatures, and the low amount of fuel in the cylinder influence UHC emissions.

Particulate matter

Within internal combustion engines, particles are considered any matter in the exhaust gases in the solid or liquid state near ambient conditions, according to Payri et al. [19]. A distinction has to be made between compression ignition and spark ignition engines regarding particulate matter (PM) emissions. Com-

pression ignition engines work using high injection pressure (up to 200 MPa), with a mixture formation within the cylinder, causing considerable particulate emissions, according to Uberall et al. [37]. Meanwhile, spark ignition engines can operate with an internal or external mixture, with an injection pressure of 20 MPa when a direct injection is performed. Due to the internal mixture and partially diffusive combustion, direct injection spark ignition engines also emits particles. Nonetheless, the emissions are 80 % lower than for a compression ignition engine without a particulate filter [37].

Particles in compression ignition engines usually are hydrocarbon particles and compounds that form soot, according to Basshuyen et al. [17]. Several intermediate reactions, such as cracking, dehydration, and polymerization, are involved in soot formation, primarily determined by the local temperature (800 to 1,400 K) and the oxygen concentration [17]. The premixed combustion region with relative fuel-air ratios higher than 4 promotes the soot formation, depending on the hydrogen and oxygen content of the used fuel [19].

On the other hand, spark ignition engines' particulate formation occurs in six processes according to [37]: pyrolysis, nucleation, surface growth, coalescence, agglomeration, and oxidation. During pyrolysis, the higher molecular hydrocarbon particles decomposed into smaller molecules in a reaction of high activation energy, occurring at 1,900 to 2,300 K and low oxygen concentration. The primary particles formed during this process coagulate in a nucleation process after the temperature peaks in the cylinder, forming bigger particles. Then, the particles collide in the exhaust line, increasing the particle size [37].

On compression ignition engines, Rakoupoulos et al. [33] study the impact of EGR in the formation of emissions of an engine of 0.4 L with a compression ratio of 19.8 under different injection timings and loads. Retarding the injection timing leads to less time for mixture formation, increasing soot emissions while decreasing NO emissions. Additionally, soot emission increases with the increment of EGR rate due to the reduction of temperature and oxygen concentration that ensures complete combustion while decreasing NOx.

The effects of fuel injection and dilution using EGR in a diesel engine of 0.55 L are also analyzed by Sindhu et al. [34]. Higher in-cylinder temperatures with advanced injection timing lead to a reduction in soot formation due to an improvement in the homogeneity of the mixture, which ensures a better combustion process. An opposite effect is found with increasing the EGR, which increases PM generation, especially soot.

Selvan et al. [30] study the performance of a compression engine with different fuel blends at different load conditions. The engine has 0.66 L and a compression ratio of 18. As mentioned, PM is formed due to rich-fuel zones promoting a low combustion efficiency. It was found that the particle emissions increased with the engine's load.

On spark ignition engines, Saw and Mallikarjuna. [22] studies a spark

ignition engine of 0.4 L and a compression ratio of 10.6, showing that increasing combustion efficiency, a consequence of a good mixing process, reduces soot emissions. Nonetheless, this promotes the formation of NOx due to high temperatures in the cylinder.

Jiang et al. [23] studied the effect of different gasoline blends at different spark timing and equivalence ratios in engine performance and emissions in a spark ignition engine of 1.5 L. Regarding particulate emissions, they found that advanced spark timings reduce the formation of the particles while retarding the spark timing promotes their oxidation. The fuels with more heavy components produce a higher density of particles in the exhaust. Additionally, increasing the oxygen content was found to promote complete combustion, thus, reducing PM formation.

It can be seen that there is a trade-off between the formation of NOx and PM. The conditions that lead to higher rates of NOx formation induce the reduction of PM and vice-versa. Thus, the operating conditions must be selected to ensure better conditions for the emissions of the NOx and PM.

2.2.2 Standards

Road transport is a significant source of pollutant emissions worldwide. According to the International Council on Clean Transportation [38], the transportation sector accounts for 29 % of the total greenhouse emissions in the European Union, while in the United States, this value is 28 % according to EPA [39].

In this sense, international efforts are being made; where global leaders created the Paris Agreement in 2015, whose main objective is to reduce greenhouse emissions substantially to limit the global temperature increase to 2 °C, proposing more significant efforts to even limit this increase in 1.5 °C [40].

According to Ribeiro et al., [41], the European Union and the United States are pioneers in creating regulations, guiding the rest of the world authorities to generate their normative. Thus, an overview of the leading governments, the European Union and the United States, regarding emissions limitations in the transport sector is presented, showing their progression over time and their effects on emissions.

United States

The first vehicular emission standard was established in the United States in 1965, based on the federal law Clear Air Act [41]. Since then, California has pioneered these regulations due to its particular climate, promoting pollutant substance accumulation with lower thresholds except for CO [17].

Currently, Tier regulations established emissions limitations, where Tier 1 and 2 were defined in the Clear Air Act Amendments of 1990, while EPA adopted the Tier 3 emission regulations [42].

The application of these regulations does not start with a sharp cut-off date. Instead, the emission standards are phased-in over some years, where manufacturers must certify that the percentage of new vehicles that are up to the new standards is growing in a particular value [42]. In this sense, the strategy intends to consolidate all the requirements in the national territory, for which more extended periods are needed between two implementation stages [41]. The chronology of the Tier regulations follows the next order:

- Tier 1: published in 1991, progressively applied from 1994 to 1997.
- Tier 2: released in 1999, used gradually from 2004 to 2009.
- Tier 3: published in 2014, expected to be used from 2017 to 2025 [42].

Initially, Tier 1 was solely applied to light-duty vehicles below 3,855 kg. In contrast, Tier 2 extended the applicability to vehicles below 4,536 kg and, finally, Tier 3 added heavy-duty vehicles up to 6,350 kg [42].

Since Tier 2, the standards are structured in different certification levels or bins, where the manufacturers can choose to certify a particular vehicle in any of the available bins. Initially, there are temporary bins under which the manufacturers can start their fabrication, ending in permanent bins. At the same time, emissions limits apply to all vehicles regardless of the fuel they use [43]. Nonetheless, when the legislation has to be fully applicated, the whole fleet sold must have an average standard value of emissions. For Tier 2, this average value is defined regarding NOx emissions, with an average value of $0.043\,\mathrm{g\,km^{-1}}$ [43]. In contrast, a stricter value is found for Tier 3, defining its limiting average value regarding non-methane and oxygenated hydrocarbons (NMOG) and NOx as $0.018\,\mathrm{g\,km^{-1}}$ [44]. In all the cases, an intermediate life of the vehicle (5 years) is considered.

Table 2.1 shows the limit values of Tier regulations, where for Tier 2 and 3, each pollutant substance is shown as a range between the maximum and the minimum value of the permanent certification bins, while a range is shown for Tier 1, where the limits are obtained between the maximum and the minimum limit among the vehicle categories.

Regarding its effects, Ribeiro et al. [41] reported from different authors that a reduction of 80 % in organic compounds is achieved associated to the application of Tier 1 regulations. On the other hand, a reduction of 24 % and 21 % on particular matter concentration was achieved in Los Angeles, comparing the periods 2002-2006 and 2008-2012. Meanwhile, from 2014 to 2017, the decrease

Spark-ignition	CO [$g km^{-1}$]	UHC [$g km^{-1}$]	NMOG [$g km^{-1}$]	NMOG + NOx [$g km^{-1}$]	NOx [$g km^{-1}$]	PM [$g km^{-1}$]
Tier 1	2.11 3.10	0.24 0.25	-	-	0.25 0.68	0.05
Tier 2	2.11	-	0.05 0.06	-	0.03 0.09	0.006 0.012
Tier 3	0 2.61	-	-	0 0.01	-	0 0.002
Comp.-ignition	CO [$g km^{-1}$]	UHC [$g km^{-1}$]	NMOG [$g km^{-1}$]	NMOG + NOx [$g km^{-1}$]	NOx [$g km^{-1}$]	PM [$g km^{-1}$]
Tier 1	2.11 3.10	0.24 0.25	-	-	0.25 0.62	0.05
Tier 2	2.11	-	0.05 0.06	-	0.03 0.09	0.006 0.012
Tier 3	0 2.61	-	-	0 0.01	-	0 0.002

Table 2.1: Tier limits for light-duty vehicles. Data obtained from [43, 44, 45]

in annual mean concentrations was 7.94 to 19.54 %, depending on the type of particulate matter.

Currently, Tier 3 is being applied. According to EPA [46], Tier 3 intends to reduce the emissions of NOx in 25 %, CO in 24 % and UHC in a maximum value of 29 %, depending on the component. These actions intend to reduce up to 2,000 premature deaths and 30,000 upper and lower respiratory symptoms in children.

European Union

European regulations started in 1970 with the directive 70/220/CE, from which the following standards are derived. The most significant shift occurred in 1992, beginning with Euro standards, dramatically reducing the emission limits while accounting for the emissions in cold-starting of engines, leading to a substantial improvement from the manufacturers, being the leading cause of the introduction of three-way catalysts (TWC) in spark-ignition engines [19]. In this sense, the chronology of the Euro regulations follows the next order:

- Euro 1: Released in 1992, initially for passenger cars, dividing the emission limits for petrol and diesel engines.
- Euro 2: Started its implementation in 1996, lowering the CO emission limits, as well as the combined limit for UHC and NOx.
- Euro 3: Began in 2000, changing the test procedures, where the emissions sampling started since the engine's start-up, eliminating the idling period. Additionally, the CO and PM emissions were further lowered for compression-ignition engines. In this stage, a separate limit for NOx emissions was introduced in compression-ignition engines, while for spark-ignition, different limits of UHC and NOx were introduced.
- Euro 4: Started its implementation in 2005, whose primary focus was the reduction of emissions in compression-ignition engines, especially regarding the particulate matter and NOx.
- Euro 5: Implemented in 2009, the standard was introduced in two stages in compression-ignition engines, while for spark-ignition engines, only one step was implemented. Particulate matter was remarkedly tightened, leading to compression-ignition engines requiring filters in all cases. Meanwhile, due to the increasing use of direct injection in spark-ignition engines, particulate matter limits were imposed for the first time. Additionally, NOx emissions limits were made stricter.
- Euro 6: Started in 2014, this stage imposed a considerable decrement in NOx emissions for compression-ignition engines. In this sense, effective after-treatments such as selective catalytic reduction (SCR) or diesel oxidation catalyst (DOC) were required to achieve the new limits. Additionally, stricter and more realistic tests were added to measure emissions [47].

Considering this, Table 2.2 shows the limit values of Euro regulations.

Regarding its effects, Ribeiro et al. [41] reported that different authors agree on the effectiveness of these standards since the application of Euro 1. From 2006 to 2015, a significant decrease in particulate matter and NO_2 concentrations was reported due to the application of Euro 4 to Euro 6 standards.

Euro 7 is the next stage in Euro standards, where the new air quality standards were proposed in October 2022 to ensure cleaner transportation, especially in big cities. The further emission limitations do not depend on the type of technology or fuel used in the engines, placing the same limits independently if the engine is a spark-ignition or compression-ignition or even an electric car [48]. Table 2.3 show the limits of Euro 7.

The standard intends to broaden the range of driving conditions while testing, including temperatures higher than 45 °C in the test conditions, to

Spark-ignition	CO [$g km^{-1}$]	UHC [$g km^{-1}$]	UHC + NOx [$g km^{-1}$]	NOx [$g km^{-1}$]	PM [$g km^{-1}$]
Euro 1	2.72	-	0.97	-	-
Euro 2	2.20	-	0.50	-	-
Euro 3	2.30	0.20	-	0.15	-
Euro 4	1.00	0.10	-	0.08	-
Euro 5	1.00	0.10	-	0.06	0.005
Euro 6	1.00	0.10	-	0.06	0.005
Euro 7*	0.50	0.10	-	0.06	0.0045
Compression-ignition	CO [$g km^{-1}$]	UHC [$g km^{-1}$]	UHC + NOx [$g km^{-1}$]	NOx [$g km^{-1}$]	PM [$g km^{-1}$]
Euro 1	2.72	-	0.97	-	0.14
Euro 2	1.00	-	0.90	-	0.10
Euro 3	0.66	-	0.56	0.50	0.05
Euro 4	0.50	-	0.30	0.25	0.025
Euro 5	0.50	-	0.23	0.18	0.005
Euro 6	0.50	-	0.17	0.08	0.005

Table 2.2: Euro limits for light-duty vehicles. Data obtained from [19, 47]

NOx [$g km^{-1}$]	0.060
PM [$g km^{-1}$]	0.0045
CO [$g km^{-1}$]	0.500
HC [$g km^{-1}$]	0.100

Table 2.3: Euro 7 limits for light-duty engines. Data obtained from [49]

ensure better emissions control. Additionally, the limits are tightened again, setting specific limits on N_2O in heavy-duty automobiles. Euro 7 is also the first emission standard that regulates tire microplastic emissions. The compliance for cars checking double the requirements compared with Euro 6, ensuring that vehicles stay clean for extended periods. Finally, an important issue supported in Euro 7 is the deployment of electric vehicles, regulating the durability of batteries installed in cars [48].

Euro 7 is expected to be implemented in 2025 for light-duty vehicles and in 2027 for heavy-duty vehicles, where NOx and PM reduction is expected to be lowered by 35 % and 13 % in light-duty and 56 % and 39 % in heavy-duty

vehicles, respectively, from a sector that represents 39 % of NOx (47 % in urban areas) and 11 % of particulate matter emissions [50].

Other standards

Other standards, such as China's and India's, are increasing their importance due to their population and economic growth weight, which are mainly based on European and American standards. In China, the current standard China 6 was issued at the end of 2016, starting its application in two phases: China 6a was proposed to begin in 2020, although delayed to 2021, while China 6b is planned to start applying in July 2023. China 6 uses European standards as a reference while coordinating the technical regulations with the standards of the United States. Nonetheless, the China 6 restrictions are slightly stricter than its equivalent European and less severe than American standards [51]. Meanwhile, the current Indian standard, Bharat Stage VI, was first issued in 2016, while started its application in 2020, aligning the Indian motor regulations with European Union standards [52].

2.2.3 Reduction strategies

According to Payri et al. [19], there are two types of technical solutions to reduce the emissions from internal combustion engines:

- Active solutions: The engine design and its components are affected.
- Passive solutions: The emissions are reduced using certain elements in the exhaust line of the engine, which are called aftertreatment systems.

Among the active solutions, it can be found strategies such as the redesign of the combustion chamber to avoid UHC accumulation in cylinder crevices, changes in the injection system to enhance the fuel distribution in the in-cylinder mixture, or modifications in valve timing to reduce NOx emissions. Exhaust gas recirculation (EGR) and turbocharging are the treated active solutions in this section, two of the most extended strategies for compression and spark ignition engines.

On the other hand, according to Heywood [20] and Leach et al.[53], in spark-ignition engines, the most common strategy to reduce emissions in the exhaust gases is the application of three-way catalysts (TWC), which are mainly used when stoichiometric combustion is performed. On the other hand, compression-ignition engines use diesel oxidation catalysts (DOC) to reduce hydrocarbon concentration and CO emissions. At the same time, selective catalytic reduction (SCR) is applied to diminish NOx emissions. Additionally, gasoline and diesel particulate filters (GPF and DPF) reduce particulate emissions.

Active strategies

Regarding active solutions, EGR is the principal technique to control NOx formation, according to Heywood [20]. Part of the exhaust gases are recirculated, whose rate is controlled by a throttling valve that controls the flow to the engine intake. According to Payri et al. [19], the addition of CO_2 and steam to the in-cylinder mixture leads to an increase in the specific heat and a reduction in the combustion speed, for which the flame temperature decreases, affecting NO formation. Nonetheless, according to Heywood [20], the decrease in the burning rate leads to higher UHC emissions. On the other hand, EGR does not significantly affect CO emissions.

Piqueras et al. [54] study the effect of EGR in a turbocharged spark-ignition engine. The engine displacement is 1.3 L, with a compression ratio of 10.6. At 3,000 rpm and medium load (1.2 MPa of BMEP), an EGR rate of 26.3 % leads to a reduction of 93 % in the NOx emissions, while increasing in 60 % the UHC emissions and a slight decrease of CO emissions of 15 %. In general, an approximately linear decay of NOx and an increase in UHC is obtained, showing the reduction of the in-cylinder temperature and the flame rate as the main reasons for this phenomenon. Additionally, if an additional aftertreatment process, such as a catalyst, is implemented, the oxygen concentration reduction in the exhaust line affects the aftertreatment performance.

Shen et al. [55] studied the effect of low-pressure and high-pressure EGR on the performance and emissions of a turbocharged spark ignition engine with direct injection. An engine of 1.5 L is implemented, with a compression ratio of 10.5. The low-pressure EGR consists of recirculating exhaust gases from the exhaust turbine to the compressor intake. Meanwhile, the high-pressure EGR takes the exhaust gases immediately after the exhaust manifold to the intake manifold. A previous cooling process is performed not to harm the performance of the compressor or the engine.

In general, the expected behavior of NOx, UHC, and CO emissions are achieved, where the higher NOx reduction is found at full load and 2,000 rpm, where an EGR rate of nearly 14 % leads to a reduction of NOx around 70 % compared with the case without EGR. Simultaneously, the UHC emissions increased by around 50 %.

Regarding the differences in EGR strategies, low-pressure EGR demands more power from the turbocharger to boost the mixture of fresh air and EGR. At the same time, high-pressure EGR leaves the turbine with less available energy to move the compressor. Additionally, the limitation of low-pressure EGR is mainly limited at high speed due to the increase of the coefficient for variation of the indicated mean effective pressure. High-pressure EGR at low engine speed is limited because of the minor pressure difference between the exhaust and intake manifolds.

Rakopoulos et al. [33] studied the effect of EGR rate and temperature on the combustion and emissions of a compression ignition engine. The engine displacement of the studied engine is 0.4 litre with a compression ratio of 19.8. Using hot EGR leads to higher levels of in-cylinder temperature, which reduces the effect of NOx reduction. Compared with the base case without EGR, hot EGR decreases in 57.09 % the NOx emissions using a EGR rate of 30 %, while cold EGR leads to a decrease of 64.78 % for the same operation conditions.

On the other hand, the main objective of turbocharging is to increase the specific power production of an engine by increasing the intake density, according to Payri et al [19] and Heywood [20]. In this sense, for similar power production, smaller engines with turbocharging have fewer emissions of UHC and CO due to a better mixing process. This enhances the mixing process, which leads to a better combustion process, a relative reduction in the heat losses, and a possible improvement in the pumping losses are the reasons for better engine performance, for which the brake fuel consumption is reduced, and the emissions per power produced are diminished. Nonetheless, special attention must be given to NOx emissions due to increased in-cylinder temperatures and better combustion process. This effect is reduced by implementing intercooling at the engine intake.

Mahmoudi et al. [56] simulate the effect of turbocharging on the emissions of a spark-ignition engine. The engine has a displacement of 3 L and a compression ratio of 10. The addition of turbocharging increases the maximum delivered power by 95 %. For all the emissions concentrations, the turbocharged case exhibits higher concentrations. Nonetheless, if the brake-specific emissions are considered, the turbocharged emissions values are lower than the naturally aspirated case. The latter suggests that using a smaller turbocharged engine capable of delivering the same power range as the naturally aspirated engine will improve emissions performance for all the pollutants.

Silva et al. [57] studied the effect of downsizing and turbocharging on the performance and emissions in a series of engines. A base naturally aspirated engine of 1.6 L is selected to perform the study, where a geometry reduction of the engine is made, maintaining the main geometry proportions of the engine, creating four turbocharged engines from 1.0 to 1.6 L. The specific emissions of CO_2, UHC, and CO are reduced by decreasing the engine displacement and operating above 3,000 rpm, being comparatively lower than the emissions of the base naturally aspirated engine. In contrast, the specific emissions of NOx grow with the displacement decrease but are still smaller than that for naturally aspirated 1.6 L engine.

Passive strategies

For spark-ignition engines, three-way catalysts (TWC) are the main aftertreament device used to reduce the emissions of CO, NOx and UHC [19]. In general, the catalytic reactors promote the oxidation and reduction reactions that have not reached the chemical equilibrium at the temperature of the exhaust gases at the outlet of the engine cylinders [19]. The presence of a catalytic substance allows the system to perform better and lower working temperatures are required.

At the TWC, oxidation and reduction reactions are performed. For the oxidation reactions, the oxygen reacts with CO and UHC, forming CO_2, while the reduction reactions are performed in the presence of CO, UHC and H_2, elements that promote the reduction of NOx into N_2.

In this sense, the TWC can only operate adequately in a narrow range of air-fuel equivalence ratio (0.998 to 1.007 according to Payri et al. [19]), for which these devices are mainly used in spark-ignition engines that operate with homogeneous mixture, requiring an exact control system.

Lou et al. [58] study the effect of various engine operation parameters in a spark-ignition engine working with natural gas. The engine has a displacement of 12.4 L and a compression ratio of 11.46. An optimum air-fuel equivalence ratio range between 0.995 to 1 was found, agreeing with the range shown previously, where conversion efficiencies near 100 % are found. Compared with engine speed, engine load has a relatively small effect on exhaust temperature but greatly affects the flow velocity and NOx and UHC emissions.

Bae et al. [59] study the response of a TWC at different temperatures and air-fuel equivalence ratios. In this case, the exhaust gases compositions are simulated in function of the combustion stoichiometry. Temperatures higher than 200 °C promote the conversion of NOx, CO, and UHC. Working with an air-fuel equivalence ratio of 1.01 leads to a maximum NOx conversion of 40 %, while using stoichiometric combustion allows a conversion rate near 100 % at temperatures higher than 400 °C. In contrast, maximum CO conversion rates of 60 % can be achieved working with an air-fuel equivalence ratio of 0.98, while values from 1 to 1.03 allow a conversion near 100 % at temperatures higher than 250 °C.

Regarding compression-ignition engines, catalytic reactors for oxidation are suitable due to the high concentration of oxygen because the performance of lean combustion in these engines. In this sense, diesel oxidation catalysts (DOC) are used to accelerate the oxidation of CO and UHC into CO_2, with a poor reduction of NOx. However, the oxidation of NO into NO_2 is promoted. Usually, they are specifically designed for each particular application and located immediately after the turbine, working at temperatures between 100 to 550 °C [19].

The coupled effect of working with a DOC and a DPF in a compression

ignition engine is studied by Hu et al. [60]. They used an engine with a displacement of 3.8 L with a compression ratio of 17.5. Regarding the DOC performance, CO and UHC are almost totally reduced to zero, although the conversion of CH_4 is only about 30 %. On the other hand, NOx conversion was found around 24.3 %.

Resitoglu et al. [61] studied the effect of two different catalytic materials working in a DOC and a SCR. The selected engine for the study is a single-cylinder engine with a displacement of 0.66 L and a compression ratio of 18. Regarding the DOC operation, the conversion of CO and UHC is up to 83.51 % and 80.83 %, respectively, at the maximum evaluated torque. DOC caused a slight increase in the engine's fuel consumption.

On the other hand, the reduction of NOx in compression ignition engines is performed using a selective catalytic reduction (SCR), which works in engines that operate at lean conditions, reducing the NOx into N_2 and H_2O. This type of device reduces the concentration of NOx based on chemical reactions, generally adding a substance that reacts with the exhaust gases. Usually, NH_3 is added to react with NOx in the presence of a catalyst. Nonetheless, urea solutions are currently being used due to their non-toxic behavior, being a biodegradable substance with reduced costs. A previous hydrolysis reaction that produces NH_3 is required in this case [19].

To reach higher NOx conversion rates (over 90 %), a NH_3/NOx molar ratio higher than 0.9 is required, and higher SCR volumes are also needed due to the higher residence times that the reaction need for suitable performance. Currently, urea consumption is estimated between 3 to 6 % of the total fuel consumption [19].

The modelling of SCR systems to understand the effects of different variables regarding the operation of these systems is studied by Tan et al. [62]. The boundary conditions of operation are taken from the operation of a compression ignition engine that has a displacement of 8.4 L with a maximum power production of 274 kW. Increasing geometry parameters such as diameter and length favors the increment of residence time for the reactions, leading to higher NOx conversion rates. A maximum conversion rate of 98 % was obtained at a temperature of 300 °C. The NO_2/NOx ratio affects the NOx conversion, where higher ratios than 0.5 affect NOx conversion due to a reduced velocity in the conversion reactions. This said, special attention must be given to the coupling with DOC. Finally, NH_3/NOx ratios between 1 to 1.5 provides the best conversion rates.

Resitoglu et al. [61] studied the effect of two different catalytic materials working in a DOC and a SCR. Regarding the SCR operation, the highest conversion rate achieved in the study was 80.29 %. The conversion rate increases with the engine torque, where higher temperatures are found, enhancing the reactions within the component.

Finally, particulate emissions have always been a significant problem in compression ignition engines. The emissions regulations are becoming stricter, and diesel particulate filters (DPF) are becoming indispensable to reduce particulate emissions [19]. Nonetheless, the application of direct injection in spark-ignition engines has increased particulate emissions, requiring the application of gasoline particulate filters (GPF), where filtration efficiencies between 60 to 99 % are found, depending on the design and particle side [53].

A filter with a tolerance of high-temperature operation is used to trap the particulate material, which is regenerated by oxidizing the accumulated emissions [20]. This regeneration process is essential because the accumulation of particulate matter can increase the exhaust line's counterpressure, affecting the engine's fuel consumption [19]. Additionally, a trade-off decision on the geometry has to be made when a DPF or GPF is designed, where a reduction in the porous size increases the filtering capacity and the engine's counterpressure [19].

Ko et al. [63] studied the coupling working of a TWC and a GPF in a spark-ignition engine with a displacement of 2.4 L and a compression ratio of 11.3. The engine is operated under real driving emissions tests, including the cold start phase. The urban section of the cycle exhibits higher PM emissions due to the more idle time and acceleration/deceleration sections. On the contrary, motorway and rural sections performed the best filtering process. A maximum contribution of 89.3 % in PM emissions reduction could be found. Regarding DPF, Hu et al. [60] studied the effect of working with a DOC and a DPF in a 3.8 L engine with a compression ratio of 17.5. Regarding DPF performance, the overall filtration is around 99.9 %.

2.3 Oxycombustion

Oxycombustion is a promising alternative to reduce the polluting gases produced by industrial facilities. It consists of a combustion process that is performed using a mixture of high-purity oxygen and a thermal buffer (typically recycled flue gases composed mainly of CO_2/H_2O), used to control the combustor temperature instead of atmospheric air [5]. Oxycombustion is usually implemented with carbon dioxide capturing and storage (CCS), which is a procedure to separate CO_2 from flue gases, transport it, and then store in long-term storage, avoiding its emission to the atmosphere [5, 64]. On the other hand, there are technologies in development for CO_2 capture and utilization (CCU), considered in sectors such as chemical and oil, food, or pharmaceutical, according to Koytsoumpa et al. [65].

The main characteristics that come from oxycombustion application are:

- Due to the elimination of N_2 from the combustion process, NOx emissions

are almost eliminated. It has been reported by Ozsari et al. [66] that NOx emissions can be 40 times smaller when using the same oxygen concentration due to the removal of nitrogen. Possible sources of NOx generation under oxycombustion are the presence of nitrogen in the fuel composition and sealing problems that lead to atmospheric air entrance in the cylinders.

- Enables an easy separation of CO_2 from the exhaust gases for CCS because it is mainly mixed with water vapor in flue gases. In this sense, the different condensation temperatures of both components allow a simple separation, according to Koohestanian and Shahraki [6].

- Due to the reduction of the adiabatic flame temperature because of the high concentration of CO_2, oxycombustion requires higher oxygen content than atmospheric air [67]. In this sense, the temperature can surpass the values of conventional combustion at considerably high oxygen concentrations.

- There is a high potential for integration with industrial facilities such as power or cement plants, where possible high temperatures can enhance thermal efficiency, according to Koohestanian and Shahraki [6].

Oxycombustion application is suitable for different fuels, where high cycle efficiencies and carbon capture are obtained. Shi et al. [68] studied different fuel types, such as coal, lignite, and sawdust in plants that use oxycombustion, finding high efficiencies and more than 97 % of the produced CO_2 could be captured. Liang et al. [69] studied an oxycombustion power plant run with liquefied natural gas, where thermal efficiencies as high as 58.78 % were obtained, capturing 94.8 % of the CO_2 produced with a purity of 97.2 %. Similarly, Cai et al. [70] ran a power plant using natural gas, where the purity of the captured CO_2 was around 98 %, achieving maximum efficiency of 67.6 %.

Nonetheless, regarding power plants, applying oxycombustion in power production can reduce the net power production and thermal efficiency due to the addition of CO_2 capture systems and O_2 production cycles, being the primary technical challenges for oxycombustion [5]. Park et al. [71] studied a power generation system with oxycombustion that generates 1 MW, whose net system efficiency drops by 4.2 % due to the CO_2 compression power for carbon capture. Thorbergsson and Grönstedt [72] studied two promising oxycombustion combined cycles whose gross efficiencies are near 60 %. However, applying oxygen production and carbon capture reduces the efficiency by 14 %. Hanak et al. [73] performed a techno-economic analysis of an oxycombustion coal-fired with net load variations during the day. A maximum average penalty in the net efficiency of 12.3 % is achieved because of CO_2 capture and O_2 production.

Specifically on engines, oxycombustion has been studied in diesel and gasoline engines of different sizes and applications. The use of CO_2 instead of N_2 affects the rate of flame speed, reducing the combustion performance [67]. On the other hand, due to differences in specific heat capacity ratio, the different steps in the cylinders are affected, such as gas exchanging or expansion, affecting power production, as can be seen in Van Blarigan et al. [74] and Mohammed et al. [75]. In this sense, oxygen concentration and exhaust gas recirculation (EGR), water injection, or increasing the compression ratio are strategies to achieve good performance with low emissions.

Wu et al. [76] studied a 0.125 L single-cylinder spark-ignition engine that implements different EGR rates and water injection. The engine uses propane as fuel and has a compression ratio of 9.2. A maximum increase in efficiency of 9.4 % was achieved. On the other hand, thermal efficiency decreases when high amounts of water and EGR rates are implemented due to a reduction in flame speed.

Due to the limited flame speed and the higher heat-specific ratio, Kang et al. [77] found that adding CO_2 in their experiments remarkably impacts the combustion process. They used a 0.8 L single-cylinder engine working under HCCI mode, with a compression ratio of 17 and n-heptane as fuel. The addition of 15 % of CO_2 extends 8° the combustion duration compared with conventional combustion using atmospheric air. The authors found that water injection at high temperatures and pressure controls combustion issues and improves performance.

A four-cylinder compression-ignition engine using diesel as fuel, with a compression ratio of 17, is studied by Tan and Hu [78], which is tested in the range of 600 to 800 rpm at different load conditions. Different N_2, O_2, CO_2 concentrations are used as working fluid. While using N_2 in the mixture, the increment of oxygen concentration leads to increased pollutant emissions and combustion efficiency. On the other hand, using solely O_2 and CO_2 eliminates NOx production, preserving a high combustion efficiency.

On compression ratio, Gao et al. [79] use similar conditions as Wu et al. [76]. The increment of the engine compression ratio from 9.2 to 14 leads to an improvement of 4.9 % in the engine's thermal efficiency. Nonetheless, this increment can be as high as 22.4 %due to water injection, which increases the in-cylinder mass, and reduces the gas heat capacity while decreasing the knocking tendency.

Considering the latter, the benefits regarding emissions when applying oxycombustion in engines are studied in Serrano et al. [13]. Using stoichiometric combustion, NOx emissions were reduced for more than 99 % due to the removal of N_2 from the working fluid. The small NOx production was due to the small N_2 content in the fuel. On the other hand, increasing the EGR concentration leads to a slight decrease in the NOx production due to the reduction of in-cylinder

temperature. In addition, the oxygen excess in the cylinder ($\lambda = 1.1$) increases NOx due to the higher oxygen concentration that enhances the combustion and promotes NOx formation. Nonetheless, the reduction is still over 99 % when compared with conventional combustion. Thus, no specific after treatment regarding NOx elimination is needed.

The UHC emissions were cut down by almost 95 % for the best case, using an EGR concentration of 67 % at the intake. Higher oxygen concentrations than conventional combustion enhance the combustion efficiency, reducing the UHC content in the exhaust gases. On the other hand, increasing the EGR concentration reduces the oxygen content in the cylinder, increasing the UHC emissions. In this case, an increment in 6 % (from 67 to 73 % of EGR) leads to a 95 % of UHC reduction to 81 %. Moreover, working with a $\lambda = 1.1$ increases the oxygen concentration, promoting combustion completeness and decreasing the UHC emissions.

As expected, CO emissions had high sensitivity regarding the oxygen excess in the cylinder. Stoichiometric combustion leads to increase CO emissions at an EGR concentration of 70 % for about 24 % while reducing the EGR concentration by 1 % lead to a decrease the CO emissions by about 35 %. The increase of CO_2 concentration could promote CO formation, increasing its emissions compared with conventional combustion. On the other hand, a slight O_2 excess remarkably reduces the CO production, where a 94 % decrease is achieved.

In summary, it can be seen that oxycombustion is a promising strategy to reduce pollutant emissions, especially NOx due to the avoidance of N_2 in the combustion process. It also facilitates the application of carbon dioxide capture, which can be performed by condensing the water vapor in the flue gases. In addition, it is seen that the implementation of oxycombustion leads to worsening performance due to the addition of oxygen production and carbon dioxide capture, which represent high power consumption, reducing the net power production.

Regarding engines, the presence of CO_2 instead of N_2 affects the combustion process, the expansion stroke, and the gas exchanging. Nonetheless, strategies such as water injection or increasing the engine compression ratio can enhance performance. The latter can be applied due to the reduction of knocking tendency, as also explained in Serrano et al [13].

The engine emissions are enhanced due to oxycombustion application. NOx emissions are almost eliminated, accomplishing the current regulations regarding its emissions, for which the aftertreatments regarding NOx can be removed, or their sizes can be widely reduced. Similar conclusions regarding aftertreatments can be stated on CO and UHC emissions.

2.4 Oxygen production methdods

It was explained that oxycombustion requires high-purity oxygen to work in industrial facilities properly. Thus, air separation methods are needed within the installations, adding that high-purity oxygen purchasing could be expensive to some sectors due to transport and storage costs and the increasing demand in the last few years. As an example of the latter, the oxygen price in the US has increased by over 65 % in the previous 20 years accoring to Li et al. [80], while the COVID-19 pandemic caused an additional 24 % increment. Considering the latter, a primary step for oxycombustion application is installing an oxygen production method that works within the facility's main system, such as a power plant, an internal combustion engine, or any industrial process.

Thus, the main air separation methods currently being researched are explained. Currently, the most extended method for oxygen production is cryogenic air separation (CAS), which is a system with high power consumption, for which most of the researchers are mostly working on the development of three different technologies according to Wu et al. [7]: pressure and temperature swing adsorption, chemical looping air separation (CLAS) and membrane separation.

2.4.1 CAS

Cryogenic air separation produces high-purity oxygen by separating air in a multi-column cryogenic distillation process. The process takes advantage of the different boiling temperatures of the primary components, nitrogen, and oxygen. Currently, state-of-the-art air separation processes based on CAS can produce oxygen streams with purities higher than 99.5 % and recover more than 98 % of the oxygen in the air, producing up to $150\,\mathrm{t\,d^{-1}}$, according to Wu et al.[7].

Nonetheless, CAS does not exhibit a profitable behavior in different applications, as shown in Escudero et al. [81], Cau et al. [82], or Xiong et al. [83]. These cases show that efficiency penalties of around 10 % are achieved due to the integration of CAS in power plants. Escudero et al. [81] explained that CAS integration in industrial facilities is expected to be a reasonable alternative in the mid-term, according to the electricity costs behavior. However, according to Cau et al. [82], considerable financial risks are expected.

CAS is a highly energy-intensive process whose consumption could represent between 10 to 40 % of the gross output power in an oxycombustion plant [7]. The electric power consumption of a typical CAS installation oscillates between 160 to $270\,\mathrm{kWh\,t^{-1}}$according to Habib et al. [84], where 85 % of the energy used represents the air compression and distillation process according to Zhu et al. [8].

The cases shown in Thorgbersson and Grönstedt [72] achieved an energy consumption between 16 to 17 % of the gross power output regarding oxygen

production with CAS. Escudero et al. [81] reported that 14.6 % of the gross power is used for oxygen production, Xiong et al. [83] reported 16 %, while Cau et al. [82], 12.76 %.

2.4.2 Pressure and temperature swing adsorption

Firstly, pressure swing adsorption (PSA) separates air components using a sorbent material that selectively adsorbs nitrogen at its surface, taking advantage of nitrogen being more polarizable than oxygen, generating an oxygen-enriched stream, according to Yang [85]. For gas separation, the sorbent material must preferentially adsorb nitrogen, which depends on pressure: high pressures (0.2 to 0.7 MPa) induce nitrogen to adhere to the material, while low pressures (0.1 MPa, atmospheric pressure) decrease the adsorption capacity of the material. The latter creates a pressure cycle where high pressures separate nitrogen while low pressures allow material regeneration [7, 86]. The system usually works at ambient temperature, but high-temperature air separation is being studied for some applications, according to Alipour et al. [87]. Additionally, some applications use temperature cycles, where low or ambient temperatures are implemented to adsorb while the regeneration is performed at high temperatures. In this scenario, the process is called temperature swing adsorption (TSA) [7].

This technology is used for small and medium oxygen productions, in industry sectors such as paper or medical applications, according to the NZ Institute of Chemistry [88]. Currently, the most significant issue to improve to increase the size of these types of installations is the limited adsorption when higher oxygen flow rates are required, decreasing the production, according to Wu et al. [7].

A dual-column PSA system is studied by Liu et al. [89], where the pressure cycle duration effect on oxygen production was studied. A maximum oxygen recovery from the air of 39.2 % was achieved, reaching a purity of 93 % and requiring 55.75 kg of adsorbent material for each tonne of production in a day ($\mathrm{kg\,t^{-1}\,d^{-1}}$).

Chang et al. [90] studied the improvement of the typical cylindrical configuration of the adsorbers using a semi-cylindrical configuration. A better heat transfer in the semi-cylindrical configuration explains a better performance in this case, where purities higher than 95 % can be achieved, while oxygen recovery of 34 % is obtained, producing up to 30 $\mathrm{L\,min^{-1}}$ (0.7 $\mathrm{g\,s^{-1}}$, approximately).

A small-scale vacuum pressure system of PSA is studied by Zhu et al. [91]. The system operates at 3,800 m and is used to supply oxygen for hypoxia cases. The authors assessed the influence of pressure cycle duration and feed temperature on system performance. In the optimum case, the system could produce 270 $\mathrm{m^3\,h^{-1}}$ at normal conditions with a purity of 90 % while recovering 62.6 %

of the oxygen from the air. The minimum energy consumption obtained was $0.55\,\mathrm{kW\,h\,m^{-3}}$ at normal conditions.

2.4.3 Chemical looping air separation

According to Wu et al. [7], CLAS oxygen production is performed using two interconnected reactors that use a substance that acts as a carrier for oxygen transportation. The oxygen carrier contacts atmospheric air in the first reactor, where the carrier is oxidized. Then, the oxygen is released in the fuel reactor, where a typical combustion process occurs.

As found in Zhou et al. [92, 93], thermodynamics assessments demonstrate that CLAS oxygen production exhibits an energy consumption lower than 4-5 times compared with CAS, a promising technology to implement. On the other hand, Shi et al. [94] study oxygen production with CLAS using different oxygen carriers. They found a reduction of 47 % in operating costs regarding energy consumption. In addition, Zhu et al. [95] studied a coal gasification plant using CAS and CLAS for comparison, finding that 3 % of the energy penalty associated with the CAS usage can be compensated by implementing CLAS.

Nonetheless, CLAS has only been performed under laboratory experiments and small pilot plants for real-life applications, requiring further research, especially regarding oxygen carrier development that operates in a wide range of temperatures, according to Wu et al. [7].

Nonetheless, CLAS has only been performed under laboratory experiments and small pilot plants for real-life applications, requiring further research, especially regarding oxygen carrier development that operates in a wide range of temperatures, according to Wu et al. [7].

2.4.4 Membranes

Two types of membranes are used for oxygen production, which operates with different principles for air separation. First, the polymeric membranes work because the oxygen and nitrogen diffusion rates through a membrane are different when a pressure gradient is applied. Due to differences in molecular sizes, most membrane materials permeate better oxygen than nitrogen. However, producing high-purity oxygen is difficult to achieve due to the unavoidable filtration of nitrogen, which results in an oxygen-enriched stream with oxygen concentrations around 40 % rather than high-purity oxygen. Nonetheless, a two-stage polymeric membrane can be used if higher purities are required, according to Wu et al. [7] and Smith and Klosek [86].

On the other hand, in ion transport membranes (ITM), oxygen ions are transported through the bulk from a high-oxygen partial pressure side or feed side to the low-oxygen partial pressure side or permeate side, according to Wu et

al. [7] . Zhu and Yang [8] explain the mechanism of oxygen permeation through this type of membrane in three simple steps:

- Interfacial oxygen exchange on the feed side: The oxygen molecules are adsorbed in the gas-solid interface of the feed side, reacting with electrons to create oxygen ions before incorporating into the lattice.
- Bulk diffusion across grains and grain boundaries: The oxygen ions move through the vacancies or interstitial sites of the membrane, depending on the material used to build the membrane.
- Interfacial oxygen exchange on the permeation side: The oxygen ions react to form oxygen molecules on the permeate side, releasing the obtained electrons on the feed side.

As seen, the oxygen permeation consists of oxygen ions transportation from the feed to the permeate side, while an electron transfer is performed in the inverse direction, keeping the membrane electrically neutral. In this sense, these membranes can transfer electrons internally, reducing the complexity of the installation and facilitating large-scale application.

Usually, these membranes are fabricated with a dense ceramic compound with a particular crystal lattice structure that allows the transportation of oxygen ions and electrons, according to Zhu and Yang [8]. These compounds are often called mixed oxygen ionic and electronic conducting materials (MIEC), the preferred term in this thesis. MIEC membranes have a selectivity for oxygen permeation of 100 %, while energy consumption and capital investment are lower than typical CAS installations, according to Zhu and Yang [8] and Arratibel Plazaola et al. [96].

One of the most common materials implemented in MIEC membranes fabrication is $Ba_{0.5}Sr_{0.5}Co_{0.8}Fe_{0.2}O_{3-\delta}$ (BSCF), due to its high permeation and stable operation at temperatures above 850ºC, according to Zhu and Yang [8] and Arratibel et al. [96].

Moreover, the optimum conditions to operate MIEC membranes are high temperatures (700 to 1,000 °C) and high pressure gradients (1 to 2 MPa at the feed side and vacuum pressure at permeate side, although lower feed pressures work properly) [8]. Nonetheless, there are studies in development that are researching low-temperature membranes (300 to 650 °C) to reduce energy consumption [8].

According to Portillo et al. [11], there are two operation modes for MIEC membranes: 3-end and 4-end. These modes differ in reducing oxygen partial pressure method on the permeate side. In the 3-end, a vacuum pump is implemented for reducing the pressure on the permeate side, while for the 4-end, a

sweeping gas is used to reduce the oxygen concentration, creating the partial pressure gradient.

There are studies of oxygen production using MIEC membranes for applications as power plants that exhibit better economic performance and efficiency improvement compared with cryogenic methods. Castillo [9] studied the coupling operation of membrane air separation in a hard coal plant with oxycombustion, comparing its performance with CAS. Working with membrane separation could improve the plant efficiency by 4 %. Portillo et al. [11] compared cryogenic and membrane methods for oxygen production in a coal-power plan, finding a 5 % improvement in energy efficiency and a lower specific CO_2 capture when membranes were used compared with CAS. Skorek-Osikowska et al. [10] studied two cases of a 460 MW power plant that uses oxycombustion, where applying a CAS unit for oxygen obtention is compared with a hybrid membrane-cryogenic installation. Adding a membrane improved the efficiency by 1.1 %, reducing the auxiliary power consumption by 13 %.

The leading research organization working on the commercialization of MIEC membranes for air separation has been Air Products & Chemicals. They have worked with several companies and institutes on this topic, designing a multiphase project, starting with prototypes that generate high-purity oxygen at a rate of $0.1\,\mathrm{t\,d^{-1}}$ to a commercial installation of $2{,}000\,\mathrm{t\,d^{-1}}$ [8]). Regarding this project, Anderson et al. [97] explained the construction and operation of a test facility that produces $100\,\mathrm{t\,d^{-1}}$ and small-scale experiments that continuously operate for 15,000 h. Also, Praxair can be highlighted as an organization that is working in advance to generate commercial-scale units [98], reporting patents of MIEC membranes development that can be applied in the chemical industry or power plants [99, 100]. With the above said, there are efforts to create the first commercial-scale units in the next few years to compete in energy consumption and production with CAS. The main research topics necessary to achieve a reliable installation for practical applications are improving mechanical strength and density of membrane area per volume [101].

2.5 Summary

This chapter presents an overview of the main concepts treated in this thesis. Initially, some generalities regarding emissions are presented. Initially, the formation mechanisms of the main pollutant substances in engines are presented. In this sense, CO formation is promoted in rich-mixture zones, where the oxygen concentration is diminished, and the formation of CO_2 from CO is affected. On the other hand, NOx emissions are promoted in high-temperature and high oxygen concentration zones, typically found in near-stoichiometric combustion with oxygen excess (λ around 1.1).

Regarding UHC emissions, they occur due to incomplete fuel combustion. This situation can be found in lean mixtures that affect flame propagation or rich mixtures, where the lack of oxygen does not allow fuel to oxidize correctly. The most important phenomenon that causes unburned hydrocarbon emissions is the flame quenching or misfiring in the walls of the engine combustion chambers. Particulate matter formation is found in incomplete combustion scenarios, occurring under complex reactions in the cylinder or the exhaust pipes. It can be seen that situations that promote particular pollutant emissions avoid forming others; thus, a trade-off between the emissions is found.

Considering the latter, global efforts are being made to reduce emissions, as the Paris Agreement framework, designed to substantially reduce greenhouse emissions to limit the global temperature increase even in 1.5 °C.

The United States and the European Union are the two pioneers regarding emissions standards. The Tier standards in the United States are the current regulations limiting emissions. Starting in 1991, the authorities intend to consolidate all the requirements in the national territory, for which more extended periods are needed between two different implementation stages. The last release stage of Tier standards is Tier 3, which pretends to reduce the emissions of NOx in 25 %, CO in 24 % and UHC in a maximum value of 29 %. Euro standards are the current European Union regulations, starting in 1992. Euro 7 is the next stage in these regulations, expected to be implemented in 2025 for light-duty vehicles and in 2027 for heavy-duty vehicles, where high reductions of NOx and PM are expected.

Several reduction strategies have been implemented to reduce emissions and accomplish the imposed limits in the mentioned regulations. There are two types of reduction strategies. First, active solutions, such as EGR and turbocharging, affect the engine design and its components, while passive solutions, such as TWC, DOC, SCR, or filters, are devices located in the exhaust line of the engine, called after-treatment systems.

Regarding active solutions, exhaust gases recirculation (EGR) is the primary strategy for NOx controlling, where part of the exhaust gases are recirculated to reduce oxygen concentration and in-cylinder temperatures, conditions that

affect NOx formation. Nonetheless, the decrease in the burning rate caused by EGR leads to higher UHC emissions.

Turbocharging main objective is to increase the specific power production of an engine by increasing the intake density; thus, smaller engines with turbocharging have fewer emissions of UHC and CO. A better combustion process, reduction in the heat losses, and a possible improvement in the gas exchange process are the reasons for better engine performance when using turbocharging. Nonetheless, special attention must be given to NOx emissions due to increased in-cylinder temperatures and better combustion process.

Regarding passive solutions, three-way catalysts are the primary components to reduce exhaust emissions of CO, NOx, and UHC in spark-ignition engines. The operation range of TWC is very narrow, requiring a nearly-stoichiometric operation to perform properly. For this reason, it requires a precise control system.

Diesel oxidation catalysts (DOC) are used in compression-ignition engines that operate correctly at high oxygen concentrations. They accelerate the oxidation of CO and UHC into CO_2. On the other hand, for NOx reduction, selective catalytic reduction (SCR) is used, where chemical reactions between NH_3 and NOx are performed to reduce NOx in N_2 and H_2O. Particulate filters (GPF or DPF) reduce particulate matter emissions. In these devices, the regeneration process is essential because PM accumulation leads to an exhaust line's counterpressure increase, affecting fuel consumption.

In this context, oxycombustion appears as an alternative to reduce polluting emissions, where a high-purity oxygen stream is used in combustion, with a thermal buffer, typically EGR, to control the temperature. It can be mentioned the elimination of NOx due to the absence of N_2 from the combustion process, the facility of carbon capture, and its easy integration with industrial facilities are among the benefits of oxycombustion.

Different studies regarding oxycombustion have been performed in various industrial contexts, such as power plants or engines. High-efficiency facilities are obtained after oxycombustion application, with a great potential for carbon capture.

Regarding engines, oxycombustion has been studied in various engines with different sizes and fuel types. The replacement of N_2 with CO_2 as the principal bulk gas in the combustion process affects the combustion performance due to a reduction in the flame speed. Moreover, differences in specific heat capacity ratio affect the in-cylinder processes, thus, power production.

Nonetheless, different studies have been performed to enhance engine performances working under oxycombustion, studying the effect of oxygen concentration or water injection to improve the performance. However, special attention must be given to combustion advancement and compression ratio

increment, which can be performed due to the low knock propensity of engine oxycombustion.

Regarding the benefits of oxycombustion in emissions, special attention was given to the study by Serrano et al. [13], where almost a total reduction of NOx was obtained. In this sense, after-treatment devices can reduce their sizes or even be eliminated, reducing the system's complexity.

In this sense, to apply oxycombustion, air separation is needed to produce high-purity oxygen. Currently, the most common air separation system is cryogenic air separation. However, its consumption can represent a high proportion of the power production, for which other alternatives are required. Thus, strategies like pressure and temperature swing adsorption, chemical looping air separation (CLAS), and membrane separation appear as oxygen production alternatives.

This thesis uses ion transport membranes for oxygen production, often called mixed oxygen ionic and electronic conducting materials (MIEC). Oxygen is transported through the crystal lattice of the membrane, requiring a high oxygen partial pressure ratio and temperatures. Several authors report enhancing industrial facilities' performance when oxygen production based on MIEC membranes is implemented instead of CAS. MIEC membranes have a selectivity for oxygen permeation of 100 %, ensuring the elimination of N_2 from the combustion process.

2.6 References

[5] X. Huang, J. Guo, Z. Liu, and C. Zheng. “Opportunities and Challenges of Oxy-fuel Combustion”. In: *Oxy-Fuel Combustion*. Elsevier, 2018, pp. 1–12. DOI: 10.1016/b978-0-12-812145-0.00001-3 (cit. on pp. 2, 31, 32).

[6] E. Koohestanian and F. Shahraki. “Review on principles, recent progress, and future challenges for oxy-fuel combustion CO2 capture using compression and purification unit”. In: *Journal of Environmental Chemical Engineering* 9.4 (Aug. 2021), p. 105777. DOI: 10.1016/j.jece.2021.105777 (cit. on pp. 2, 32).

[7] F. Wu, M. D. Argyle, P. A. Dellenback, and M. Fan. “Progress in O2 separation for oxy-fuel combustion–A promising way for cost-effective CO2 capture: A review”. In: *Progress in Energy and Combustion Science* 67 (July 2018), pp. 188–205. DOI: 10.1016/j.pecs.2018.01.004 (cit. on pp. 2, 35–38).

[8] X. Zhu and W. Yang. “Introduction to Mixed Ionic–Electronic Conducting Membranes”. In: *Green Chemistry and Sustainable Technology*. Springer Berlin Heidelberg, Nov. 2016, pp. 1–10. DOI: 10.1007/978-3-662-53534-9_1 (cit. on pp. 2, 35, 38, 39, 112, 135, 140).

[9] R. Castillo. “Thermodynamic analysis of a hard coal oxyfuel power plant with high temperature three-end membrane for air separation”. In: *Applied Energy* 88.5 (May 2011), pp. 1480–1493. DOI: 10.1016/j.apenergy.2010.10.044 (cit. on pp. 2, 39, 141).

[10] A. Skorek-Osikowska, Ł. Bartela, and J. Kotowicz. “A comparative thermodynamic, economic and risk analysis concerning implementation of oxy-combustion power plants integrated with cryogenic and hybrid air separation units”. In: *Energy Conversion and Management* 92 (Mar. 2015), pp. 421–430. DOI: 10.1016/j.enconman.2014.12.079 (cit. on pp. 2, 39).

[11] E. Portillo, L. M. G. Fernández, F. Vega, B. Alonso-Fariñas, and B. Navarrete. “Oxygen transport membrane unit applied to oxy-combustion coal power plants: A thermodynamic assessment”. In: *Journal of Environmental Chemical Engineering* 9.4 (Aug. 2021), p. 105266. DOI: 10.1016/j.jece.2021.105266 (cit. on pp. 2, 38, 39, 141).

[13] J. R. Serrano, J. M. Díaz, J. Gomez-Soriano, and R. Raggi. “Exploring the Oxy-Fuel Combustion in Spark-Ignition Engines for Future Clean Powerplants”. In: *ASME 2022 ICE Forward Conference*. American Society of Mechanical Engineers, Oct. 2022. DOI: 10.1115/icef2022-89167 (cit. on pp. 2, 33, 34, 42, 58, 59, 61, 62, 151, 156, 161).

[17] *Internal Combustion Engine Handbook. Basics, Components, Systems, and Perspectives*. SAE International, 2004, p. 868. ISBN: 9780768011395 (cit. on pp. 10–14, 17, 20, 21).

[18] G. Baumbach and M. Kobayashi. *Air Quality Control Formation and Sources, Dispersion, Characteristics and Impact of Air Pollutants - Measuring Methods, Techniques for Reduction of ... Formation and Sources, Dispersion, Characteristics and Impact of Air Pollutants - Measuring Methods, Techniques for Reduction of ...* Brand: Springer, p. 508. ISBN: 9783642790034 (cit. on pp. 10–14).

[19] J. M. D. Fernández and F. P. González. *MOTORES DE COMBUSTIÓN INTERNA ALTERNATIVOS*. Universitat Politècnica de València, p. 1024. ISBN: 9788483637050 (cit. on pp. 11–15, 17–20, 23, 25–31).

[20] J. Heywood. *Internal combustion engine fundamentals*. McGraw-Hill Education, 2018. ISBN: 9781260116106 (cit. on pp. 12–15, 17, 18, 26–28, 31).

[21] L. Zhao, X. Yu, D. Qian, W. Dong, P. Sun, L. He, and S. Yang. "The effects of EGR and ignition timing on emissions of GDI engine". In: *Science China Technological Sciences* 56.12 (Dec. 2013), pp. 3144–3150. DOI: 10.1007/s11431-013-5379-y (cit. on pp. 12, 15, 18).

[22] O. P. Saw and J. M. Mallikarjuna. "Effect of spark plug and fuel injector location on mixture stratification in a GDI engine - A CFD analysis". In: *IOP Conference Series: Materials Science and Engineering* 243 (Sept. 2017), p. 012025. DOI: 10.1088/1757-899x/243/1/012025 (cit. on pp. 12, 15, 20).

[23] C. Jiang, Z. Li, Y. Qian, X. Wang, Y. Zhang, and X. Lu. "Experimental studies on the co-effects of engine operating parameters and fuel functional groups on the performance and emissions of a GDI engine". In: *Applied Thermal Engineering* 140 (July 2018), pp. 707–715. DOI: 10.1016/j.applthermaleng.2018.05.095 (cit. on pp. 12, 16, 18, 21).

[24] B. Deng, Q. Li, Y. Chen, M. Li, A. Liu, J. Ran, Y. Xu, X. Liu, J. Fu, and R. Feng. "The effect of air/fuel ratio on the CO and NOx emissions for a twin-spark motorcycle gasoline engine under wide range of operating conditions". In: *Energy* 169 (Feb. 2019), pp. 1202–1213. DOI: 10.1016/j.energy.2018.12.113 (cit. on pp. 13, 16).

[25] F. Duronio, A. D. Vita, A. Montanaro, and C. Villante. "Gasoline direct injection engines – A review of latest technologies and trends. Part 2". In: *Fuel* 265 (Apr. 2020), p. 116947. DOI: 10.1016/j.fuel.2019.116947 (cit. on p. 13).

[26] G. Zhu, J. Liu, J. Fu, Z. Xu, Q. Guo, and H. Zhao. "Experimental study on combustion and emission characteristics of turbocharged gasoline direct injection (GDI) engine under cold start new European driving cycle (NEDC)". In: *Fuel* 215 (Mar. 2018), pp. 272–284. DOI: 10.1016/j.fuel.2017.10.048 (cit. on pp. 13, 17, 19).

[27] İ. A. Reşitoğlu, K. Altinişik, and A. Keskin. "The pollutant emissions from diesel-engine vehicles and exhaust aftertreatment systems". In: *Clean Technologies and Environmental Policy* 17.1 (June 2014), pp. 15–27. DOI: 10.1007/s10098-014-0793-9 (cit. on pp. 13, 18, 19).

[28] W. Pan, C. Yao, G. Han, H. Wei, and Q. Wang. "The impact of intake air temperature on performance and exhaust emissions of a diesel methanol dual fuel engine". In: *Fuel* 162 (Dec. 2015), pp. 101–110. DOI: 10.1016/j.fuel.2015.08.073 (cit. on pp. 13, 16, 19).

[29] A. O. Hasan, A. I. Osman, A. H. Al-Muhtaseb, H. Al-Rawashdeh, A. Abu-jrai, R. Ahmad, M. R. Gomaa, T. J. Deka, and D. W. Rooney. "An experimental study of engine characteristics and tailpipe emissions from modern DI diesel engine fuelled with methanol/diesel blends". In: *Fuel Processing Technology* 220 (Sept. 2021), p. 106901. DOI: 10.1016/j.fuproc.2021.106901 (cit. on pp. 13, 17, 19).

[30] B. K. Selvan, S. Das, M. Chandrasekar, R. Girija, S. J. Vennison, N. Jaya, P. Saravanan, M. Rajasimman, Y. Vasseghian, and N. Rajamohan. "Utilization of biodiesel blended fuel in a diesel engine – Combustion engine performance and emission characteristics study". In: *Fuel* 311 (Mar. 2022), p. 122621. DOI: 10.1016/j.fuel.2021.122621 (cit. on pp. 13, 17, 19, 20).

[31] T. Lattimore, C. Wang, H. Xu, M. L. Wyszynski, and S. Shuai. "Investigation of EGR Effect on Combustion and PM Emissions in a DISI Engine". In: *Applied Energy* 161 (Jan. 2016), pp. 256–267. DOI: 10.1016/j.apenergy.2015.09.080 (cit. on pp. 15, 18).

[32] S. Polat, A. Uyumaz, H. Solmaz, E. Yilmaz, T. Topgül, and H. S. Yücesu. "A numerical study on the effects of EGR and spark timing to combustion characteristics and NOx emission of a GDI engine". In: *International Journal of Green Energy* 13.1 (May 2014), pp. 63–70. DOI: 10.1080/15435075.2014.909361 (cit. on p. 15).

[33] C. D. Rakopoulos, D. C. Rakopoulos, G. C. Mavropoulos, and G. M. Kosmadakis. "Investigating the EGR rate and temperature impact on diesel engine combustion and emissions under various injection timings and loads by comprehensive two-zone modeling". In: *Energy* 157 (Aug. 2018), pp. 990–1014. DOI: 10.1016/j.energy.2018.05.178 (cit. on pp. 16, 20, 28).

[34] R. Sindhu, G. A. P. Rao, and K. M. Murthy. "Effective reduction of NOx emissions from diesel engine using split injections". In: *Alexandria Engineering Journal* 57.3 (Sept. 2018), pp. 1379–1392. DOI: 10.1016/j.aej.2017.06.009 (cit. on pp. 16, 20).

[35] M. C. Drake, D. T. French, and T. D. Fansler. "Advanced diagnostics for minimizing hydrocarbon emissions from a direct-injection gasoline engine". In: *Symposium (International) on Combustion* 26.2 (1996), pp. 2581–2587. DOI: 10.1016/s0082-0784(96)80091-9 (cit. on p. 18).

[36] M. Zhang, W. Hong, F. Xie, Y. Su, H. Liu, and S. Zhou. "Combustion, performance and particulate matter emissions analysis of operating parameters on a GDI engine by traditional experimental investigation and Taguchi method". In: *Energy Conversion and Management* 164 (May 2018), pp. 344–352. DOI: 10.1016/j.enconman.2018.03.017 (cit. on pp. 18, 19).

[37] A. Überall, R. Otte, P. Eilts, and J. Krahl. "A literature research about particle emissions from engines with direct gasoline injection and the potential to reduce these emissions". In: *Fuel* 147 (May 2015), pp. 203–207. DOI: 10.1016/j.fuel.2015.01.012 (cit. on p. 20).

[38] C. Buysse and J. Miller. *TRANSPORT COULD BURN UP THE EU'S ENTIRE CARBON BUDGET*. Web page. Apr. 2021. URL: https://theicct.org/transport-could-burn-up-the-eus-entire-carbon-budget/ (cit. on p. 21).

[39] EPA. *Inventory of U.S. Greenhouse Gas Emissions and Sinks*. Web page. Apr. 2023. URL: https://www.epa.gov/ghgemissions/inventory-us-greenhouse-gas-emissions-and-sinks (cit. on p. 21).

[40] ONU. *The Paris Agreement*. Web page. URL: https://www.un.org/en/climatechange/paris-agreement (cit. on p. 21).

[41] C. B. Ribeiro, F. H. C. Rodella, and L. Hoinaski. "Regulating light-duty vehicle emissions: an overview of US, EU, China and Brazil programs and its effect on air quality". In: *Clean Technologies and Environmental Policy* 24.3 (Nov. 2021), pp. 851–862. DOI: 10.1007/s10098-021-02238-1 (cit. on pp. 21, 22, 24).

[42] Dieselnet. *United States: Cars and Light-Duty Trucks*. Webpage. July 2021. URL: https://dieselnet.com/standards/us/ld.php (cit. on p. 22).

[43] Dieselnet. *United States: Cars and Light-Duty Trucks: Tier 2*. Webpage. Dec. 2006. URL: https://dieselnet.com/standards/us/ld_t2.php (cit. on pp. 22, 23).

[44] Dieselnet. *United States: Cars and Light-Duty Trucks: Tier 3*. Webpage. Aug. 2016. URL: https://dieselnet.com/standards/us/ld_t3.php (cit. on pp. 22, 23).

[45] Dieselnet. *United States: Cars and Light-Duty Trucks: Tier 1*. Webpage. Apr. 2007. URL: https://dieselnet.com/standards/us/ld_t1.php (cit. on p. 23).

[46] EPA. *EPA Sets Tier 3 Motor VehicleEmission and Fuel Standards*. Regulatory Announcement. EPA, 2014. URL: https://nepis.epa.gov/Exe/ZyPDF.cgi/P100HW00.PDF?Dockey=P100HW00.PDF (cit. on p. 23).

[47] R. S. Bharj, R. Kumar, and G. N. Singh. "On-Board Post-Combustion Emission Control Strategies for Diesel Engine in India to Meet Bharat Stage VI Norms". In: *Advanced Engine Diagnostics*. Springer Singapore, Nov. 2018, pp. 105–125. DOI: 10.1007/978-981-13-3275-3_6 (cit. on pp. 24, 25).

[48] EU. *Commission proposes new Euro 7 standards to reduce pollutant emissions from vehicles and improve air quality*. Webpage. Nov. 2022. URL: https://ec.europa.eu/commission/presscorner/detail/en/ip_22_6495 (cit. on pp. 24, 25).

[49] UE. *Annexes to the Proposal for a Regulation of the European Parliament and the Councilon type-approval of motor vehicles and engines and of systems, components andseparate technical units intended for such vehicles, with respect to their emissions andbattery durability (Euro 7) and repealing Regulations (EC) No 715/2007 and (EC) No595/2009*. Tech. rep. UE, 2022. URL: https://single-market-economy.ec.europa.eu/publications/euro-7-standard-proposal_en (cit. on p. 25).

[50] EU. *Questions and Answers: Commission proposal on the new Euro 7 standards*. Webpage. Nov. 2022. URL: https://ec.europa.eu/commission/presscorner/detail/en/QANDA_22_6496 (cit. on p. 26).

[51] M. Lyu, X. Bao, R. Zhu, and R. Matthews. "State-of-the-art outlook for light-duty vehicle emission control standards and technologies in China". In: *Clean Technologies and Environmental Policy* 22.4 (Mar. 2020), pp. 757–771. DOI: 10.1007/s10098-020-01834-x (cit. on p. 26).

[52] ICCT. *INDIA BHARAT STAGE VI EMISSION STANDARDS*. Policy update. International Council on Clean Transportation, Apr. 2016. URL: https://theicct.org/sites/default/files/publications/India%20BS%20VI%20Policy%20Update%20vF.pdf (cit. on p. 26).

[53] F. Leach, G. Kalghatgi, R. Stone, and P. Miles. "The scope for improving the efficiency and environmental impact of internal combustion engines". In: *Transportation Engineering* 1 (June 2020), p. 100005. DOI: 10.1016/j.treng.2020.100005 (cit. on pp. 26, 31).

[54] P. Piqueras, J. D. la Morena, E. J. Sanchis, and R. Pitarch. "Impact of Exhaust Gas Recirculation on Gaseous Emissions of Turbocharged Spark-Ignition Engines". In: *Applied Sciences* 10.21 (Oct. 2020), p. 7634. DOI: 10.3390/app10217634 (cit. on p. 27).

[55] K. Shen, F. Li, Z. Zhang, Y. Sun, and C. Yin. "Effects of LP and HP cooled EGR on performance and emissions in turbocharged GDI engine". In: *Applied Thermal Engineering* 125 (Oct. 2017), pp. 746–755. DOI: 10.1016/j.applthermaleng.2017.07.064 (cit. on p. 27).

[56] A. R. Mahmoudi, I. Khazaee, and M. Ghazikhani. "Simulating the effects of turbocharging on the emission levels of a gasoline engine". In: *Alexandria Engineering Journal* 56.4 (Dec. 2017), pp. 737–748. DOI: 10.1016/j.aej.2017.03.005 (cit. on p. 28).

[57] L. S. Silva, J. A. Silva, J. R. Henrıquez, and J. C. de Lira Junior. "Numerical Analysis of Effects of Engine Downsizing and Turbocharging on the Parameters of Performance and Emissions of an Internal Combustion Engine". In: *Arabian Journal for Science and Engineering* 48.3 (June 2022), pp. 2795–2805. DOI: 10.1007/s13369-022-06947-7 (cit. on p. 28).

[58] D. Lou, Y. Ren, X. Li, Y. Zhang, and X. Sun. "Effect of Operating Conditions and TWC Parameters on Emissions Characteristics of a Stoichiometric Natural Gas Engine". In: *Energies* 13.18 (Sept. 2020), p. 4905. DOI: 10.3390/en13184905 (cit. on p. 29).

[59] W. B. Bae, D. Y. Kim, S. W. Byun, M. Hazlett, D. Y. Yoon, C. Jung, C. H. Kim, and S. B. Kang. "Emission of NH3 and N2O during NO reduction over commercial aged three-way catalyst (TWC): Role of individual reductants in simulated exhausts". In: *Chemical Engineering Journal Advances* 9 (Mar. 2022), p. 100222. DOI: 10.1016/j.ceja.2021.100222 (cit. on p. 29).

[60] S. Hu, B. Deng, D. Wu, and K. Hou. "Energy flow behavior and emission reduction of a turbo-charging and EGR non-road diesel engine equipped with DOC and DPF under NRTC (non-road transient cycle)". In: *Fuel* 305 (Dec. 2021), p. 121571. DOI: 10.1016/j.fuel.2021.121571 (cit. on pp. 30, 31).

[61] I. A. Resitoglu, K. Altinisik, A. Keskin, and K. Ocakoglu. “The effects of Fe2O3 based DOC and SCR catalyst on the exhaust emissions of diesel engines”. In: *Fuel* 262 (Feb. 2020), p. 116501. DOI: 10.1016/j.fuel.2019.116501 (cit. on p. 30).

[62] L. Tan, Y. Guo, Z. Liu, P. Feng, and Z. Li. “An investigation on the catalytic characteristic of NO reduction in SCR systems”. In: *Journal of the Taiwan Institute of Chemical Engineers* 99 (June 2019), pp. 53–59. DOI: 10.1016/j.jtice.2019.02.020 (cit. on p. 30).

[63] J. Ko, K. Kim, W. Chung, C.-L. Myung, and S. Park. “Characteristics of on-road particle number (PN) emissions from a GDI vehicle depending on a catalytic stripper (CS) and a metal-foam gasoline particulate filter (GPF)”. In: *Fuel* 238 (Feb. 2019), pp. 363–374. DOI: 10.1016/j.fuel.2018.10.091 (cit. on p. 31).

[64] T. Wilberforce, A. Olabi, E. T. Sayed, K. Elsaid, and M. A. Abdelkareem. “Progress in carbon capture technologies”. In: *Science of The Total Environment* 761 (Mar. 2021), p. 143203. DOI: 10.1016/j.scitotenv.2020.143203 (cit. on p. 31).

[65] E. I. Koytsoumpa, C. Bergins, and E. Kakaras. “The CO2 economy: Review of CO2 capture and reuse technologies”. In: *The Journal of Supercritical Fluids* 132 (Feb. 2018), pp. 3–16. DOI: 10.1016/j.supflu.2017.07.029 (cit. on p. 31).

[66] I. Ozsari, Y. Ust, and H. K. Kayadelen. “Comparative Energy and Emission Analysis of Oxy-Combustion and Conventional Air Combustion”. In: *Arabian Journal for Science and Engineering* 46.3 (Jan. 2021), pp. 2477–2492. DOI: 10.1007/s13369-020-05130-0 (cit. on p. 32).

[67] S. Chen. “Fundamentals of Oxy-fuel Combustion”. In: *Oxy-Fuel Combustion*. Elsevier, 2018, pp. 13–30. DOI: 10.1016/b978-0-12-812145-0.00002-5 (cit. on pp. 32, 33).

[68] Y. Shi, Q. Liu, Y. Shao, and W. Zhong. “Energy and exergy analysis of oxy-fuel combustion based on circulating fluidized bed power plant firing coal, lignite and biomass”. In: *Fuel* 269 (June 2020), p. 117424. DOI: 10.1016/j.fuel.2020.117424 (cit. on p. 32).

[69] Y. Liang, L. Cai, Y. Guan, W. Liu, Y. Xiang, J. Li, and T. He. “Numerical study on an original oxy-fuel combustion power plant with efficient utilization of flue gas waste heat”. In: *Energy* 193 (Feb. 2020), p. 116854. DOI: 10.1016/j.energy.2019.116854 (cit. on p. 32).

[70] L. Cai, L. Tan, Y. Liang, X. Yin, C. Liu, and Y. Guan. "Numerical study on sulfur-bearing natural gas oxy-fuel combustion power plant". In: *Applied Thermal Engineering* 196 (Sept. 2021), p. 117292. DOI: 10.1016/j.applthermaleng.2021.117292 (cit. on p. 32).

[71] S. K. Park, T. S. Kim, J. L. Sohn, and Y. D. Lee. "An integrated power generation system combining solid oxide fuel cell and oxy-fuel combustion for high performance and CO2 capture". In: *Applied Energy* 88.4 (Apr. 2011), pp. 1187–1196. DOI: 10.1016/j.apenergy.2010.10.037 (cit. on p. 32).

[72] E. Thorbergsson and T. Grönstedt. "A Thermodynamic Analysis of Two Competing Mid-Sized Oxyfuel Combustion Combined Cycles". In: *Journal of Energy* 2016 (2016), pp. 1–14. DOI: 10.1155/2016/2438431 (cit. on pp. 32, 35).

[73] D. P. Hanak, D. Powell, and V. Manovic. "Techno-economic analysis of oxy-combustion coal-fired power plant with cryogenic oxygen storage". In: *Applied Energy* 191 (Apr. 2017), pp. 193–203. DOI: 10.1016/j.apenergy.2017.01.049 (cit. on p. 32).

[74] A. V. Blarigan, D. Kozarac, R. Seiser, J. Chen, R. Cattolica, and R. Dibble. "Spark-ignited engine NOx emissions in a low-nitrogen oxycombustion environment". In: *Applied Energy* 118 (Apr. 2014), pp. 22–31. DOI: 10.1016/j.apenergy.2013.12.007 (cit. on p. 33).

[75] A. Mohammed, A. Elkhazraji, S. Jan, and B. Johansson. "A Study on the Performance and Emissions of HCCI Oxy-Fuel Combustion in a CFR Engine with Recirculated Carbon Dioxide". In: *SAE Technical Paper Series*. SAE International, Sept. 2020. DOI: 10.4271/2020-01-2065 (cit. on pp. 33, 161).

[76] Z.-J. Wu, X. Yu, L.-Z. Fu, J. Deng, Z.-J. Hu, and L.-G. Li. "A high efficiency oxyfuel internal combustion engine cycle with water direct injection for waste heat recovery". In: *Energy* 70 (June 2014), pp. 110–120. DOI: 10.1016/j.energy.2014.03.095 (cit. on p. 33).

[77] Z. Kang, Z. Wu, Z. Zhang, J. Deng, Z. Hu, and L. Li. "Study of the Combustion Characteristics of a HCCI Engine Coupled with Oxy-Fuel Combustion Mode". In: *SAE International Journal of Engines* 10.3 (Mar. 2017), pp. 908–916. DOI: 10.4271/2017-01-0649 (cit. on p. 33).

[78] Q. Tan and Y. Hu. "A study on the combustion and emission performance of diesel engines under different proportions of O2 &amp N2 &amp CO2". In: *Applied Thermal Engineering* 108 (Sept. 2016), pp. 508–515. DOI: 10.1016/j.applthermaleng.2016.07.151 (cit. on p. 33).

[79] Y. Gao, L. Li, X. Yu, J. Deng, and Z. Wu. “Effect of Compression Ratio on Internal Combustion Rankine Cycle Based on Simulations”. In: *Lecture Notes in Electrical Engineering*. Springer Berlin Heidelberg, Dec. 2014, pp. 129–138. DOI: 10.1007/978-3-662-45043-7_14 (cit. on p. 33).

[80] C. Li, J. J. Chew, A. Mahmoud, S. Liu, and J. Sunarso. “Modelling of oxygen transport through mixed ionic-electronic conducting (MIEC) ceramic-based membranes: An overview”. In: *Journal of Membrane Science* 567 (Dec. 2018), pp. 228–260. DOI: 10.1016/j.memsci.2018.09.016 (cit. on p. 35).

[81] A. I. Escudero, S. Espatolero, and L. M. Romeo. “Oxy-combustion power plant integration in an oil refinery to reduce CO 2 emissions”. In: *International Journal of Greenhouse Gas Control* 45 (Feb. 2016), pp. 118–129. DOI: 10.1016/j.ijggc.2015.12.018 (cit. on pp. 35, 36).

[82] G. Cau, V. Tola, F. Ferrara, A. Porcu, and A. Pettinau. “CO2-free coal-fired power generation by partial oxy-fuel and post-combustion CO2 capture: Techno-economic analysis”. In: *Fuel* 214 (Feb. 2018), pp. 423–435. DOI: 10.1016/j.fuel.2017.10.023 (cit. on pp. 35, 36).

[83] J. Xiong, H. Zhao, and C. Zheng. “Exergy Analysis of a 600 MWe Oxy-combustion Pulverized-Coal-Fired Power Plant”. In: *Energy Fuels* 25.8 (July 2011), pp. 3854–3864. DOI: 10.1021/ef200702k (cit. on pp. 35, 36).

[84] M. A. Habib, M. Nemitallah, and R. Ben-Mansour. “Recent Development in Oxy-Combustion Technology and Its Applications to Gas Turbine Combustors and ITM Reactors”. In: *Energy &amp Fuels* 27.1 (Dec. 2012), pp. 2–19. DOI: 10.1021/ef301266j (cit. on p. 35).

[85] R. T. Yang. *Gas separation by adsorption processes*. World Scientific, 1997, p. 352. ISBN: 1860940471 (cit. on p. 36).

[86] A. Smith and J. Klosek. “A review of air separation technologies and their integration with energy conversion processes”. In: *Fuel Processing Technology* 70.2 (May 2001), pp. 115–134. DOI: 10.1016/s0378-3820(01)00131-x (cit. on pp. 36, 37).

[87] M. Alipour, D. Pudasainee, J. A. Nychka, and R. Gupta. “ZrO_2–CuO Sorbents for High-Temperature Air Separation”. In: *Industrial Engineering Chemistry Research* 53.27 (June 2014), pp. 10990–10999. DOI: 10.1021/ie501068d (cit. on p. 36).

[88] N. Z. Institute of Chemistry. *Production of Chemicals*. 2018. URL: https://nzic.org.nz/chemical-processes-new-zealand/production-of chemicals (cit. on p. 36).

[89] Y. Liu, Q. Zhang, Y. Cao, X. Yang, Z. Li, W. Liu, J. B. Habyarimana, Y. Cui, H. Wang, and R. T. Yang. "Effect of intermittent purge on O2 production with rapid pressure swing adsorption technology". In: *Adsorption* 27.2 (Nov. 2020), pp. 181–189. DOI: 10.1007/s10450-020-00284-7 (cit. on p. 36).

[90] C.-S. Chang, S.-H. Ni, H.-S. Yang, and C.-T. Chou. "Simulation study of separating oxygen from air by pressure swing adsorption process with semicylindrical adsorber". In: *Journal of the Taiwan Institute of Chemical Engineers* 120 (Mar. 2021), pp. 67–76. DOI: 10.1016/j.jtice.2021.03.027 (cit. on p. 36).

[91] X. Zhu, Y. Sun, Y. Liu, X. Sun, and J. Shi. "Experimental performance analysis of vacuum pressure swing adsorption air separation process under plateau special conditions". In: *Separation Science and Technology* 57.18 (June 2022), pp. 2885–2893. DOI: 10.1080/01496395.2022.2085115 (cit. on p. 36).

[92] C. Zhou, K. Shah, and B. Moghtaderi. "Techno-Economic Assessment of Integrated Chemical Looping Air Separation for Oxy-Fuel Combustion: An Australian Case Study". In: *Energy &amp Fuels* 29.4 (Mar. 2015), pp. 2074–2088. DOI: 10.1021/ef5022076 (cit. on p. 37).

[93] C. Zhou, K. Shah, H. Song, J. Zanganeh, E. Doroodchi, and B. Moghtaderi. "Integration Options and Economic Analysis of an Integrated Chemical Looping Air Separation Process for Oxy-fuel Combustion". In: *Energy &amp Fuels* 30.3 (Dec. 2015), pp. 1741–1755. DOI: 10.1021/acs.energyfuels.5b02209 (cit. on p. 37).

[94] B. Shi, E. Wu, and W. Wu. "Novel design of chemical looping air separation process for generating electricity and oxygen". In: *Energy* 134 (Sept. 2017), pp. 449–457. DOI: 10.1016/j.energy.2017.05.080 (cit. on p. 37).

[95] L. Zhu, F. Wang, and Z. Zhang. "Thermodynamic evaluation of a conceptual process for coal gasification coupled with chemical looping air separation". In: *Chemical Engineering and Processing: Process Intensification* 106 (Aug. 2016), pp. 33–41. DOI: 10.1016/j.cep.2016.05.002 (cit. on p. 37).

[96] A. A. Plazaola, A. C. Labella, Y. Liu, N. B. Porras, D. P. Tanaka, M. S. Annaland, and F. Gallucci. "Mixed Ionic-Electronic Conducting Membranes (MIEC) for Their Application in Membrane Reactors: A Review". In: *Processes* 7.3 (Mar. 2019), p. 128. DOI: 10.3390/pr7030128 (cit. on p. 38).

[97] L. L. Anderson et al. “Advances in ion transport membrane technology for oxygen and syngas production”. In: *Solid State Ionics* 288 (May 2016), pp. 331–337. DOI: 10.1016/j.ssi.2015.11.010 (cit. on p. 39).

[98] G. Maxwell Christie and J. Lane. “COMPOSITE OXYGEN TRANSPORT MEMBRANE”. English. US 2013/0156978 A1. 2013 (cit. on p. 39).

[99] R. Prasad, J. M. Schwartz, E. T. Robinson, and C. F. Gottzmann. “Syngas production metjod utilizing an oxygen transport membrane”. English. US 6,695,983 B2. Feb. 2004 (cit. on p. 39).

[100] S. Kelly, S. Chakravarti, and J. Li. “Oxygen transport membrane reactor based method and system for generating electric power”. English. US 9,562.472 B2. Feb. 2017 (cit. on p. 39).

[101] W. Bai, J. Feng, C. Luo, P. Zhang, H. Wang, Y. Yang, Y. Zhao, and H. Fan. “A comprehensive review on oxygen transport membranes: Development history, current status, and future directions”. In: *International Journal of Hydrogen Energy* 46.73 (Oct. 2021), pp. 36257–36290. DOI: 10.1016/j.ijhydene.2021.08.177 (cit. on pp. 39, 140).

CHAPTER 3

Methodology

Contents

Figures

Tables

3.1 Introduction

THe calculation and analysis of oxygen production cycles using membranes can be performed using different tools. These tools must ensure the proper development of models that express the real-life phenomena that govern these systems.

In this sense, the combination of experimental results and 0D/1D modeling is implemented in the current thesis to accomplish the study. From the experimental part, the oxycombustion parameters in a spark-ignition engine are obtained from the work of associated researchers that developed their work in the same framework as the current thesis.

For 0D/1D calculation, two software have been used to model and perform calculations. In the first instance, VEMOD (abbreviation for Virtual Engine Modeling) is an in-house software developed in CMT-Motores Térmicos, which is specialized in engine modeling but is currently capable of performing calculations with different industrial systems. On the other hand, IPSE-Pro is a software system for the calculation of heat balances and simulating processes, developed at SimTech, a spin-off company of the Graz University of Technology, which is implemented in the modeling of the coupled function of a power plant with a membrane-based oxygen production cycle (Chapter 5 of the current document). Both software use different submodels of turbochargers, heat exchangers, piping, or cooling processes, as explained in this section.

Particular assumptions and procedures for each studied case are described in their respective chapter as indicators for evaluating performance and optimization processes.

3.2 Software

VEMOD [102] is a software developed in CMT-Motores Termicos that is used for calculations in this thesis (except those performed in Chapter 5). VEMOD was initially designed for computing engines; however, several models have been added over the last years, demonstrating to be capable of correctly assessing different industrial cycles, as the one performed by Serrano et al. [2]. Different studies, especially regarding engines, have been performed successfully in VEMOD, as seen in Olmeda et al. [103], used in the energy balance at warm and cold conditions during transient mode of a test cycle. Additionally, Serrano et al. [15] demonstrate the capability of using VEMOD to calculate an engine under oxycombustion conditions, while Arnau et al. [104] studied with VEMOD the effect of thermal insulation in the performance of a compression ignition engine.

VEMOD solves Euler's fluid dynamics equations in 1D inside ducts using a finite-volume approach. MUSCL method is selected for the solution of

the equations, including heat transfer and friction losses, using Colburn and Colebrook-White's equations, respectively. On the other hand, several elements are solved using 0D calculations.

On the other hand, IPSE-Pro is the software used to perform calculations regarding chapter 5 of the thesis [105]. IPSE-Pro is used for calculating heat balances and simulating processes, composed of modules that can be used in various applications such as thermal and solar power, refrigeration, or gasification. The model used in this thesis allows calculations regarding conventional power plants, cogeneration, and combined cycle plants. The calculations performed for chapter 5 use 0D modeling for the different components used, applying fundamental principles to calculate turbomachines, coolers, and combustion chambers.

3.3 Membrane model

The membrane is the core of the oxygen production of this thesis, as well as the operation center that couples the oxygen production and the power production cycles. In this sense, its accurate modeling is indispensable to performing consistent calculations during the study.

Oxygen permeation is calculated following Wagner's equation, considering BSCF material for the membrane construction and an isothermal calculation. The use of isothermal assumption for membrane calculations has been validated in CFD and experimental studies, as those performed by Catalan-Martínez et al. [106], Shubnikova et al. [107], and Li et al. [108]. Equation 3.1 shows the expression for oxygen mass flow calculation.

$$\dot{m}_{\mathrm{O_2}} = \frac{\mathrm{C}\cdot \mathrm{e}^{\left(\frac{-K}{T}\right)} \cdot \ln\left(\frac{P_{O_2,\mathrm{feed}}}{P_{O_2,\mathrm{perm}}}\right) \cdot T \cdot \mathrm{MW}_{\mathrm{O_2}} \cdot A}{L} \tag{3.1}$$

In this expression, C and K represent material constants whose values are $1.004 \times 10^{-8}\,\mathrm{mol\,cm\,s^{-1}}$ and 6,201 K, respectively. T is the operating temperature of the membrane, $\mathrm{MW}_{\mathrm{O_2}}$ is the molecular weight of the oxygen, A is the membrane area, and L is the membrane thickness. The membrane thickness is set to 200 µm, a reasonable value considering the pressures and temperatures managed in this thesis, where bulk diffusion through the membrane can be presupposed as the predominant mechanism of oxygen separation.

On the other hand, $P_{O_2,\mathrm{feed}}$ is the mean oxygen partial pressure at the feed side of the membrane, while $P_{O_2,\mathrm{perm}}$ is the equivalent for the permeate or sweep side. These values are determined by the geometric mean of oxygen partial

pressure of the inlet and outlet streams of both sides of the membrane, calculated as shown in Equation 3.2, Equation 3.3, Equation 3.4 and Equation 3.5.

Feed pressure:

$$P_{O_2,\text{feed}} = P_{\text{feed}} \cdot X_{O_2,\text{feed}} \tag{3.2}$$

$$X_{O_2,\text{feed}} = \sqrt{X_{O_2,\text{in,feed}} \cdot X_{O_2,\text{out,feed}}} \tag{3.3}$$

Permeate pressure:

$$P_{O_2,\text{perm}} = P_{\text{perm}} \cdot X_{O_2,\text{perm}} \tag{3.4}$$

$$X_{O_2,\text{perm}} = 1 - \sqrt{(1 - X_{O_2,in,\text{perm}}) \cdot (1 - X_{O_2,\text{out,perm}})} \tag{3.5}$$

where $X_{O_2,\text{feed}}$ and $X_{O_2,\text{perm}}$ are the mean oxygen molar fraction at the feed and permeate side, respectively, calculated by considering the values at the inlet and outlet at each side.

Finally, the membrane's feed and permeate side are assumed to be 0D elements of finite volume, where continuity and energy conservation are used, assuming adiabatic behavior for the whole membrane.

3.4 Combustion modeling for spark-ignition engine

Combustion laws used for engine calculations follow the results of Serrano et al. [13], developed in the same framework as the present thesis. The cited study uses experimental and numerical tools to study oxycombustion in a spark-ignition engine, where different EGR rates, dilution, and spark timings were evaluated. In this sense, an engine test bench was adapted to be supplied by O_2 and CO_2 during the start-up. After the steady operation, EGR replaced the CO_2 supply. Conventional operation with air was still available during the testing campaign to obtain performance results and compare them with oxycombustion. The layout of this test bench is shown in Figure 3.1.

During the testing, different variables were measured, such as in-cylinder pressure, pressures and temperatures in the intake and exhaust manifolds, emissions, and CO_2 concentration at the intake. With in-cylinder data, parameters such as indicated mean effective pressure (IMEP), combustion phasing and misfiring, cycle-to-cycle variability, maximum cylinder pressure, and heat release rate were obtained using the in-house software CALMEC, which has demonstrated its validity for these calculations in different studies, such as those performed by Payri et al. [109] and Benajes et al. [110].

Furthermore, to reduce the experimental campaigns, 0D-1D models were used to calculate the thermochemical and fluid-dynamic behavior of oxycombustion at different conditions. These tools determine theoretical limits regarding combustion stability, exhaust temperatures, and indicated efficiency.

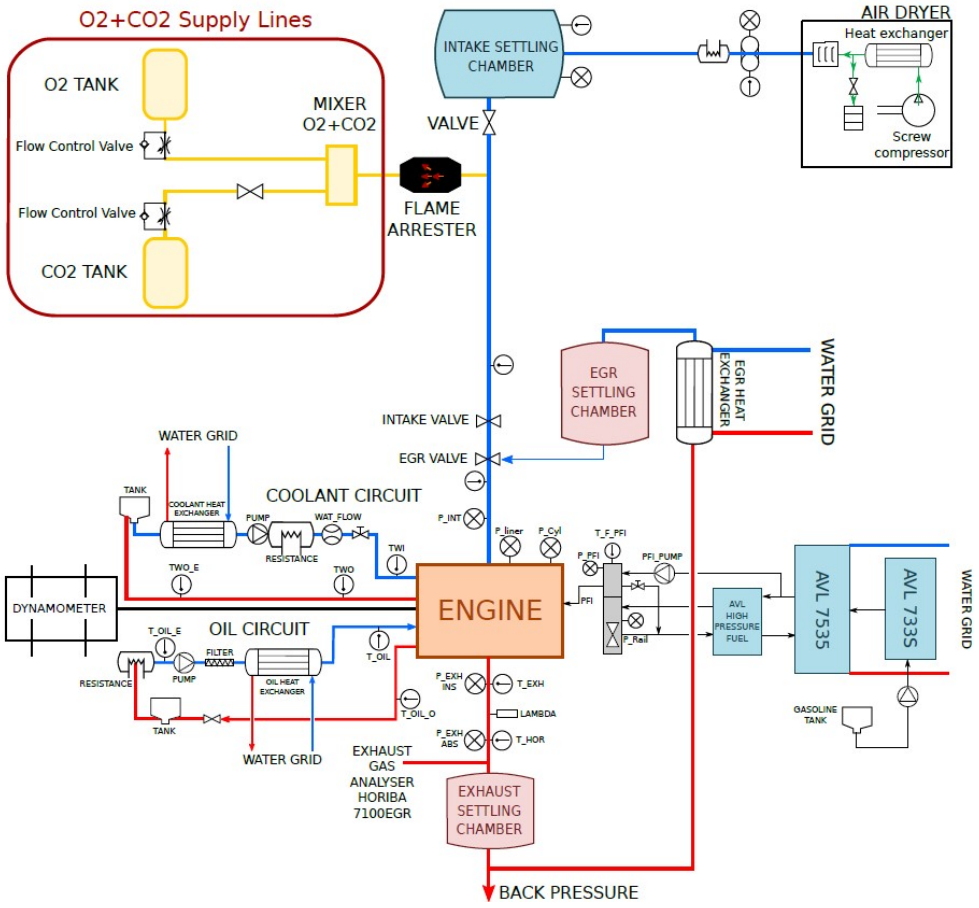

Figure 3.1: Engine test bench used by Serrano et al [13] in their experiments

0D modeling was used to calculate thermo-chemical processes, helping to determine combustion variables such as auto-ignition delay, laminar flame speed, and flame temperature for different EGR and dilution conditions. This model is based on the chemical kinetic mechanism proposed by Liu et al. [111] based on primary reference fuel. On the other hand, 0D-1D simulations are used to assess the fluid-dynamic behavior of the engine working under oxycombustion. The engine model was initially calibrated using experimental data shown by Serrano et al. [12].

Initially, oxygen and EGR dilution strategies are evaluated using 0D-1D thermochemical calculations, which determine limits using the model's variables. Due to the complexity of knocking, 0D modeling is not sufficiently accurate to predict it. Nonetheless, its probability relative to conventional combustion can set acceptable boundaries in this case. For this reason, a delimited region with a similar knocking propensity as conventional combustion was obtained. In

addition, a value of $0.5\,\mathrm{m\,s^{-1}}$ for laminar flame speed is fixed, which was found to generate the longest possible combustion duration that allows stable flame. Finally, a maximum flame temperature of 3,000 K is set to avoid engine damage. These limits are shown in Figure 3.2, which shows the mentioned variables' behavior depending on EGR rate and dilution.

According to chemical calculations, combustion near stoichiometric conditions and EGR values between 65 to 75 % are practical in a spark-ignition engine. EGR dilution demands a lower oxygen flow, which implies less energy consumption for its production, and permits a more straightforward process for carbon capture from exhaust gases.

These results are validated experimentally, where a range between 67 to 73 % with near-stoichiometric combustion was feasible. Higher EGR than 73 % exhibits instabilities during the combustion, while a lower EGR than 67 % during operation performs high exhaust temperatures that jeopardize the sensors and engine integrity. These results agree with the chemical calculations, explaining the EGR limits and the implementation of stoichiometric combustion.

Furthermore, a spark timing sweep for different EGR values is performed experimentally to optimize the indicated efficiency for each EGR rate and determine knocking limits and zones of combustion instabilities. Figure 3.3 shows IMEP variability to determine combustion instabilities and maximum amplitude of pressure oscillations (MAPO) for knocking propensity. High EGR leads to combustion stability, demanding advanced spark timings for correct operation, as shown in Figure 3.3(a). On the other hand, the whole range of EGR and spark timing exhibits a MAPO under 1, considered a safe threshold for the appearance of knocking, demonstrating the low propensity to this phenomenon under oxycombustion at the studied conditions. These results agree with those shown in Figure 3.2(a), where the region limited by the dashed lines showing high knock propensity is far from the selected EGR rates and stoichiometric combustion.

On the other hand, the black stars in Figure 3.3(b) show the conventional combustion results at different spark timings. There is a point where MAPO increases suddenly as the combustion keeps advancing, finding its optimum point with a MAPO value almost five times higher than the recommended threshold. This indicated that optimal conventional combustion performs at a value of auto-ignition delay near the one that is found near the dashed lines in Figure 3.2(a).

The explained methodology was implemented while operating the engine at an IMEP of 1.1 MPa at 3,000 rpm. Higher load conditions must be evaluated to determine knocking propensity in the engine. In this sense, 0D-1D-CFD calculations were performed at a 2.5 MPa of IMEP, running the engine at the same speed. Firstly, optimum working conditions were obtained using 0D-1D simulations at 70 % of EGR rate, using the spark timing as an optimization

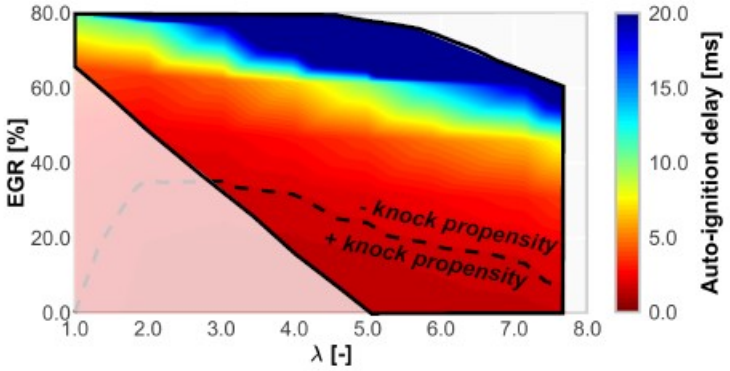

(a) Knocking propensity for different EGR and dilution levels. Results from Serrano et al. [13]

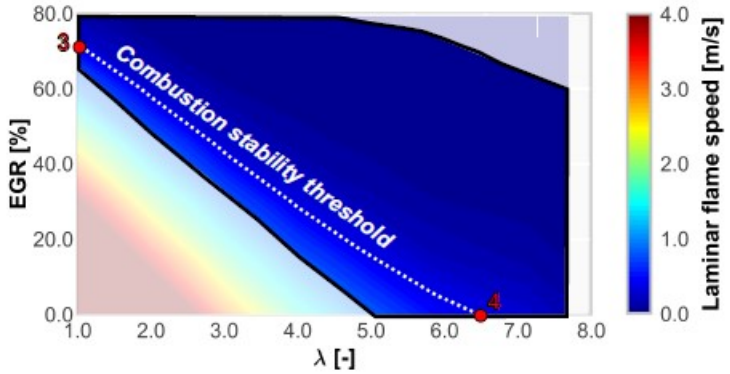

(b) Combustion stability for different EGR and dilution levels. Results from Serrano et al. [13]

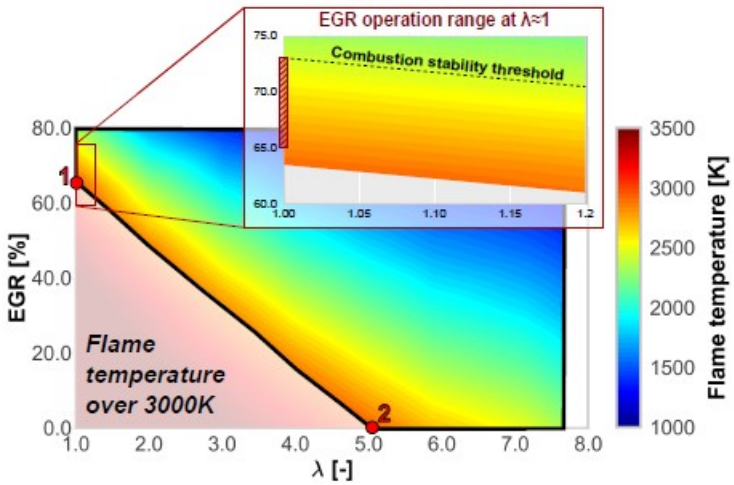

(c) Maximum flame temperature for different EGR and dilution levels. Results from Serrano et al. [13]

Figure 3.2: Analysis of chemical simulations for different EGR and dilution levels. Results from Serrano et al. [13]

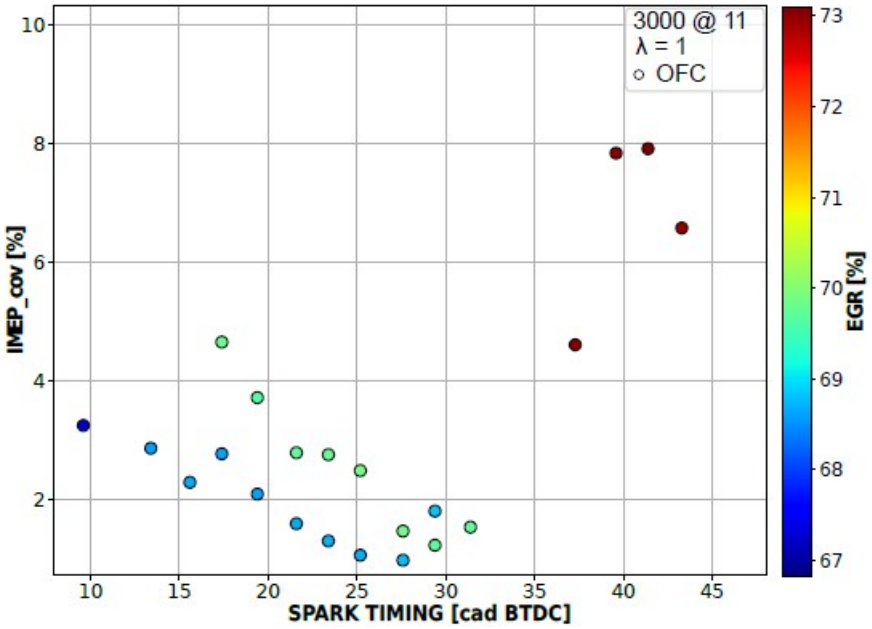

(a) IMEP variability at different EGR and spark timings. Results from Serrano et al. [13]

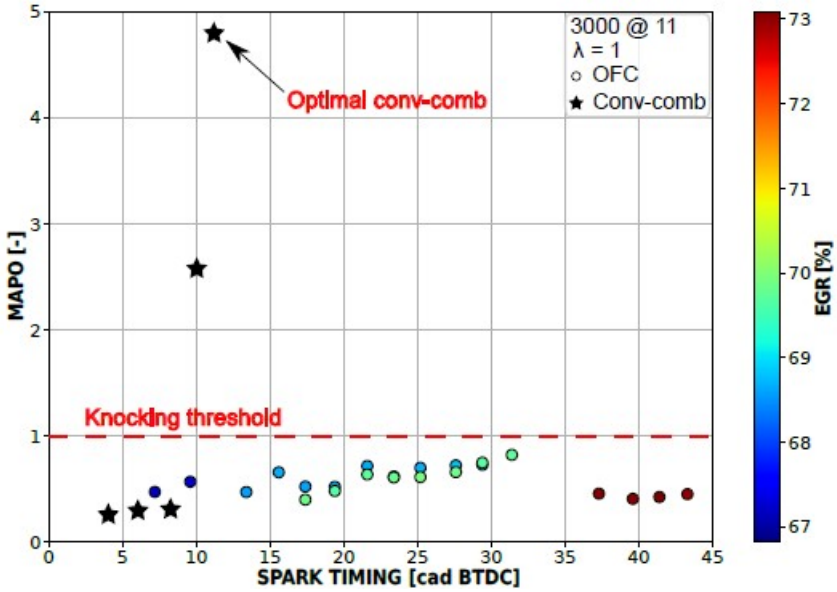

(b) Maximum amplitude of pressure oscillations at different EGR and spark timings. Results from Serrano et al. [13]

Figure 3.3: Indicators to determine combustion instabilities and knocking. Results from Serrano et al. [13]

variable. By setting the results of the latter optimization process as boundary conditions, a CFD calculation is performed to assess knocking. A low propensity for knocking was found during high-load operation, finding low oscillations in the heat release rate. These results are encouraging because they demonstrate room to increase the engine's compression ratio to improve its performance. The calculations performed in chapter 6 of this thesis follow this idea, and the engine compression ratio is increased to improve the engine performance.

Considering all of the above, a reduced premixed combustion model is developed. Feasible ranges of spark ignition and EGR are considered, finding an stable region where combustion instabilities and risky conditions such as high exhaust temperatures are avoided. This region is shown in Figure 3.4.

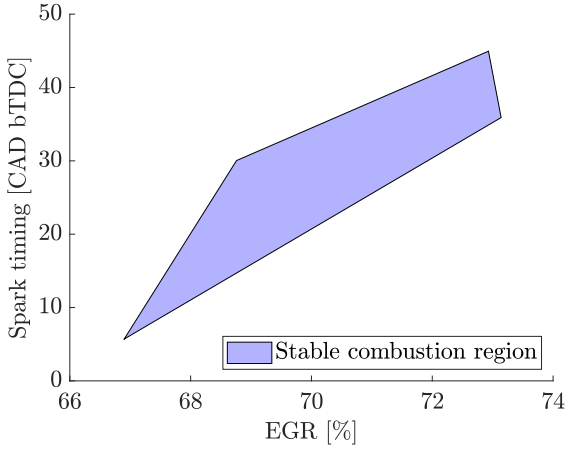

Figure 3.4: Stable combustion region

Using CALMEC, the heat release rate is determined for each studied case, determining the main parameters to feed a Wiebe-type function: combustion duration ($\Delta\alpha$), shape form (m) and ignition delay (α) (to determine the start of combustion). Considering this information, three different correlations are developed to obtain these variables, which depend on EGR rate and spark timing. These correlations are shown in Equation 3.6, Equation 3.7 and Equation 3.8.

$$\Delta\alpha = 51.79 + 6.34 \cdot (EGR - 69.92) + 0.62 \cdot (ST + 26) \tag{3.6}$$

$$\begin{aligned} m =& 3.15 - 0.26 \cdot (EGR - 69.92) - 0.02 \cdot (ST + 26) \\ &+ 0.016 \cdot (EGR - 69.92) \cdot (ST + 26) + 0.00275 \cdot (ST + 26)^2 \end{aligned} \tag{3.7}$$

$$\begin{aligned} \alpha =& -14.41 + 2.22 \cdot (EGR - 69.92) + 0.81 \cdot (ST + 26) \\ &- 0.16 \cdot (EGR - 69.92) \cdot (ST + 26) - 0.026 \cdot (ST + 26)^2 \end{aligned} \tag{3.8}$$

In this expressions, EGR corresponds to the exhaust gases recirculation fraction at the engine intake, while ST is the spark-timing at the cylinders.

Considering these expressions, a combustion law is set for a particular engine operation point, imposed during the calculation of the studied spark-ignition engine in this thesis.

3.5 Turbocharging modeling and scaling

Different sets of turbochargers are implemented depending on the studied case of the current thesis. In addition, two different software are used for calculations; thus, different approaches are followed to calculate turbomachines.

Firstly, VEMOD solved turbochargers as actuator disks connected to equivalent 1D ducts, using characteristic curves map data to introduce momentum and energy sources and sinks. The turbocharger calculations consider friction and heat losses as described in the works performed by Serrano et al. [112, 113, 114, 115].

Additionally, turbine and compressor maps are extrapolated and interpolated (depending on the operation point demanded in the studied case) based on the works by Serrano et al.[116], Payri et al [117] and Galindo et al [118].

In this sense, a typical commercial off-the-shelf (COTS) component from the automotive industry is used depending on the case. Each turbomachine is scaled according to inlet temperature and pressure conditions, where the best performance is pursued. COTS turbochargers are selected considering that similar components are available in the market, with competitive price and high disponibility of replacement parts if necessary.

The scaling is based on maintaining non-dimensional mass flow and speed constant for each turbomachine for similarity purposes. The mentioned non-dimensional groups are determined using Equation 3.9 and Equation 3.10:

$$\hat{m} = \frac{\dot{m}\sqrt{\gamma R T_{01}}}{D^2 p_{01} \gamma} \tag{3.9}$$

$$\hat{N} = \frac{ND}{\sqrt{\gamma R T_{01}}} \tag{3.10}$$

where $\hat{m}$ is the non-dimensional mass flow, $\dot{m}$ is the mass flow, γ is the heat capacities ratio, R is the gas constant, $T_{1,\mathrm{t}}$ is the total temperature at the inlet of the turbomachine, D is the wheel diameter, $p_{1,\mathrm{t}}$ is the total pressure at the inlet of the turbomachine, $\hat{N}$ is the non-dimensional rotational speed, and N is the rotational speed.

Considering the latter, adiabatic maps are obtained, keeping the efficiency values for each operation point constant. Then, real efficiencies are determined

considering the heat and friction losses, which change depending on the geometric variation due to the applied scale.

Finally, the approach used in Chapter 5 (using IPSE-Pro) differs from the one formerly explained. The system evaluated in this chapter is in a phase where feasibility studies are being performed, and no detailed design has been performed, nor has a selection of specific components for experimental evaluation. In this sense, the turbomachines used in the oxygen production cycle in chapter 5 are modeled by assuming a reasonable adiabatic efficiency according to the mass flow and pressure ratios that manage each turbomachine, with high mechanical efficiency according to the application. On the other hand, a set of high-temperature turbines are calculated using the model described by Sanz et al [119], where the cooling process is considered to set a maximum metal temperature and temperature difference between the metal surface and cooling temperature at the cooling outlet to the main flow.

3.6 Subsystems modeling

The simulations required several submodels for their accurate performance. The present thesis also calculates coolers, heaters, heat exchangers, pipes, and engine cylinders. For the 0D models, continuity and energy conservation equations are used, including, depending on the case, heat transfer or species permeation (for membrane modeling).

The heat flux of the coolers is calculated depending on the required outlet temperature, where a normal energy balance is performed to determine the dissipated energy. For heat exchangers, constant effectiveness is set for all the components, whose value is selected according to their context of use, as there are still not detailed specifications of heat exchangers in this stage of the analyses. For both elements, the pressure losses are modeled by considering the dissipation of the dynamic pressure component as the source of pressure drop.

A heater is used in the first analysis of an oxygen production cycle to increase air temperature and improve oxygen production conditions. A constant efficiency is set, considering heat losses and combustion efficiency. Further explanation will be given in chapter 4.

Pipes are modeled by solving 1D Euler fluid dynamics equations using a finite-volume approach and the MUSCL method. Colebrook-White and Colburn's correlations are implemented for friction and heat transfer calculations, respectively.

Finally, engine cylinders are calculated also using 0D modeling, where heat transfer and friction calculations are made using calibrated versions of the Woshcni and Chen-Fylnn equations, respectively. Energy balance is performed,

determining the heat released by the fuel by following the methodology explained in section 3.4.

For chapter 5, coolers in the oxygen production cycle are calculated following the same methodology as described. Heat exchangers are calculated by considering a temperature difference between the outlet stream of the hot side and the inlet stream of the cold side, as countercurrent disposition is assumed. A combustion chamber is modeled using energy and continuity equations, considering a constant percentage of heat losses. These elements also considered a constant percentage of pressure losses. More details are given in chapter 5.

3.7 Summary

Different elements are modeled to accurate proper calculations during this thesis development. Firstly, two software are used to perform simulations: VEMOD and IPSE-Pro, which are in-house software developed to assess industrial processes.

The membrane model implemented uses Wagner's equation, using a membrane thickness of 200 µm, which is an acceptable value considering the thermodynamic conditions in which the membranes operate in the context of this thesis. Isothermal performance is assumed, as it is an accurate hypothesis to calculate oxygen permeation in this membrane type. 0D calculations regarding energy and mass balances are also considered.

The heat release laws applied in the spark-ignition engine study of oxycombustion are determined through combined experimental and numerical studies. Initially, a thermochemical model is implemented to establish a reasonable operation region that permits avoiding combustion issues such as knocking or misfiring and reducing the risk of compromising the facilities' integrity. Then, this operation region is validated experimentally, where a good agreement is found with the model results.

Considering the obtained results, a spark timing sweep is performed at the EGR range that was previously determined. An operation zone is determined in the engine's operation, where stable combustion is ensured to operate under oxycombustion. At each studied point, heat release laws were determined using the in-house tool CALMEC, where the parameters that characterize combustion were found. Then, considering Wiebe-type functions for combustion laws, three correlations are obtained that determine the combustion duration, shape form, and ignition delay to determine the start of combustion. For each studied point, these parameters are calculated, which are required to feed the Wiebe function.

On the other hand, the feasibility of high-load operation (2.5 MPa of IMEP) is evaluated using CFD calculations. Low knocking propensity was found in CFD

results, demonstrating the possibility of increasing the engine's compression ratio to improve performance.

Turbochargers are modeled using characteristic maps of commercial off-the-shelf components to introduce energy and momentum sources and sinks. Several models are used to determine friction and heat losses and to extrapolate and interpolate the characteristic maps of the turbomachines. The scaling process of COTS turbomachines is based on maintaining constant non-dimensional mass flow and speed for similarity purposes. In Chapter 5, turbomachines are modeled by assuming a reasonable adiabatic efficiency according to operating conditions of each turbomachine, with high mechanical efficiency according to the application.

Other submodels used, such as coolers, heaters, heat exchangers, pipes, and engine cylinders, implement continuity and energy conservation equations, where particular assumptions are considered depending on the element.

3.8 References

[2] J. R. Serrano, F. J. Arnau, L. M. García-Cuevas, and F. A. Gutiérrez. "Thermo-economic analysis of an oxygen production plant powered by an innovative energy recovery system". In: *Energy* 255 (Sept. 2022), p. 124419. DOI: 10.1016/j.energy.2022.124419 (cit. on pp. vii, 56).

[12] J. Serrano, J. Martín, J. Gomez-Soriano, and R. Raggi. "Theoretical and experimental evaluation of the spark-ignition premixed oxy-fuel combustion concept for future CO2 captive powerplants". In: *Energy Conversion and Management* 244 (Sept. 2021), p. 114498. DOI: 10.1016/j.enconman.2021.114498 (cit. on pp. 2, 59, 151, 156, 161).

[13] J. R. Serrano, J. M. Díaz, J. Gomez-Soriano, and R. Raggi. "Exploring the Oxy-Fuel Combustion in Spark-Ignition Engines for Future Clean Powerplants". In: *ASME 2022 ICE Forward Conference*. American Society of Mechanical Engineers, Oct. 2022. DOI: 10.1115/icef2022-89167 (cit. on pp. 2, 33, 34, 42, 58, 59, 61, 62, 151, 156, 161).

[15] J. Serrano, F. Arnau, L. García-Cuevas, and V. Farias. "Oxy-fuel combustion feasibility of compression ignition engines using oxygen separation membranes for enabling carbon dioxide capture". In: *Energy Conversion and Management* 247 (Nov. 2021), p. 114732. DOI: 10.1016/j.enconman.2021.114732 (cit. on pp. 3, 56, 152, 153).

[102] J. Martin, F. Arnau, P. Piqueras, and A. Auñon. "Development of an Integrated Virtual Engine Model to Simulate New Standard Testing Cycles". In: *SAE Technical Paper Series*. SAE International, Apr. 2018. DOI: 10.4271/2018-01-1413 (cit. on p. 56).

[103] P. Olmeda, J. Martın, F. J. Arnau, and S. Artham. "Analysis of the energy balance during World harmonized Light vehicles Test Cycle in warmed and cold conditions using a Virtual Engine". In: *International Journal of Engine Research* 21.6 (Oct. 2019), pp. 1037–1054. DOI: 10.1177/1468087419878593 (cit. on p. 56).

[104] F. J. Arnau, J. Martın, P. Piqueras, and Á. Auñón. "Effect of the exhaust thermal insulation on the engine efficiency and the exhaust temperature under transient conditions". In: *International Journal of Engine Research* 22.9 (Oct. 2020), pp. 2869–2883. DOI: 10.1177/1468087420961206 (cit. on p. 56).

[105] S. GmbH. *Introducing IPSEpro Simulation Environment*. May 2023. URL: https://www.simtechnology.com/cms/ipsepro-menu/ipse-pro (cit. on p. 57).

[106] D. Catalán-Martınez, A. Santafé-Moros, J. Gozálvez-Zafrilla, J. Garcıa-Fayos, and J. Serra. “Characterization of oxygen transport phenomena on BSCF membranes assisted by fluid dynamic simulations including surface exchange”. In: *Chemical Engineering Journal* 387 (May 2020), p. 124069. DOI: 10.1016/j.cej.2020.124069 (cit. on p. 57).

[107] E. Shubnikova, M. Popov, S. Bychkov, S. Chizhik, and A. Nemudry. “The modeling of oxygen transport in MIEC oxide hollow fiber membranes”. In: *Chemical Engineering Journal* 372 (Sept. 2019), pp. 251–259. DOI: 10.1016/j.cej.2019.04.126 (cit. on p. 57).

[108] C. Li, W. Li, J. J. Chew, S. Liu, X. Zhu, and J. Sunarso. “Oxygen permeation through single-phase perovskite membrane: Modeling study and comparison with the dual-phase membrane”. In: *Separation and Purification Technology* 235 (Mar. 2020), p. 116224. DOI: 10.1016/j.seppur.2019.116224 (cit. on p. 57).

[109] F. Payri, P. Olmeda, J. Martin, and R. Carreño. “A New Tool to Perform Global Energy Balances in DI Diesel Engines”. In: *SAE International Journal of Engines* 7.1 (Apr. 2014), pp. 43–59. DOI: 10.4271/2014-01-0665 (cit. on p. 58).

[110] J. Benajes, P. Olmeda, J. Martın, and R. Carreño. “A new methodology for uncertainties characterization in combustion diagnosis and thermodynamic modelling”. In: *Applied Thermal Engineering* 71.1 (Oct. 2014), pp. 389–399. DOI: 10.1016/j.applthermaleng.2014.07.010 (cit. on p. 58).

[111] Y.-D. Liu, M. Jia, M.-Z. Xie, and B. Pang. “Enhancement on a Skeletal Kinetic Model for Primary Reference Fuel Oxidation by Using a Semidecoupling Methodology”. In: *Energy &amp Fuels* 26.12 (Nov. 2012), pp. 7069–7083. DOI: 10.1021/ef301242b (cit. on p. 59).

[112] J. R. Serrano, P. Olmeda, A. Tiseira, L. M. Garcıa-Cuevas, and A. Lefebvre. “Theoretical and experimental study of mechanical losses in automotive turbochargers”. In: *Energy* 55 (June 2013), pp. 888–898. DOI: 10.1016/j.energy.2013.04.042 (cit. on p. 64).

[113] J. R. Serrano, P. Olmeda, F. J. Arnau, M. A. Reyes-Belmonte, and H. Tartoussi. “A study on the internal convection in small turbochargers. Proposal of heat transfer convective coefficients”. In: *Applied Thermal Engineering* 89 (Oct. 2015), pp. 587–599. DOI: 10.1016/j.applthermaleng.2015.06.053 (cit. on p. 64).

[114] J. Serrano, P. Olmeda, F. Arnau, and A. Dombrovsky. "General Procedure for the Determination of Heat Transfer Properties in Small Automotive Turbochargers". In: *SAE International Journal of Engines* 8.1 (Oct. 2014), pp. 30–41. DOI: 10.4271/2014-01-2857 (cit. on p. 64).

[115] J. R. Serrano, P. Olmeda, F. J. Arnau, A. Dombrovsky, and L. Smith. "Methodology to Characterize Heat Transfer Phenomena in Small Automotive Turbochargers: Experiments and Modelling Based Analysis". In: *Volume 1B: Marine; Microturbines, Turbochargers and Small Turbomachines; Steam Turbines*. American Society of Mechanical Engineers, June 2014. DOI: 10.1115/gt2014-25179 (cit. on p. 64).

[116] J. Serrano, F. Arnau, V. Dolz, A. Tiseira, and C. Cervelló. "A model of turbocharger radial turbines appropriate to be used in zero- and one-dimensional gas dynamics codes for internal combustion engines modelling". In: *Energy Conversion and Management* 49.12 (Dec. 2008), pp. 3729–3745. DOI: 10.1016/j.enconman.2008.06.031 (cit. on p. 64).

[117] F. Payri, J. Serrano, P. Fajardo, M. Reyes-Belmonte, and R. Gozalbo-Belles. "A physically based methodology to extrapolate performance maps of radial turbines". In: *Energy Conversion and Management* 55 (Mar. 2012), pp. 149–163. DOI: 10.1016/j.enconman.2011.11.003 (cit. on p. 64).

[118] J. Galindo, R. Navarro, L. M. Garcıa-Cuevas, D. Tarı, H. Tartoussi, and S. Guilain. "A zonal approach for estimating pressure ratio at compressor extreme off-design conditions". In: *International Journal of Engine Research* 20.4 (Feb. 2018), pp. 393–404. DOI: 10.1177/1468087418754899 (cit. on p. 64).

[119] W. Sanz, H. Jericha, F. Luckel, E. Göttlich, and F. Heitmeir. "A Further Step Towards a Graz Cycle Power Plant for CO2 Capture". In: *Volume 5: Turbo Expo 2005*. ASMEDC, Jan. 2005. DOI: 10.1115/gt2005-68456 (cit. on pp. 65, 104, 107).

CHAPTER 4

Evaluation of an oxygen production cycle using MIEC membranes for industrial applications.

Contents

Figures

Tables

4.1 Introduction

THIS chapter aims to perform a thermoeconomic analysis of an oxygen production cycle that uses a ceramic membrane for air separation. The initial motivation for studying this system is to assess the viability of implementing this type of facility in the context of a ceramic plant to feed with high-purity oxygen the different furnaces needed in this kind of factory, which could require temperatures higher than 2,000 °C. The study was carried out in the context of an industrial project in which the host institute of the present thesis was involved.

Some studies demonstrate the improvement in the energy efficiency of using oxygen production cycles within industrial contexts against using typical air separation methods (as described in Chapter 2 and in the obtained results of Chapter 5). However, off-design conditions of the systems are not commonly evaluated, analyzing the influence of controllable variables such as turbomachine speeds or valve openings in the cycle performance.

Each operating point is assessed in terms of oxygen production, energy consumption, and operational costs where pre-COVID (and pre-energy crisis, in contrast with what is being faced while finishing this document) prices of natural gas and electricity are considered. The prices were obtained in 2019.

The performance of the cycle is then compared with other oxygen production alternatives in terms of energy consumption, as well as considering typical purchase costs found in O_2 wholesale markets ($50\,€\,t^{-1}$).

On that basis, the main objectives of this chapter are:

- Design and optimize two cases of a cycle of O_2 production using MIEC membranes boosted by the waste heat of flue gases of a furnace and a set of turbomachines. Critical elements are determined from the point of view of the performance of the cycles.
- Assess the behavior of the cycle from a thermoeconomical perspective in off-design conditions, using performance indicators such as oxygen production ($kg\,s^{-1}$), unitary cost of production cost ($€\,t^{-1}$), and oxygen production per consumed energy ($kg\,kW^{-1}\,h^{-1}$).
- Assess the operative feasibility of the proposed cycles regarding direct operation costs, comparing against typical purchase costs found in oxygen wholesale markets and other oxygen production cycles.

4.2 System description

The final configurations of the proposed system in this chapter were obtained after successive iterations considering the initial requirements of $0.12\,kg\,s^{-1}$ of

high-purity oxygen for combustion purposes in a furnace within a ceramic plant. Their layouts are shown in Figure 4.1 and Figure 4.2. Initially, atmospheric air at ambient conditions (assumed 25 °C and 0.1 MPa) is driven through three intercooled mechanical compression stages (C1, C2, and C3), working in series, whose performance is supported by an electric compressor implemented to start the operation.

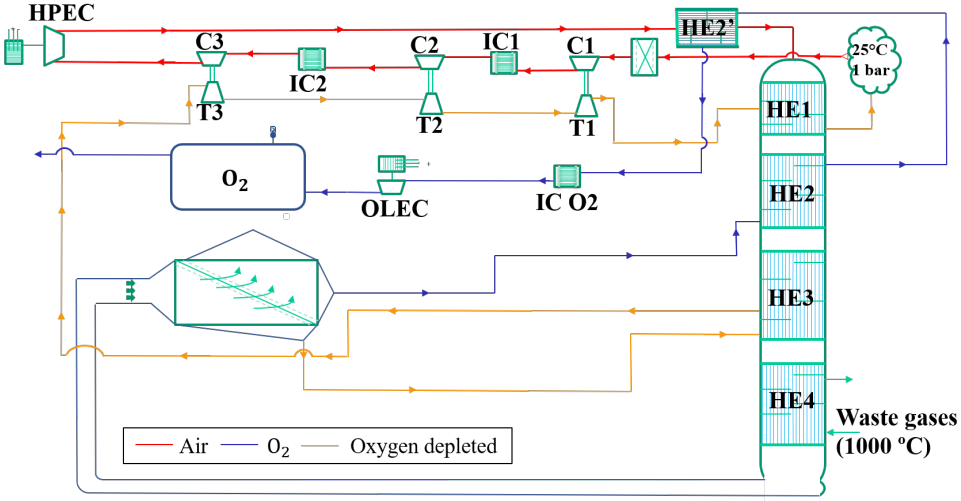

Figure 4.1: Oxygen production cycle: Case 1 configuration.

The pressurized air stream goes through a set of heat exchangers to increase the air temperature, accomplishing the operating requirements for optimum membrane functioning. Waste gases from a furnace within the ceramic plant heat the air stream (at HE4 in Case 1 and HE3 in Case 2) is one of the possible external thermal energy sources. This furnace typically produces waste gases with a mass flow of 0.27 $kg\,s^{-1}$, mainly composed of combustion products (CO_2 and H_2O) at a temperature that could be as high as 1,000 °C. On the other hand, another possible external source of thermal energy could be the addition of a heater at the outlet of the heat exchanger system to create an additional temperature increase.

Air at high pressure and temperature feeds a three-end ceramic membrane of BSCF material, producing a high-purity oxygen stream and an oxygen-depleted air stream. The oxygen stream goes through two heat exchangers to increase air temperature (HE2 and HE2' in both configurations). Then, its temperature is reduced before passing through a vacuum pump, which reduces this pipeline pressure to increase the membrane permeability, delivering oxygen production at atmospheric pressure.

The oxygen-depleted stream is first used to recover its thermal energy in

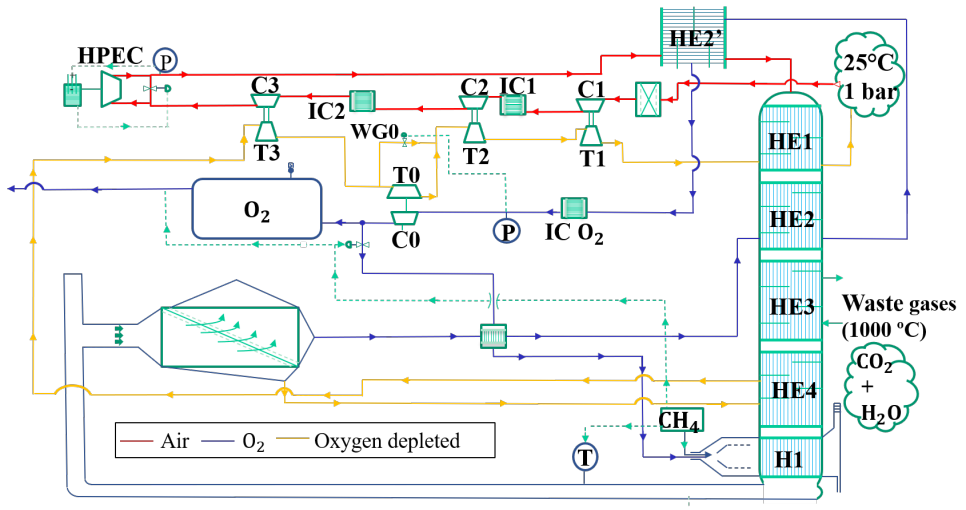

Figure 4.2: Oxygen production cycle: Case 2 configuration.

two of the heat exchangers (HE1 and HE3 for Case 1 and HE1 and HE4 for Case 2) and then to drive a group of turbines (T1, T2, T3) that move the mechanical compressors that move the air to the system. This stream can also be used to impulse the vacuum pump of the oxygen stream pipeline if sufficient energy is available. If it is not the case, this vacuum pump can be boosted electrically.

Considering all the above, two different cases were identified to be studied, considering the possibility of another external heat source or power source for the vacuum pump:

- Case 1: This case has limited availability of thermal energy due to the presence of only one source of external heat (waste gases from the furnace). In this sense, the vacuum pump is driven electrically..

- Case 2: This case works with a heater at the end of the set of heat exchangers, increasing air temperature to 1,000 °C. There is more available energy than in Case 1, for which a turbocharger (T0-C0) is used to reduce the pressure in the oxygen line. A turbine is located between T2 and T3 to boost a compressor, whose enthalpy flow is controlled by a valve that bypasses the mass flow that goes through T1, T2, and T3.

4.3 Considerations, variables, and indicators for performance evaluation

The following particular simplifications are considered in this chapter:

- As stated in chapter 3, heat exchanger effectiveness remains constant as there are no detailed specifications at this stage. However, the effectiveness of the heat exchangers is set at 80 %, avoiding outlet temperatures at the electric compressor higher than 200 °C to prevent damages, simplifying the installation technically and maximizing the oxygen production. Nonetheless, the effectiveness of the first heat exchanger in the stream path of the oxygen-depleted flow (HE3 for Case 1 and HE4 for Case 2) is studied as it affects the energy availability at the expansion stages and heat availability for air heat simultaneously for which a coupling effect is presented.

- The installation cost is estimated at 570,000 € according to several developers of this type of facility, including manufacturing, installation, and labor costs. Assuming an oxygen production of $8.64\,\mathrm{t\,d^{-1}}$ (which gives an oxygen mass flow of $0.1\,\mathrm{kg\,s^{-1}}$) during a lifetime of 10 years, being the average oxygen consumption of the ceramic factory for which this facility has been sized, an additional production cost of $18\,€\,\mathrm{t^{-1}}$ must be added to the operational costs that are determined in each calculated point.

- An efficiency of 85 % is considered for heater operation in Case 2; a reasonable value that embraces combustion efficiency and heat losses. The air is heated with the gas products of burning part of the produced O_2 with natural gas (mainly CH_4). The gases are assumed to leave the heater at 10 °C higher than the inlet air.

- Energy consumption of auxiliary components (cooler pumps, electrical and electronic devices) is not considered.

Three controllable variables are swept to obtain off-design maps of the operation of the whole cycle. Firstly, the speed of the electric compressor in the air line (HPEC) is varied, a parameter that affects the air mass flow through the compressors and the inlet feed pressure at the membrane. As there are two mechanisms to control the vacuum pressure of the oxygen line according to the case, two different control variable are varied: for Case 1, the speed of the electric compressor in the oxygen line (OLEC) is used, while for Case 2, the valve opening that controls the mass flow through T0, which boost the compressor in the oxygen line, is considered.

In this sense, three different indicators are considered for the analysis, determined for each calculated operation point: net oxygen production (in $\mathrm{kg\,s^{-1}}$), unitary cost of production (in $€\,\mathrm{t^{-1}}$), and oxygen production per consumed energy (in $\mathrm{kg\,kW^{-1}\,h^{-1}}$). They are used to evaluate the system in terms of production, economy, and energy.

The unitary cost of production (C) and oxygen production per consumed energy (E) expressions for Case 1 are described in Equation 4.1 and Equation 4.2, respectively.

$$C(€/\mathrm{t}) = \frac{(\dot{W}_{\mathrm{HPEC}}(\mathrm{kWe}) + \dot{W}_{\mathrm{OLEC}}(\mathrm{kWe})) \cdot AEP}{\dot{m}_{\mathrm{O_2}}(\mathrm{kg\,s^{-1}})} \cdot \frac{1\,\mathrm{h}}{3{,}600\,\mathrm{s}} \cdot \frac{1{,}000\,\mathrm{kg}}{1\,\mathrm{t}} \tag{4.1}$$

$$E(\mathrm{kg/kWh}) = \frac{\dot{m}_{\mathrm{O_2}}(\mathrm{kg\,s^{-1}})}{\dot{W}_{\mathrm{HPEC}}(\mathrm{kW}) + \dot{W}_{\mathrm{OLEC}}(\mathrm{kW})} \cdot \frac{3{,}600\,\mathrm{s}}{1\,\mathrm{h}} \tag{4.2}$$

On the other hand, for Case 2, the equivalent expressions are shown in Equation 4.3 and Equation 4.4.

$$C(€/\mathrm{t}) = \frac{\dot{W}_{\mathrm{HPEC}}(\mathrm{kWe}) \cdot AEP \cdot \frac{1\,\mathrm{h}}{3{,}600\,\mathrm{s}} + \dot{m}_{\mathrm{NG}}(\mathrm{kg\,s^{-1}}) \cdot ANP \cdot CF}{\dot{m}_{\mathrm{O_2}}(\mathrm{kg\,s^{-1}})} \cdot \frac{1{,}000\,\mathrm{kg}}{1\,\mathrm{t}} \tag{4.3}$$

$$E(\mathrm{kg/kWh}) = \frac{\dot{m}_{\mathrm{O_2}}(\mathrm{kg\,s^{-1}})}{\dot{W}_{\mathrm{HPEC}}(\mathrm{kWe}) + \dot{Q}_{\mathrm{h}}(\mathrm{kWth})} \cdot \frac{3{,}600\,\mathrm{s}}{1\,\mathrm{h}} \tag{4.4}$$

where $\dot{m}_{\mathrm{O_2}}$ is the oxygen production, $\dot{m}_{\mathrm{NG}}$ is the natural gas consumption, CF is the conversion factor for natural gas, $\dot{W}_{\mathrm{HPEC}}$ is the power consumption of HPEC, $\dot{W}_{\mathrm{OLEC}}$ is the power consumption of OLEC and AEP and ANP are the average electricity and natural gas prices considered for the study. AEP, ANP, and CF (which is the conversion factor for natural gas) are presented in Table 4.1. It is seen that the heating from the waste gases from the furnaces is not considered in the latter expressions, as it is not considered an additional cost from the energy input.

Table 4.1: Average prices of natural gas and electricity in Spanish market for 2019.

Average natural gas price (ANP)	0.026 €/kWh
Average electricity price (AEP)	0.100 €/kWh
Conversion factor for natural gas (CF)	$13.89\,\mathrm{kWh\,kg^{-1}}$

Finally, the base turbocharger considered for scaling consists of a radial compressor with a wheel diameter of 40 mm and a maximum corrected speed of 229,000 rpm, with a maximum corrected mass flow of $0.14\,\mathrm{kg\,s^{-1}}$.

The corrected variables are defined using standard practices: the corrected rotational speed is the rotational speed times the square root of the ratio of the reference temperature and the compressor inlet total temperature. Additionally,

the corrected mass flow is the mass flow times the ratio of the reference pressure and the inlet total pressure times the square root of the ratio of the inlet total temperature and the reference temperature. The reference temperature is 298 K, and the reference pressure is 101,325 Pa.

This compressor is boosted by a radial turbine of variable geometry (VGT) with a wheel diameter of 37.5 mm. Additionally, the turbine has a maximum reduced mass flow of $12.16\,\mathrm{kg\,s^{-1}\,K^{0.5}\,MPa^{-1}}$, and a maximum reduced speed of $112.2\,\mathrm{Hz\,K^{-0.5}}$. The turbocharger shaft has a diameter of 6 mm.

Again, the reduced variables are defined using standard practices: the reduced rotational speed is the rotational speed divided by the square root of the turbine inlet total temperature. Additionally, the reduced mass flow is the mass flow times the square root of the inlet total temperature, divided by the inlet total pressure.

On the other hand, electric compressors are not scaled, where their original characteristic maps are implemented in the calculations without any additional preprocessing. In this sense, the selected compressor for HPEC in both cases has a wheel diameter of 55 mm, and a maximum corrected speed of 120,000 rpm. The compressor for OLEC in Case 1 has a wheel diameter of 80 mm mm, and a maximum corrected speed of 90,000 rpm. Both models are commercially available.

4.4 Case 1: Oxygen production without an additional heat source

As explained earlier, this case has only one heat source to drive the system. In this sense, lower temperatures in membrane operation are found, affecting the permeability and, thus, the oxygen production. Moreover, removing natural gas consumption and a more efficient vacuum generation mechanism can lead to a better system regarding energy and economy.

4.4.1 Sizing of critical elements

An iterative process has been performed to size critical components in both studied configurations. The results presented in this section show trends in the system performance concerning the sizing parameters variation. Scaling values to determine turbocharger sizing and membrane area are determined considering reference conditions of $0.65\,\mathrm{kg\,s^{-1}}$ of air mass flow and a vacuum pressure of 0.04 MPa in the oxygen line. As variable geometry turbines are implemented, the turbine opening positions are optimized, using the oxygen mass flow produced as the objective function during calculation, pursuing high

efficiency in the turbomachines. HE-3 effectiveness is also selected for the study to determine its size's effect on the system performance.

The selected scaling values for this case are exhibited in Table 4.2. As expected, it is seen that higher values of scaling are chosen as the inlet pressure of the turbocharger is lower, which increments the value of the corrected mass flow. The design air mass flow value of $0.65\,\mathrm{kg\,s^{-1}}$ is four times the maximum mass flow of the reference turbocharger, demanding a minimum scaling value of 4 to at least drive the required air, if the same inlet conditions are considered. This is nearly the case for the low-pressure compressor (C1).

Table 4.2: Turbocharging scaling for Case 1.

Turbocharger	Compressor	Turbine
Low pressure	9	9
Medium pressure	4	4
High pressure	3	4

In this sense, the selected scale moves the expected operating point to a zone of the characteristic map near the optimum region, avoiding choking and surge lines. The same reasoning is followed for C2 and C3, whose inlet pressures are higher, requiring a lower scaling to move the air properly and, thus, to operate in an optimum zone of the characteristic map.

Figure 4.3 shows the operation maps of these compressors with optimum operating points regarding oxygen production values and optimum energy consumption of the whole cycle. The maps demonstrate that a proper selection has been made regarding scaling values, where the optimum operating points perform in the central zone of the compressor maps for the three mechanical turbochargers.

Concerning the turbine positions, these values are shown in Table 4.3 for the optimum point of oxygen production shown in Figure 4.3. It is seen that efficiency values are kept between 60 to 70 %, an acceptable range for radial turbomachines, achieving a high oxygen production.

Table 4.3: Optimum turbine positions and efficiencies for Case 1.

Turbocharger	Turbine position [%]	Turbine efficiency [%]	Compressor efficiency [%]	Speed [rpm]
Low pressure	20	75	74	50000
Medium pressure	20	77	72	91000
High pressure	16	59	74	59000

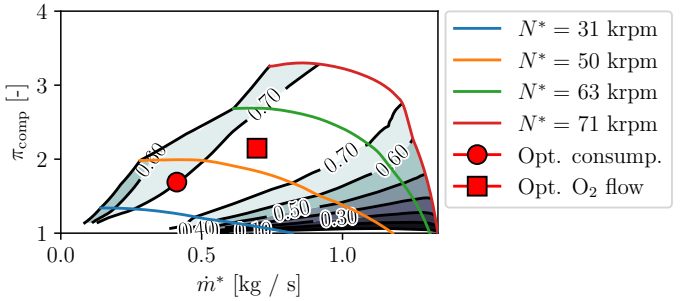

(a) Low-pressure compressor.

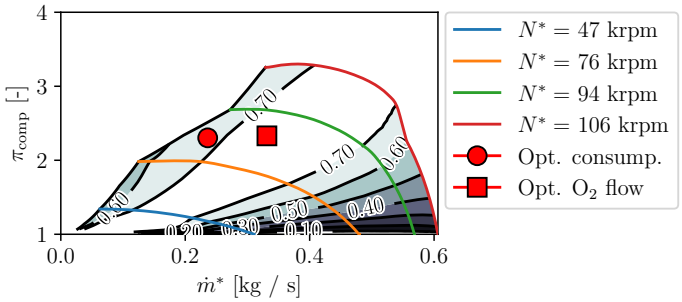

(b) Medium-pressure compressor.

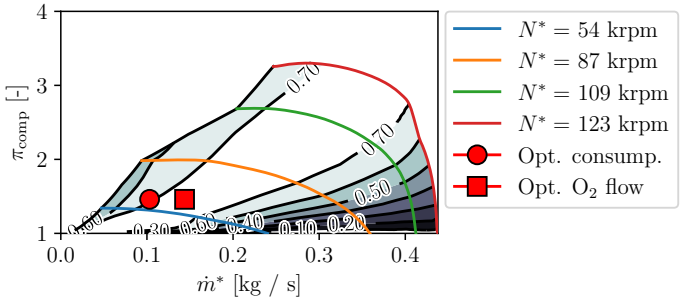

(c) High-pressure compressor.

Figure 4.3: Compressor maps operating at optimum operating points for Case 1

On the other hand, the effect of HE-3 effectiveness on the performance of the cycle is shown in Figure 4.4. It is seen from Figure 4.4(a) that increasing HE-3 effectiveness leads to an increase in oxygen production. A more efficient heat exchange leads to a higher membrane feed temperature, as seen in Figure 4.5(a), which improves membrane permeability. However, Figure 4.5(b) depicts that due to a reduction in the available energy for the expansion stages, there is a decrease in the feed pressure of the membrane, as well as an increment in the HPEC power consumption to keep the air mass flow, shown in Figure 4.5(c). For this reason, the oxygen price starts growing at a higher heat exchanger effectiveness, and the production also starts to decrease when the effectiveness value is higher than 70 %, as seen in Figure 4.4(b).

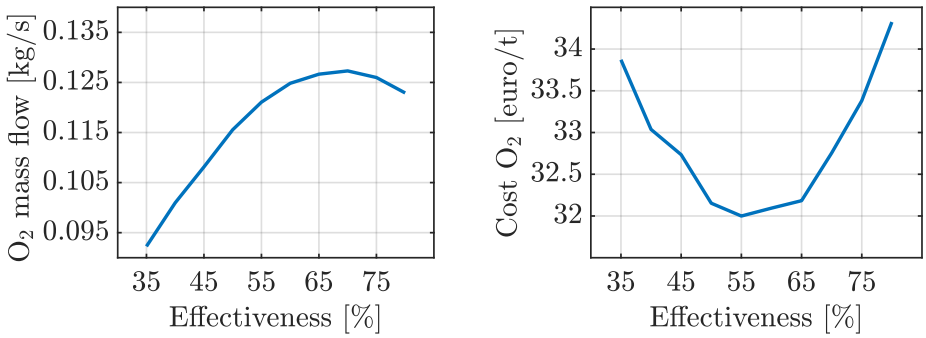

(a) Oxygen production.

(b) Operating cost.

Figure 4.4: Oxygen production and operating cost at different HE-3 effectiveness in Case 1.

Hence, for this configuration, it is seen that improving the heat exchange does not necessarily affect the cycle's performance positively after a particular value due to the effect of HE-3 performance in air compression. Thus, selecting an effectiveness of 55 % for this heat exchanger leads to the best oxygen production cost, with reasonable oxygen production.

On the other hand, the membrane size is a parameter that directly affects oxygen production. Increasing membrane area helps in increasing oxygen production, as well as reducing its cost, as is seen in Figure 4.6(a). However, from a particular value, a larger membrane does not significantly benefit the cycle. As oxygen production increases, the oxygen-depleted flow is diminished due to constant air mass flow, reducing the energy available in the expansion stages. This leaves an asymptotic behavior in oxygen production and cost, as Figure 4.6(b) also depicts. A membrane area of 300 m^2 is seen as a size that gives a good performance, from which adding membrane area implies higher costs in facilities installation and maintenance, without a significant benefit in

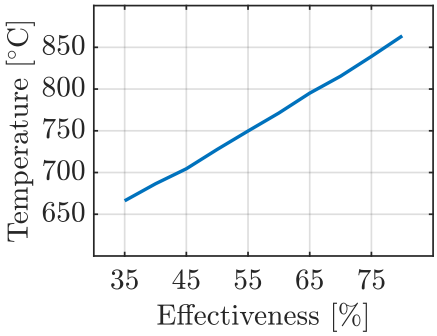

(a) Membrane feed temperature.

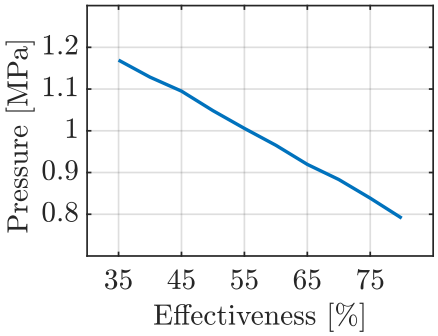

(b) Membrane feed pressure.

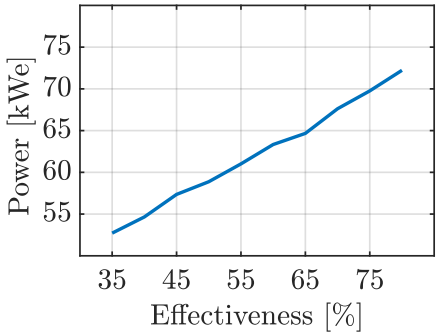

(c) Power consumption.

Figure 4.5: Feed conditions and energy consumption at different HE-3 effectiveness in Case 1

production and costs.

4.4.2 Off-design performance evaluation and analysis

An operative map of the whole system, which delivers oxygen production, operating costs, and production per energy consumed in terms of HPEC and OLEC speeds, is seen in Figure 4.7. Optimum oxygen production is found at 75 % of the maximum HPEC speed and the maximum speed of OLEC. The higher the speed of OLEC, the lower the pressure of the oxygen pipeline, as seen in Figure 4.8(d), which positively affects oxygen production. Consequently, it is seen that for a constant HPEC value, the production increases with the OLEC speed increment.

On the other hand, the maximum oxygen production is exhibited at a medium HPEC speed of the studied range (red marker in Figure 4.7(a)). For a

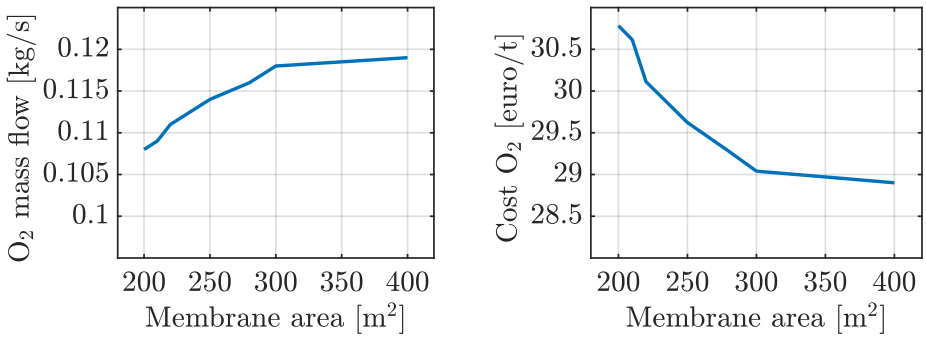

(a) Oxygen production.

(b) Operating cost.

Figure 4.6: Oxygen production and operating cost at different membrane areas in Case 1.

constant OLEC speed, it is seen that a maximum oxygen production is achieved. High HPEC speeds increase the membrane's air mass flow and feed pressure (Figure 4.8(a) and Figure 4.8(b)), which is beneficial for the cycle operation. However, as Figure 4.8(c) shows, at high HPEC, the heat capacity of the airflow increases, implying that a lower temperature can be reached at the heat exchanger network outlet, affecting oxygen production. From this perspective, a HPEC speed of around 75 % of its maximum is preferred for oxygen production, which balances the effect of feed pressure, temperature, and air mass flow in the performance.

Furthermore, the operating costs and oxygen production per energy consumed are depicted in Figure 4.7(b) and Figure 4.7(c). An optimum operating point regarding costs has been found at 44.7 % of the maximum HPEC speed and 49.5 % of the maximum OLEC speed (blue marker in Figure 4.7(b)). Regarding energy consumption, the analysis is analogous, as electricity is the only external source to power the system. This economic pole is found in a low air mass flow and low membrane pressure ratio zone, as feed pressure is reduced and oxygen line pressure increases. Nonetheless, reducing air mass flow permits a higher feed temperature, which benefits oxygen production. In this sense, the temperature dominates the optimum cost operating point region. Therefore, low electric power consumption is achieved, as both electric compressors work at lower speeds, with diminished streams and compression ratios.

Continuing with the analysis, Table 4.4 summarizes the main parameters of both optimum points found. As stated, higher oxygen production at the maximum production operation point results from a relatively large air mass flow and pressure and a diminished oxygen pressure line. On the other hand, the optimum cost point produces oxygen at a temperature 175 °C higher but with an air mass flow and a feed pressure of 38.7 % and 31.4 % less, respectively. In

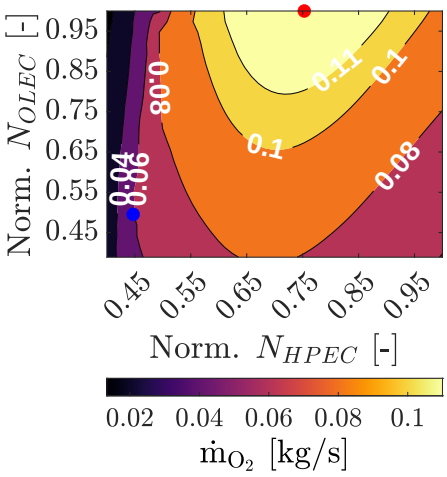

(a) Oxygen production.

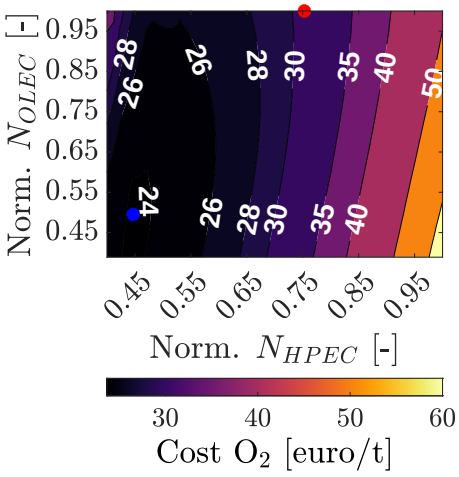

(b) Operating cost.

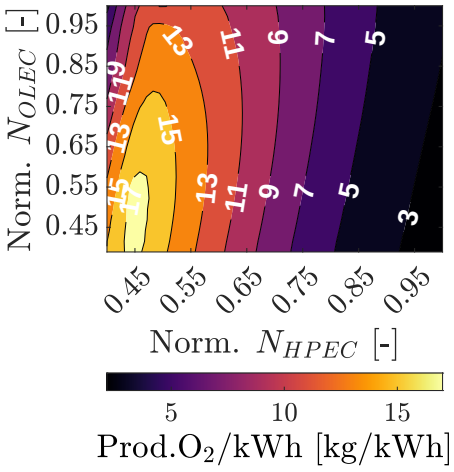

(c) Production per energy consumption.

Figure 4.7: Oxygen production, costs and production per energy consumption in Case 1.

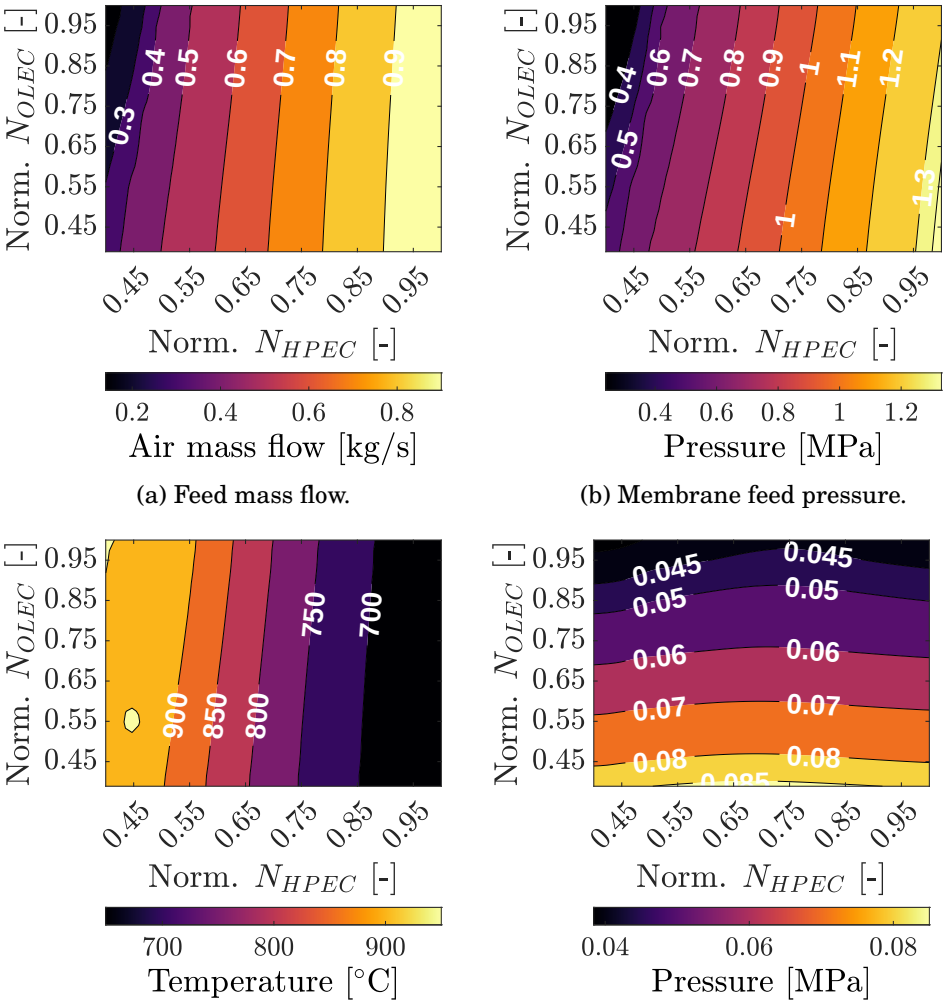

(a) Feed mass flow.

(b) Membrane feed pressure.

(c) Membrane feed temperature.

(d) Membrane permeate pressure.

Figure 4.8: Membrane operation conditions in Case 1

addition, the oxygen pipeline pressure at the optimum cost point almost doubles the pressure of the maximum production point. Considering the above, a range of production between both points of 0.060 to 0.124 $\mathrm{kg\,s^{-1}}$ is achieved, with operating costs between 23.7 to 30.8 $€\,\mathrm{t^{-1}}$, being 38 to 53 % lower compared with the reference prices commonly available in the wholesale marktets (50 $€\,\mathrm{t^{-1}}$).

Table 4.4: Comparison of production and cost optimum points for Case 1.

	Maximum oxygen flow	Minimum operating cost
$\dot{m}_{O_2}$ [$\mathrm{kg\,s^{-1}}$]	0.124	0.059
C [$€\,\mathrm{t^{-1}}$]	30.8	23.7
$\dot{m}_{air}$[$\mathrm{kg\,s^{-1}}$]	0.726	0.445
$P_{feed,air}$ [MPa]	9.58	6.57
$T_{feed,air}$ [°C]	768	943
$P_{permeate}$ [MPa]	0.44	0.80

Also, the results show that a reduced non-profitable zone is found (costs higher than 50 $€\,\mathrm{t^{-1}}$ in Figure 4.7(b)). HPEC speeds near the maximum, and low OLEC speeds lead to the poorest performance of the system, where a high air mass flow is heated, leading to a reduced temperature. Consequently, a low oxygen production is presented. This situation leads to low oxygen production and high power demand.

Considering all of these, this configuration shows flexibility during its operation, where the oxygen production can be varied depending on the requirement of the plant according to the planned ceramic production at a particular moment, reducing the production cost even if less oxygen is demanded. The variation in oxygen production can be achieved by modifying the speeds of both electric compressors through the gradient line between the maximum production and minimum cost points, allowing operation at the optimum cost point at intermediate demand values.

4.5 Case 2: Oxygen production with an additional heat source

This case has two heat sources of external energy: the heater to increase the air temperature to 1,000 °C and HPEC to move the air. In this sense, an increase in mean permeability is found in the membrane compared with Case 1 and, thus, oxygen production. Moreover, adding natural gas consumption

and a less efficient vacuum generation mechanism can lead to a worse system regarding energy and economy.

4.5.1 Sizing of critical elements

Similar to Case 1, an iterative process has been performed to determine the size of critical components. In this case, reference conditions of $0.70\,\mathrm{kg\,s^{-1}}$ of air mass flow and a vacuum pressure of 0.035 MPa in the oxygen line are considered.

The selected scaling values for this case are exhibited in Table 4.5. Higher scaling values for low and medium-pressure turbochargers are selected, compared with those in Case 1. Due to the energy consumption of the oxygen line compressor (C0), there is a reduction in pressure and temperature in the oxygen-depleted flow, for which larger turbochargers are required.

Table 4.5: Turbocharging scaling for Case 2.

Turbocharger	Compressor	Turbine
Low pressure	15	20
Medium pressure	7	9
High pressure	3	4
O_2 line	4	4

In this sense, Figure 4.9 shows the operation maps of these compressors with optimum operating points regarding oxygen production and energy consumption, showing that a proper selection has been made regarding scaling values, as for Case 1.

Concerning the turbine positions, these values are shown in Table 4.6 for the same optimum points shown in Figure 4.9. Efficiency values are kept between 60 to 70 %, an acceptable range for radial turbomachines, achieving a high oxygen production. An exception to this is the turbocharger's efficiency in the oxygen line, whose turbine displays a low efficiency due to the notorious mass flow unbalance with the compressor, causing a considerable energy loss in this element.

The effect of HE-4 effectiveness on the performance of the cycle is shown in Figure 4.10. It is seen from Figure 4.10(a) that increasing HE-4 effectiveness leads to an increase in net oxygen production. A more efficient heat exchange leads to a higher outlet temperature from the heat exchanger before the heater, as seen in Figure 4.11(a)—consequently, there is less extra heat requirement to reach 1,000 °C.

The energy available for the expansion stages is reduced, which leads to a decrease in the feed pressure of the membrane, as shown in Figure 4.11(b),

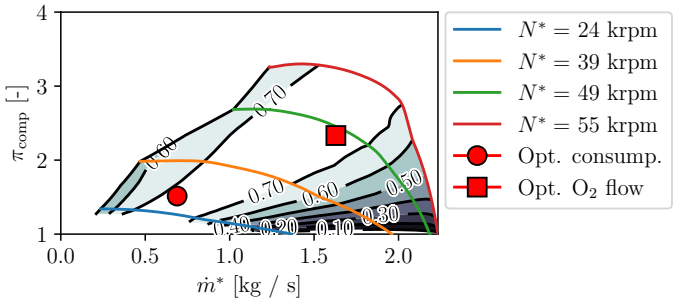

(a) Low-pressure compressor.

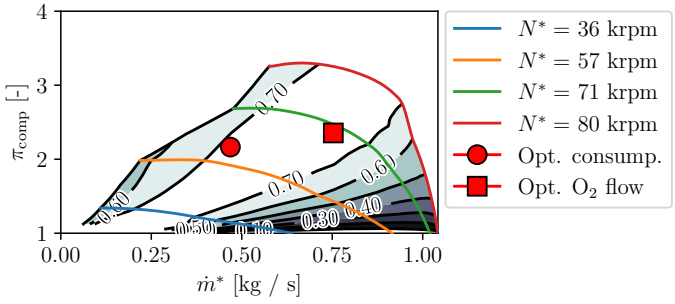

(b) Medium-pressure compressor.

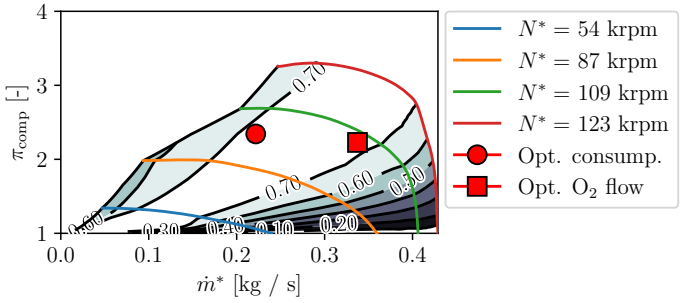

(c) High-pressure compressor.

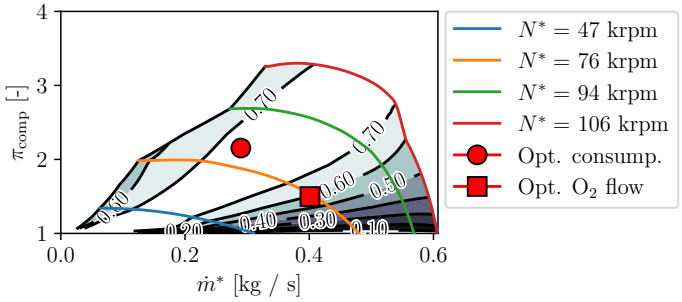

(d) Oxygen line compressor.

Figure 4.9: Compressor maps operating at optimum operating points for Case 2

Table 4.6: Optimum turbine positions and efficiencies for Case 2.

Turbocharger	Turbine position [%]	Turbine efficiency [%]	Compressor efficiency [%]	Speed [rpm]
Low pressure	20	66	72	30000
Medium pressure	20	73	71	61000
High pressure	15	67	74	88000
O_2 line	80	36	72	102000

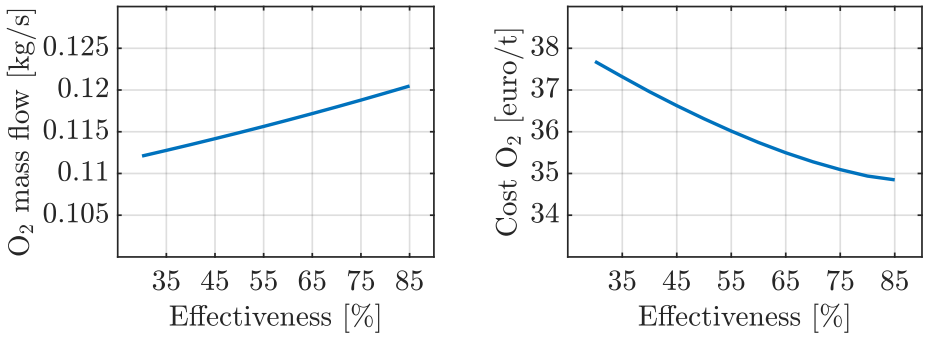

(a) Oxygen production.

(b) Operating cost.

Figure 4.10: Oxygen production and operating cost at different HE-3 effectiveness in Case 2.

reducing the gross production. However, this effect is compensated by reducing the oxygen requirement for combustion in the heater, with a final result of increasing the net production.

Both oxygen production and costs seem to have a positive trend on the system performance as the heat exchanger's effectiveness grows. Higher effectiveness values lead to an increase in the electric compressor work, as shown in Figure 4.11(c), which is overcompensated by reduced consumption of natural gas, thus, a reduced added heat, as shown in Figure 4.11(d). Consequently, oxygen production costs are reduced, as shown in Figure 4.10(b).

Thus, selecting an effectiveness of 70 % for this heat exchanger leads to a reasonable oxygen production cost and oxygen production. Higher values seem to reduce oxygen production costs slightly. Additionally, technical issues regarding size, cost, and maintenance expenses can appear for larger heat exchangers.

Higher membrane areas enhance the oxygen production and reduce its cost, as seen in Figure 4.16. However, for similar reasons, an asymptotic behavior in oxygen production and its cost is found in Case 1. Increasing oxygen production

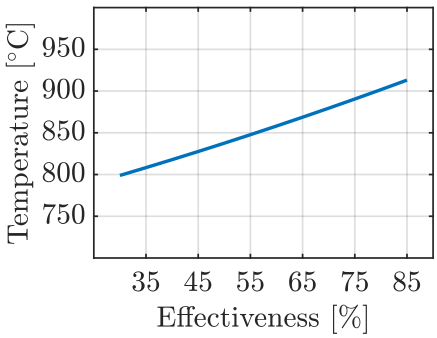

(a) Air temperature before heater.

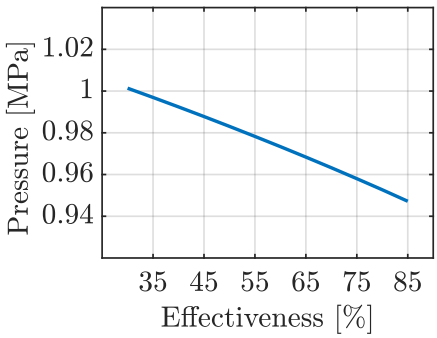

(b) Membrane feed pressure.

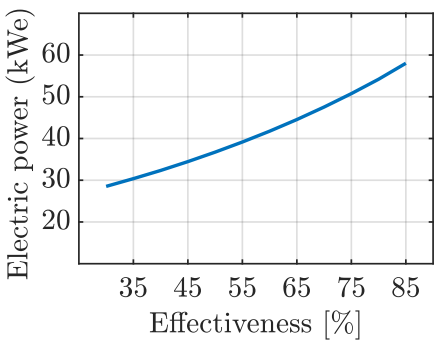

(c) Electric power consumption.

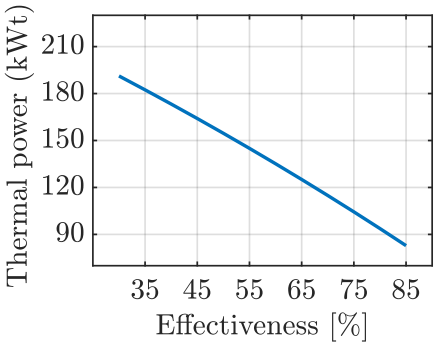

(d) Thermal power consumption.

Figure 4.11: Feed conditions and energy consumption at different HE-4 effectiveness in Case 2

diminishes the oxygen-depleted stream, reducing the available enthalpy flow to move the mechanical turbochargers. Hence, the electric power consumption increases, as it is depicted in Figure 4.11(c). A membrane area of 150 m^2 is seen as a size that gives an acceptable compromise for this configuration. Adding membrane area increases installation and maintenance costs without a significant benefit.

4.5.2 Off-design performance evaluation and analysis

Figure 4.13 shows the net oxygen production of the cycle, its operating cost, and production per energy consumed depending on HPEC speed and the wastegate opening for the oxygen line turbocharger. Due to a constant feed temperature of 1,000 °C in the membrane operation, higher HPEC speeds increase oxygen production, as there is an increment in air mass flow and feed pressure, as clearly stated in Figure 4.14(a) and Figure 4.14(b). Moreover,

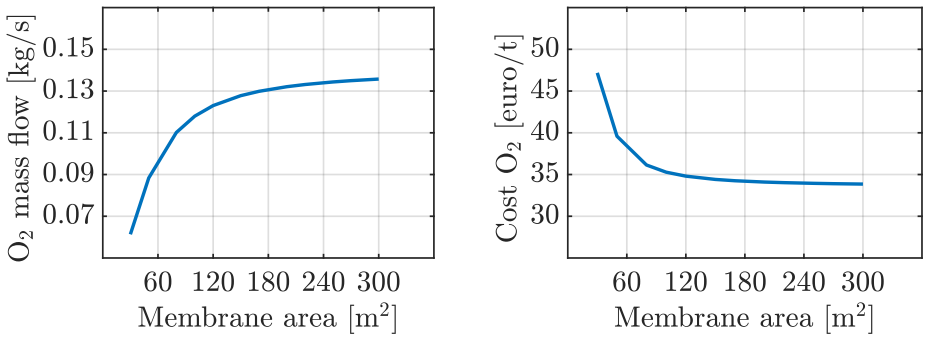

(a) Oxygen production.

(b) Operating cost.

Figure 4.12: Oxygen production and operating cost at different membrane areas in Case 1.

as HPEC speed increases, the influence of the waste gate opening is more significant, where a maximum production can be identified as this valve is opened for each HPEC speed near the maximum. An optimum net oxygen production of $0.227\,\mathrm{kg\,s^{-1}}$ is achieved at the maximum HPEC speed and 30 % of the wastegate valve opening.

However, Figure 4.13(b) shows that the maximum production point lies in an operating region of non-profitability, with a production cost of $65.4\,€\,\mathrm{t^{-1}}$, 30.1 % higher than the $50\,€\,\mathrm{t^{-1}}$ reference value. Regarding Figure 4.14(a) and Figure 4.14(b), it seems that pressure and air mass flow not only increase when HPEC speed increases but there is an influence of wastegate opening. When the wastegate is opened, less oxygen-depleted gases go through the turbocharger of the oxygen line, leaving more available energy to drive more air and pressurize it. However, this valve opening also increases the oxygen line pressure, as seen in Figure 4.14(d), affecting the cycle performance. The observed change in trend at low HPEC speeds in oxygen line pressure is due to a reduced flow in the oxygen-depleted line, which demands a more open turbine to boost the compressor in the oxygen line. For cases with a lower HPEC speed than 50 % of its maximum, the position of the oxygen turbine is fully open (100 %).

With this in mind, Figure 4.15 shows the membrane and oxygen partial pressure ratio, which decreases as the wastegate valve is opened at high HPEC speed, showing that the effect of increasing the feed pressure of the membrane is overcompensated with the increase of the oxygen line pressure. In addition, the increased air mass flow also leads to higher heat requirements due to the decreased air temperature at the heater inlet, as shown in Figure 4.14(c).

From this perspective, the maximum oxygen production point is reached at an operating point with high air mass flow, guaranteed by the high HPEC speed. At maximum HPEC speed, a more opened wastegate valve than the maximum

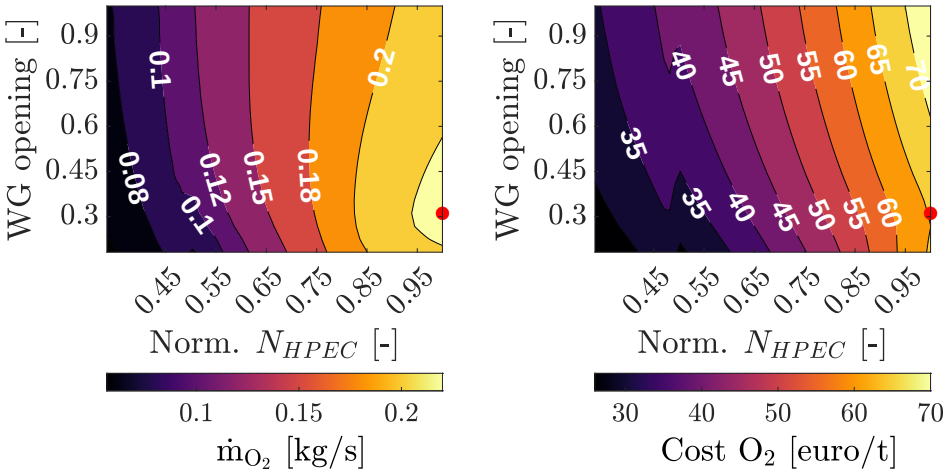

(a) Oxygen production.

(b) Operating cost.

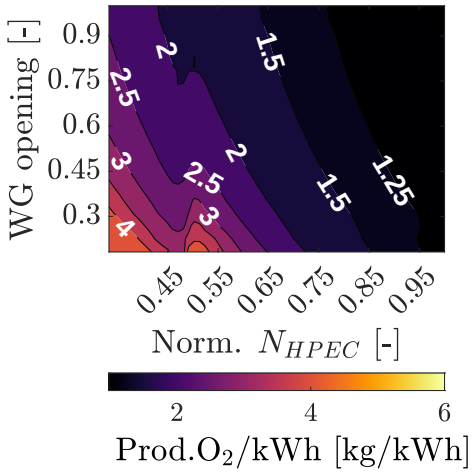

(c) Production per energy consumption.

Figure 4.13: Oxygen production, costs and production per energy consumption in Case 2.

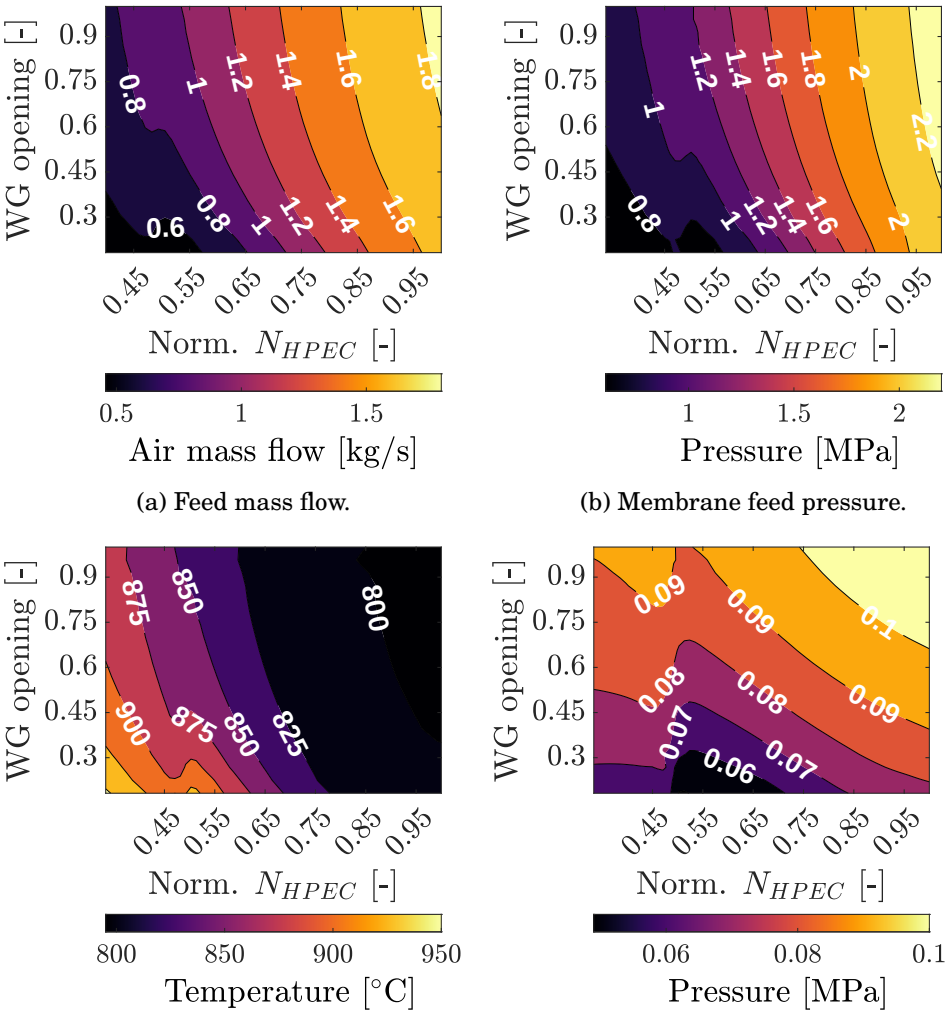

(a) Feed mass flow.

(b) Membrane feed pressure.

(c) Air temperature before heater.

(d) Membrane permeate pressure.

Figure 4.14: Membrane operation conditions in Case 2

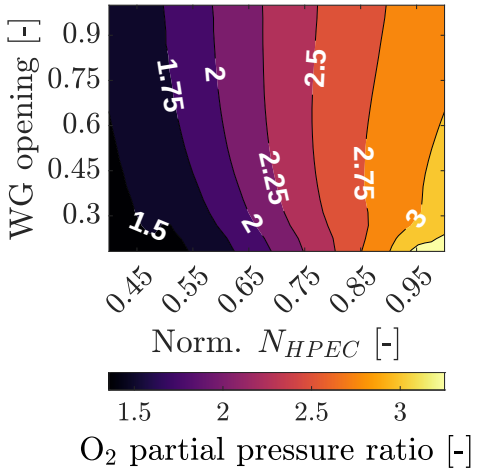

Figure 4.15: Oxygen partial pressure in Case 2.

net oxygen production point leads to a higher thermal energy requirement. On the other hand, a more closed wastegate leads to a decrease in the airflow and feed pressure, which is not compensated by the reduction of the oxygen line pressure, producing less net oxygen.

In order to choose a better operating point in economic terms, it is seen that an optimum point regarding costs has not been found in the studied range. In this sense, it is considered the oxygen production reference of $0.12\,\mathrm{kg\,s^{-1}}$, where operation points with this production flow are mainly found below 60 % of the maximum HPEC speed. With this in mind, a minimum cost is found near 60 % of the maximum speed and an opening of the wastegate valve of 18 %, with a cost of $36\,€\,\mathrm{t^{-1}}$, 28 % lower than the reference cost. Table 4.7 compares the data of maximum production and the referenced minimum cost points, stating their differences in terms of membrane operation conditions and turbochargers operation points.

Also, the results show that a considerable non-profitable zone is found (costs higher than $50\,€\,\mathrm{t^{-1}}$ in Figure 4.13(b)). HPEC speeds higher than 68 to 75 % of the maximum HPEC speed (depending on the opening of the wastegate valve) lead to the poorest performance of the system, where a high air mass flow is heated and driven, leading to a high thermal and electric energy consumption. This situation leads to a high oxygen production, but with high power demand.

4.6 Cases performance comparison

It is seen that both presented configurations of an oxygen production cycle have similar critical elements. For both cases, the heat exchanger where the

Table 4.7: Comparison of production and cost optimum points for Case 2.

	Maximum oxygen flow	Minimum operating cost
$\dot{m}_{O_2}$ [kg s^{-1}]	0.227	0.120
C [€ t^{-1}]	65.4	36.0
$\dot{m}_{air}$[kg s^{-1}]	1.690	0.726
$P_{feed,air}$ [MPa]	21.56	9.67
$T_{feed,air}$ [°C]	1000	1000
$P_{permeate}$ [MPa]	0.84	0.53

air is heated with a high-temperature oxygen-depleted stream (HE-3 in Case 1 and HE-4 in Case 2) is critical due to its coupling with the available energy for the expansion stages, affecting air feed temperature and pressure, as well as mass flow. Additionally, it is important to remark on the importance of HE-4 in Case 1, where flue gases from the plant contribute to the air heating before the membrane, this being the primary source of thermal energy for this scenario.

For Case 2, a critical component is the turbocharger T0-C0, which restricts the available energy in the medium and low-pressure turbines, affecting the electric energy consumption and the membrane inlet pressure. It should be mentioned that a larger membrane is required for Case 1 due to its membrane operation conditions, where lower feed pressures and temperatures can be achieved compared with Case 2.

Comparing the maximum oxygen production of both cases, Case 2 almost doubles the reference production of 0.12 kg s^{-1}. Meanwhile, a similar value to the design goal is accomplished for Case 1. Regarding costs, both cases can achieve the original objective with promising results, where 38 % and 28 % lower costs compared with the reference market for Case 1 and Case 2 are obtained, respectively.

Given the above, Case 2 demonstrates a higher oxygen production due to maintaining a constant membrane operation at 1,000 °C, leading to a high thermal energy consumption. Nonetheless, the fuel consumption to air heating limits the range where the system can operate, where a considerable part of the studied operating points was found not profitable compared to when the reference oxygen cost is considered.

Conversely, lower oxygen production values are obtained in Case 1, whose profitability is only limited for high speeds in HPEC and medium to low speeds in OLEC. In these conditions, a relatively high air mass flow is driven, and a high membrane feed pressure is reached. However, the oxygen line pressure increases, and the membrane operates at low temperatures, producing a lower

oxygen stream and high energy consumption.

Furthermore, a secondary reason that leads to better production costs in Case 1 is a more efficient method for vacuum generation. Figure 4.16(a) shows the efficiency of OLEC of Case 1, while Figure 4.16(b) depicts the efficiency of the turbocharger system used to drive the oxygen stream in Case 2. Lower efficiencies than 30 % are found in Figure 4.16(b) due to a inefficient use of the available energy, a consequence of the mass flow unbalance of the turbocharger components. On the other hand, Figure 4.16(a) shows typical compressor efficiency values between 60 to 70 % obtained in almost the whole operating range. The misused energy in Case 2 affects the performance of medium and low-pressure turbochargers, which is compensated with power consumption at the HPEC, increasing the electric power consumption.

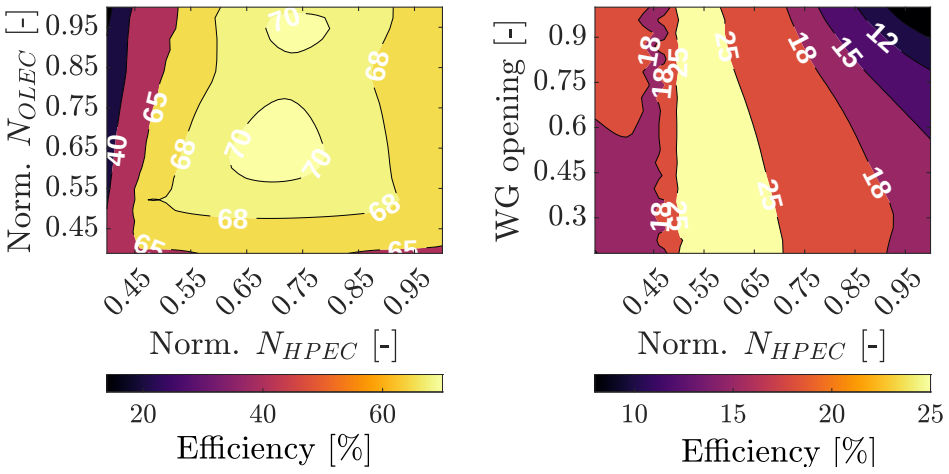

(a) OLEC efficiency in Case 1

(b) T0-C0 total efficiency in Case 2.

Figure 4.16: Oxygen production and operating cost at different membrane areas in Case 1.

With this said, both cycles can be implemented depending on the specific requirements and conditions of the user. When higher levels of oxygen production are required, trading off in a certain way the production cost, Case 2 could be implemented. Furthermore, when there is a lower oxygen demand and the price is a more critical variable, Case 1 is an acceptable option.

4.7 Comparison with other oxygen production methods

Table 4.8 displays the results of different studies implementing three oxygen production technologies compared with the obtained results in this chapter. In terms of oxygen purity, cryogenic air separation exhibits similar values. The nature of CAS leads to producing an oxygen stream with other air components dissolved, generating impurities. Compared with CLAS, Case 1 of the present chapter is energy-competitive with the referenced studies, with the added value of higher purity, due to the exclusive oxygen permeation of MIEC membranes. Adsorption exhibits production levels in the same range as both studied cases, with the poorest performance regarding purity and energy consumption, according to the cited studies regarding this method.

Table 4.8: Comparing different oxygen production methods by their energy consumption

Type	O_2 prod. [kg/kWh]	Purity [%]	O_2 flow [$t\,h^{-1}$]	Reference
Cryogenic	3.165	99.9	54.2	[120]
Cryogenic	2.915	99.6	142.9	[121]
CLAS	16.580	96.35	100	[122]
CLAS	8.906	30		[123]
CLAS	14.990	95	150	[124]
Adsorption	1.121	94	0.064	[125]
Adsorption	1.374	95	0.137	[126]
This study (Case 1)	8.000–17.000	100	0.214–0.445	
This study (Case 2)	1.200–2.800	100	0.432–0.817	

Moreover, higher oxygen production is reached in most of the cited cases. The above could modify their specific production if similar oxygen production is demanded, similar to the presented results in this Chapter.

4.8 Summary

The design of an oxygen production cycle using a configuration based on typical radial turbochargers, a set of heat exchangers, and a MIEC membrane is presented in this Chapter. Two different configurations are optimized, whose critical components have been sized, explaining their effect on oxygen production and costs.

For Case 1, heat exchanger sizing is a more critical step for design due to the lack of external heat sources apart from the outlet furnaces gases at HE-4. Special attention was given to HE-3 because it is coupled with air heating and electric energy consumption. The corresponding element for Case 2 (HE-4) is less critical than for Case 1; however, it still affects thermal and electric energy consumption, for which its size must also be considered. On the other hand, T0-C0 turbocharger operation affects the performance of the Case 2 configuration, where the vacuum generation reduces the available energy for air boosting, affecting oxygen production.

Membrane sizing is an essential issue to address. The Case 1 membrane doubles the size compared with Case 2 ($300\,m^2$ against $150\,m^2$) due to less energy available, increasing the membrane area to improve oxygen production. The membrane size effect is asymptotical, where adding membrane area for oxygen production could increase the complexity of the whole cycle without any significant improvement. Based on this premise, a membrane area was selected for both cases.

For Case 1, optimal production of $0.124\,kg\,s^{-1}$ is found, agreeing with the initial production goal. At this point, the operation costs are estimated to be $30.8\,€\,t^{-1}$, 38 % lower than the wholesale market prices. This operation point is in a trade-off region for HPEC speed, where the membrane feed pressure, temperature, and air mass flow are balanced. In this sense, increasing HPEC speed reduces the membrane feed temperature while reducing it diminishes the air feed pressure and air mass flow, affecting the cycle performance. In addition, the oxygen line compressor works at maximum speed, creating the lowest vacuum pressure possible according to the component selection, improving oxygen production.

The optimum cost point for Case 1 is found in a zone of low electric compressors speeds. Low HPEC speed allows higher temperatures due to the reduced heat capacity of the air stream, while low OLEC speed reduces electric consumption. However, as the air flow decreases and the oxygen line pressure increases, production is affected. In this optimum cost point, the produced oxygen is $0.060\,kg\,s^{-1}$, half the maximum production optimum. However, operating costs are $23.7\,€\,t^{-1}$, 53 % lower than the reference market price.

Case 1 shows a suitable option to operate when changes in oxygen demand occur while the ceramic plant is run. Intermediate operating points between both optimum points can be operated, considering the better option regarding energy consumption and costs for a particular oxygen demand.

On the other hand, Case 2 optimum production of $0.227\,kg\,s^{-1}$ was performed at HPEC maximum speed and 30 % of wastegate opening. Under these conditions, the membrane operates with a high-pressure gradient and a high air mass flow. However, due to the constant membrane feed temperature of 1,000 °C, an operating cost of $61\,€\,t^{-1}$ is achieved, 22 % higher than the reference

market price of oxygen. An optimum cost point has not been found for this case. Nevertheless, considering a reference oxygen stream of $0.12\,\mathrm{kg\,s^{-1}}$, an operating cost of $36\,€\,\mathrm{t^{-1}}$ was achieved, 28 % lower than the reference price.

It can be said that oxygen production for Case 1 is lower than for Case 2, also being more profitable. In this sense, depending on the context, both cases could be applied to industrial contexts as ceramic plants, with good profitability in a wide range of the studied points.

Compared to the results obtained in this chapter with other oxygen production methods, it is shown as an energy-competitive alternative. Additionally, the cycle produces an oxygen stream with higher purity than CAS due to the nature of the MIEC membranes, which have selectivity only for oxygen. Finally, it can be remarked that the obtained results in this chapter clearly show that a system of oxygen production using membranes can be profitable and competitive compared with retail prices and other production methods.

These results can be extended to other industrial contexts with energy sources at high-temperature to drive the cycle. It is seen that the external addition of heat, as for Case 2, drastically increases the oxygen production cost. In this sense, correctly using heat sources within the facilities is the most efficient option. Finally, reducing oxygen partial pressure on the permeate side using a mechanism that is uncoupled to the air driving is highly recommended to avoid inefficient energy use. Even further, adding a sweeping gas in the permeate side for oxygen partial pressure reduction can be even better, as the energy consumption can be avoided. These ideas will be further explored in chapter 5.

4.9 References

[120] M. Aneke and M. Wang. "Potential for improving the energy efficiency of cryogenic air separation unit (ASU) using binary heat recovery cycles". In: *Applied Thermal Engineering* 81 (Apr. 2015), pp. 223–231. DOI: 10.1016/j.applthermaleng.2015.02.034 (cit. on p. 97).

[121] J. Xu, T. Wang, Q. Chen, S. Zhang, and J. Tan. "Performance design of a cryogenic air separation unit for variable working conditions using the lumped parameter model". In: *Frontiers of Mechanical Engineering* 15.1 (Nov. 2019), pp. 24–42. DOI: 10.1007/s11465-019-0558-6 (cit. on p. 97).

[122] C.-C. Cormos. "Energy and cost efficient manganese chemical looping air separation cycle for decarbonized power generation based on oxy-fuel combustion and gasification". In: *Energy* 191 (Jan. 2020), p. 116579. DOI: 10.1016/j.energy.2019.116579 (cit. on p. 97).

[123] M. Qing, B. Jin, J. Ma, X. Zou, X. Wang, C. Zheng, and H. Zhao. "Thermodynamic and economic performance of oxy-combustion power plants integrating chemical looping air separation". In: *Energy* 206 (Sept. 2020), p. 118136. DOI: 10.1016/j.energy.2020.118136 (cit. on p. 97).

[124] D. Zhang, R. Duan, H. Li, Q. Yang, and H. Zhou. "Optimal design, thermodynamic, cost and CO2 emission analyses of coal-to-methanol process integrated with chemical looping air separation and hydrogen technology". In: *Energy* 203 (July 2020), p. 117876. DOI: 10.1016/j.energy.2020.117876 (cit. on p. 97).

[125] T. Banaszkiewicz and M. Chorowski. "Energy Consumption of Air Separation Adsorption Methods". In: *Entropy* 20.4 (Mar. 2018), p. 232. DOI: 10.3390/e20040232 (cit. on p. 97).

[126] S. Radek and D. Pavel. "The Potential of Energy Savings in Oxygen Production by Pressure Swing Adsorption". In: *Chemical Engineering Transactions* 86 (2021), pp. 313–318. DOI: 10.3303/CET2186053 (cit. on p. 97).

CHAPTER 5

Assessment of an oxygen production cycle and a power production cycle (Graz Cycle) coupling

Contents

Figures

Tables

5.1 Introduction

This chapter aims to perform a comparative analysis between two methods of oxygen production implemented in the context of a power production plant. The Graz cycle is an oxyfuel power cycle of high efficiency developed at the Graz University of Technology, which works under oxycombustion using cryogenic air separation as its primary oxygen source. The study presented in this chapter was first developed during the doctoral stay of the author of the present thesis, whose results were finally refined afterward. As stated in chapter 4, using a high-temperature energy source could be beneficial to drive an oxygen production cycle based on MIEC membranes, finding it a promising alternative in terms of energy consumption and operating costs. However, the energy source of this case study is a medium-temperature stream found among two expansion stages used for power production.

In this sense, two configurations of a membrane-based oxygen production cycle are considered, where three-end and four-end membranes are applied, comparing their performance with the baseline case of the Graz cycle operation with its base oxygen production method. In this regard, the main objectives of the present chapter are:

- Optimize the main operation parameters of an oxygen production cycle using membranes coupled to the Graz Cycle for both proposed cases.
- Compare the performance of the three mentioned cases, considering the power plant production, the efficiency of the whole system, and the energy cost of oxygen production.

5.2 System description

The base Graz cycle working with cryogenic air separation is described as coupling two different power production cycles: a Brayton cycle and a Rankine cycle. Then, the coupling of this whole cycle with the oxygen production cycle is presented, showing the differences according to the number of entrances of the membrane.

5.2.1 Graz cycle concept

The Graz Cycle is an oxyfuel power cycle of high efficiency that was developed at the Graz University of Technology and has passed through several optimizations and studies processes over the years [119, 127, 128, 129, 130, 131, 132, 133, 134]. The initial publications regarding the Graz cycle, such as the study performed by Sanz et al. [119], report 63 MW of net power output,

increasing to 400 MW in the study by Jericha et al [128]. Additional studies has been made regarding the part-load behavior, such as those made by Sanz et al. [132] and Mitterrutzner et al. [134], as well as a comparative analysis with other power plant designs, as the one reported by Wimmer and Sanz [133].

In this sense, the baseline configuration and results of the Graz Cycle considered in this chapter were presented in the work of Wimmer and Sanz [133], shown in Figure 5.1. It consists of a high-temperature Brayton Cycle (Compressors C1/C2, combustion chamber (CC), and a High-Temperature Turbine (HTT)) coupled with a low-temperature Rankine cycle (Low-Pressure Turbine (LPT), condenser, heat recovery steam generator (HRSG) and a High-Pressure Turbine (HPT))

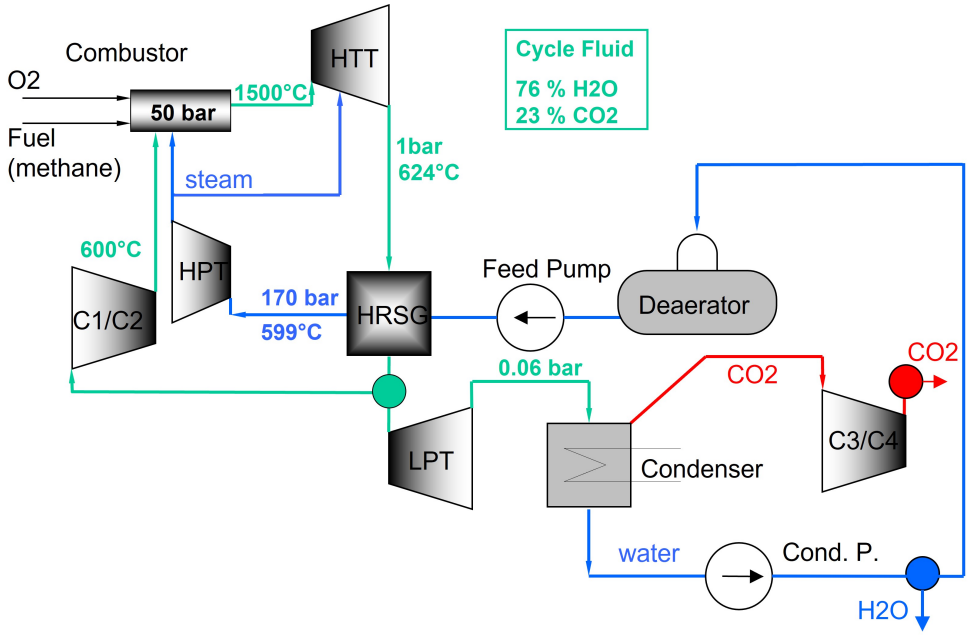

Figure 5.1: Basic layout of the Graz Cycle. Extracted from Wimmer and Sanz [133].

The combustion chamber works at 5 MPa under near-stoichiometric combustion (3 % of oxygen excess) using an oxygen mass flow produced by CAS methods. The system is suited to operate with different types of fuels, but in this case, it is run with natural gas (mainly methane). The combustion products leave the chamber at 1,500 °C, a temperature mainly controlled by water steam and a CO_2/H_2O mixture. The composition of the combustion products is 76 % water vapor, 23 % CO_2, and residual components such as nitrogen and argon. Nonetheless, this composition may vary around similar values as changes in the system operation are performed.

Then, this stream is driven through a High-Temperature Turbine (HTT), a three-stage turbine, which expands the outlet combustion chamber stream. This turbine is cooled using part of the steam from the HPT outlet, increasing the steam mass fraction of the working fluid. The outlet HTT flow is used to heat the water stream of the Rankine cycle at the HRSG, achieving superheated steam.

In this sense, Figure 5.2 shows the heat recovery steam generator (HRSG) used in the Graz Cycle, which consists of two preheaters (PH1 and PH2), one evaporator (EV), and two superheaters (SH1 and SH2). The outlet stream of HTT goes through all the heat exchangers except SH1, where the recycling gases that are driven to the combustion chamber are cooled to improve the performance of the C1/C2 system.

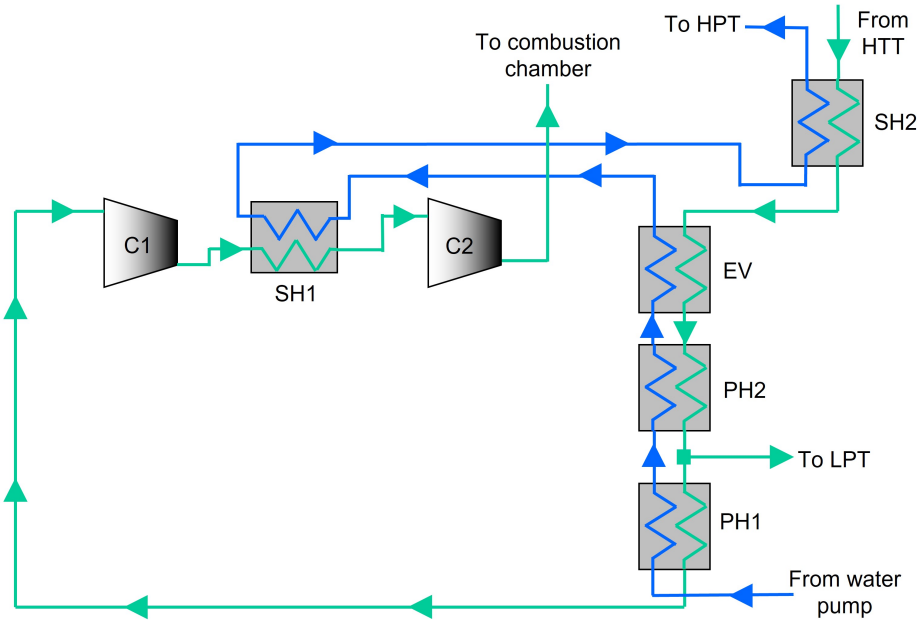

Figure 5.2: Layout of the HRSG of the Graz Cycle. Adapted from Wimmer and Sanz [133]

Between PH2 and PH1, the outlet HTT stream is branched. Around half of the mass flow is compressed in C1/C2 to feed the combustion chamber, regulating its temperature and the inlet temperature of HTT. On the other hand, the other part of the gases are expanded in the Low-Pressure Turbine (LPT) and then are passed through two condensation stages, separating CO_2 and H_2O. The resultant liquid water is pumped and superheated in the HRSG, reaching the two-stage High-Pressure Turbine (HPT) inlet conditions. After its first stage (HPT-1), the turbine is bypassed, where part of the steam goes to the second

stage (HPT-2), whose outlet is used to cool the second stage of HTT, and the other part directly cools the first stage of HTT, with a remanent flow that is directly driven to control the combustion chamber operation. These cooled turbine calculations follow the methodology found by Sanz et al. [119], where half of the cooling flow is mixed with the main flow at the stage inlet, while the other half goes directly to the stage outlet.

For the carbon capture line, the condensation stages after LPT are intercooling elements found between the two compressors (C3 and C4) that increase the high-purity carbon dioxide pressure. After C4, the compressors C5 and C6 (not included in Figure 5.1) continue the compression process, after which the CO_2 is sent to the compression and purification unit (CPU).

The main thermodynamic parameters of the cycle are summarized in Table 5.1.

Table 5.1: Main thermodynamic conditions of Graz Cycle.

Power plant output	400 MW
Fuel consumption	16.09 kg/s
HTT inlet temperature	1,500 °C
HPT inlet pressure	17 MPa
LPT inlet pressure	0.1 MPa
Condensation pressure	6 kPa
Combustion chamber pressure	5 MPa
Thermal electric efficiency	65.82 %
Efficiency considering O_2 supply	56.00 %
Efficiency considering O_2 supply and CO_2 compression	53.47 %

5.2.2 Case 1: Three-end membrane

The configuration of an oxygen production cycle based on a three-end MIEC membrane design to be coupled with the Graz Cycle is shown in Figure 5.3. Fresh air at atmospheric conditions (0.1 MPa and 25 °C) is driven through three intercooled mechanical compressors (LPC, MPC, and HPC) and an electric compressor (EC), increasing its pressure to reach optimum membrane operating conditions. The pressurized air is then heated in HE-1 and HE-2, which use the outlet streams of the membrane to recover their energy. A final heat exchanger is implemented (HE-3), which uses the energy between the second and the third stage of HTT to increase the air temperature. As a cooling restriction established by Wimmer and Sanz [133], the outlet temperature of the second HTT stage is set at 860 °C, establishing a limit in the membrane temperature operation.

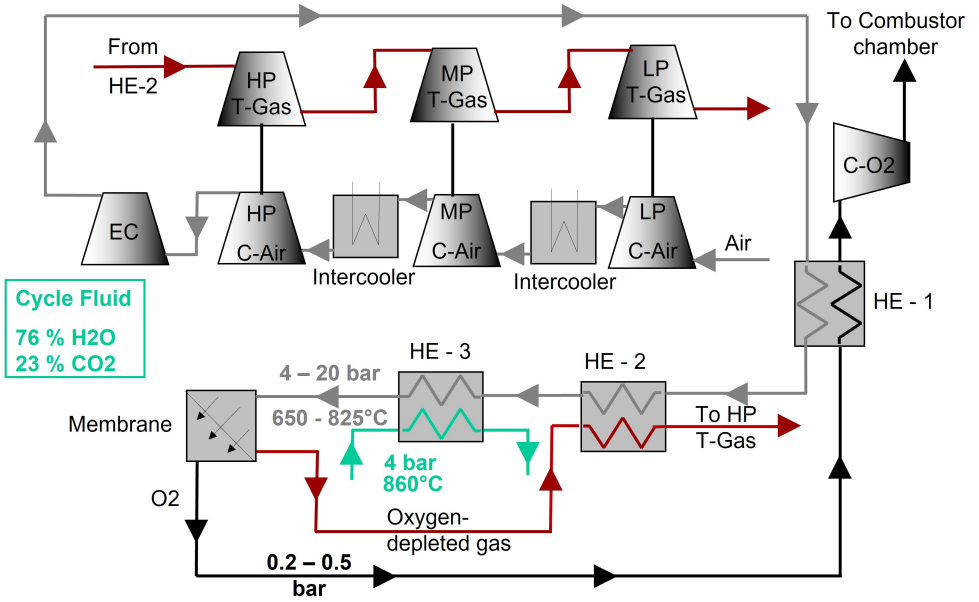

Figure 5.3: Flow scheme of a oxygen production cycle with a 3-end membrane.

The air then enters the inlet feed of the membrane at high pressure and high-temperature conditions, which leads to oxygen separation from the air flow. The high-purity oxygen stream is at vacuum pressure to promote oxygen production. As it leaves the membrane at a high temperature (depending on the membrane temperature operation), oxygen energy is used to heat air at HE-1, and then it is compressed in C-O2, a set of electric compressors that deliver the oxygen at 1.6 MPa. Finally, the final compression stage makes it reach the combustion chamber conditions.

The other outlet stream of the membrane, an oxygen-depleted flow (mainly nitrogen), is first used to heat the air in HE-2. Then, it energizes three turbines (LPT, MPT, and HPT) to drive their corresponding compressors. The coupling of this configuration and the Graz Cycle is shown in Figure 5.4. For clarity of the reader, HE-1 is shown in both layouts. In addition to this, it must be mentioned that the steam heating (HRSG) has not been modified.

This layout is similar to the one described in Chapter 4, particularly the first case that uses an electric compressor to reduce the oxygen partial pressure at the permeate side. The main differences are in the thermal energy sources and the oxygen delivery pressure. The primary energy source of Case 1 of the oxygen production cycle in the ceramic plant is taken from waste gases from the furnaces at 1,000 °C, used only to drive the coupled oxygen generation cycle. Meanwhile, the cycle coupled to the Graz cycle uses a thermal energy source at a temperature 140 °C lower. In addition, this stream is still used for power

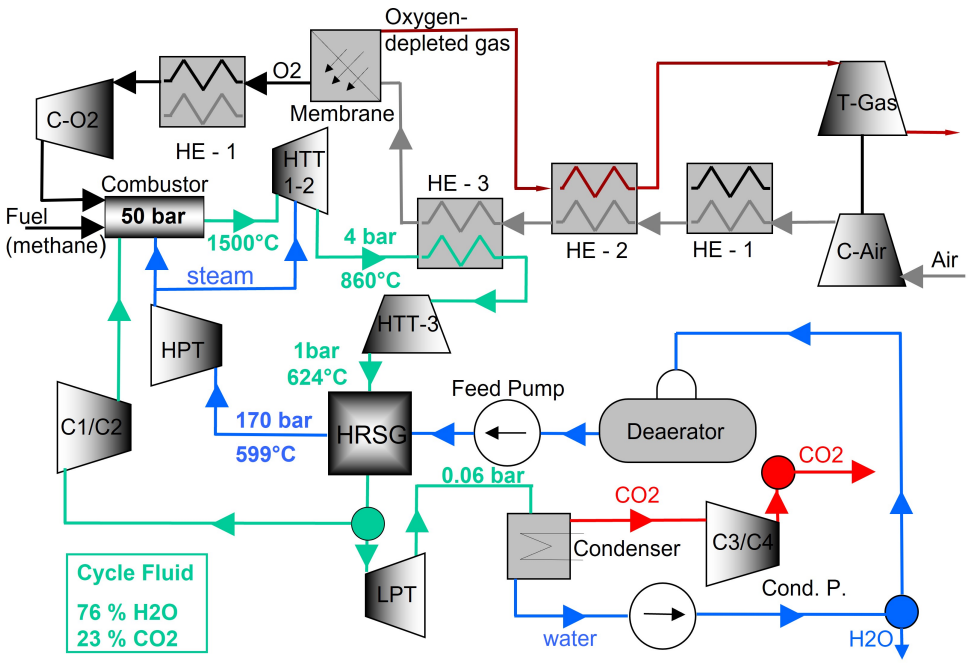

Figure 5.4: Coupling of Graz cycle with a 3-end membrane oxygen production cycle.

generation after it passes through HE-3. On the oxygen delivery pressure, the outlet pressure of the oxygen production in the case of chapter 4 is 0.1 MPa, while in this study, it must match the combustion chamber conditions, for which it must be delivered at a higher pressure.

5.2.3 Case 2: Four-end membrane

The four-end membrane case, depicted in Figure 5.5, works under a similar working principle to that of the three-end: a set of compressors and heat exchangers that pressurize and heat air, respectively, to achieve adequate membrane conditions for oxygen production. Moreover, the main difference is the method for reducing the oxygen partial pressure at the permeate side. While the three-end membrane requires vacuum generation, the four-end membrane is swept with recycled gases that will be used as a thermal buffer in the combustion chamber.

These recycled gases are taken from the C1 outlet, composed mainly of CO_2 and steam. C1 outlet conditions usually are around 1.5 MPa and 480 °C. At these conditions, the gases sweep the membrane at its permeate side, reducing the oxygen partial pressure. In this sense, adding electric compressors that

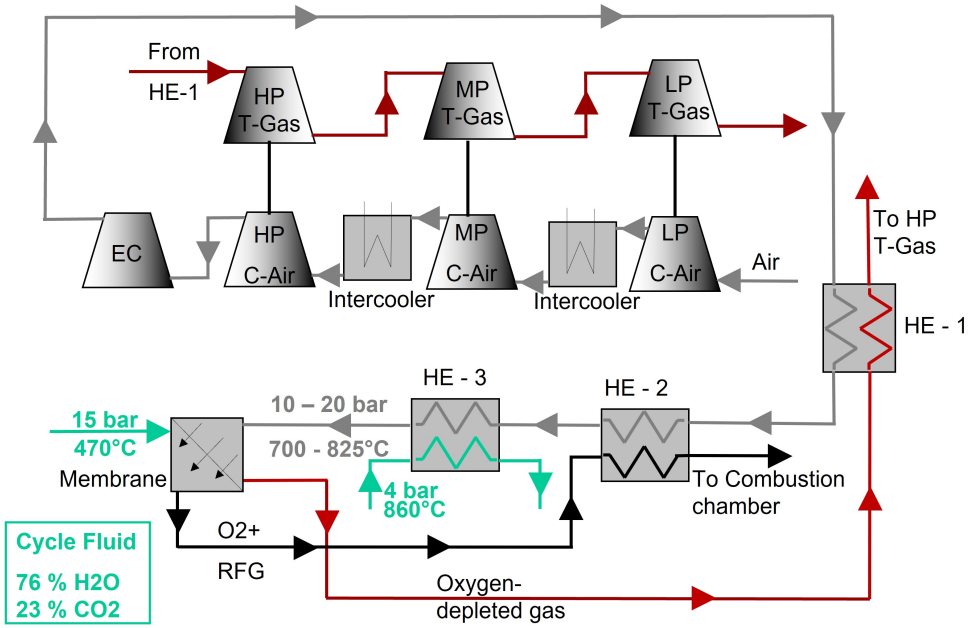

Figure 5.5: Flow scheme of a oxygen production cycle with a 4-end membrane.

work as vacuum pumps is unnecessary.

Considering the above, the recycling flue gases (RFG) drive the oxygen production, creating an O_2/RFG mixture used to heat the air in HE-2. After this, the mixture goes through SH1 of the HRSG and is compressed in C2 to reach combustion chamber conditions. Modifications in the base HRSG are depicted in Figure 5.6.

The whole layout of this configuration and its coupling with the Graz Cycle can be seen in Figure 5.7. The heat exchanger HE-2 is repeated twice for the reader's clarity.

5.3 Considerations, variables, and indicators for performance evaluation.

The calculations in the present chapter use IPSEpro v8 from Simtech Simulation Technology, as described in Chapter 3. A different approach regarding heat exchanger and turbomachine calculations is considered when comparing to the rest of the thesis, as the recommendations of the doctoral stay advisor, where this work was first developed, are taken into account.

In this sense, the following particular simplifications are considered in this chapter:

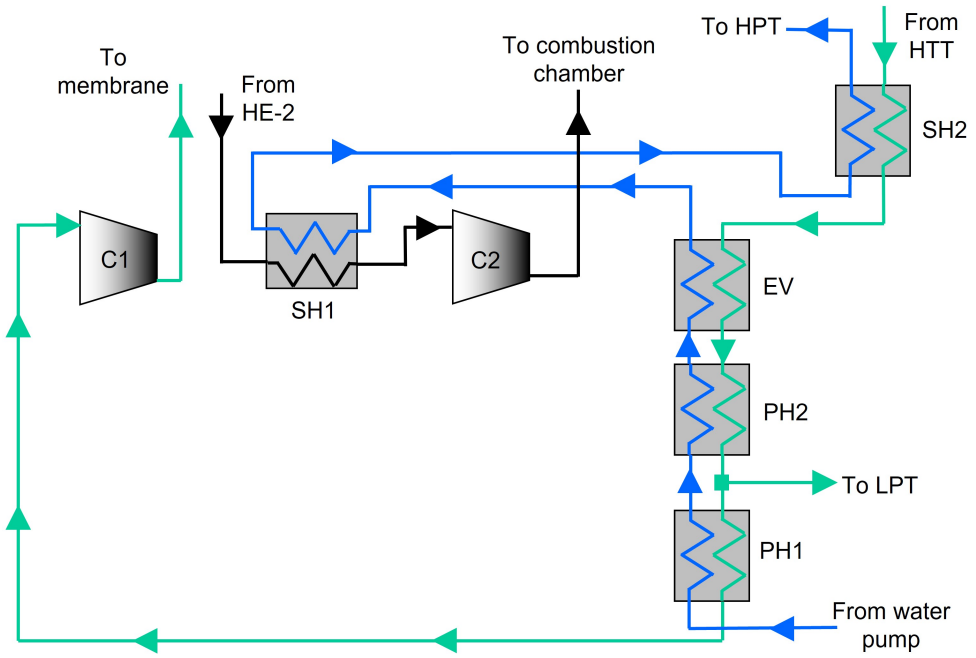

Figure 5.6: Layout of the HRSG of the Graz Cycle for Case 2. Adapted from [133]

- Regarding the Graz Cycle elements, the calculations are performed considering the methodology found in Wimmer and Sanz [133]. The pressure losses and turbomachine efficiencies are shown in Table 5.2.

- CAS method in the baseline case delivers the oxygen at 1.6 MPa and 15 °C, demanding a specific energy consumption of 1,049 $kJ\,kg^{-1}$. Similarly, the oxygen outlet pressure from the membrane cases is around 1.6 MPa. Then, the oxygen is pressurized to combustion chamber conditions for all the cases.

- The specific energy consumption of CO_2 compression from C3/C4 outlet to storage conditions is assumed to be 114.5 $kJ\,kg^{-1}$. The carbon capture final conditions are set at 11 MPa and 30 °C, as stated in Wimmer and Sanz [133]

- A pressure drop of 1 % of the inlet pressure is assumed at both sides of the heat exchangers of the oxygen production cycle.

- The turbomachines of the oxygen production cycle are assumed to have a constant efficiency, shown in Table 5.3.

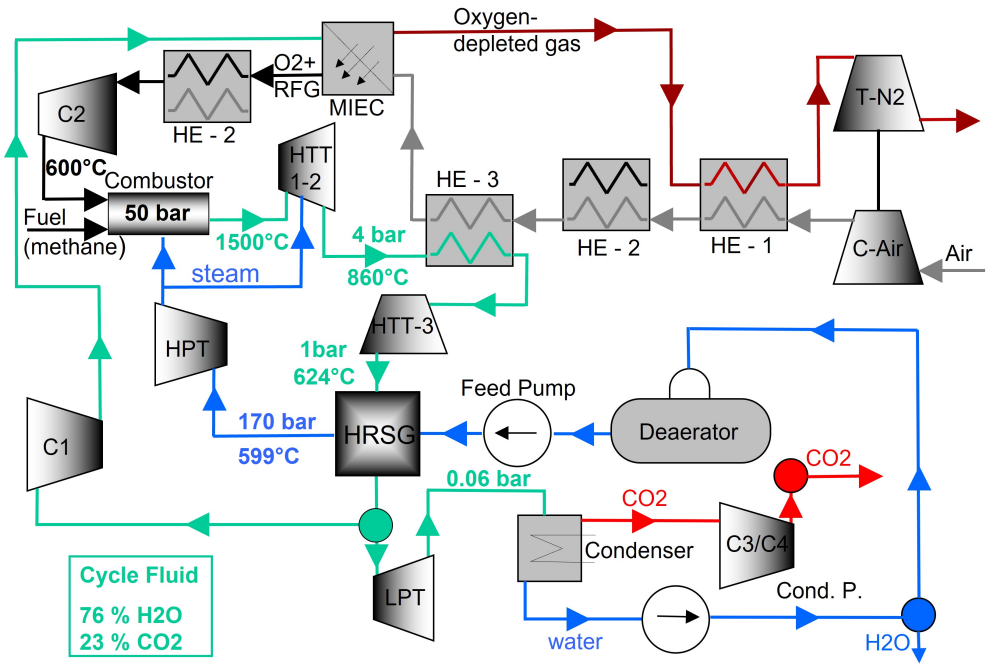

Figure 5.7: Flow scheme of Graz cycle with a 4-end membrane oxygen production cycle.

- The expansion ratios of the turbines in the oxygen production cycle are considered equal.

Considering the above, the membrane operation parameters are optimized in the membrane-based cases. For this purpose, the fuel mass flow in the combustion chamber is kept constant according to the results of Wimmer and Sanz [133], where a fuel mass flow of 16.09 $\mathrm{kg\,s^{-1}}$ was required to deliver a net power production of 400 MW. The latter ensures a constant heat input in all the cases.

The membrane conditions are modified for both membrane-based cases, determining the effects of this on the whole system's performance. The ranges of the membrane parameters are established by considering a maximum air pressure of 2 MPa, where higher pressures are nowadays a technological barrier due to the sealing difficulties in MIEC membranes, according to Zhu and Yang [8]. In addition, membranes operate at a temperature range between 700 to 1,000 °C, although there are studies where temperatures lower than 500 °C are examined with certain success [8].

For Case 1, the membrane feed pressure and temperature are varied, as well as the permeate side pressure. The following ranges are considered for the

Table 5.2: Pressure losses and turbomachine efficiencies of Graz cycle

Turbomachine efficiencies		Pressure losses	
C1/C2	88 %	PH-1 (hot side)	0.125 %
C3/C4	85 %	PH-1 (cold side)	1 %
C5/C6	85 %	PH-2 (hot side)	0.125 %
HTT	90 %	PH-2 (cold side)	1 %
HPT	90 %	Evaporator (hot side	0.125 %
LPT	88 %	Evaporator (cold side	1 %
O_2 compressor	82.8 %	SH-1 (hot side)	1 %
Mechanical efficiency	99 %	SH-1 (cold side)	2 %
Generator efficiency	98.5 %	SH-2 (hot side)	0.125 %
Transformer efficiency	99.7 %	SH-2 (cold side)	1 %
		Deaerator (hot side)	0.125 %
		Deaerator (cold side)	1 %
		Combustion chamber	2 %
		Condenser	1 %
		HPT feed pipe	0.5 MPa

Table 5.3: Turbomachine efficiencies of the O_2 production cycle

Mechanical compressors	84 %
Turbines	88 %
High-pressure electric compressor	84 %
Oxygen line compressors (Case 1)	82.8 %

mentioned variables:

- $P_{\text{air,feed}}$: 0.4 to 2 MPa
- P_{perm}: 0.02 to 0.05 MPa
- $T_{\text{air,feed}}$: 650 to 825 °C

The oxygen partial pressure at the permeate side is not directly controlled in Case 2, as it depends on the outlet conditions of C1. For this reason, the membrane feed conditions (pressure and temperature) are varied in the following ranges:

- $P_{\text{air,feed}}$: 1 to 2 MPa
- $T_{\text{air,feed}}$: 700 to 825 °C

A membrane area selection is required as performed in Chapter 4. Mean values of the presented ranges are maintained for each Case while the membrane area value is swept. This area variation changes the feeding air requirement, affecting the power consumption for oxygen production. The membrane sizes are then selected to obtain the system's maximum power and thermal efficiency under the membrane operation conditions imposed for this purpose. However, technical limitations of working with excessive membrane sizes are considered. Table 5.4 shows the used conditions for each Case to determine membrane sizing.

	Case 1 (3-end membrane)	Case 2 (4-end membrane)
$P_{\text{air,feed}}$ [MPa]	1.2	1.5
$T_{\text{air,feed}}$ [°C]	750	750
P_{perm} [MPa]	0.35	***

Table 5.4: Mean used conditions to determine membrane area

An additional study is performed regarding the effect of changing the heat power of the intercooling used between the compression stages. Initially, intercooler outlet temperatures are set to 25 °C to minimize the compression power requirements. Increasing this temperature can modify the heat demanded from HE-3 and the electric power consumption, for which the variation of outlet temperature from intercoolers is studied.

Case 1 has two sets of intercoolers: in between the air compressors and oxygen-driving compressors. For the first set, the outlet temperature of the first intercooler is varied between 25 to 55 °C, while for the second intercooler, its outlet temperature is swept from 25 °C until its cooling requirements are unnecessary, for which the cooler is removed. Only the second and third intercoolers are considered for the set of intercoolers among the oxygen-driving compressors. The outlet temperature for the second cooler is varied from 25 to 85 °C, while the third cooler is varied from 25 to 117 °C. This final temperature limit ensures that the electric compressor temperature to achieve combustion chamber conditions does not reach 600 °C, a limit imposed to keep its integrity.

Similarly, as only one set of intercoolers is required in Case 2, a similar study is performed for the air compressors cooling. In this sense, the first cooler varies from 25 to 85 °C, while the second cooler follows the same idea for Case 1.

Considering the above, three different figures of merit are used to evaluate each calculated operation point. These are the net thermal efficiency, net power generation, and the specific energy consumed for oxygen production. As mentioned earlier, the results are compared with the baseline parameters: a net power production of 400 MW, a specific energy consumption of 1,049 $\mathrm{kJ\,kg^{-1}}$, and 16.09 $\mathrm{kg\,s^{-1}}$ of fuel flow.

The net thermal efficiency for Case 1 is calculated as described in Equation 5.1.

$$\eta_{\text{net, C1}} = \frac{\left(\sum(P_{\text{T}} \cdot \eta_{\text{m}}) - \frac{P_{\text{C1+2}}}{\eta_{\text{m}}}\right) \cdot \eta_{\text{gen}} \cdot \eta_{\text{tr}} - \frac{P_{\text{C3+4}}}{\eta_{\text{m}}} - \frac{P_{\text{C5+6}}}{\eta_{\text{m}}} - \frac{\sum P_{\text{p}}}{\eta_{\text{m}}}}{\dot{Q}_{\text{in}}} + \frac{-P_{\text{aux}} - \frac{P_{\text{C,O2}}}{\eta_{\text{m}}} - P_{\text{CPU}} - \frac{P_{\text{C-HP}}}{\eta_{\text{m}}} - \frac{P_{\text{C, O}_2\text{ vacuum}}}{\eta_{\text{m}}}}{\dot{Q}_{\text{in}}} \tag{5.1}$$

For Case 2, the expression used is shown in Equation 5.2.

$$\eta_{\text{net, C2}} = \frac{\left[\sum(P_{\text{T}} \cdot \eta_{\text{m}}) - \frac{P_{\text{C1+2}}}{\eta_{\text{m}}}\right] \cdot \eta_{\text{gen}} \cdot \eta_{\text{tr}} - \frac{P_{\text{C3+4}}}{\eta_{\text{m}}} - \frac{P_{\text{C5+6}}}{\eta_{\text{m}}} - \frac{\sum P_{\text{p}}}{\eta_{\text{m}}}}{\dot{Q}_{\text{in}}} + \frac{-P_{\text{aux}} - P_{\text{CPU}} - \frac{P_{\text{C-HP}}}{\eta_{\text{m}}}}{\dot{Q}_{\text{in}}} \tag{5.2}$$

where $\sum P_{\text{T}}$ is the total gross power of the turbines, η_{m} is the mechanical efficiency, $P_{\text{C1+2}}$ is the C1 and C2 power, η_{gen} is the generator efficiency, η_{tr} is the transformer efficiency, $P_{\text{C3+4}}$ is the C3 and C4 power, $P_{\text{C5+6}}$ is the C5 and C6 power, $\sum P_{\text{p}}$ is the total power for water pumping, P_{aux} is the power consumption of the auxiliar components.

Additionally, P_{CPU} is the power consumption of the compression and purification unit to reach the final conditions of carbon capture (11 MPa and 30 °C), $P_{\text{C-HP}}$ is the power of the electric compressor in the air line of the oxygen production cycle, $P_{\text{C, O}_2\text{ vacuum}}$ is the compression power to reach 1.6 MPa in the oxygen line for Case 1, $P_{\text{C,O2}}$ is the compression power to reach the combustion chamber conditions for Case 1 and $\dot{Q}_{\text{in}}$ is the heat input in the combustion chamber.

It is seen that the different energy consumptions and losses, as well as auxiliary elements of the baseline case are considered for all the membrane-based cases. However, it is also seen that the energy consumption of the electric compressors for oxygen production is taken into account.

For specific energy consumption for oxygen production in Case 1, Equation 5.3 is implemented:

$$E_{\text{spec,O}_2\text{, Case 1}} = \frac{P_{\text{C,HP}} + P_{\text{C,O2 vacuum}} + \dot{Q}_{\text{HE-3}}}{\dot{m}_{\text{O2}}} \tag{5.3}$$

While for Case 2, the expression is shown in Equation 5.4:

$$E_{\text{spec,O}_2\text{,Case 2}} = \frac{P_{\text{C,HP}} + \dot{Q}_{\text{HE-3}} + (\dot{m}h)_{\text{PS inlet}} - (\dot{m}h)_{\text{HE-2 outlet}}}{\dot{m}_{\text{O2}}} \tag{5.4}$$

The electric compressor consumption for air driving pressurizing and the thermal power at HE-3 for air heating are considered in both cases. Nonetheless, the electric compressors in the oxygen line are considered for Case 1. Furthermore, an enthalpy flow goes into the permeate side that comes from C1 in Case 2. This stream is also delivered to the power cycle part after HE-2, containing the oxygen that has been separated. In this sense, this enthalpy difference, Δh , is considered in the calculation of energy consumption for Case 2.

5.4 System evaluation using a three-end membrane

5.4.1 Membrane sizing

Increasing the membrane area leads to increase the net power production of the whole system, as well as increasing the thermal efficiency. The effect of the membrane area on these variables are depicted in Figure 5.8(a) and Figure 5.8(b), respectively.

Larger membranes allow a better oxygen separation from the air, for which less air flow is required. In this sense, the electric power for air boosting is reduced. Besides this, the exchanged thermal power in HE-3 is also diminished, for which there is more available enthalpy for power production in the HTT, improving the system performance.

Nonetheless, reducing the air mass flow for the same oxygen production leads to decreased available enthalpy flow for the expansion stages and heat

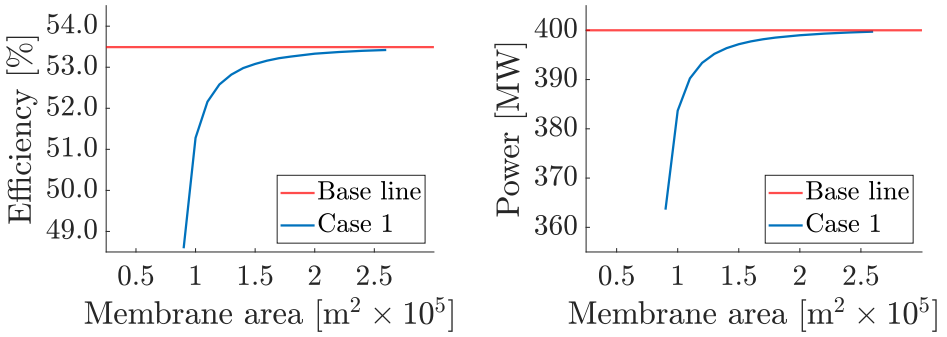

(a) Net power.

(b) Thermal efficiency.

Figure 5.8: Net power and thermal efficiency in function of membrane area - Case 1

recovery, mainly due to a reduced oxygen-depleted flow. For this reason, the heat in HE-2 and the power consumption are affected, leading to an asymptotic behavior where the effect of reducing air mass flow in energy consumption is compensated. This trend in air mass flow, HE-3 heat and electric power consumption is depicted in Figure 5.9.

Consequently, the net power increment as the membrane area grows stagnated with larger areas. Figure 5.10 shows that adding 1,000 m^2 when the membrane area is 170,000 m^2 results in an increase smaller than 0.05 MW of net power. With this in mind, a membrane area of 170,000 m^2 is selected for this case. Increasing the membrane size would not bring considerable benefits to the system operation but would increase the complexity of the facility in terms of costs and maintenance. Additionally, it allows the membrane to produce oxygen at many points of the proposed study ranges.

5.4.2 Parameters influence on the Graz cycle performance (Feed and permeate side pressure, feed temperature)

The optimum net power production and thermal efficiency for each permeate side pressure are found with the membrane working with an air feed pressure below 1 MPa, while the feed temperature is kept at the highest possible temperature (825 °C), considering that the heat source is at 860 °C. As the permeate side pressure is reduced, oxygen production is promoted, and a higher optimum net power can be produced. For each studied permeate pressure, the net power production and the thermal efficiency are shown in Figure 5.11 and Figure 5.12.

The effect of changing the thermodynamic working conditions of the membrane can be explained by considering the air mass flow demanded, the thermal

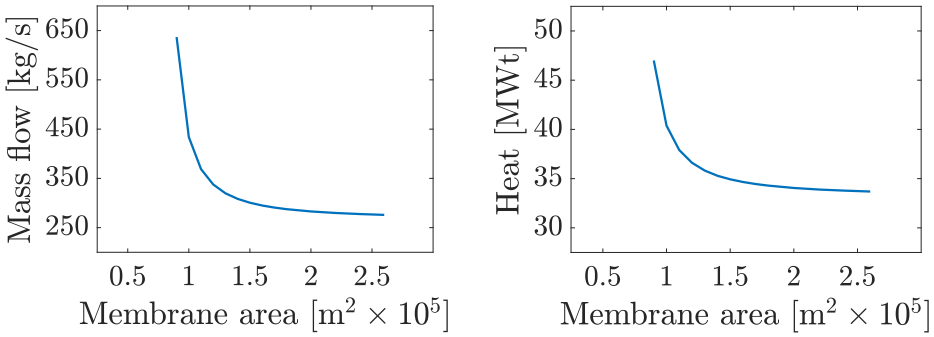

(a) Air mass flow.

(b) HE-3 heat power.

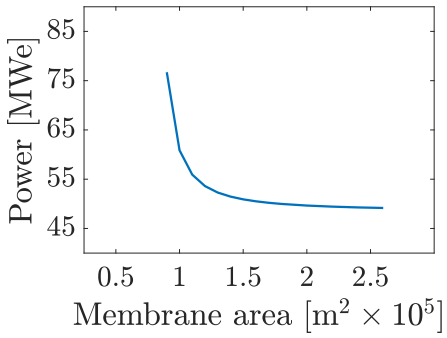

(c) Electric power.

Figure 5.9: Operating parameters of oxygen production in function of membrane area - Case 1

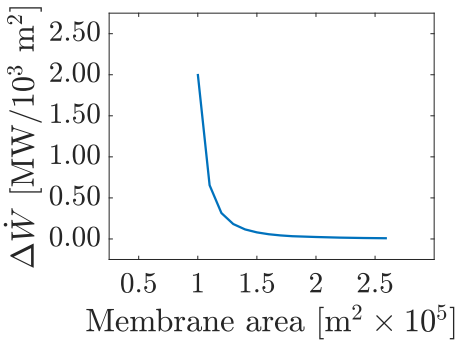

Figure 5.10: Variation of power increment with membrane area - Case 1

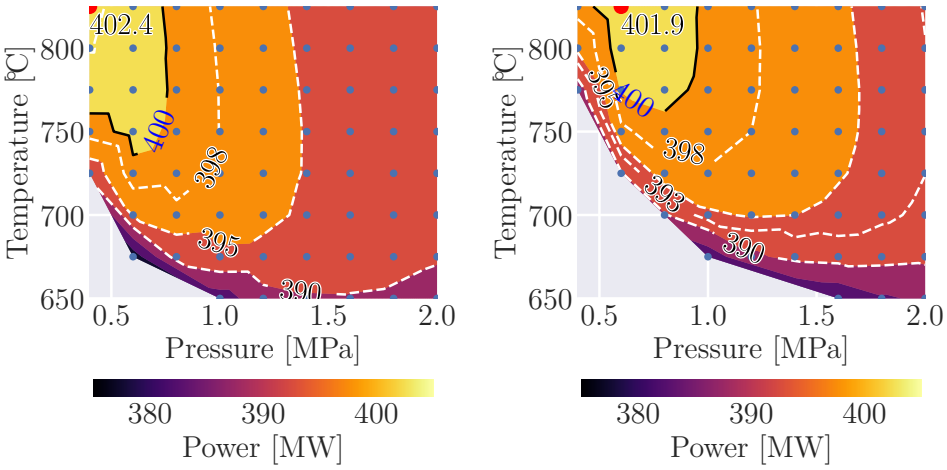

(a) Permeate pressure = 0.02 MPa

(b) Permeate pressure = 0.03 MPa

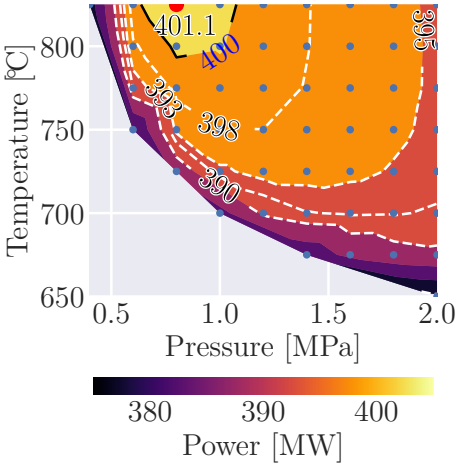

(c) Permeate pressure = 0.04 MPa

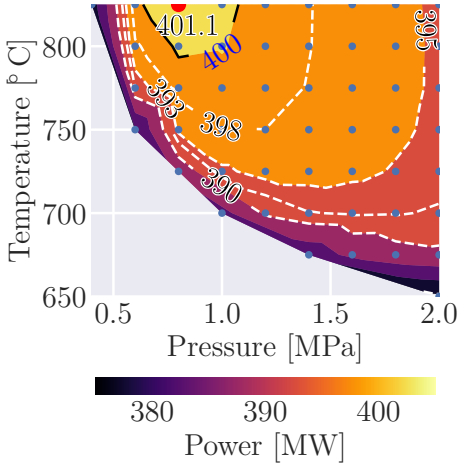

(d) Permeate pressure = 0.05 MPa

Figure 5.11: Net power behavior in function of air feed pressure and temperature for different permeate pressures - Case 1

energy exchanged in the primary heat source of the oxygen production cycle, HE-3, and the electric power consumption for air boosting.

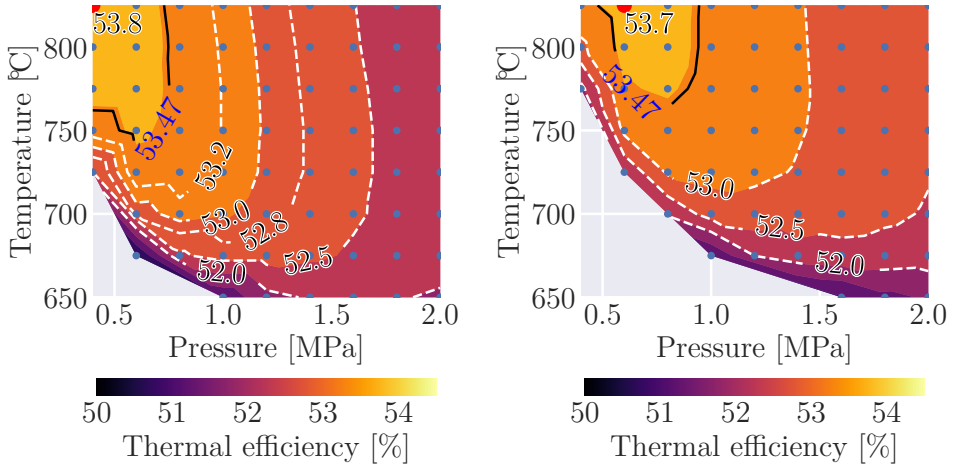

(a) Permeate pressure = 0.02 MPa

(b) Permeate pressure = 0.03 MPa

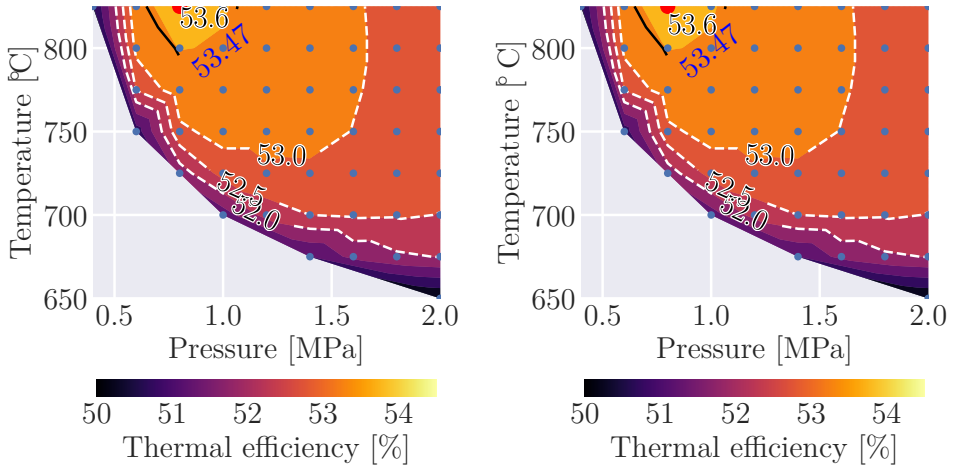

(c) Permeate pressure = 0.04 MPa

(d) Permeate pressure = 0.05 MPa

Figure 5.12: Thermal efficiency as a function of air feed pressure and temperature for different permeate pressures - Case 1

Figure 5.13 depicts the air mass flow required to produce the oxygen needed at the combustion chamber when the feed air pressure and temperature change at different permeate side pressures. High pressures and temperatures at the feed side benefit the membrane permeability, for which the air stream is reduced when operating at these conditions. This explains the trend in Figure 5.13, where for each permeate pressure, a reduction is seen in the air mass flow as

both pressure and temperature are incremented.

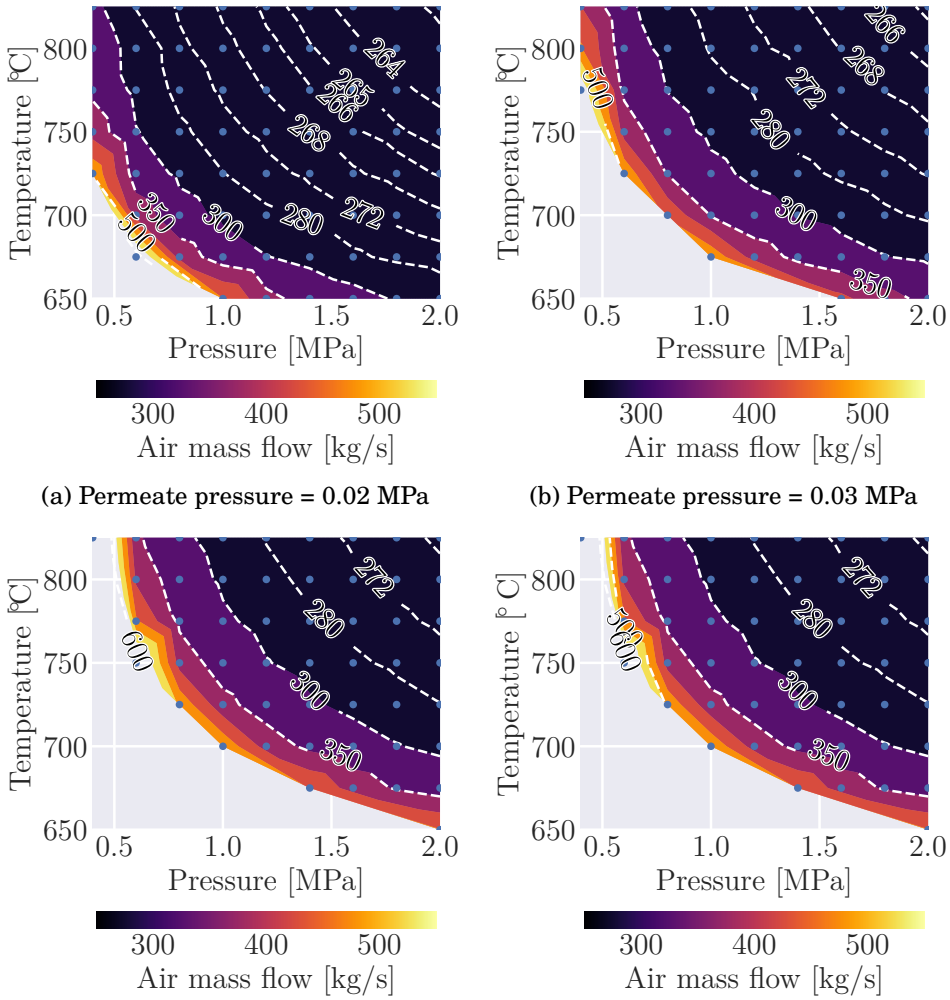

(a) Permeate pressure = 0.02 MPa

(b) Permeate pressure = 0.03 MPa

(c) Permeate pressure = 0.04 MPa

(d) Permeate pressure = 0.05 MPa

Figure 5.13: Required air mass flow as a function of air feed pressure and temperature for different permeate pressures - Case 1

In this sense, thermal and electric energy consumption are affected. Figure 5.14 exhibits the trend of the thermal heat power at HE-3. The minimum required heat power is always located in an operation region of high feed pressure and low feed temperature. In this zone, there is a relatively low air mass flow and a low-temperature increase, for which the thermal power in HE-3 is the lowest.

This trend can be explained by considering each variable separately. For

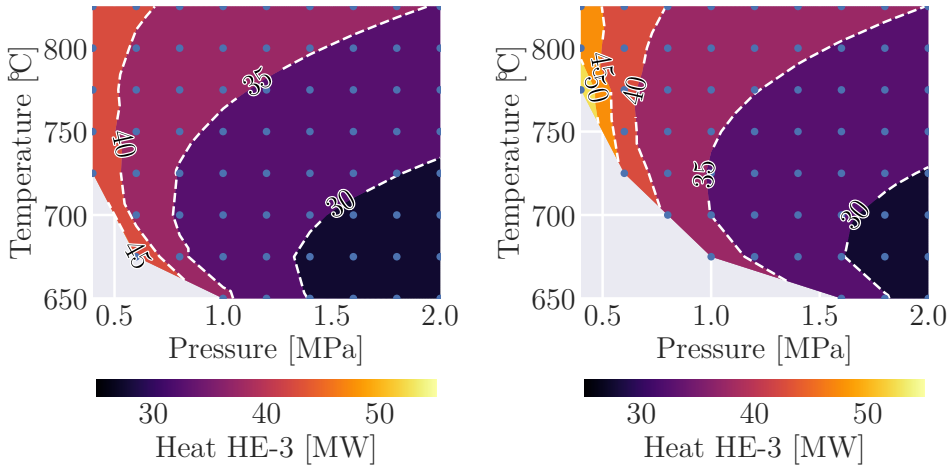

(a) Permeate pressure = 0.02 MPa

(b) Permeate pressure = 0.03 MPa

(c) Permeate pressure = 0.04 MPa

(d) Permeate pressure = 0.05 MPa

Figure 5.14: Heat power at HE-3 as a function of air feed pressure and temperature for different permeate pressures - Case 1

a constant temperature, the heat required is reduced as the feed pressure increases due to the reduction of air mass flow. On the other hand, for each constant pressure, an optimum temperature is seen that ensures a minimum heat in HE-3. The heat increases for low temperatures in the studied range due to a high air mass flow demanded for oxygen production. On the other hand, the air mass flow is reduced for higher temperatures, but the imposed air temperature increase now dominates the thermal power in HE-3. In this sense, there is a trade-off between the air mass flow and the temperature increase for each pressure level.

The electric consumption for each permeate side pressure is depicted in Figure 5.15. Considering that there is a constant component of electric power consumption due to the oxygen production demand remaining the same in all the studied points, and the pressure ratio from the outlet permeate side and the combustion chamber is the same, the variation in the electric power depends solely on the changes in the electric air compressor.

The minimum value of electric consumption for each permeate side pressure scenario can be found at the highest air feed temperature and low feed pressures. For a constant feed pressure, the electric power requirement decreases as the feed temperature increases due to a diminishing air mass flow needed for oxygen production as the membrane operating conditions are improved. On the other hand, there is a minimum electric power consumption for each constant feed temperature. The air mass flow is increased for low pressures to produce the oxygen demanded. Additionally, higher pressures demand a higher compression ratio in the electric compressor, which increases the power demand. Similar to the thermal power behavior, there is a trade-off in the feed pressure for a constant feed temperature.

Considering all the above, an optimum value of power and efficiency is observed for an air supply at the feed side of the membrane of 0.4 MPa, a permeate side pressure of 0.02 MPa, and a feed side temperature of 825 °C. In this case, a net power of 402.4 MW is achieved with a net thermal efficiency of 53.80 %, corresponding to 2.4 MW higher net power and 0.33 % points higher in efficiency than the baseline case.

Low permeate side pressures promote oxygen permeation at the membrane, for which the feed side pressure can be reduced. More vacuum in the permeate side implies an increase in the power the compressors need in this oxygen line. Nonetheless, the air mass flow reduction that this action brings reduces the electric air compressor consumption, compensating for the increment in vacuum generation.

Finally, it must be said that the increase of permeate side pressure reduces the viability of operating under some feed conditions due to the reduction of membrane permeability. The latter is represented in the increment of the gray zones of the presented figures.

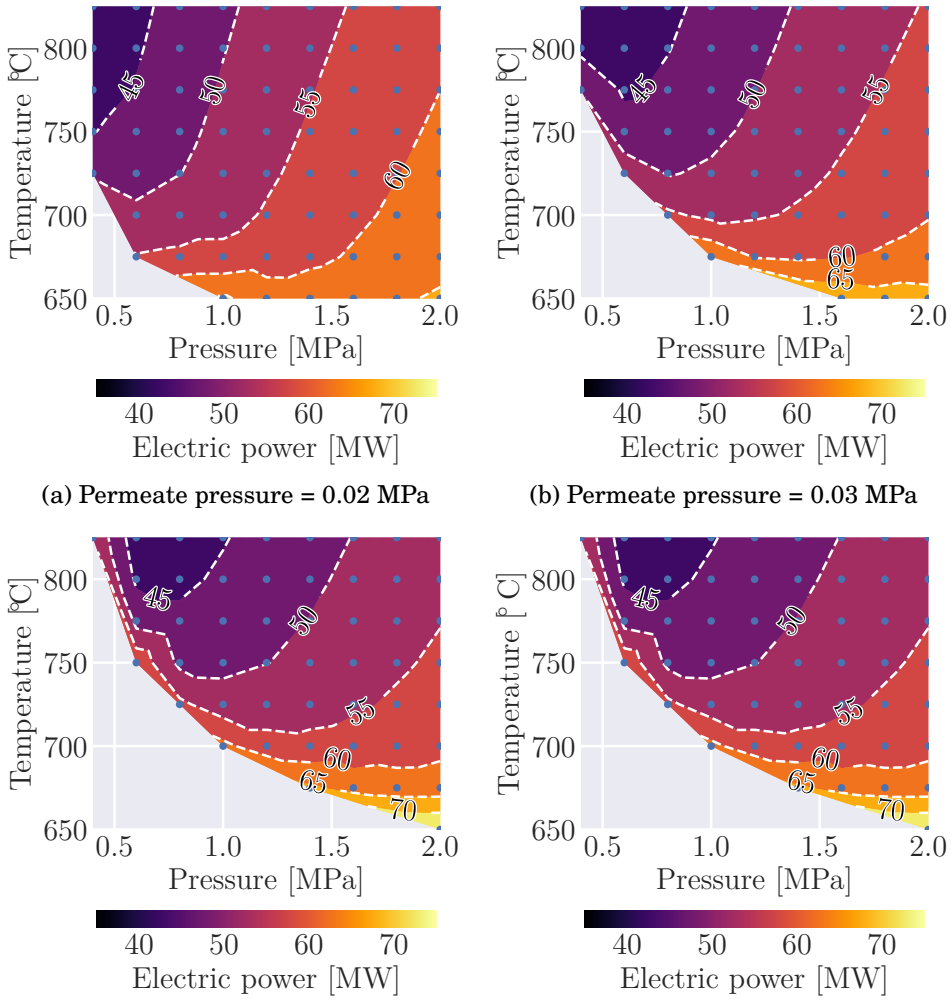

(a) Permeate pressure = 0.02 MPa

(b) Permeate pressure = 0.03 MPa

(c) Permeate pressure = 0.04 MPa

(d) Permeate pressure = 0.05 MPa

Figure 5.15: Electric power consumption as a function of air feed pressure and temperature for different permeate pressures - Case 1

5.4.3 Intercooling optimization

Considering the obtained optimum value, the heat dissipated in the intercoolers in between the compressors is optimized to improve the net power production of the whole system. Since the membrane operation conditions are kept, according to the results in the last optimization, the driven air mass flow is maintained constant.

For a constant outlet temperature of the first cooler, the net power production and thermal efficiency increase as the second cooler's outlet temperature increases, as seen in Figure 5.16. The required power of the electric compressor goes up due to the compression process being performed at a higher temperature, as seen in Figure 5.17(a). Nonetheless, two positive effects compensate for this increase in electric power consumption: First, the temperature at the expansion stages inlet is increased, leading to a higher enthalpy flow that moves the mechanical compressors, which helps to avoid a more remarked increment in the power consumption of the electric air compressor. Second, the air temperature before HE-3 slightly increases, reducing the heat power in this component as seen in Figure 5.17(b). The latter avoids the reduction in the enthalpy of the third stage of the HTT, which contributes to the system's power production.

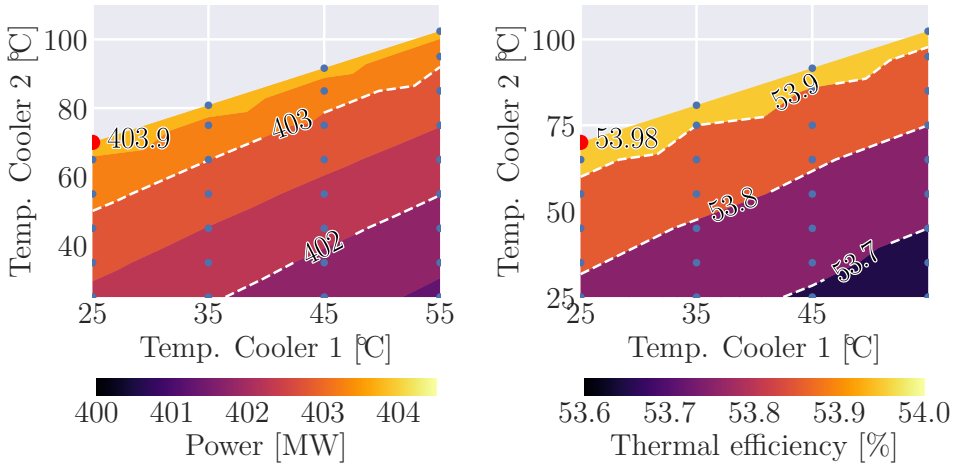

(a) Net power

(b) Thermal efficiency

Figure 5.16: Graz cycle performance as a function of outlet air cooler temperatures in the air line - Case 1

For variations in the outlet temperature of the first cooler, the effect on the performance of the second mechanical compressor is directly affected, which impacts the power of the electric air compressor.

It must be explained that the observed wiggles in the isolines of electric

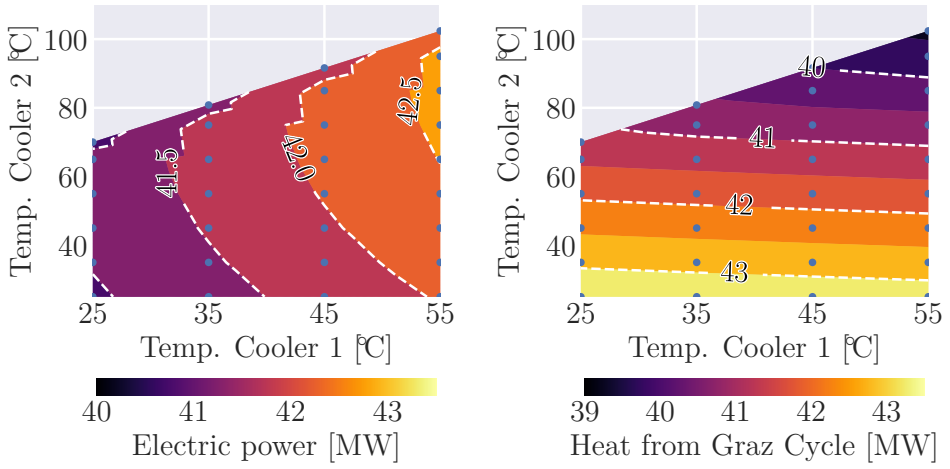

(a) Electric power consumption

(b) Heat power at HE-3

Figure 5.17: Electric and thermal power consumption as a function of outlet air cooler temperatures in the air line - Case 1

power in Figure 5.17(a) are generated due to the second cooler being removed. In this sense, the pressure losses associated with this element are eliminated, changing the trends in electric power consumption.

The latter optimization leads to an increase of 1.5 MW and 0.2 % points in net power production and thermal efficiency, respectively, when compared with the initial optimization of membrane parameters. In this scenario, the first cooler outlet temperature is kept at 25 °C, while the second cooler is eliminated, leaving an inlet temperature at the third mechanical compression stage of 70 °C.

On the other hand, an additional cooling optimization is performed for the oxygen line compressors. In this case, the first cooler outlet temperature is maintained while the calculations are performed considering the second and third coolers.

For a constant outlet temperature at the second cooler, it is seen in Figure 5.18 that an increment in the outlet temperature of the third cooler leads to improve net power production and the system's thermal efficiency. An increment in the electric power consumption is expected, as depicted in Figure 5.19(a), due to the compression process at the third stage being performed at higher temperatures. However, this increases the inlet oxygen temperature at the combustion chamber, as shown in Figure 5.19(b), which gives an additional enthalpy flow to the combustion process, improving the performance. This effect will be further explained in the comparison section of the current chapter.

In addition, an increase in the outlet temperature of the second cooler results in a rise in the required power to boost the oxygen compression stages, affecting

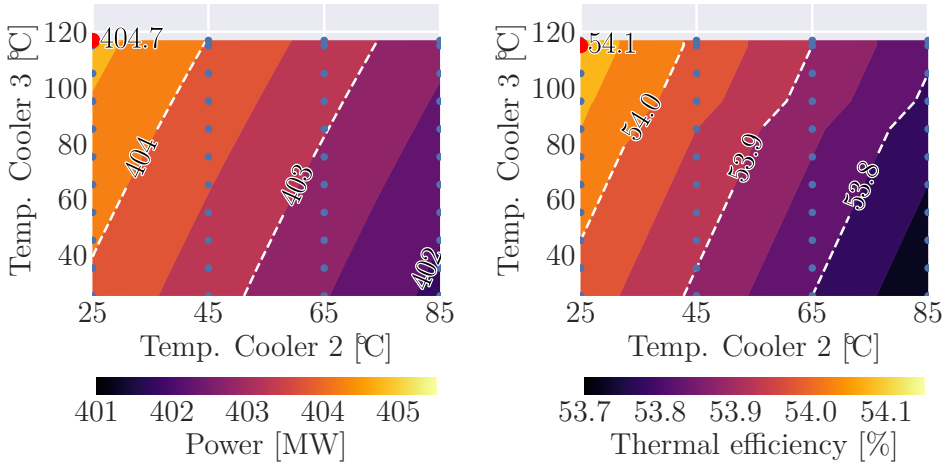

(a) Net power

(b) Thermal efficiency

Figure 5.18: Graz cycle performance as a function of outlet air cooler temperatures in the oxygen line on cycle performance - Case 1

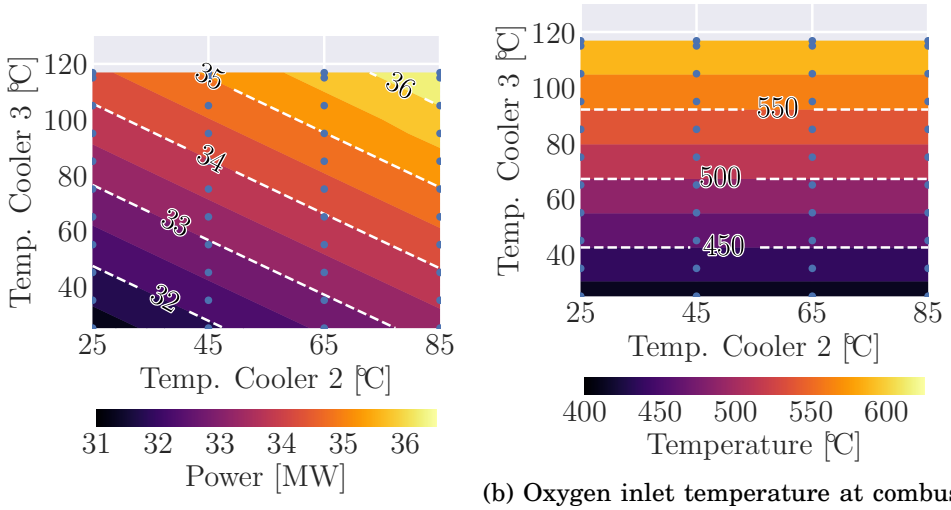

(a) Oxygen line compression power

(b) Oxygen inlet temperature at combustion chamber

Figure 5.19: Influence of outlet oxygen line cooler temperatures on oxygen production cycle variables - Case 1

the net power production.

That said, an improved net power output of 404.67 MW is now achieved, as well as a thermal efficiency of 54.08 %. In this sense, there is a power increment of 0.77 MW and 0.1 %points regarding the first intercooling optimization. In this scenario, the second intercooler outlet temperature is kept at 25 °C, while the third cooler increases its outlet temperature to 117 °C, maintaining a limit of 600 °C in the electric compressors.

5.5 System evaluation using a four-end membrane

5.5.1 Membrane sizing

Similar behavior to Case 1 is obtained for the membrane selection in Case 2, as seen in Figure 5.20, reaching the same asymptotic behavior in the power production benefits as larger membranes are used. The reasons for this trend are shared in both cases: the reduction of air mass flow due to the increase in the membrane permeability leads to a reduction in the power consumption and the thermal power requirements, as depicted in Figure 5.21. This also affects the available enthalpy at the expansion stages and the air heating at HE-1.

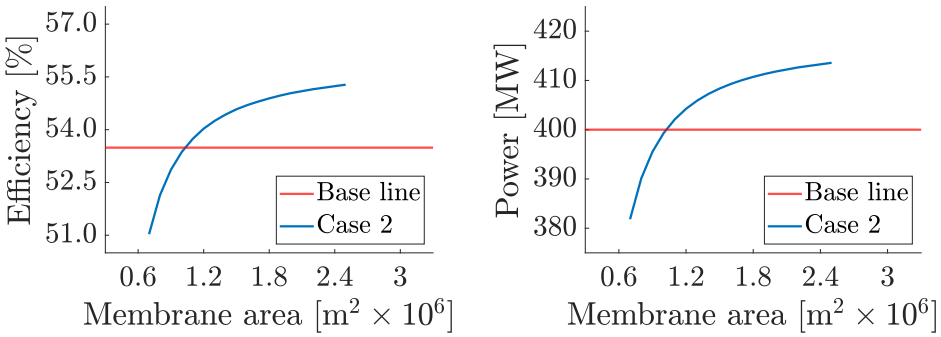

(a) Thermal efficiency

(b) Net power

Figure 5.20: Net power and thermal efficiency as a function of membrane area - Case 2

However, an additional reason that affects the membrane sizing was also found. The air outlet temperature from HE-1 is reduced due to the reasons above. In this sense, the temperature difference between the air inlet temperature and the O_2/RFG inlet temperature at HE-2 is increased, affecting the thermal power exchanged in this element. This finally reduces the enthalpy difference, Δh, described in the presentation of the indicators for the system assessment. In this sense, the enthalpy flow that returns to the Graz Cycle layout is affected,

directly reducing the superheating process at SH1 and consequently net power production.

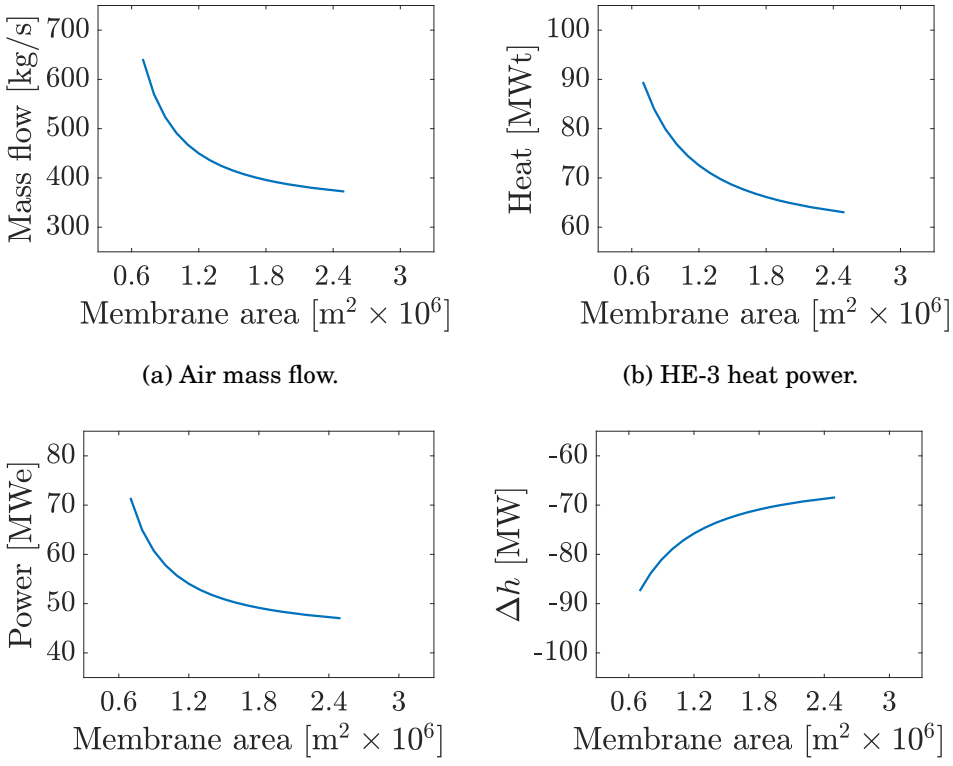

(a) Air mass flow.

(b) HE-3 heat power.

(c) Electric power.

(d) Δh.

Figure 5.21: Operating parameters of oxygen production as a function of membrane area - Case 2

In this context, a membrane area of 1,600,000 m^2 is selected. Increasing the membrane size above this value does not significantly benefit the system performance, bringing complexity to the facility regarding costs and maintenance. At this value, adding 1,000 m^2 only means an increment of 0.01 MW in power production, as shown in Figure 5.22. Similarly to Case 1, this membrane size selection allows the calculations to be performed for a wide range of the proposed values to be studied.

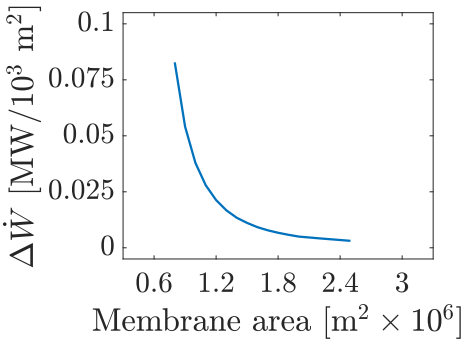

Figure 5.22: Variation of power increment with membrane area - Case 2

5.5.2 Parameters influence on the Graz cycle performance (Feed air pressure and temperature)

Similar to Case 1, the analysis of the membrane operation parameters in the system performance is evaluated regarding the required air mass flow and the energy consumption for oxygen production. Figure 5.23 shows that the higher net power production and thermal efficiency levels can be found at high air feed pressures and medium air feed temperatures.

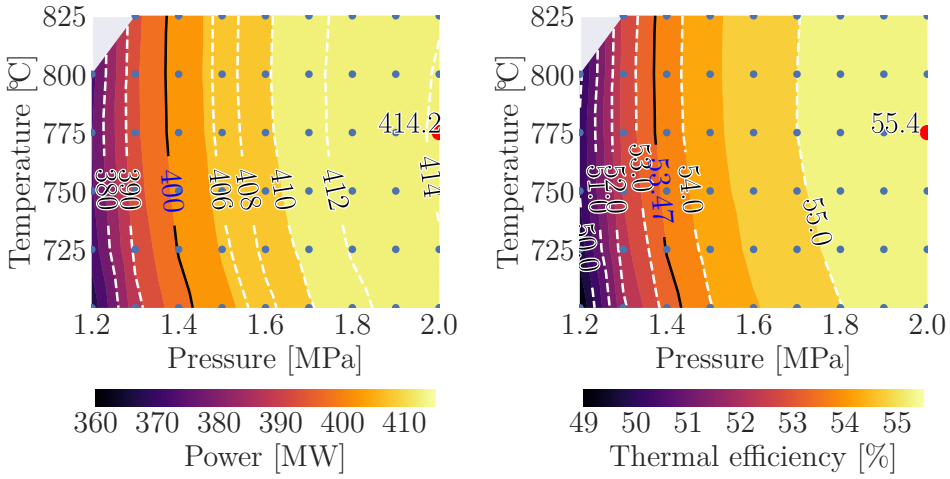

(a) Net power.

(b) Thermal efficiency.

Figure 5.23: Graz cycle performance as a function of air feed pressure and temperature - Case 2

The air mass flow required is highly dependent on the membrane's working feed pressure. It shows a pronounced increment, achieving a wide range between

300 to 800 $kg\,s^{-1}$ depending on the pressure and temperature at the membrane feed side. However, as seen in Figure 5.24(a), it is seen that operating zones with high pressures and temperatures need less air mass flow, as explained in Case 1.

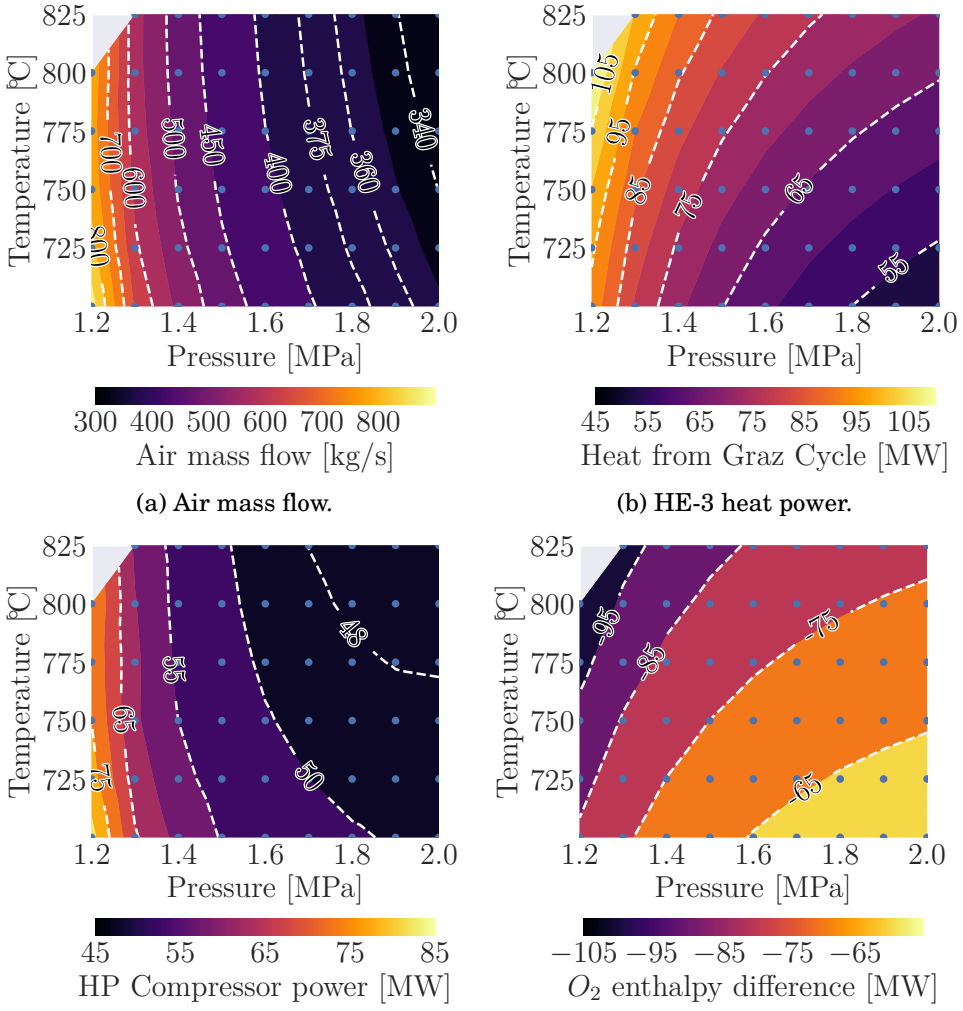

(a) Air mass flow.

(b) HE-3 heat power.

(c) Electric power consumption.

(d) Δh

Figure 5.24: Oxygen production cycle variables as a function of air feed pressure and temperature - Case 2

Figure 5.24(c) depicts the electric power consumption for different feed pressures and temperatures. In this case, the electric consumption corresponds exclusively to the electric air compressor in the air line. The air stream through the compressors dominates the electric consumption. Even if the compressor

ratio at the electric air compressor increases, the remarked diminishing in the air mass flow reduces power consumption. However, a minor effect as the temperature increases can be perceived, naturally expected, as the membrane permeability improves.

On the other hand, the thermal power exchanged in HE-3 is shown in Figure 5.24(b) for different feed pressures and temperatures. Feed air temperature increments lead to a considerable increase in the thermal power of this element for a constant pressure, although there is a slight decrease in air mass flow. However, the most critical effect comes from feed side pressure variation, which finally affects the air mass flow variation, changing the thermal and electric power demands.

In this case, it must be considered that the membrane temperature operation is not the same as the feed air temperature, as for Case 1, due to the nature of four-end membranes with different temperatures at the inlet of both sides. The sweeping mass flow at the permeate side (which is at 480 °C) reduces the effective temperature of the membrane, as seen in Figure 5.25.

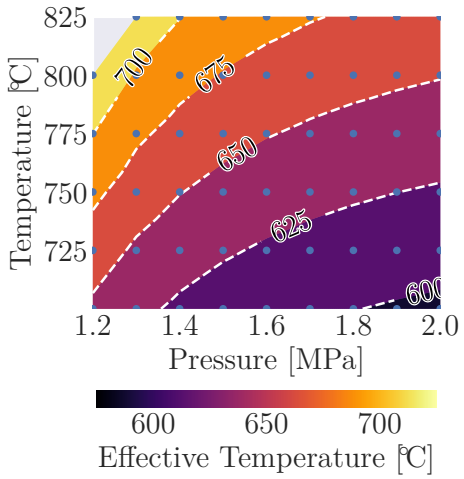

Figure 5.25: Effective membrane temperature as a function of air feed pressure and temperature - Case 2

It is seen that the effective membrane operation is in the range of 600 to 700 °C, although the air feed mass flow could be as high as 825 °C. This reduced temperature leads to higher air mass flow levels than for Case 1 and a higher dependency on the feed pressure to compensate for the effect of low temperatures.

The effective temperature naturally increases at constant pressure as the feed inlet temperature increases, despite the slight reduction in the air mass flow. On the other hand, for a particular feed side temperature, the effective mem-

brane temperature is reduced due to the reduction of air mass flow, for which the sweeping stream temperature at the permeate side takes more importance, decreasing the overall membrane temperature.

In this sense, the effective temperature's behavior affects the enthalpy difference, Δh, as shown in Figure 5.24(d). Higher values of effective temperature can be found at low-pressure and high temperatures. For this reason, a higher enthalpy flow is driven from the HE-2 outlet of the O_2/RFG stream. Therefore, there is more available energy in SH1 to superheat the steam, improving the performance of the cycle.

Considering the above, this case's net power and thermal efficiency optimum is achieved at 2 MPa of air feed pressure and 775 °C of feed temperature. At these conditions, the net power value is 414.17 MW and the thermal efficiency is 55.35 %, 14.17 MW and 1.88 % points higher than the baseline case.

The optimum is found at a zone of low electric power consumption and mean values of HE-3 heat and Δh. The feed temperature permits operating without excessive thermal power exchanged at HE-3 while keeping a considerable Δh to improve HPT performance by heating at SH1.

5.5.3 Intercooling optimization

Case 2 only has one set of intercoolers in between the compressors in the air line, for which one optimization process regarding outlet cooler temperature is performed. In this sense, Figure 5.26 shows how the net power and the thermal efficiency are affected, while Figure 5.27 shows the electric power consumption and Δh.

The consumed electric power is increased when the outlet temperature of the second cooler is incremented, as shown in Figure 5.27(a). This is due to a compression process performed at a higher temperature as expected. However, the increment in outlet temperature of the electric compressor implies an increment in the outlet temperature of the oxygen-depleted and the O_2/RFG streams, which has two consequences: First, as for Case 1, there is a rise in the enthalpy flow at the inlet of the expansion stages that partially compensates for the increment in electric power. Second, as shown in Figure 5.27(b), the available energy of the O_2/RFG stream at the HE-2 outlet increases, affecting the Δh value and improving the superheating process at SH1.

On the other hand, increasing the outlet temperature of the first cooler affects the operation of the second stage of mechanical compression, which affects the electric energy consumed and, finally, the power production of the whole cycle.

Considering the above, the optimum point of this optimization process achieved a net power of 417.24 MW and a thermal efficiency of 55.76 %, increasing 3 MW and 0.41 % compared to Case 2 without optimization. At this

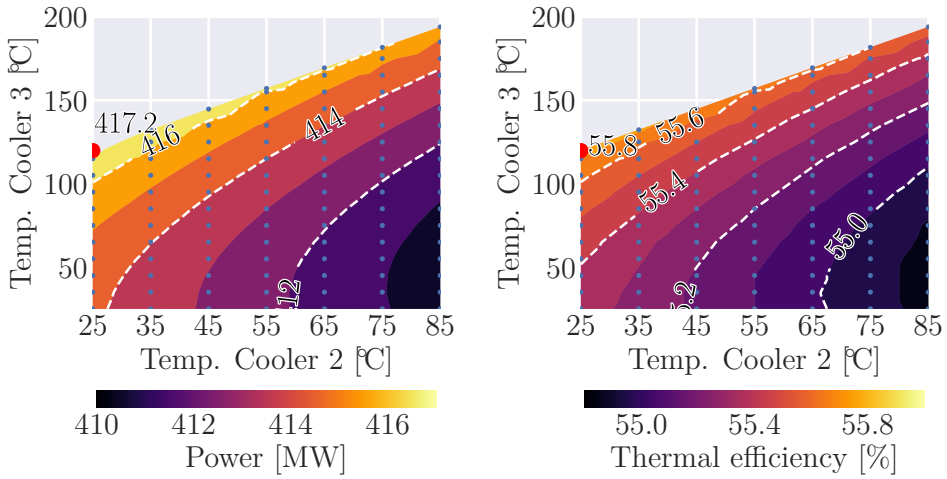

(a) Net power cycle.

(b) Thermal efficiency.

Figure 5.26: Cycle performance as a function of the outlet air cooler temperatures in the air line - Case 2

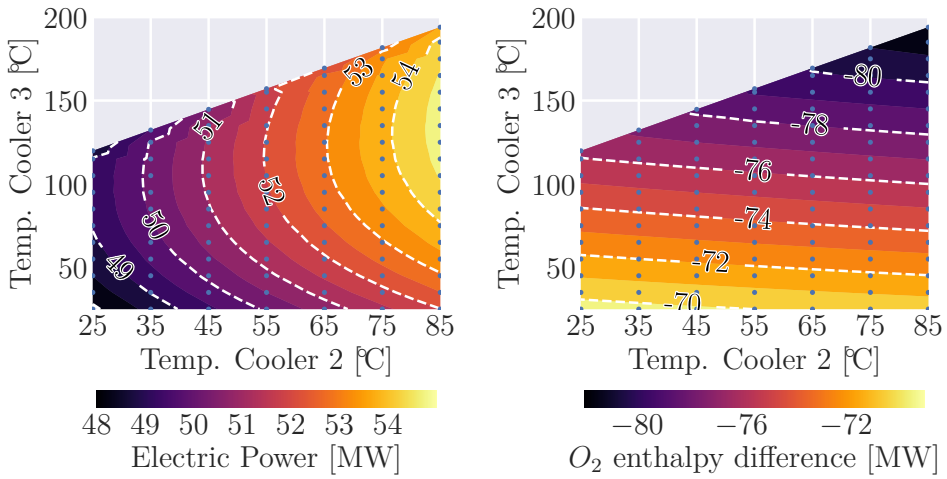

(a) Electric power consumption.

(b) Δh.

Figure 5.27: Cycle performance as a function of the outlet air cooler temperatures - Case 2

point, the outlet temperature of the first cooler is maintained at 25 °C, while the second cooler is eliminated, for which the temperature at the third mechanical compressor inlet reaches 125 °C, as seen in Figure 5.26.

5.6 Performance comparison

Table 5.5 helps to compare both membrane-based cases regarding net power production and membrane operation parameters. Firstly, a remarkable difference in the effective temperature of membrane operation can be noticed. The effective operating temperature range of Case 2 is 600 to 700 °C for the studied points, even when the air temperature at the feed side could reach 825 °C as in Case 1. Specifically, the optimum point found for Case 2 operates at an effective membrane temperature of 635 °C. The latter is due to the relatively low temperature of the recycled gases (480 °C) that sweep the permeate side to reduce the oxygen partial pressure. These sweeping gases increase the oxygen partial pressure ratio and diminish the membrane's temperature. For instance, Case 1's optimum temperature is 825ºC. This temperature difference generates two main differences: First, a difference in the membrane area size, which is ten times larger for Case 2, is found. Second, different trends concerning air mass flow and power requirements are obtained. Case 1 has higher temperature values at the membrane, for which the air mass flow variation across the studied points is lower than the Case 2 air mass flow. However, there is a steep growth in air mass flow at low temperatures and pressures due to a considerable affect of membrane permeability. Considering the above, heat at HE-3 and electric power consumption depends on the air mass flow or the temperature variation and compression ratio, depending on the element. Case 2 operating points behave different. Due to the low effective temperatures of the membrane, there is always a high dependency on the air mass flow for oxygen production, which directly affects thermal and electric power consumption.

Nonetheless, the performance of the whole cycle is better for Case 2 due to the removal of the compression stages in the oxygen line, for which the electric power consumption is diminished, and the additional enthalpy flow in SH1 from the O_2/RFG stream. However, this case is currently limited from a technological perspective. According to Zhu and Yang [8], the fabrication of membranes that operate at low temperatures (350 to 700 °C) is still in development. On the other hand, the size of this membrane can be unpractical in terms of cost and maintenance, considering that sweeping with CO_2 is another issue still being studied [8]. Case 1 generates less net power than Case 2, but its membrane operates at reasonable conditions regarding the state-of-the-art with a size that can be found in other studies in the specialized literature.

That said, it could be stated that there is a promising improvement for the

Table 5.5: Comparison of membrane-based oxygen production cycles variables

	Case 1	Case 1 optimized refrigeration	Case 2	Case 2 optimized refrigeration
Net power [MW]	402.40	404.67	414.17	417.24
Thermal efficiency [%]	53.78	54.08	55.35	55.76
$\dot{m}_{\text{air}}$ [kg s^{-1}]	306.57	306.57	335.8	339.70
$P_{\text{air,feed}}$ [MPa]	0.4	0.4	2.0	2.0
$T_{\text{air,feed}}$ [°C]	825	825	775	775
T_{memb} [°C]	825	825	635	639
A [m^2]	170,000	170,000	1,600,000	1,600,000

membrane-based cases compared to the baseline case due to the energy integration of the Graz Cycle and the oxygen production cycle. Table 5.7 compares the main variables of the oxygen production cycles for the studied cases and the baseline case scenario. Despite an increment in the specific work required for oxygen production in Case 1, the performance is still better than for the baseline case. On the other hand, both the specific work for oxygen production and the performance of the cycle are better for Case 2 compared with the baseline case.

For all the membrane-based cases, the oxygen temperature at the inlet of the combustion chamber increases, adding enthalpy flow from the produced oxygen stream compared with the baseline case, which improves the combustion process. The effect of an improvement in combustion is analyzed by considering the mass and balance of the compared cases, shown in Table 5.8, Table 5.9, and Table 5.10 .

Compared with the baseline case, the steam mass flow driven through HPT is reduced in Case 1. The HTT outlet temperature is deceased due to the presence of HE-3, and the inlet conditions at HPT (17 MPa and 599 °C) are constant for all the studied cases. In this sense, the steam mass flow must be diminished to maintain these conditions, affecting the HPT power production.

On the other hand, considering a reduced thermal buffering effect from the steam and a higher inlet temperature of the oxygen, the RFG must be increased

Table 5.6: Oxygen production comparison between cases

	Case 1	Case 1 optimized refrigeration	Case 2	Case 2 optimized refrigeration	Baseline case
$\dot{Q}_{\mathrm{HE-3}}$ [MW]	43.42	41.21	61.75	61.93	***
$\dot{W}_{\mathrm{elec}}$ [MW]	40.93	44.01	47.90	48.60	***
Δh [MW]	***	***	-69.56	-76.20	***
$\dot{m}_{\mathrm{O_2}}$ [$\mathrm{kg\,s^{-1}}$]	60.37	60.37	60.49	60.51	62.50
O_2 purity [%]	100	100	100	100	96.65
O_2 spec. energy [$\mathrm{kJ\,kg^{-1}}$]	1,397	1,412	663	567	1,049
O_2 temp. at inlet CC [°C]	414	599	599	599	150

Table 5.7: Oxygen production comparison between cases

	Membrane 4-end	Baseline case
$\dot{Q}_{\mathrm{HE-3}}$ [MW]	61.93	***
$\dot{W}_{\mathrm{elec}}$ [MW]	48.60	***
Δh [MW]	-76.20	***
$\dot{m}_{\mathrm{O_2}}$ [$\mathrm{kg\,s^{-1}}$]	60.51	62.50
O_2 purity [%]	100	96.65
O_2 spec. energy [$\mathrm{kJ\,kg^{-1}}$]	567	1,049
O_2 temp. at inlet CC [°C]	599	150

Table 5.8: Mass balance of Graz cycle

	Case 1	Case 1 optimized cooling	Case 2	Case 2 optimized cooling	Base-line case
Captured CO_2 stream [$kg\,s^{-1}$]	43.80	43.80	43.92	43.94	45.94
CO_2 purity [%]	97.28	97.01	97.28	96.97	92.74
H_2O stream [$kg\,s^{-1}$]	100.12	102.63	121.02	124.18	108.2
H_2O stream HTT cooling [$kg\,s^{-1}$]	27.29	27.90	26.34	26.46	30.24
H_2O stream CC inlet [$kg\,s^{-1}$]	72.84	74.74	94.68	97.71	77.96
Recycled stream [$kg\,s^{-1}$]	187.40	190.50	218.70	214.01	174.90
% H_2O	75.25	75.60	56.93	56.06	75.91
% CO_2	24.13	23.79	15.60	15.22	22.39
% N_2	0.13	0.12	0.08	0.08	0.40
% O_2	0.49	0.48	28.02	28.64	0.48
CC outlet stream [$kg\,s^{-1}$]	336.70	341.70	329.47	327.81	331.45
Stream HTT1 outlet [$kg\,s^{-1}$]	354.49	359.92	346.31	344.64	351.25
Stream HTT3 outlet [$kg\,s^{-1}$]	363.99	369.60	355.81	354.28	361.69

to regulate the outlet temperature of the combustion chamber. For this reason, the power consumption of C1/C2 increases. Additionally, the power output of HTT-1 and HTT-2 increases due to an increment in the mass flow that is driven through them, while the HTT-3 power production is naturally decreased due to the enthalpy loss in HE-3.

The intercooling optimizations in Case 1 led to a decrease in the HE-3 heat exchanged due to the first optimization process, leading to improved power production at HTT-3. In this sense, the steam mass flow through HPT also increases due to a higher HTT-3 outlet temperature that improves steam heating, improving the HPT performance. Additionally, the second intercooling optimization increases the oxygen temperature at the combustion chamber inlet even more, reaching 600 °C as it is the limit for the outlet temperature of the

electric compressors. Nonetheless, this increases the RFG stream to reduce the combustion temperature, slightly incrementing the C1/C2 power consumption. In addition, as mentioned earlier, the electric power in the oxygen production cycle increments due to the compression process being performed at a higher temperature.

Furthermore, the HPT steam mass flow increases in Case 2 due to the additional heating at SH1 from the O_2/RFG stream, improving HPT performance. This additional heating compensates for the enthalpy loss at the HTT-3 outlet due to HE-3, also presented in Case 1. Simultaneously, the RFG stream required to control the combustion chamber temperature is diminished, reducing the power required in C1. Nonetheless, C2 power increases because it contains the oxygen produced, which increases the mass flow through this compressor, affecting its consumption. Similarly to Case 1, HTT-1 and HTT-2 generate more power due to increased mass flow, and HTT-3 power is decreased due to HE-3 presence.

The intercooling optimization in Case 2 leads to an increase in Δh, for which the available energy in SH1 increments, improving the steam mass flow even further and consequently the HPT power. Additionally, a reduction in RFG decreases the power output of HTT-1, which drives C1 and C2, according to Wimmer and Sanz [133], leaving more enthalpy for HTT-2. Finally, as for Case 1, the power consumption of the electric air compressor in the oxygen production cycle increases due to the compression process being performed at a higher temperature.

That said, the primary performance improvement for the membrane-based cases is found in the power consumption for oxygen production. For oxygen production at 1.6 MPa, the power consumption is higher in the baseline case than in the membrane-based cases, as seen in Table 5.9. On the other hand, the oxygen compression to reach combustion chamber conditions requires more power for the membrane cases because it is performed at a higher temperature.

Simultaneously, another performance improvement factor is eliminating the oxygen compression stage towards the CC in Case 2. In this case, the oxygen pressurization to combustion chamber conditions is performed in C2 with the RFG stream.

Three studies using the same MIEC membranes are considered to validate the obtained results in the membrane-based cases, whose main results are shown in Table 5.11. Different oxygen production levels are obtained in these studies, but specific membrane areas (in $m^2\,kW^{-1}$) are in the same order as found in the present chapter.

As final considerations for applying these types of facilities, current developments for the availability of this technology are still being performed. Air Products is an organization that stands out as a leader in the research of membrane-based installations for oxygen production. Currently, as Zhu

Table 5.9: Power balance for the different studied cases - Part 1

	Case 1	Case 1 optimized cooling	Case 2	Case 2 optimized cooling	Base-line case
$\dot{Q}_{\text{in}}$ **[MW]**	748.22	748.22	748.22	748.22	748.06
$\sum P_{\text{T}}$ **[MW]**	697.07	709.74	693.36	692.68	704.70
HTT-1 [MW]	194.17	197.80	183.67	179.04	181.72
HTT-2 [MW]	249.45	253.20	256.97	259.93	251.69
HTT-3 [MW]	158.17	161.78	154.11	154.12	171.55
HPT-1 [MW]	32.54	33.52	37.63	38.53	37.67
HPT-2 [MW]	2.12	2.17	1.93	1.95	2.35
LPT [MW]	60.63	61.27	59.05	59.10	59.69
RFG compression power [MW]	194.17	197.80	183.67	179.04	181.72
C1 [MW]	116.72	118.95	102.85	100.08	109.56
C2 [MW]	77.45	78.85	80.82	78.97	72.16
Net turbomachinery power [MW]	493.87	502.76	500.54	504.41	513.59

and Yang [8] state, Air Products was developing a project in 2016 whose final phase looks for the operation of an oxygen production cycle that delivers 2,000 $\text{t}\,\text{d}^{-1}$(approximately 23 $\text{kg}\,\text{s}^{-1}$). Another required improvement is the mechanical properties that allow high-pressure ratios during membrane operation and larger packing density of the membranes, allowing larger areas per unit volume, which is required for practical applications, according to Bai et al. [101].

Another insight that can be expressed is the technical risk due to the reactivity of high-purity oxygen streams, especially for Case 1. In Case 2, the risk is relieved because oxygen compression is performed in C2, mixed with the RFG. Meanwhile, Case 1 operates with high-purity oxygen in its line, requiring the implementation of special compressors, as they have to be oil-free and completely sealed [136]. On the other hand, as the ignition temperature of steel is about 1,150 °C, temperatures below 1,000 °C are acceptable under these working conditions to avoid metal firing.

Table 5.10: Power balance for the different studied cases - Part 2

	Case 1	Case 1 optimized cooling	Case 2	Case 2 optimized cooling	Base-line case
CO_2 compression [MW]	33.14	33.13	33.09	33.08	35.11
O_2 compression [MW]	12.51	16.00	0.00	0.00	7.82
O_2 prod. consumption [MW]	40.93	44.01	47.90	48.60	65.60
Water pumps [MW]	2.28	2.34	2.76	2.83	2.47
Auxiliary losses [MW]	2.62	2.62	2.62	2.62	2.62
Net power [MW]	402.39	404.67	414.17	417.28	400.00
Thermal efficiency [%]	53.80	54.08	55.35	55.76	53.47

	Specific membrane area ($m^2 kW^{-1}$)	O_2 production ($kg s^{-1}$)
Portillo et al.[11]	0.69	202.0
Chen et al.[135]	1.38	15.2
Castillo [9]	0.80	96.6
Case 1	0.42	60.4
Case 2	3.83	60.5

Table 5.11: Specific membrane area comparison with literature studies

5.7 Summary

This chapter thermodynamically assessed two membrane-based cases working with the Graz Cycle, comparing their performance with the baseline case configuration that works with cryogenic air separation. Initially, the membrane operation conditions and the cooling stages among their respective compressors were optimized.

An optimum operating point was found for Case 1, at a feed pressure of 0.4 MPa, a permeate pressure of 0.02 MPa, and a feed temperature of 825 °C. At these conditions, and considering both intercooling optimizations, a net power of 404.67 MW was obtained, producing a thermal efficiency of 54.08 %. In this case, the whole system delivers 4.67 MW more with 0.61 % points of higher efficiency when compared with the baseline case.

On the other hand, Case 2 exhibits a better performance. Its optimum point is at a feed pressure of 2 MPa, and a feed temperature of 775 °C, meaning an effective membrane operation temperature of 635 °C. At these conditions, and considering the intercooling optimization, a net power of 417.24 MW was obtained, producing a thermal efficiency of 55.76 %. In this case, the system delivers 17.24 MW more with 2.30 % points of higher efficiency when compared with the baseline case.

Comparing both cases, Case 1 seems more feasible due to its membrane size and working conditions than Case 2. Creating reliable membranes operating at medium and low temperatures is the main technological barrier for Case 2, as well as the presence of CO_2 in the sweeping gases, which can degrade the membrane operation over time. Additional care must be given to the high-purity oxygen compressors in Case 1, as they reach considerable temperatures with high-purity oxygen, which can be threatening due to the high reactivity of the stream.

When the baseline case is considered for comparison, the power reduction at HTT-3 due to the upstream location of HE-3 is the dominant cause that reduces the total power output from the turbines in the membrane-based cases. Nonetheless, the power consumption of oxygen production in the baseline case surpasses the membrane-based cases, which diminishes the net power output of the baseline case, leading to a better performance for the membrane-based cases.

That said, oxygen production using MIEC membranes seems to be a promising alternative that can be energetically integrated with oxycombustion power plants, as long as technical issues are correctly addressed, such as membrane limitations and high-purity oxygen stream through pipelines and turbomachines.

Moreover, the membrane-based cases performance can be improved with a heat source at a higher temperature, as it was developed in Chapter 4. Addi-

tionally, using a stream to drive oxygen production without affecting the power production in the primary cycle can benefit the whole system's performance, as exhaust gas energy is used.

Additionally, when a four-end membrane is implemented, the sweeping gases could be at a higher temperature and lower pressure, improving, even more, the performance without requiring an excessive increase in the membrane area. Finally, the behavior of coupling a membrane-based cycle with a power production cycle has been assessed at a single load condition. The power production cycle can be operated at different load conditions, which can give more information about the coupling of these cycles.

These final insights will be further explained in chapter 6

5.8 References

[8] X. Zhu and W. Yang. "Introduction to Mixed Ionic–Electronic Conducting Membranes". In: *Green Chemistry and Sustainable Technology*. Springer Berlin Heidelberg, Nov. 2016, pp. 1–10. DOI: 10.1007/978-3-662-53534-9_1 (cit. on pp. 2, 35, 38, 39, 112, 135, 140).

[9] R. Castillo. "Thermodynamic analysis of a hard coal oxyfuel power plant with high temperature three-end membrane for air separation". In: *Applied Energy* 88.5 (May 2011), pp. 1480–1493. DOI: 10.1016/j.apenergy.2010.10.044 (cit. on pp. 2, 39, 141).

[11] E. Portillo, L. M. G. Fernández, F. Vega, B. Alonso-Fariñas, and B. Navarrete. "Oxygen transport membrane unit applied to oxy-combustion coal power plants: A thermodynamic assessment". In: *Journal of Environmental Chemical Engineering* 9.4 (Aug. 2021), p. 105266. DOI: 10.1016/j.jece.2021.105266 (cit. on pp. 2, 38, 39, 141).

[101] W. Bai, J. Feng, C. Luo, P. Zhang, H. Wang, Y. Yang, Y. Zhao, and H. Fan. "A comprehensive review on oxygen transport membranes: Development history, current status, and future directions". In: *International Journal of Hydrogen Energy* 46.73 (Oct. 2021), pp. 36257–36290. DOI: 10.1016/j.ijhydene.2021.08.177 (cit. on pp. 39, 140).

[119] W. Sanz, H. Jericha, F. Luckel, E. Göttlich, and F. Heitmeir. "A Further Step Towards a Graz Cycle Power Plant for CO2 Capture". In: *Volume 5: Turbo Expo 2005*. ASMEDC, Jan. 2005. DOI: 10.1115/gt2005-68456 (cit. on pp. 65, 104, 107).

[127] W. Sanz, H. Jericha, M. Moser, and F. Heitmeir. "Thermodynamic and Economic Investigation of an Improved Graz Cycle Power Plant for CO2 Capture". In: *Journal of Engineering for Gas Turbines and Power* 127.4 (Sept. 2005), pp. 765–772. DOI: 10.1115/1.1850944 (cit. on p. 104).

[128] H. Jericha, W. Sanz, and E. Go¨ttlich. "Design Concept for Large Output Graz Cycle Gas Turbines". In: *Volume 4: Cycle Innovations Electric Power Industrial and Cogeneration Manufacturing Materials and Metallurgy*. ASMEDC, Jan. 2006. DOI: 10.1115/gt2006-90032 (cit. on pp. 104, 105).

[129] H. Jericha, W. Sanz, E. Go¨ttlich, and F. Neumayer. "Design Details of a 600 MW Graz Cycle Thermal Power Plant for CO2 Capture". In: *Volume 2: Controls, Diagnostics and Instrumentation Cycle Innovations Electric Power*. ASMEDC, Jan. 2008. DOI: 10.1115/gt2008-50515 (cit. on p. 104).

[130] W. Sanz, M. Mayr, and H. Jericha. “Thermodynamic and Economic Evaluation of an IGCC Plant Based on the Graz Cycle for CO2 Capture”. In: *Volume 3: Controls, Diagnostics and Instrumentation Cycle Innovations Marine*. ASMEDC, Oct. 2010. DOI: 10.1115/gt2010-22189 (cit. on p. 104).

[131] W. Sanz, C.-W. Hustad, and H. Jericha. “First Generation Graz Cycle Power Plant for Near-Term Deployment”. In: *Volume 4: Cycle Innovations Fans and Blowers Industrial and Cogeneration Manufacturing Materials and Metallurgy Marine Oil and Gas Applications*. ASMEDC, Jan. 2011. DOI: 10.1115/gt2011-45135 (cit. on p. 104).

[132] W. Sanz, M. Braun, H. Jericha, and M. F. Platzer. “Adapting the Zero-Emission Graz Cycle for Hydrogen Combustion and Investigation of Its Part Load Behaviour”. In: *Volume 3: Coal, Biomass and Alternative Fuels Cycle Innovations Electric Power Industrial and Cogeneration Organic Rankine Cycle Power Systems*. American Society of Mechanical Engineers, June 2016. DOI: 10.1115/gt2016-57988 (cit. on pp. 104, 105).

[133] K. Wimmer and W. Sanz. “Optimization and comparison of the two promising oxy-combustion cycles NET Power cycle and Graz Cycle”. In: *International Journal of Greenhouse Gas Control* 99 (Aug. 2020), p. 103055. DOI: 10.1016/j.ijggc.2020.103055 (cit. on pp. 104–107, 111, 112, 139).

[134] B. Mitterrutzner, W. Sanz, and L. O. Nord. “A part-load analysis and control strategies for the Graz Cycle”. In: *International Journal of Greenhouse Gas Control* 113 (Jan. 2022), p. 103521. DOI: 10.1016/j.ijggc.2021.103521 (cit. on pp. 104, 105).

[135] W. Chen, L. van der Ham, A. Nijmeijer, and L. Winnubst. “Membrane-integrated oxy-fuel combustion of coal: Process design and simulation”. In: *Journal of Membrane Science* 492 (Oct. 2015), pp. 461–470. DOI: 10.1016/j.memsci.2015.05.062 (cit. on p. 141).

[136] BailianCompressors. *What is an oxygen compressor?* May 2023. URL: https://www.oxygen-compressors.com/oxygen-compressor.html (cit. on p. 140).

CHAPTER 6

Oxygen production using a MIEC membrane for spark-ignition engines operation.

Contents

Figures

Tables

6.1 Introduction

THIS chapter evaluates the concept of coupling an oxygen production cycle that uses a MIEC membrane within a spark-ignition engine operation. The studies performed in this chapter researches the feasibility of operating a reciprocating engine that uses a conventional fuel (in this case, gasoline) but with near-zero emissions in its exhaust gases. The proposed design is expected to have a considerable advantage when compared with other alternatives, such as battery-electric powerplants, in terms of the overall specific energy of the system.

The simulations performed in the present section of the thesis are mainly based on the obtained results in Serrano et al. [12, 13], which lay the foundations to set limits in terms of the implemented oxygen concentrations, engine compression ratios, and spark-timings in the cylinders. In addition to this, the work performed by Serrano et al. [137] set the basis for the considered engine baseline during this chapter.

Considering the latter, the pursued objectives in this chapter are:

- Examine the influence of the oxygen concentration and the engine compression ratio on the performance of a spark-ignition engine with a coupled oxygen production cycle working under oxycombustion, comparing its performance with the conventional operation.
- Assess the behavior of a spark-ignition engine with a coupled oxygen production cycle working under oxycombustion at full-load operation at a wide range of speeds, comparing its performance with the conventional operation.
- Determine a spark-ignition engine's energy and operative limits with a coupled oxygen production cycle working under oxycombustion in part-load conditions.
- Examine the operation of a spark-ignition engine with a coupled oxygen production cycle working under oxycombustion at different altitude conditions.

6.2 System description

The initial design of the studied system is based on the patent by Arnau et al. [138]. Considering that configuration, an iterative process has been performed to improve the usage of exhaust gas energy and the system's performance. The resulting standard layout studied in this chapter is shown in Figure 6.1.

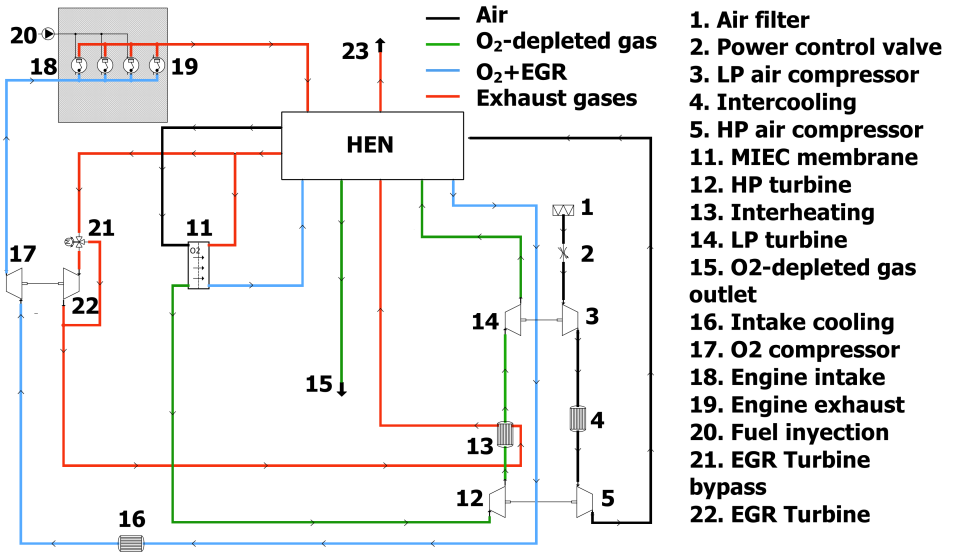

Figure 6.1: Layout of spark ignition engine working by oxy-fuel combustion means and in situ oxygen production.

Two different cycles are coupled for power production under oxycombustion. Firstly, an oxygen production cycle is implemented, which initially drives atmospheric air through two intercooled compression stages (3 and 5 in Figure 6.1). A valve (2) controls the amount of air used for oxygen production, thus, regulating the power production. Then, a heat exchanger network (HEN) is implemented to heat the air by recovering energy from different streams within the system. The configuration of this HEN is depicted in Figure 6.2, which is based on the setup used in Serrano et al. [15]. Initially, the air mass flow is branched into two streams, which are heated in 6 and 7, and then, the streams are rejoined to pass through three additional heating steps (8,9,10). This version of an oxygen production cycle shares the same working principle compared with the configurations found in Chapter 4 and Chapter 5, using an energy source that varies according to the operation point of the engine, reducing the number of air-driven turbochargers by two due to a reduction in the space availability and less requirement in terms of oxygen production.

After being driven through the mentioned elements, the air is at high temperature and pressure conditions required to operate MIEC membranes. In the membrane (11), the oxygen is separated from the primary air stream, leaving an oxygen-depleted mass flow composed principally of nitrogen with a low percentage of oxygen. This oxygen-depleted stream is still at high temperature and

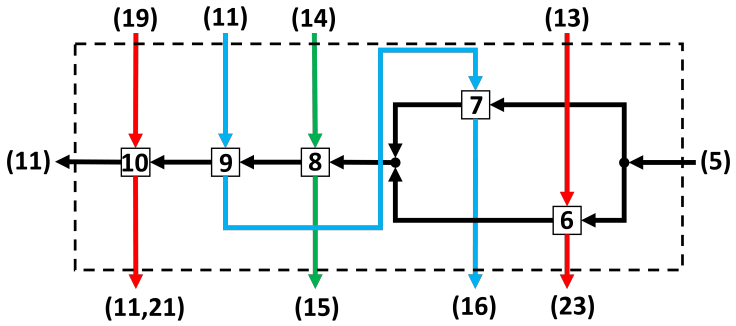

Figure 6.2: Heat exchanger network adapted from the work by Serrano et al. [15].

pressure, which is implemented to drive the compression stages by using two turbines (12 and 14). This stream is heated between the expansion stages in a heat exchanger (13) using exhaust gases and then used to heat the air (8) after passing the turbines.

Secondly, there is a power production cycle that is a spark-ignition engine. Its exhaust gases are firstly used to heat the air (10) in a high-temperature heat exchanger. Then, the exhaust stream is branched into two streams. The amount of exhaust gases in each branch is determined according to the turbine opening (22), which is implemented to control the sweep gases through the permeate side of the membrane, which finally stipulates the oxygen concentration at the engine intake. The more the turbine is opened, the more gases go through the turbine, and less sweeping gases are driven through the membrane, increasing the oxygen concentration. The outlet gases from this EGR turbine controller are used in 13 to reheat the stream between the air-driven turbines (12 and 14) and to increase the air temperature (6).

The other branch of exhaust gases is then used to sweep the membrane, reducing the oxygen partial pressure in the permeate side while maintaining a high temperature (differently from Case 2 of Chapter 5). Consequently, a high-temperature stream of carbon dioxide, steam, and oxygen (O_2/EGR) is obtained. The stream is directed toward the engine intake, after its thermal energy is used to heat air in 9 and 7, and then passed through a cooler to reach a suitable temperature for the engine operation. A temperature of 85 °C is imposed at the engine intake to ensure no liquid water is present. Before the engine intake, the O_2/EGR mixture goes through a compressor (17) that takes advantage of the energy that produces the exhaust gas turbine (22).

Finally, the O_2/EGR stream comes into the engine for power production, completing the cycle of the power production section of the system.

6.3 Engine specifications and benchmarking

The specifications of the studied engine are enlisted in Table 6.1. The results of the conventional operation mode to compare with the oxycombustion regime are obtained from the study performed by Serrano et al. [137], where a methodology to analyze the impact of different variable geometry turbines (VGT) on the engine performance operating at full-load is presented, obtaining torque and brake specific fuel consumption (BSFC) data.

Type	4-cylinder 4-stroke spark ignition
Valves per cylinder	4
Bore [mm]	72.2
Stroke [mm]	81.35
Original compression ratio [-]	9.6
Displacement [cm^3]	1,332
Connecting rod length [mm]	128.128

Table 6.1: Specifications of the studied engine.

These data are considered as the baseline for comparison in the present chapter. The engine operating under oxycombustion with an oxygen production cycle aims for the same power value at each engine speed studied, setting the reference full-load torque of the oxycombustion engine.

The characteristics of the considered fuel in both oxycombustion and conventional modes are shown in Table 6.2.

Type	Gasoline
Formula	$CH_{1.992}O_{0.016}$
Heat value $MJ\,kg^{-1}$	42.399
Density $kg\,m^{-3}$	730.3

Table 6.2: Fuel characteristics used in the study.

6.4 Considerations, variables, and indicators for performance evaluation

The simulations were performed using the in-house software VEMOD, as described in chapter 3. The following particular simplifications are considered:

- For air heating, the maximum heat transfer is required to meet the optimum conditions for the membrane operation. In this sense, a constant effectiveness of 95 % is assumed for all the heat exchangers, following the results obtained by Komminos and Rodgakis [139], where heat exchangers under similar conditions are implemented, resulting in effectiveness around the proposed value.

- The outlet temperature of the intercooler between the air-driven compressors is imposed at 25 °C.

- The estimation of mechanical losses considers the energy consumption of auxiliary elements.

- The assumed air composition in mass fraction is 77 %N_2 and 23 % O_2.

The global turbocharger efficiency, η_{total}, is optimized for the oxygen production cycle by changing the VGT position. The objective function to be maximized is stated in Equation 6.1:

$$\eta_{\text{total}} = \eta_{\text{LP turb}} \cdot \eta_{\text{LP comp}} \cdot \eta_{\text{HP turb}} \cdot \eta_{\text{HP comp}} \tag{6.1}$$

Where $\eta_{\text{LP turb}}$ is the efficiency of the low-pressure turbine, $\eta_{\text{LP comp}}$ is the efficiency of the low-pressure compressor, $\eta_{\text{HP turb}}$ is the efficiency of the high-pressure turbine, and $\eta_{\text{HP comp}}$ corresponds to the efficiency of the high-pressure compressor.

For each calculated point, the engine's performance is optimized, considering the minimization of the BSFC. In this sense, the spark timing is varied, considering a maximum in-cylinder pressure of 15 MPa and a maximum in-cylinder temperature of 3,000 K. This restriction is set due to the thermomechanical limitations of the experimental facilities where the studies used to determine the oxycombustion parameters were performed. The methodology to determine the input parameters for the combustion behavior under oxycombustion was extensively described in Chapter 3.

As mentioned in the system description, the O_2 concentration at the engine intake is controlled by changing the VGT position of the turbine in the exhaust line (element 22 in Figure 6.1). The VGT position variation changes the flow-passing area for the driven stream, controlling the amount of EGR gases driven through the turbine, thus, changing the flow of the sweeping gases at the permeate side of the membrane.

The engine power output for each operating point is controlled with a throttle valve (2 at Figure 6.1), located before the low-pressure compressor inlet in the air line. Varying the air stream that goes into the system, the feed conditions of the membrane as air mass flow, pressure and temperature are changed. This

Turbine	
Wheel diameter (mm)	37.5
Max. reduced mass flow	$12.6\,\mathrm{kg\,s^{-1}\,K^{0.5}\,MPa^{-1}}$
Max. reduced speed	$112.2\,\mathrm{Hz\,K^{-0.5}}$
Compressor	
Wheel diameter (mm)	40
Max. corrected mass flow	0.14
Max. corrected speed (krpm)	229
Shaft diameter (mm)	6

Table 6.3: Specifications of reference turbocharger

modifies the oxygen separated from the air. In this sense, as the oxycombustion process is always performed at stoichiometric conditions, this strategy ensures the power output at each studied point. This throttling valve does not affect the pumping losses of the engine because it is not directly located at the engine intake.

Considering the above, it must be clarified that stoichiometric combustion is pursued to maximize the exhaust temperature for a particular oxygen flow, enhancing energy recovery to drive the air separation process. Additionally, there is no oxygen in the exhaust gases, facilitating carbon capture in case this process is installed.

The characteristics of the selected turbocharger for scaling in this chapter are shown in Table 6.3. As explained in Chapter 3, a scale factor is used for the turbocharger according to its inlet conditions, ensuring the operation at a zone of high efficiency. In this case, the full-load operation is considered to select the scaling values, making the operation suitable in the studied speed range.

Firstly, different oxygen concentrations and compression ratios are studied, examining their effect on the system performance. A medium engine speed is used for this part of the study, comparing the engine performance for all the studied cases with the conventional operation. Considering the combustion ranges stated in Chapter 3, the oxygen concentrations selected are 28 %, 30 %, and 32 %, evaluating low, medium, and high oxygen concentrations. Additionally, the compression ratio range is varied between 9.6 - 20. The original compression ratio is 9.6, the initial step to consider.

On the other hand, following the CFD methodology explained by Serrano et al. [12, 13] has demonstrated that compression ratios higher than 20 lead to the conditions for knocking appearance, setting this value as an upper limit in this study. Then, the oxygen concentration with better performance is chosen,

using the original (9.6) and the highest (20) compression ratios to assess the system behavior at a wide engine speed range at the reference full load. The performance of the oxycombustion engine is compared with the conventional operation mode.

Then, the part-load operation of the engine is studied to establish limits in terms of energy available for oxygen production and operative limits due to vacuum pressure at the engine intake, which can generate atmospheric air backflow, leading to the presence of nitrogen in the combustion process.

In this sense, the used indicators for performance evaluation at part-load are shown in the following expressions. Firstly, in Equation 6.2, $\dot{H}_{\text{miec}}$ is the energy delivered to the air to achieve the feed conditions for a particular operation point (engine speed and load). In this sense, $\dot{H}_{\text{air,feed}}$ corresponds to the air enthalpy flow at the feed inlet, while $\dot{H}_{\text{air,in}}$ is the air enthalpy flow at the atmospheric conditions (0.1 MPa, 25 °C). $\dot{Q}_{\text{C-1}}$ is the dissipated heat of the intercooler between the air-driven compressors.

$$\dot{H}_{\text{miec}} = \dot{H}_{\text{air,feed}} - \dot{H}_{\text{air,in}} + \dot{Q}_{\text{C-1}} \tag{6.2}$$

Based on this parameter, two indicators evaluate energy usage for oxygen production. First, I_1, as seen in Equation 6.3, establishes the ratio of energy usage for oxygen production regarding the heat release in the cylinders (HR in Equation 6.3).

$$I_1 = \frac{\dot{H}_{miec}}{\text{HR}} \tag{6.3}$$

On the other hand, I_2 sets the same ratio but regarding the available energy flow at the exhaust manifold, which is obtained after subtracting from HR, the brake power production ($\dot{W}$), and the dissipated heat in the cylinders ($\dot{Q}_{cyl}$) and the exhaust pipes ($\dot{Q}_{\text{exh}}$).

$$I_2 = \frac{\dot{H}_{miec}}{HR - \dot{W} - \dot{Q}_{cyl} - \dot{Q}_{exh}} \tag{6.4}$$

Moreover, two additional parameters, based on I_1 and I_2, are considered regarding the oxygen production per engine cycle and the total engine displacement. In this sense, I_1^* and I_2^* represent the energy required per gram of oxygen produced for a unit volume of the engine regarding the energy released by the fuel in the cylinders (I_1^*) or the available energy in the exhaust gases (I_2^*). Equation 6.5 and Equation 6.6 show the used expressions to determine the mentioned indicators.

$$I_1^* = \frac{\dot{m}^*_{\text{O}_2}}{I_1 \cdot V_t} \tag{6.5}$$

$$I_2^* = \frac{\dot{m}_{O_2}^*}{I_2 \cdot V_t} \tag{6.6}$$

Where $\dot{m}_{O_2}^*$ represents the oxygen production in a cycle, determined as expressed in Equation 6.7, and V_t is the total engine displacement.

$$\dot{m}_{O_2}^* \text{ [g/cycle]} = \frac{\dot{m}_{O_2}[\text{kg s}^{-1}] \cdot 2 \cdot 60 \cdot 1000}{\dot{\omega}_{\text{eng}}[\text{rpm}]}$$

6.5 Component selection

6.5.1 Turbocharger scaling

The implemented scaling factors in the current layout are shown in Table 6.4. It can be seen that the low-pressure turbocharger has a scaling value that is 2.25 times higher than the high-pressure one. The low-pressure turbocharger handles lower densities than the high-pressure one, requiring a higher flow area to drive the needed air stream. On the other hand, the EGR turbine must have a restrictive flow area to ensure the control of EGR mass flow driven through the permeate side of the membrane. However, lower scale values cannot be considered, as these values are not commercially available.

	LP Turbo	HP Turbo	O_2/EGR Turbo
Scaling factor	1.8	0.8	0.8
Turbocompressor eff. [%]	45.2-53.6	51.0-53.1	0.1-35.0
Turbine opening [%]	60	60	8.7-49.5
Turbo speed [krpm]	83-166	193-257	2-163

Table 6.4: Operation data of the turbochargers during the engine operation

Efficiencies in low and high-pressure turbochargers higher than 60 % are achieved in both turbines and compressors, considering correct operation over a wide range of engine speeds running at full load. Nonetheless, the O_2/EGR turbocharger exhibits low global efficiencies due to the low VGT opening values that ensure the demanded oxygen concentration, which leads to a significant unbalance between the compressor and turbine mass flow, generating a low-efficiency turbomachine. Nonetheless, the turbine is useful for controlling the EGR rate, and part of the exhaust energy is still recovered.

6.6 Full load operation

The oxygen concentration and compression ratio effect is initially studied in the oxycombustion configuration, compared with the conventional operation. A medium speed was chosen to perform this study (3,000 rpm) at a reference full-load achieved running the engine conventionally.

The conventional mode has two different strategies for operation. Firstly, the air-fuel equivalence ratio is reduced to decrease the temperature at the exhaust manifold (CS1). On the other hand, stoichiometric combustion is maintained during operation (CS2), for which the VGT opening increases, reducing the compressor power, thus, the air mass flow and pressure, which finally leads to reduce the exhaust manifold temperature.

CS1 does not affect the engine's power production but increases fuel consumption and pollution. On the other hand, CS2 considerably reduces the engine's power output, but it does not affect fuel consumption. These strategies are implemented to ensure the turbocharger's integrity.

6.6.1 Compression ratio and oxygen mass fraction effect on performance

Engine

Regarding the engine performance, Table 6.5 shows the main engine parameters resulting from the engine operation at different oxygen concentrations and compression ratios, comparing these results with the conventional operation working with CS1 and CS2.

The maximum compression ratio can be achieved at a medium oxygen concentration (30 %), where the imposed superior limit of 20 is reached. Higher compression ratios lead to in-cylinder pressures greater than 15 MPa and increase knocking probability. In contrast, a high oxygen concentration (32 %) permits a maximum compression ratio of 15 before reaching the maximum in-cylinder pressure limit.

It can be noted that the engine compression ratio increment improves the fuel consumption of the engine, expected for a regular cycle in a spark-ignition engine. The higher reduction of fuel consumption is found at medium oxygen concentration (30 %), where a 12.5 % lower fuel consumption is achieved comparing the minimum and maximum compression ratios examined.

The maximum in-cylinder temperature reduces with higher compression ratios and increases as the oxygen concentration increments. Higher oxygen concentration leads to higher in-cylinder temperatures due to a higher reactivity during the combustion. On the other hand, the reduction in fuel consumption due to the increment in the engine compression ratio helps reduce the in-cylinder

	Power (kW)	BSFC (g/kWh)	IMEP (MPa)	$\dot{Q}_{\text{cyl}}$ (kW)	P_{max} (MPa)	T_{max} (°C)	λ
Low O_2 conc.							
CR 9.6	88.40	280.32	2.87	21.91	13.56	2,252	1.000
CR 12.5	88.40	261.62	2.87	21.41	14.88	2,199	1.000
CR 15.0	88.40	253.41	2.87	20.63	14.97	2,146	1.000
CR 18.0	88.40	248.36	2.87	20.07	15.06	2,102	1.000
Medium O_2 conc.							
CR 9.6	88.40	280.21	2.87	22.22	13.54	2,422	1.000
CR 12.5	88.40	261.46	2.87	21.93	14.94	2,378	1.000
CR 15.0	88.40	252.96	2.87	21.24	14.98	2,324	1.000
CR 18.0	88.40	247.28	2.87	20.74	15.02	2,274	1.000
CR 20.0	88.40	245.10	2.87	20.50	15.03	2,245	1.000
High oxygen conc.							
CR 9.6	88.40	283.41	2.85	21.65	12.23	2,517	1.000
CR 12.5	88.40	263.62	2.86	21.93	14.24	2,499	1.000
CR 15.0	88.40	254.01	2.87	21.87	15.08	2,460	1.000
CS1 (λ = 0.861)	88.40	292.94	2.81	17.16	9.56	2,293	0.861
CS2	75.99	248.03	2.44	16.89	8.56	2,390	1.000

Table 6.5: Engine operation at different oxygen concentrations and compression ratio - Medium speed

temperature. In this sense, the maximum in-cylinder temperature is found at a high oxygen concentration (32 %) and the minimum engine compression ratio (9.6), exhibiting a value of 2,517 °C, still far from the maximum allowed value (3,000 K, 2,700 °C approx.). Similar trends are found for the dissipated heat in the cylinders, considering similar explanations to justify the behavior.

Compared with the CS1 strategy, the oxycombustion cases had better fuel consumption while maintaining the same power output (88.40 kW). CS2 exhibits better fuel consumption if the oxycombustion runs with a lower engine

compression ratio than 18, reducing the power output by 14 %.

As expected, the maximum in-cylinder pressure is considerably higher for the oxycombustion mode when the engine compression ratio increases and when all the oxycombustion and conventional cases are compared at the original compression ratio (9.6).

On the other hand, Table 6.6 shows the main thermodynamic conditions at the manifolds. The pressure at both manifolds reduces with engine compression ratio and oxygen concentration increments. Similar behavior is found for the engine's pumping losses (PMEP). The exhaust temperature increases with the oxygen concentration increment, reducing with the engine compression ratio rise. The maximum exhaust temperature is found at high oxygen concentration (32 %) and the original engine compression ratio (9.6), where 1,170 °C is reached. Finally, a greater effective area at the O_2/EGR is required as the oxygen concentration at the intake is increases, as seen in Table 6.6.

It is seen that the oxycombustion cases display higher exhaust temperatures than conventional cases, and the specific heat capacity ratios (γ) are lower. On the other hand, the intake pressure is higher while the engine operates at conventional combustion.

These results can be mainly explained by considering the differences in properties between CO_2 and N_2, the primary bulk gases in oxycombustion and conventional cases, respectively. These differences affect the temperature and pressure evolution in the cylinder and the combustion properties. Table 6.7 shows the main properties of CO_2 and N_2 that affect the process.

The higher heat capacity of the CO_2 brings lower combustion temperatures. Table 6.5 shows that reducing the oxygen concentration at 28 % leads to lower in-cylinder temperatures than the conventional cases, considering that they operate with atmospheric air (23 % of oxygen concentration in mass). The lower thermal diffusivity and oxygen mass diffusivity of CO_2 produce slower heat release rates in the combustion process due to a slowing down in the chemical reactions, for which the laminar flame speed decreases when the bulk gas is CO_2. The combustion degradation when the bulk gas is changed from N_2 to CO_2 is presented in studies like those by Li et al. [140] and Ditaranto and Hals [141], where longer combustion processes and lower heat release peaks were found.

In addition to the latter, the specific heat capacity ratios at oxycombustion are lower than the conventional operation, as Mohammed et al. reported [75]. The specific heat capacities ratio differences for both operation types at the intake are shown in Table 6.6. In typical spark-ignition engines, this means a reduction in thermal efficiency.

Given the above, it can also be mentioned that even at high load conditions and advanced spark timings, knocking problems are not expected during the oxycombustion operation, according to Serrano et al. [12, 13]. This improves the

	P_{int} (MPa)	P_{exh} (MPa)	PMEP (MPa)	T_{exh} (°C)	γ_{int}	VGT-O_2/EGR opening (%)
Low O_2 conc.						
CR 9.6	0.230	0.247	-0.074	1,078	1.312	20.46
CR 12.5	0.216	0.231	-0.067	1,034	1.312	20.94
CR 15.0	0.210	0.224	-0.064	1,017	1.312	21.20
CR 18.0	0.206	0.220	-0.062	1,007	1.312	21.30
Medium O_2 conc.						
CR 9.6	0.213	0.229	-0.071	1,118	1.314	25.63
CR 12.5	0.201	0.214	-0.064	1,070	1.314	26.09
CR 15.0	0.195	0.208	-0.061	1,051	1.314	26.28
CR 18.0	0.191	0.204	-0.058	1,038	1.314	26.35
CR 20.0	0.190	0.202	-0.058	1,033	1.314	26.34
High O_2 conc.						
CR 9.6	0.202	0.215	-0.069	1,170	1.316	30.48
CR 12.5	0.189	0.202	-0.062	1,115	1.316	30.54
CR 15.0	0.183	0.195	-0.058	1,087	1.316	30.57
CS1 ($\lambda = 0.861$)	0.252	0.252	-0.042	870	1.400	***
CS2	0.216	0.247	-0.047	931	1.400	***

Table 6.6: Intake and exhaust manifolds conditions at different oxygen concentrations and engine compression ratio

	CO_2	N_2
Molecular weight [$\mathrm{g\,mol^{-1}}$]	44	28
Density [$\mathrm{kg\,m^{-3}}$]	0.536	0.341
Heat capacity [$\mathrm{kJ\,kg^{-1}\,K^{-1}}$]	1.234	1.167
Thermal diffusivity [$\mathrm{m^2\,s^{-1}}$]	1.1e-4	1.7e-4
Mass diffusivity of oxygen [$\mathrm{m^2\,s^{-1}}$]	9.8e-5	1.3e-4

Table 6.7: Comparison of properties between CO_2 and N_2 at 1,000 K, 0.1 MPa - Adapted from [140]

engine performance due to the possibility of combustion centering at high loads,

contrasting with the conventional operation.

Considering the latter, the main parameters that describe the combustion behavior for oxycombustion and conventional cases are shown in Table 6.8, displaying the start of combustion (SOC), combustion phasing (CA50), combustion duration (CA90-10), and spark-timing values for each studied case. The spark timing was not recorded during the experiments of conventional cases.

	Duration CA90-10 (°)	ST (°ATDC)	SOC (°ATDC)	CA50 (°ATDC)
Low O_2 conc.				
CR 9.6	26.42	−37.00	−18.13	1.66
CR 12.5	27.02	−35.00	−16.10	5.40
CR 15.0	27.91	−32.50	−13.98	9.60
CR 18.0	28.46	−30.00	−12.11	12.99
Medium O_2 conc.				
CR 9.6	21.49	−32.00	−19.94	3.38
CR 12.5	22.01	−30.00	−17.84	5.40
CR 15.0	22.69	−27.10	−15.16	9.70
CR 18.0	23.58	−24.10	−12.80	12.56
CR 20.0	24.49	−22.00	−11.44	14.09
High O_2 conc.				
CR 9.6	18.88	−20.00	−12.74	8.50
CR 12.5	19.05	−20.00	−12.78	8.54
CR 15.0	19.76	−18.00	−11.23	9.80
CS1 ($\lambda = 0.861$)	16.23	***	6.71	26.50
CS2	16.44	***	0.00	24.27

Table 6.8: Combustion data at different oxygen concentrations and engine compression ratio - 3.000 rpm

Higher compression ratios in oxycombustion promote higher in-cylinder pressures, for which the combustion must be delayed to avoid the maximum in-cylinder limit (15 MPa) to ensure engine integrity. In this sense, the combustion process is delayed, and the chemical reaction is less efficient, explaining the obtained SOC, CA50, and combustion durations.

It can be noticed that typical optimum values of the combustion phasing are found in the range of 6 to 10° after the top dead center (ATDC), but some oxycombustion points are more advanced than the presented span. Considering that the spark timing for each case was selected by optimizing the brake-specific

fuel consumption (BSFC), there is no considerable variation in fuel consumption in the vicinity of the chosen spark timing. Thus, the variation of spark timing in this zone does not generate significant changes in the engine performance.

The increase in the oxygen concentration promotes the combustion reactions, reducing the combustion duration. Nonetheless, this faster combustion has two significant effects: First, the combustion must be delayed as more oxygen concentration is implemented, avoiding combustion issues that affect the operation. Second, a more remarked increment in pressure and temperature is expected as the engine compression ratio increases. Considering the latter, this explains the reduced maximum engine compression ratio (15) at high oxygen concentration (32 %).

Comparing both operation modes, the conventional combustion is shorter, which is explained by the comparison of CO_2 and N_2 properties, which gives a higher reactivity when air is used rather than a O_2/EGR mixing. On the contrary, this higher reactivity facilitates combustion issues such as knocking, for which the combustion must be delayed to avoid operating problems, affecting the efficiency. However, CS2 has a reduction in knocking propensity due to the reduction in in-cylinder pressure and temperature, for which the combustion process can be performed earlier than CS1, improving the efficiency.

For clarity, the heat release rates of the studied cases are depicted in Figure 6.3, as a function of the crank angle degree (CAD). The delay in the spark advances due to the increase in the compression ratio produces a flattening in the heat release, leading to longer combustion. As expected, the higher peaks are observed at high oxygen concentrations, where a heat release rate of $0.15\,\mathrm{kJ}^{\circ-1}$ is reached.

Considering the latter, the trends of thermodynamic variables in the cylinders are shown. Firstly, the pressure-volume diagram is depicted in Figure 6.4 for all the studied cases. This figure shows how the spark timing limitation restricts the operation in the oxycombustion cases at high compression ratios, not to surpass the restriction of 15 MPa. Additionally, a reduction in the pressure levels due to the combustion delay is seen. Moreover, with the increment of engine compression ratio and the advancement in the spark timing, the area under the curve at high pressures increases the power output. Nonetheless, the higher specific heat ratio in the conventional case helps compensate for the power production observed in the expansion process.

The pumping loops of the studied cases are seen in Figure 6.5. Larger pumping loop areas are observed for the oxycombustion cases due to high-pressure EGR, which affects the gas exchange process to guarantee the proper amount of EGR in the intake. As will be further explained later, the process of exhaust gas usage in conventional cases is performed more efficiently, generating a more favorable pressure difference between intake and exhaust pressure, improving the gas exchange process. In addition, increasing the compression

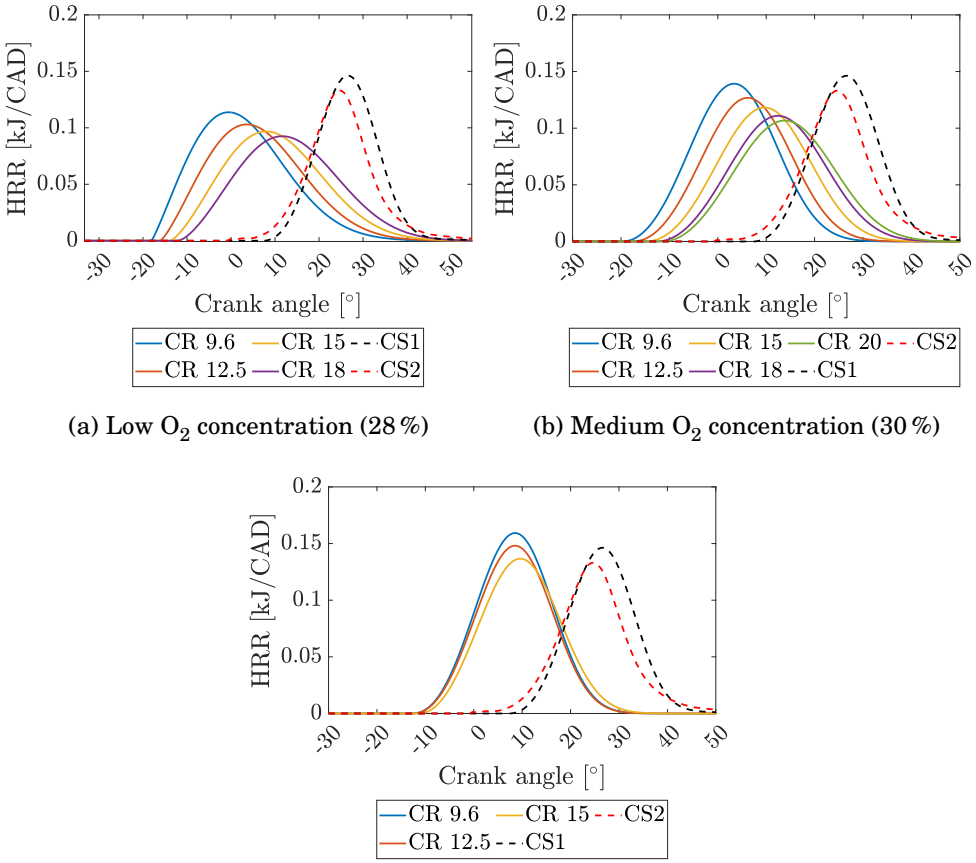

(a) Low O_2 concentration (28 %)

(b) Medium O_2 concentration (30 %)

(c) High O_2 concentration (32 %)

Figure 6.3: Heat release rate for different oxygen concentrations and compression ratios - 3.000 rpm

ratio in oxycombustion cases reduces the energy needed for the gas-exchanging process, for which the pumping loop area is reduced.

The temperature variation for the different studied cases is shown in Figure 6.6. The temperature levels are higher for the conventional cases compared with the oxycombustion operation at low oxygen concentration (28 %) due to the higher reactivity of the in-cylinder mixture when atmospheric air is used compared with O_2/EGR. For medium oxygen concentration (30 %), temperatures around the combustion process are similar, while high oxygen concentration surpasses the temperature values compared with the conventional case. On the other hand, it is seen that during the expansion process, the slope for the conventional case is higher due to the higher specific heat capacities ratio of the

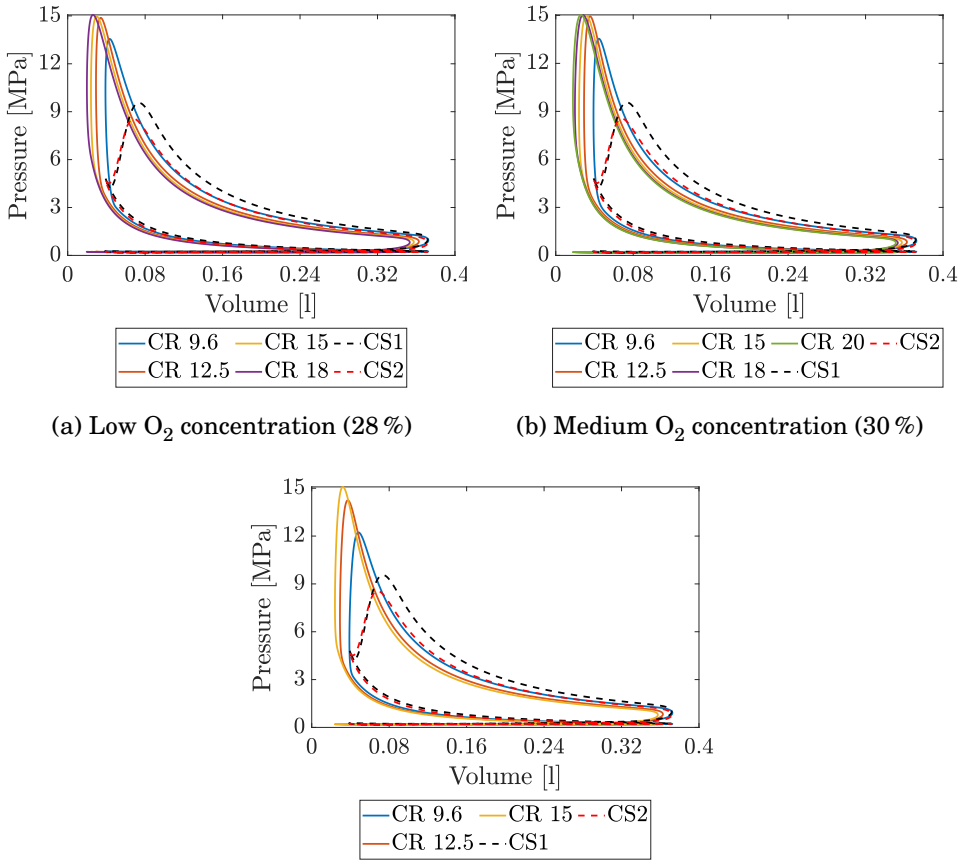

(a) Low O_2 concentration (28 %)

(b) Medium O_2 concentration (30 %)

(c) High O_2 concentration (32 %)

Figure 6.4: Pressure volume diagram for different oxygen concentrations and compression ratios - 3.000 rpm

conventional in-cylinder mixture. This phenomenon causes the temperature at the exhaust valve opening to be lower in conventional cases, reducing the exhaust manifold temperature.

Regarding the mean trapped gas in the cylinders, Figure 6.7 shows the behavior of the trapped mass for the studied cases. For the oxycombustion cases, incrementing the compression ratio improves the engine performance. In this sense, less fuel is required for power generation; thus, oxygen and the trapped mass are reduced considering a constant oxygen concentration. Otherwise, the increment in the oxygen concentration reduces the trapped mass. Similar fuel consumptions at constant engine compression ratios were obtained, for which increasing the oxygen concentration reduces the trapped mass in the cylinder

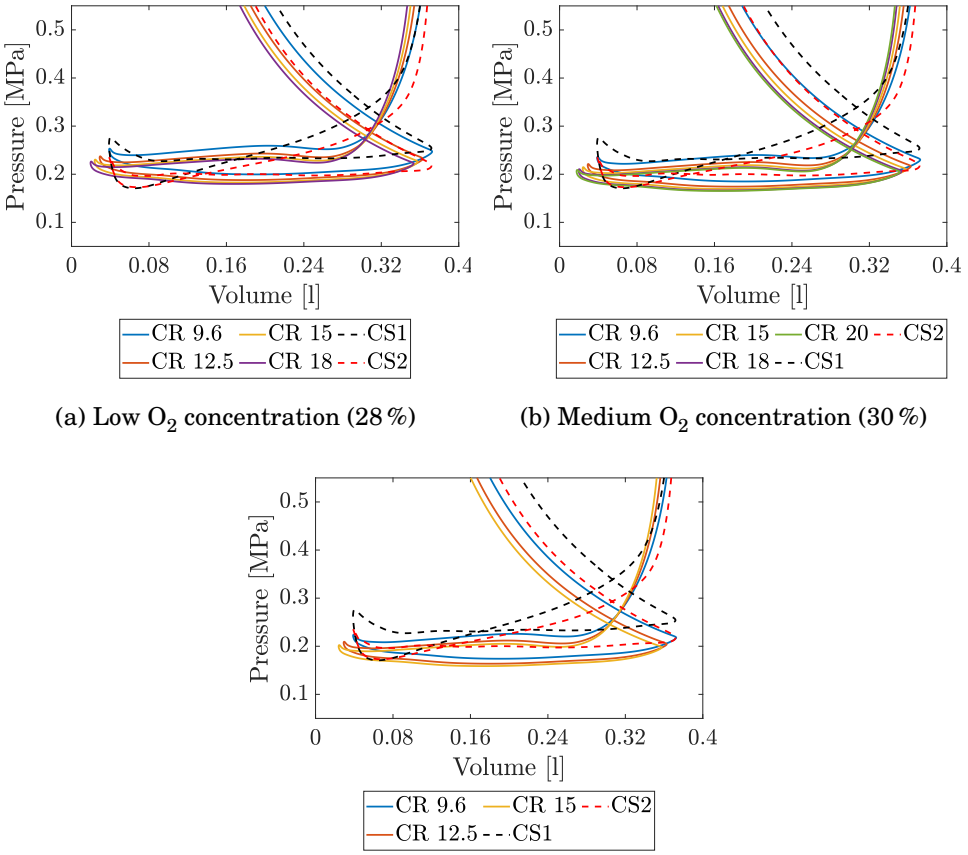

(a) Low O_2 concentration (28 %)

(b) Medium O_2 concentration (30 %)

(c) High O_2 concentration (32 %)

Figure 6.5: Pumping loop diagram for different oxygen concentrations and compression ratios - 3.000 rpm

for a similar oxygen mass. As an additional comment, it can be seen that the trapped mass is varied by modifying the intake density with a variation in the pressure, considering a constant cylinder displacement for all the cases.

Comparing with the conventional cases, it is seen that these cases have higher trapped masses due to the difference in the oxygen concentration of atmospheric air (23 %) and the oxycombustion cases studied (28 %, 30 %, and 32 %). For this reason, conventional cases perform with higher intake pressures to ensure the same oxygen for the same power output. Moreover, CS2 has a reduced trapped mass compared with CS1 due to the required power reduction to keep stoichiometric combustion.

Considering the above, it is seen that medium oxygen concentration offers

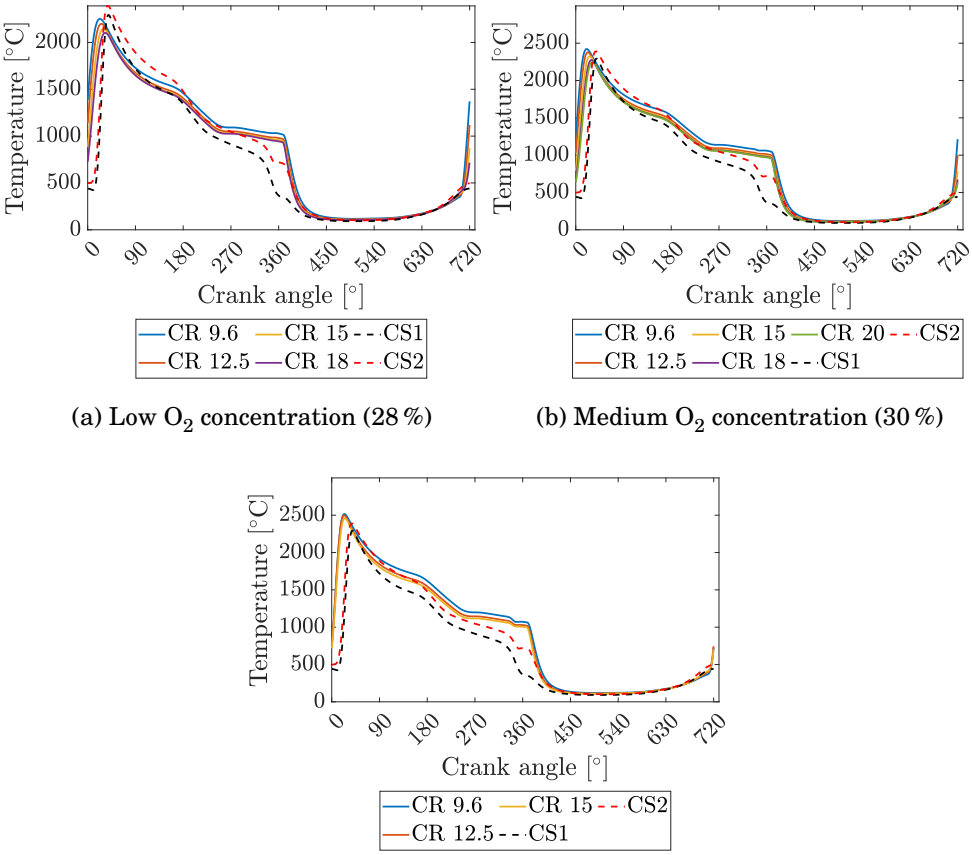

(a) Low O_2 concentration (28 %)

(b) Medium O_2 concentration (30 %)

(c) High O_2 concentration (32 %)

Figure 6.6: Temperature variation for different oxygen concentrations and compression ratios - 3.000 rpm

a trade-off in exhibited parameters that ensures better performance. Comparing low and medium oxygen concentration, low concentration allows the spark timing to be more advanced due to the lower reactivity in this scenario. Nonetheless, the same lower reactivity lags the start of combustion, for which an earlier combustion can be obtained at a medium oxygen concentration. On the other hand, the higher reactivity at medium oxygen concentration leads to shorter combustion than at low oxygen concentration, enhancing the engine's performance.

Besides, low oxygen concentration demands a higher trapped mass to obtain the required oxygen for power production, for which higher intake pressure is needed. This favors a higher in-cylinder pressure while the compression ratio increases, leading to a lower superior limit (CR=18) of the compression ratio than medium oxygen concentration (CR=20), for which a better engine

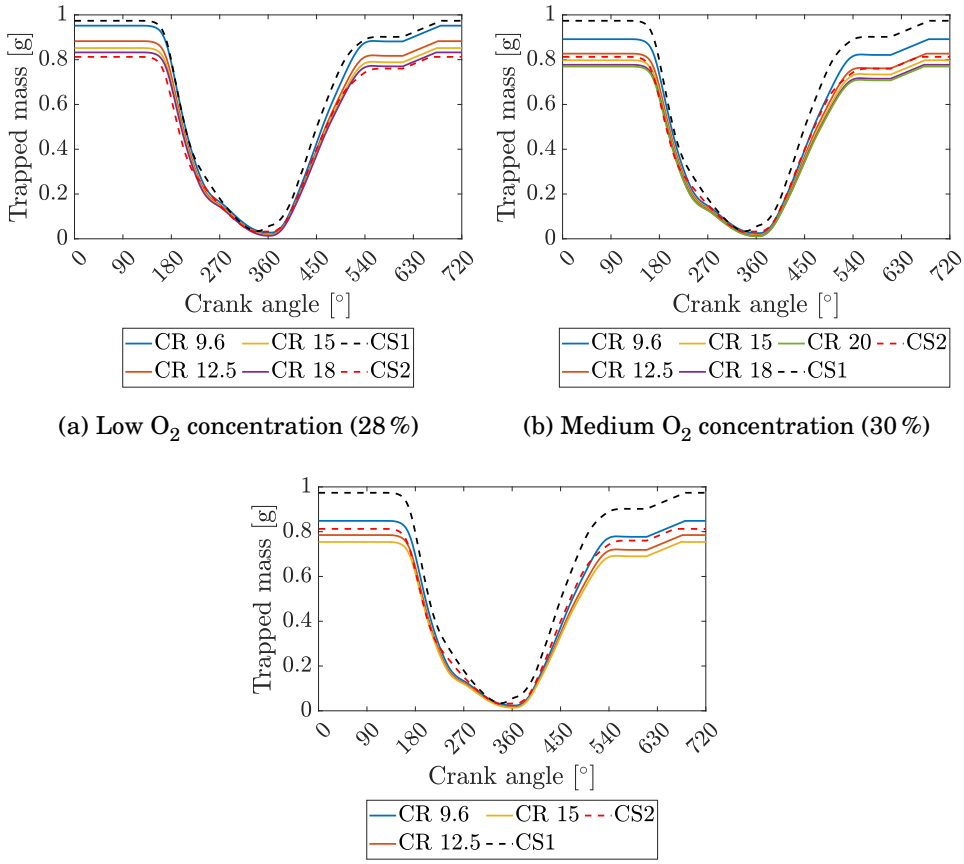

(a) Low O_2 concentration (28 %)

(b) Medium O_2 concentration (30 %)

(c) High O_2 concentration (32 %)

Figure 6.7: Cylinder trapped mass variation for different oxygen concentrations and compression ratios - 3.000 rpm

performance can be achieved at medium oxygen concentration.

On the other hand, when medium and high oxygen concentrations are compared, it is seen that shorter combustion is achieved at high oxygen concentrations due to a higher reactivity. Nonetheless, this higher reactivity at high oxygen concentration requires a delayed spark timing, for which the start of combustion starts later, affecting the engine performance. The higher reactivity also leads to a faster increment of pressure and temperature while the compression ratio increases. In this sense, higher in-cylinder pressures are reached faster, finding the lowest superior limit of engine compressor ratio (CR=15) for the three different oxygen concentrations studied, considering the maximum pressure limit.

On the other hand, when medium and high oxygen concentrations are compared, it is seen that shorter combustion is achieved at high oxygen con-

centrations due to a higher reactivity. Nonetheless, this higher reactivity at high oxygen concentration requires a delayed spark timing, for which the start of combustion starts later, affecting the engine performance. The higher reactivity also leads to a faster increment of pressure and temperature while the compression ratio increases. In this sense, higher in-cylinder pressures are reached faster, finding the lowest superior limit of engine compressor ratio (15) for the three different oxygen concentrations studied, considering the maximum pressure limit.

In summary, it is seen that the primary sources in the engine performance are the fuel enrichment in CS1 and the required combustion delay to avoid combustion issues in both conventional cases. On the other hand, in CS2, the advancement of combustion is permitted due to the in-cylinder conditions resulting from the power decrease, which leads to lower pressure and temperature that ensure less probability for combustion issues.

Oxygen production cycle

Similarly, the oxygen production cycle performance is examined for the oxycombustion cases. The feed air conditions at the membrane are shown in Table 6.9 for each studied oxycombustion operation point. For higher engine compression ratios, there is a decrease in the exhaust manifold temperature, whose stream is the primary energy source for oxygen production. Thus, the recoverable energy to drive the air is reduced, lowering the exchanged heat at HEN and the feed air temperature. Consequently, the available energy in the turbines reduces, affecting the air mass flow and feed pressure. On the other hand, the available energy increases with the oxygen concentration increment, causing higher feed pressures and temperatures and more air stream for oxygen separation.

Table 6.10 shows the membrane operation conditions for each studied case. The fuel consumption is improved with an increased engine compression ratio, reducing the oxygen production requirement for the same power output. Additionally, the mean oxygen partial pressure ratio increases with the increment of the compression ratio and the decrement of oxygen concentration. The reduction in the temperature of the membrane affects the oxygen permeation. In this sense, the oxygen partial pressure at the outlet of the feed side increases, leading to a higher mean oxygen partial pressure at the feed side. On the other hand, increasing the compression ratio reduces the intake and exhaust manifold pressures, as shown in Table 6.6, for which the oxygen partial pressure at the permeate side is reduced, increasing the oxygen partial pressure ratio.

	$\dot{m}_{\text{air}}$ (kg/h)	P_{feed} (MPa)	T_{feed} (°C)	$\dot{Q}_{HE}$ (kW)
28 % O_2				
CR 9.6	446.7	0.420	1,037	141.2
CR 12.5	421.7	0.392	992	126.9
CR 15.0	410.5	0.381	975	121.2
CR 18.0	403.7	0.374	965	117.8
30 % O_2				
CR 9.6	443.9	0.420	1,067	145.2
CR 12.5	419.0	0.392	1,019	130.2
CR 15.0	407.5	0.380	1,000	124.0
CR 18.0	399.9	0.372	987	119.9
CR 20.0	397.1	0.369	982	118.5
32 % O_2				
CR 9.6	445.6	0.426	1,111	152.3
CR 12.5	419.7	0.396	1,056	135.4
CR 15.0	407.4	0.382	1,028	127.5

Table 6.9: Feed air conditions for different oxygen concentrations and compression ratios - 3.000 rpm

Considering the latter, the membrane efficiency is also shown, whose expression is shown in Equation 6.8, which is the ratio of the oxygen separated in the membrane with the total amount of oxygen brought with the air to the feed side. Operating at lower temperatures reduces the membrane efficiency, a phenomenon that is produced at higher compression ratios and lower oxygen concentrations. Nonetheless, it is seen that more than 80 % of the oxygen can be extracted from the driven atmospheric air.

$$\eta_{\text{memb}} = \frac{\dot{m}_{O_2}}{0.23 \cdot \dot{m}_{air}} \tag{6.8}$$

Figure 6.8 depicts the membrane operation maps with the operation points of the studied cases to clarify the latter explanation. The membrane maps are displayed by showing the isolines of oxygen production. As explained, it is seen that the engine operation at higher compression ratios leads to lower membrane temperatures and higher oxygen pressure ratios. Additionally, it is seen how the operation points move to the top left superior part of the map, which is a zone of higher temperatures and lower oxygen partial pressure, resulting from the higher energy availability for oxygen production.

	$P_{O_2,\text{feed}}/P_{O_2,\text{perm}}$ (-)	T_{memb} (°C)	$\dot{m}_{O_2}$ (g/s)	η_{memb} (%)
Low O_2 conc.				
CR 9.6	1.142	1020	22.97	81.77
CR 12.5	1.158	975	21.44	81.03
CR 15.0	1.168	958	20.75	80.64
CR 18.0	1.172	948	20.35	80.42
Medium O_2 conc.				
CR 9.6	1.121	1,043	22.95	82.63
CR 12.5	1.140	996	21.42	81.68
CR 15.0	1.149	976	20.71	81.25
CR 18.0	1.155	963	20.26	80.96
CR 20.0	1.157	959	20.08	80.83
High O_2 conc.				
CR 9.6	1.106	1,077	23.22	82.98
CR 12.5	1.125	1,023	21.60	81.98
CR 15.0	1.136	996	20.82	81.41

Table 6.10: Membrane operation for different oxygen concentrations and compression ratios - 3.000 rpm

An accurate coupling between power generation and oxygen production cycles is observed, as mentioned above. With an increment in the engine's thermal efficiency, the exhaust manifold temperature is reduced, and the available energy to boost oxygen production decreases.

In this sense, the air heating and compression are affected, where the air mass flow and the pressure of the feed side inlet are reduced. Consequently, there is a reduction in the available enthalpy flow for the expansion stages, creating a feedback effect until an energy balance in the turbomachines is achieved. Nonetheless, the improvement in the engine performance leads to a lower fuel requirement; thus, less oxygen is needed for power production. Hence, both phenomena are complementary, where a reduction in the available energy for oxygen production agrees with the decrease in the oxygen production needed due to the higher thermal efficiency of the engine.

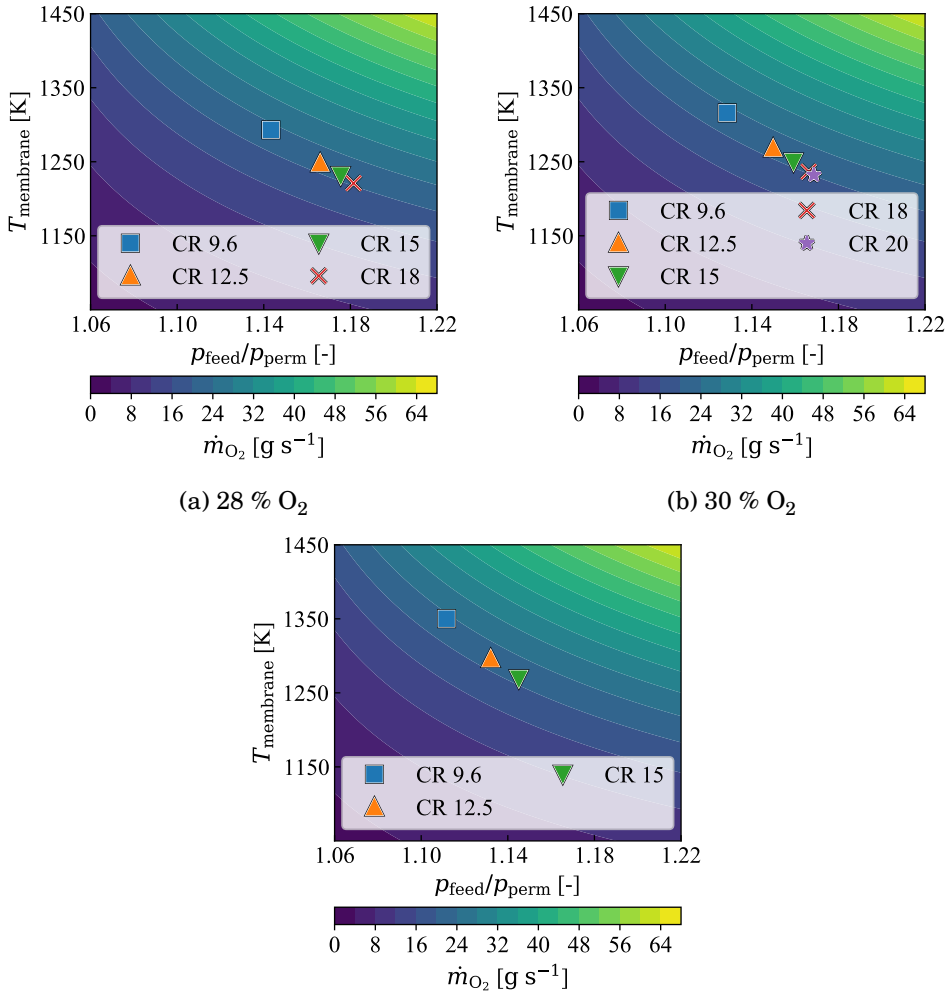

(a) 28 % O_2

(b) 30 % O_2

(c) 32 % O_2

Figure 6.8: Membrane operation map for different oxygen concentrations and compression ratios - 3.000 rpm

6.6.2 Engine speed comparison

Engine

The results of the last section show that working at medium oxygen concentration (30 %) benefits the engine performance due to the trade-off in the combustion properties and the thermodynamic variables of the engine operation. In this sense, the study is extended to a wide range of engine speeds, comparing the performance of conventional and oxycombustion operation modes between 1,500 to 5,000 rpm. The oxycombustion cases in this section operate with the original compression ratio (CR9.6) and the superior obtained limit for the applied oxygen concentration (CR20). With this, the feasibility of applying the optimum conditions found in the medium-speed study is assessed.

Initially, the fuel consumption and the power production of the oxycombustion and conventional cases are depicted in Figure 6.9, where for conventional cases, experimental and simulated data are shown. In contrast, for oxycombustion cases, the obtained results come from replicating the power production conditions established in the reference full-load.

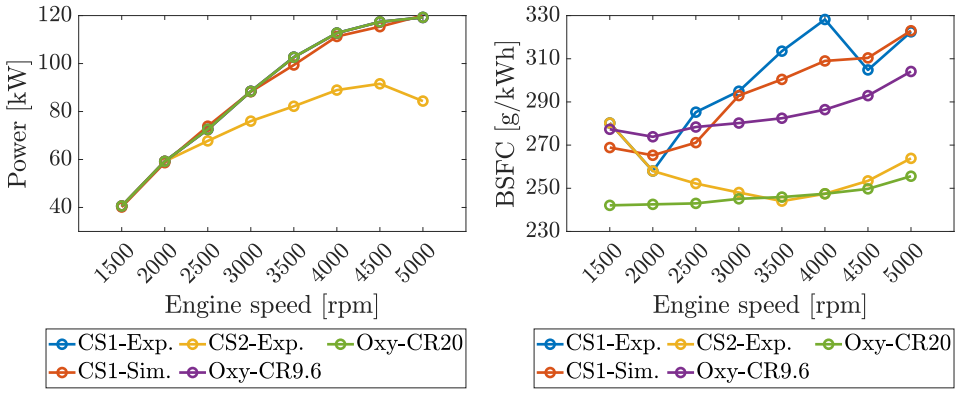

(a) Power (kW)

(b) BSFC (g/kWh)

Figure 6.9: Comparison of full load engine performance at different speeds

The fuel consumption in the experimental and simulated data for the conventional cases exhibits the same trend for both cases. On the other hand, at higher speeds, the fuel requirement for CS1 increases to maintain the exhaust manifold temperature at acceptable values. On the other hand, CS2 seems to reduce fuel consumption, where the typical curve for a spark-ignition engine operating with stoichiometric combustion is obtained.

The oxycombustion cases exhibit similar behaviors, where the curve of the engine compression ratio of 20 is displaced to a zone of lower consumption values. For the CR9.6 oxycombustion case, it is seen that the fuel consumption displays

similar values to CS1 conventional case, remarkably improving the performance at higher speeds due to the fuel enrichment in CS1. On the other hand, the CR20 case exhibits similar fuel consumption values to CS2 conventional case, finding that the performance at low and high speeds is better in the CR20 oxycombustion case.

On the other hand, it is seen that oxycombustion and conventional cases match in the power output, which is seen in the overlapping of the lines in Figure 6.9(a). CS2 reduces its power output for engine speeds higher than 2,000 rpm.

The main engine data at low (1,500 rpm) and high (5,000 rpm) speeds are shown in Table 6.11 for further understanding. Unlike high-speed operation, the conventional mode does not require enriching the in-cylinder mixture at low speed. At low speed, CR9.6 oxycombustion case consumes 3.2 % more fuel than the conventional case, and a remarkable difference in the maximum in-cylinder temperature and pressure is found. Moreover, the CR20 oxycombustion case exhibits a 10 % reduction in fuel consumption compared with the conventional case, and its maximum in-cylinder pressure nearly reaches the imposed pressure limit of the cylinder for engine integrity. Nonetheless, the maximum in-cylinder temperature in CR20 is around 200 °C lower than the CR9.6 case.

	Power (kW)	BSFC ($g kW^{-1} h^{-1}$)	IMEP (MPa)	P_{max} (MPa)	T_{max} (°C)	λ
1500 rpm						
CS2	40.18	268.86	2.51	7.19	2333	1.000
CR9.6 - 30% O_2	40.61	277.57	2.56	11.67	2348	1.000
CR20 - 30% O_2	40.61	242.13	2.59	14.79	2147	1.000
5000 rpm						
CS1 ($\lambda = 0.812$)	120.07	322.97	2.30	9.86	2265	0.812
CS2	84.35	263.86	1.76	8.57	2447	1.000
CR9.6 - 30% O_2	119.28	304.06	2.53	12.16	2326	1.000
CR20 - 30% O_2	119.21	254.79	2.51	14.93	2274	1.000

Table 6.11: Engine data at low and high speeds - Full load

On the other hand, at high-speed operation, it is seen that the CR9.6 case exhibits a reduction in fuel consumption of 5.9 % compared with CS1, while an increase of 15.2 % compared with CS2. However, considering CR20, oxycombustion brings a fuel consumption decrease of 21.1 % and 3.4 % compared with CS1 and CS2, respectively. Simultaneously, there is a 30 % of power reduction at CS2.

In addition, the maximum in-cylinder pressure increases in the oxycombustion cases while the maximum temperature is reduced.

Furthermore, Table 6.12 shows the thermodynamic conditions at the manifolds. Higher pressures at the intake and exhaust manifolds are observed for conventional cases. Additionally, due to the high water vapor content in oxycombustion cases, an intake temperature of 85 °C is considered to avoid liquid water at the cylinders' intake to ensure their mechanical integrity. On the contrary, the water content in conventional cases permits lower intake temperatures. Also, the exhaust temperatures are higher for oxycombustion cases, reaching higher values than 1,000 °C.

	P_{int} (MPa)	T_{int} (°C)	P_{exh} (MPa)	T_{exh} (°C)	PMEP (MPa)
1500 rpm					
CS2	0.247	38.28	0.211	877.6	0.053
CR9.6 - 30% O_2	0.200	84.85	0.194	1,054.9	-0.007
CR20 - 30% O_2	0.178	84.85	0.174	946.3	-0.007
5000 rpm					
CS1	0.238	43.36	0.327	867.4	-0.257
CS2	0.164	34.74	0.231	942.8	-0.163
CR9.6 - 30% O_2	0.191	84.85	0.197	1,160.2	-0.215
CR20 - 30% O_2	0.163	84.85	0.175	1,047.5	-0.167

Table 6.12: Intake and exhaust manifolds data at low and high speeds - Full load

The performance difference can be explained by considering both combustion modes' combustion and the thermodynamic parameters. The differences in combustion parameters are exhibited in Table 6.13 for low and high engine speeds. Conventional combustion is 50 % shorter on average compared with oxycombustion but requires a delayed start to avoid knocking.

The combustion at low speeds is around 30° more delayed in conventional cases than oxycombustion, affecting the combustion centering and, consequently, the engine performance. On the other hand, the CS2 strategy at high speed allows an advancement in combustion that enhances the engine's thermal efficiency. However, a remarked difference in the start of combustion is still found comparing both combustion modes at high speed. Figure 6.10 shows the heat release rates to understand better where the combustion differences are found.

	Duration (°)	SOC (°)	CA50 (°)
1500 rpm			
CS2	15.37	15.61	34.23
CR9.6 - 30% O_2	21.64	-18.85	4.91
CR20 - 30% O_2	23.28	-13.45	11.81
5000 rpm			
CS1	16.80	0.28	20.64
CS2	15.99	-9.50	12.53
CR9.6 - 30% O_2	20.95	-21.09	1.90
CR20 - 30% O_2	22.67	-14.92	10.14

Table 6.13: Combustion data at low and high speeds - Full load

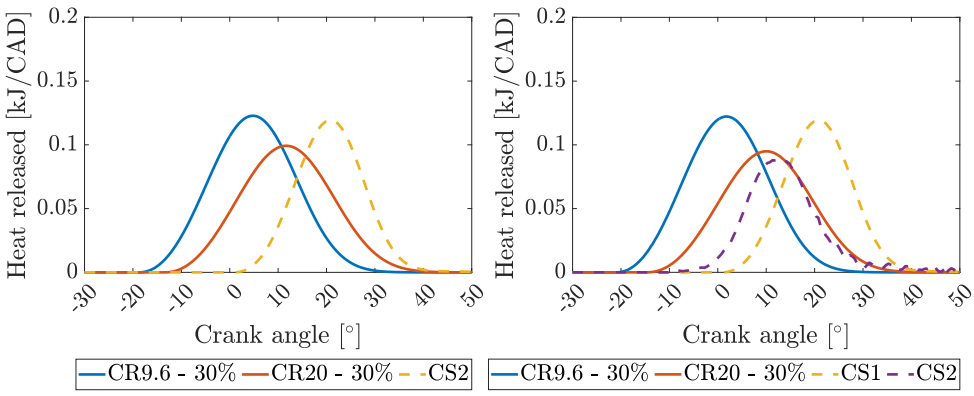

(a) Low speed (1500 rpm)

(b) High speed (5000 rpm)

Figure 6.10: Heat release law at low and high speed

The consequent differences in thermodynamic variables also explained the differences in the performance of oxycombustion and conventional operation modes. The pressure-volume diagrams are depicted in Figure 6.11(a) and Figure 6.11(b) for low and high-speed case, respectively. The difference in SOC operating at low speed can be observed in this diagram, which allows higher in-cylinder pressures in oxycombustion. For high-speed operation, SOC differences are not remarkable as for low-speed, for which similar pressure levels can be achieved for both combustion modes. Similarly to the performed study at medium speed, the effect of a higher specific heat capacities ratio in the conventional case leads to a greater area under the curve in the pressure-volume (P-V) diagram and higher slopes in the temperature evolution at the temperature-volume(T-V),as shown in Figure 6.11(c) and Figure 6.11(d),which explains higher

temperatures in the oxycombustion cases at the exhaust manifold.

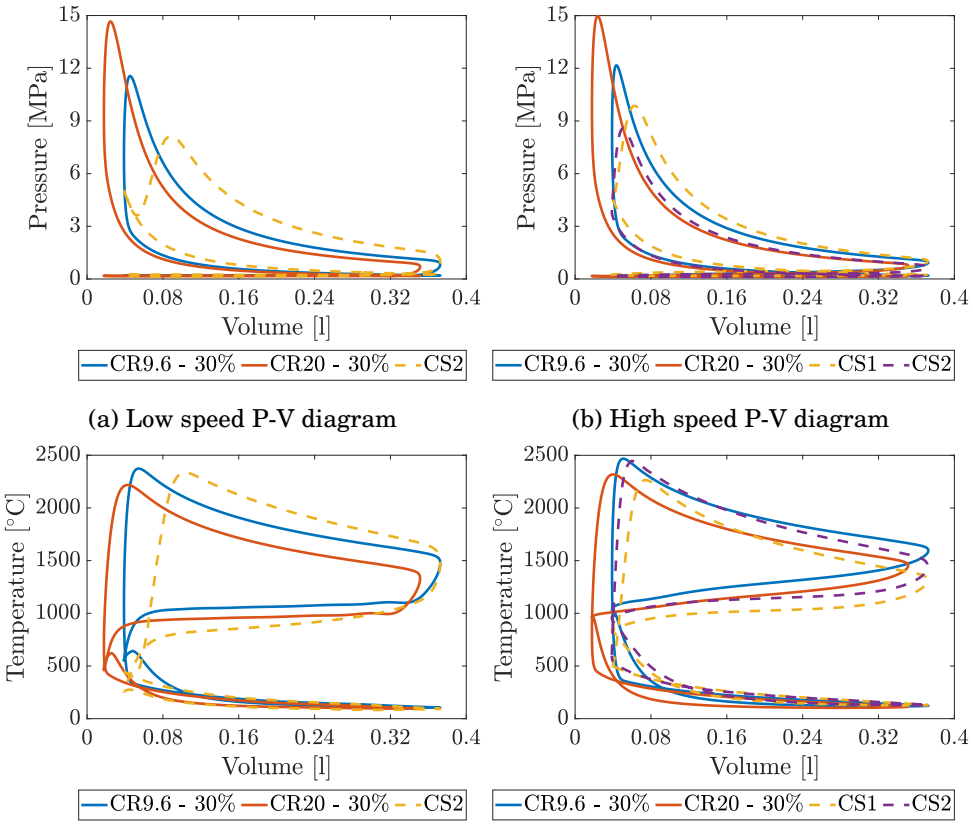

(a) Low speed P-V diagram

(b) High speed P-V diagram

(c) Low speed T-V diagram

(d) High speed T-V diagram

Figure 6.11: Pressure-volume and temperature-volume diagrams at low and high speed

The pumping loops for low and high speeds are depicted in Figure 6.12(a) and Figure 6.12(b). Low speeds working at conventional mode exhibit a positive pumping loop, while a reduced pumping area is observed in the oxycombustion mode, expected due to the slight difference between the intake and exhaust manifold pressures. On the contrary, the beneficial effect of a positive pumping loop is reduced at high speeds, whereas a negative pumping loop is presented in both combustion modes. These differences in the gas exchange section of the P-V diagram explain the variation in the pumping mean effective pressure (PMEP) shown in Table 6.12. The trapped mass has higher values in conventional cases, as seen in Figure 6.12(c) and Figure 6.12(d), due to the lower oxygen concentration in atmospheric air, which also leads to higher manifold pressures, as explained.

That said, it is seen that the performance differences under low-speed

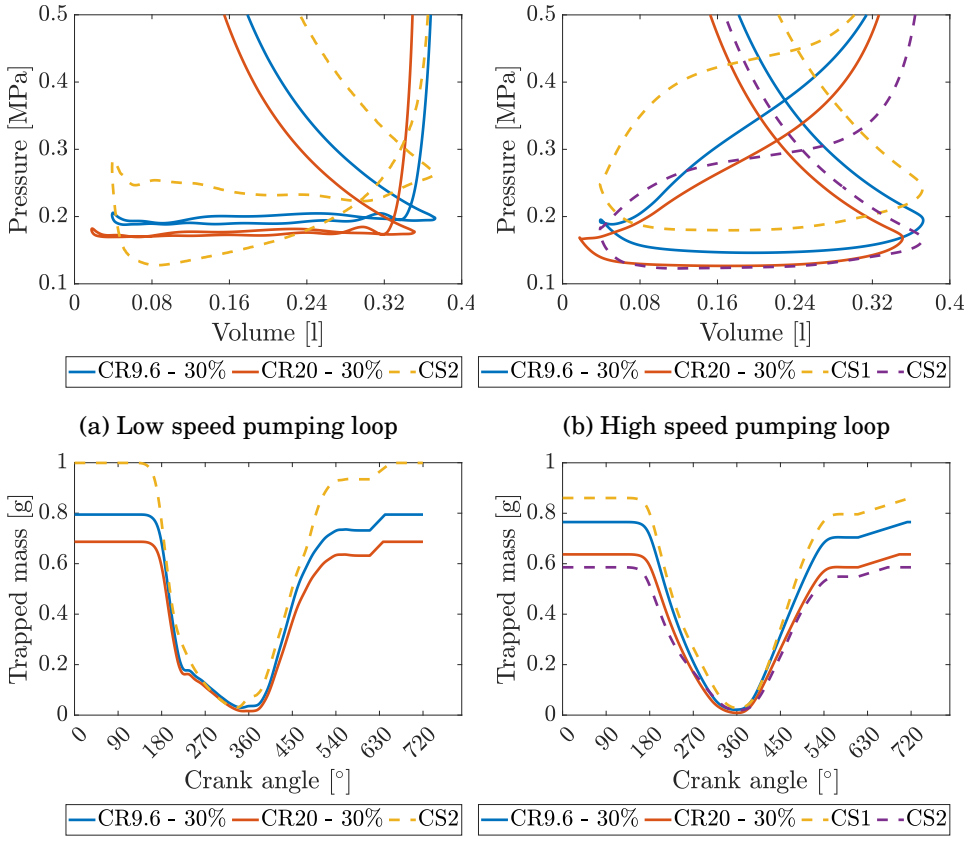

(a) Low speed pumping loop

(b) High speed pumping loop

(c) Low speed trapped mass

(d) High speed trapped mass

Figure 6.12: Pumping loop and trapped mass at low and high speed

operation for both combustion modes are found in the combustion, which is longer in oxycombustion but can be more advanced compared with conventional combustion. Also, the differences in the gas exchange process, observed in the pumping loop diagram in Figure 6.12(a), show that a positive loop in the conventional mode is obtained, compensating for the performance differences caused by combustion properties.

On the other hand, for high-speed operation, the required fuel enrichment in the CS1 strategy sets the difference in performance. CS2 performs better due to avoiding extra fuel injection but with a consequent power reduction. In addition, combustion differences play an essential role in the engine performance at these conditions, as explained for low and medium speeds.

It must be mentioned that the oxycombustion characteristics permit the increment of engine compression ratio, for which promising values in fuel consumption can be achieved. In this sense, the full load power output of CS1 cases

can be reached with similar fuel consumptions obtained working at CS2, achieving both benefits of conventional cases when oxycombustion is implemented at high engine compression ratios.

Oxygen production cycle

Regarding the oxygen production cycle operation, Figure 6.13 depicts the membrane map operation for CR9.6 and CR20 oxycombustion cases. It is seen that increasing the engine compression ratio reduces oxygen production due to the decrease in available energy to recover, which is compensated by the thermal efficiency improvement of increasing the engine compression ratio, as explained.

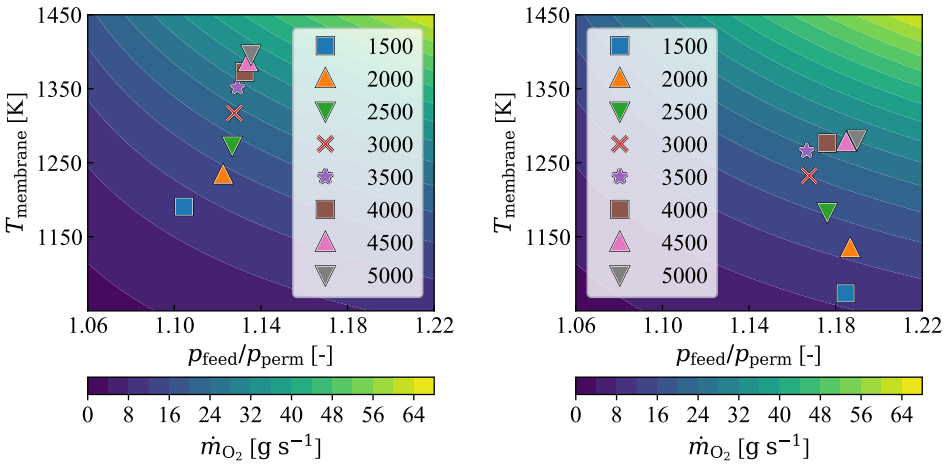

(a) CR 9.6

(b) CR 20

Figure 6.13: Membrane operation at engine full load

In this sense, the membrane in the CR9.6 case operates in a temperature range between 918 to 1,124 °C, while the CR20 case membrane operating temperature ranges between 800 to 1,009 °C. It is seen that a mean difference of 100 °C is observed between both engine compression ratios operation. Similarly, reducing the engine speed decreases the oxygen partial pressure ratio due to the reduced available energy to increase the air pressure, reducing the feed oxygen partial pressure.

It is also seen that the trends of oxygen production points between CR9.6 and CR20 are different. While in CR9.6, the engine speed increase leads to more available energy that promotes higher pressure and temperature in the membrane operation, the trend in CR20 is different. This is due to the differences in spark timing optimization strategy in both cases. CR9.6 cases are far from the maximum in-cylinder pressure limit, allowing the optimum spark timing to be

selected without restriction. Differently, CR20 cases operate near the maximum in-cylinder pressure limit, for which the spark timing limitation is noticeable in those points, changing the regular trend in the exhaust temperature, thus, changing the operating point of the oxygen production cycle.

Moreover, the performance of the involved turbomachines changes regarding the engine compression ratio, operating in a comfortable zone for both air-driven compressors. For these compressors, the operation point is always distant from the surge and choke lines, reaching a high-efficiency operation. On the other hand, there is a lower air mass flow and compression ratio at CR20, as expected.

In addition to this, the O_2/EGR compressor does not offer a considerable boosting of the intake engine stream, independently of the used engine compression ratio, resulting from the mass flow unbalance between the compressor and turbine in this turbomachine (elements 17 and 22 in Figure 6.1), leading to a low-efficiency performance. Thus, the intake conditions cannot be appropriately enhanced, affecting the gas exchange processes, as mentioned earlier.

The turbomachine maps are exhibited in Figure 6.14 and Figure 6.15.

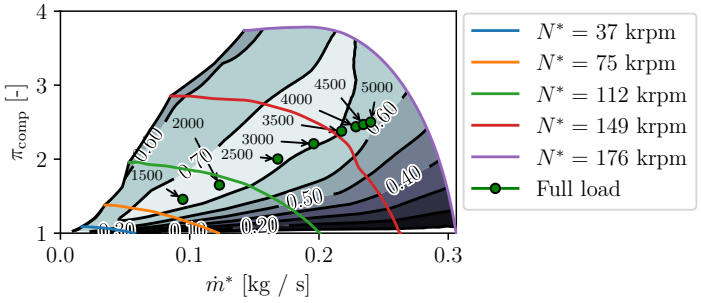

(a) Low pressure compressor

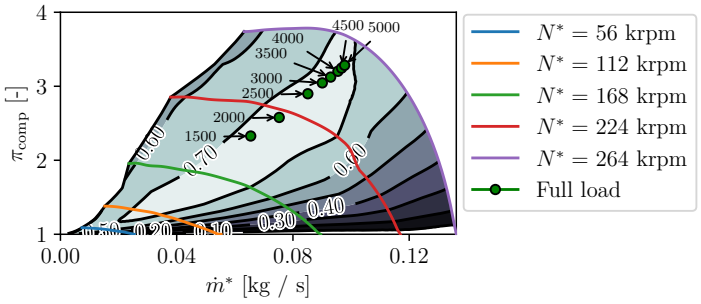

(b) High pressure compressor

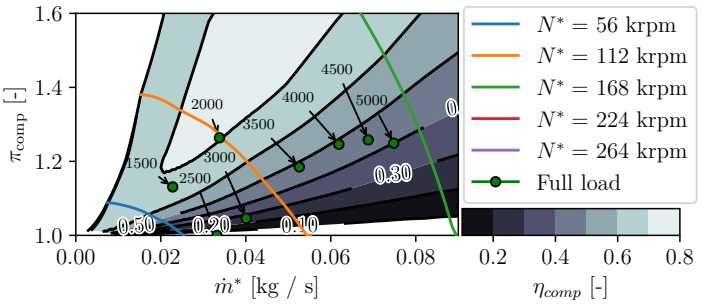

(c) Oxygen and EGR compressor

Figure 6.14: Compressor maps of the oxygen production cycle - CR9.6

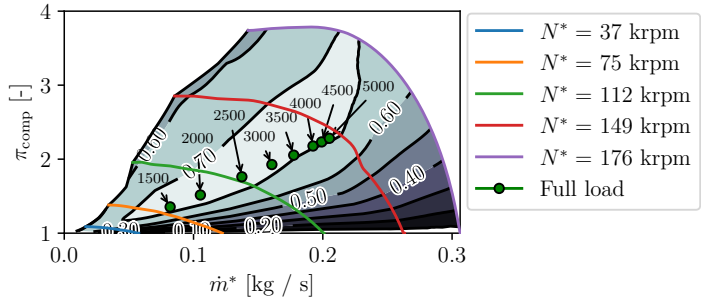

(a) Low pressure compressor

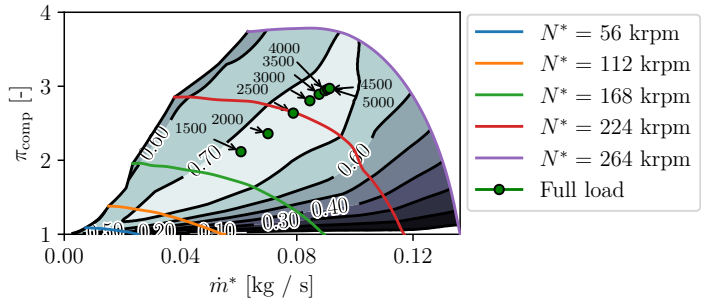

(b) High pressure compressor

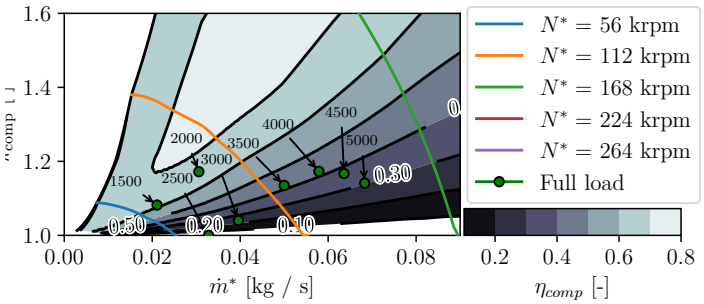

(c) Oxygen and EGR compressor

Figure 6.15: Compressor maps of the oxygen production cycle - CR20

6.7 Part-load

6.7.1 Engine

The brake-specific fuel consumption of the engine operating at both compression ratios is seen in Figure 6.16. In both scenarios, an optimum operation point can be observed at low engine speed (2,000 rpm) and high loads (full load in CR9.6 and at 80 % in CR20). The engine consumption increases mainly with the engine speed, while a slight increase regarding the load is also observed. The trends in fuel consumption are similar to a conventional turbocharged spark-ignition engine, improving a naturally aspirated that controls load by throttling the intake flow, worsening the performance.

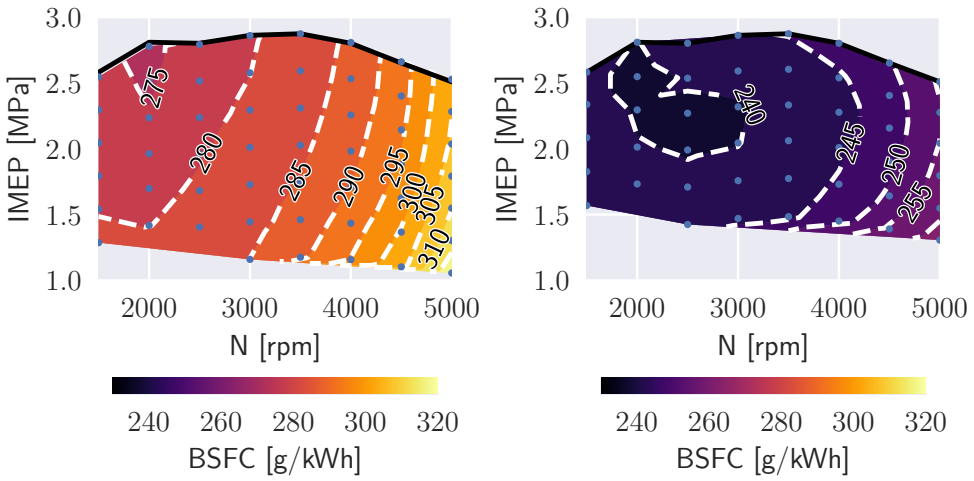

(a) CR 9.6

(b) CR 20

Figure 6.16: Brake specific fuel consumption map at part-load using two different compression ratios

As expected, due to the increment in the compression ratio, the fuel consumption using CR20 is better than the original in all the studied points. Nonetheless, the maximum improvement that could be achieved is limited due to the operating differences in both compression ratios.

First, the maximum in-cylinder pressures reached in CR20 are near the imposed limit (15 MPa) to avoid mechanical problems during operation, as observed in Figure 6.17, while for CR9.6, this limitation is far from being reached.

For this reason, the start of combustion is more delayed in CR20, as seen in Figure 6.18. As the engine load is reduced, the in-cylinder pressure decreases, and there is room to advance the start of combustion, improving the engine performance. On the contrary, the start of combustion can still be advanced

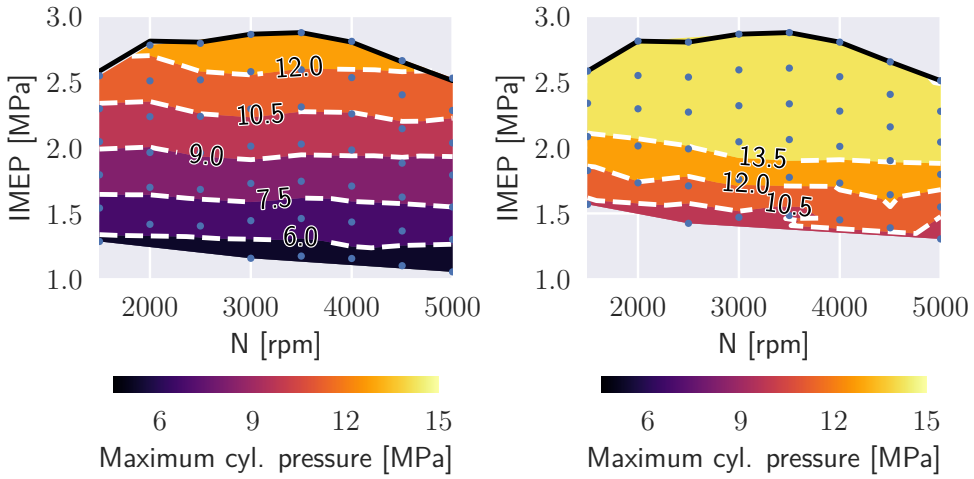

(a) CR 9.6 (b) CR 20

Figure 6.17: In-cylinder maximum pressure map at part-load using two different compression ratios

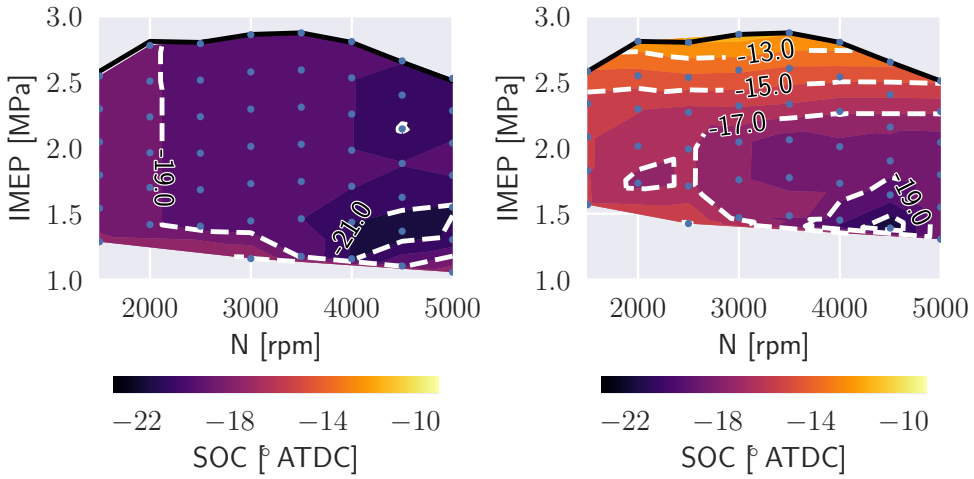

(a) CR 9.6 (b) CR 20

Figure 6.18: Start of combustion map at part-load using two different compression ratios

despite the engine load in CR9.6. As explained previously, this combustion advancement can be performed due to the reduced possibility of knocking issues due to the properties of oxycombustion in engines.

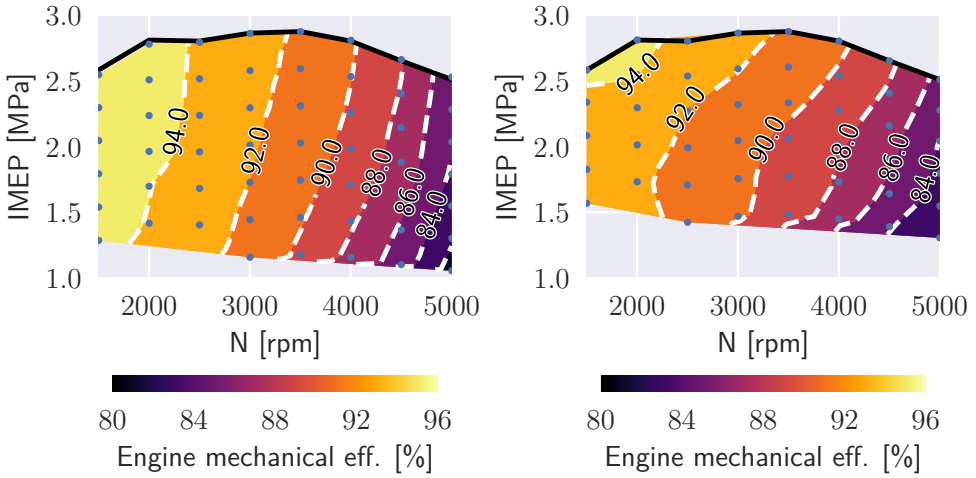

(a) CR 9.6

(b) CR 20

Figure 6.19: Mechanical efficiency map at part-load using two different compression ratios

On the other hand, Figure 6.19 depicts the engine's mechanical efficiency for both compression ratios. It can be seen in both cases that mechanical efficiency decreases at higher engine speeds and low loads. Additionally, higher mechanical efficiencies are seen at CR9.6, especially at low speeds, where values higher than 94 % are obtained for speeds lower than 2,000 rpm, which is only observed in CR20 at full load at 1,500 rpm and 2,000 rpm.

The differences in mechanical efficiencies are explained by considering friction and pumping losses. Figure 6.20 shows the friction mean effective pressure (FMEP) and the friction power for both studied scenarios. The friction depends on engine speed and the maximum in-cylinder pressure, which accounts for the mechanical load over the piston. In this sense, higher in-cylinder pressures are found in CR20, which has higher FMEP values. This effect is clarified by observing Figure 6.20(c) and Figure 6.20(d), which show the power losses regarding friction. For example, at full load, the friction power surpasses 10 kW at 5,000 rpm in CR20, being near 10 % of the net power production. Meanwhile, for CR9.6, the power losses are around 20 % lower at the same speed and load conditions.

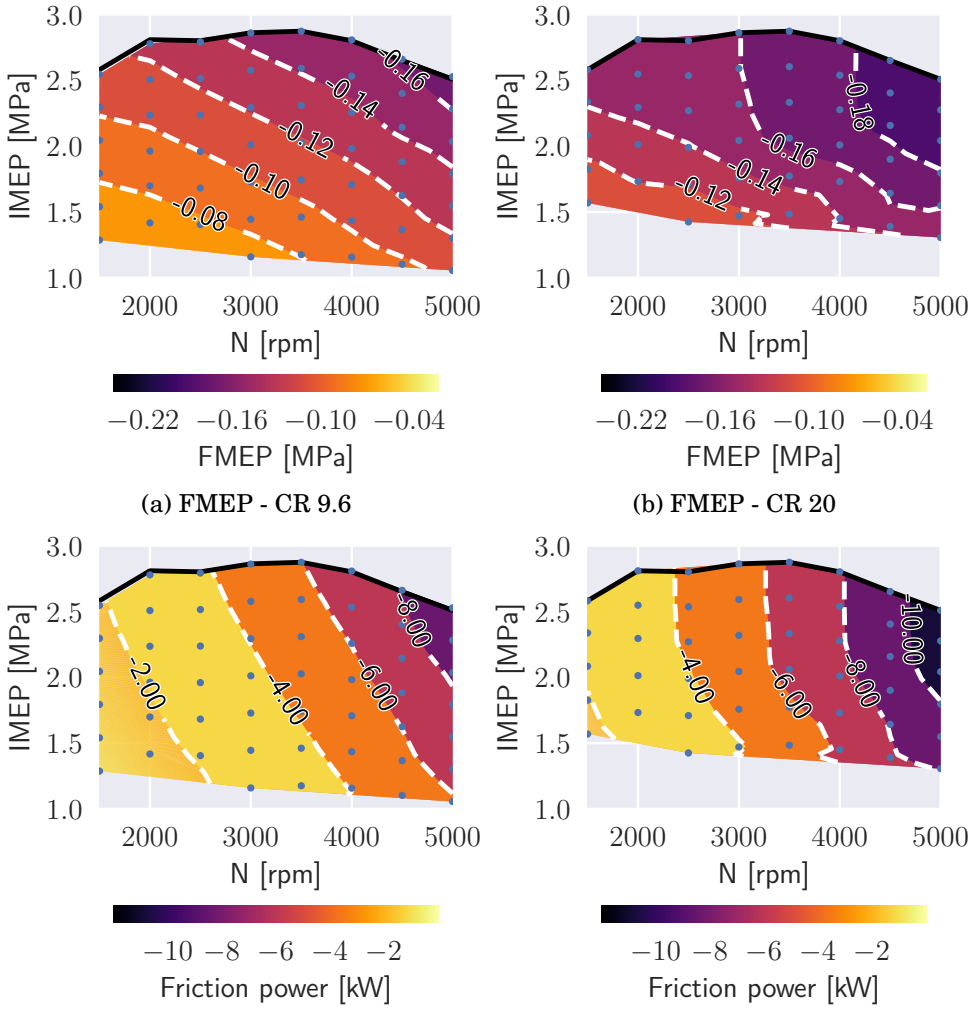

(a) FMEP - CR 9.6

(b) FMEP - CR 20

(c) Friction Power - CR 9.6

(d) Friction Power - CR 20

Figure 6.20: Friction mean effective pressure and friction power maps at part-load using two different compression ratios

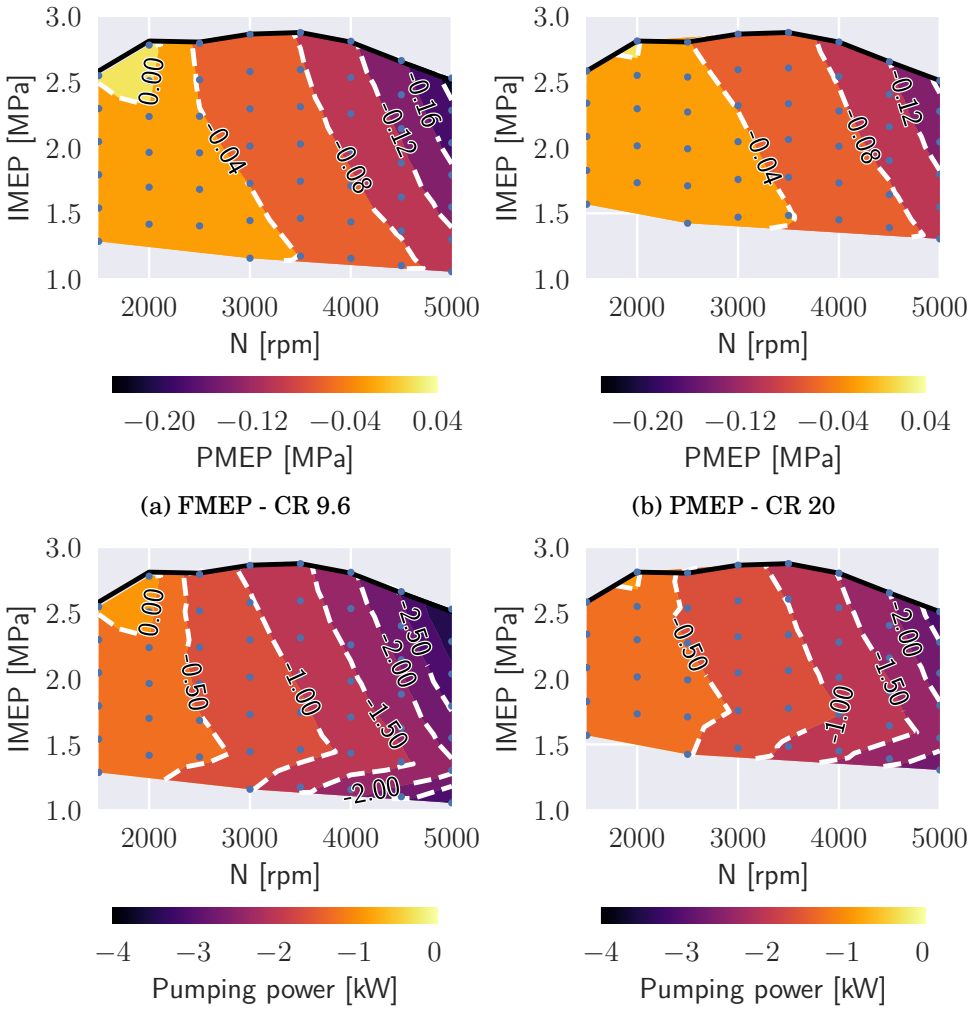

(a) FMEP - CR 9.6

(b) PMEP - CR 20

(c) Pumping Power - CR 9.6

(d) Pumping Power - CR 20

Figure 6.21: Pumping mean effective pressure and pumping power maps at part-load using two different compression ratios

Regarding pumping losses, it can be seen in Figure 6.21 that higher values are obtained at CR9.6, increasing with the engine speed and load simultaneously. Nonetheless, it must be said that this higher required energy for gas exchange is naturally expected due to higher intake flows demanded in CR9.6, due to its lower efficiency for power production, where more fuel is required. Thus, more intake mass flow is required to obtain the oxygen needed.

In this sense, the volumetric efficiency can be observed in Figure 6.22, whose reference is the pressure at the intake manifold. The volumetric efficiency reduces in both cases with the engine speed and load. A considerable part of the

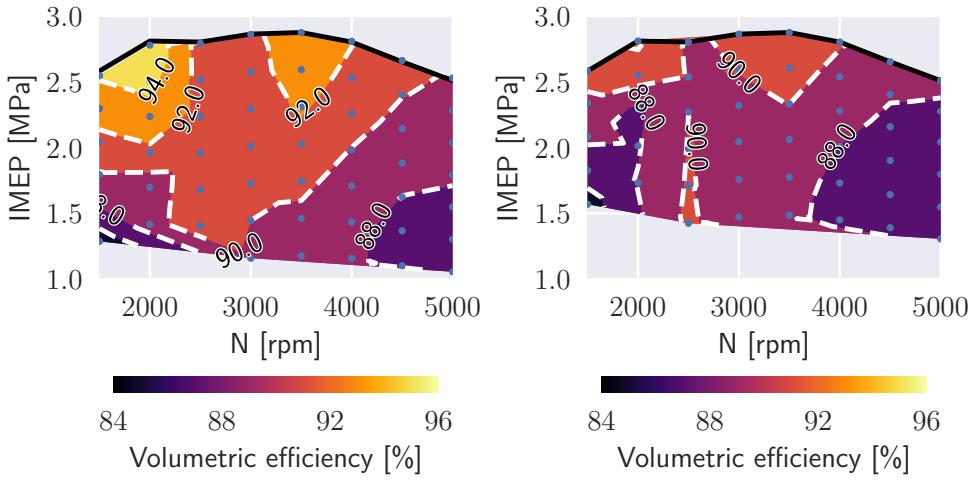

(a) CR 9.6 (b) CR 20

Figure 6.22: Volumetric efficiency map at part-load using two different compression ratios

studied points in CR20 has a volumetric efficiency lower than 90 %, surpassing this value at high loads and low to medium speeds. On the other hand, a volumetric efficiency lower than 90 % is only obtained at high speeds in CR9.6, especially when the engine load is reduced.

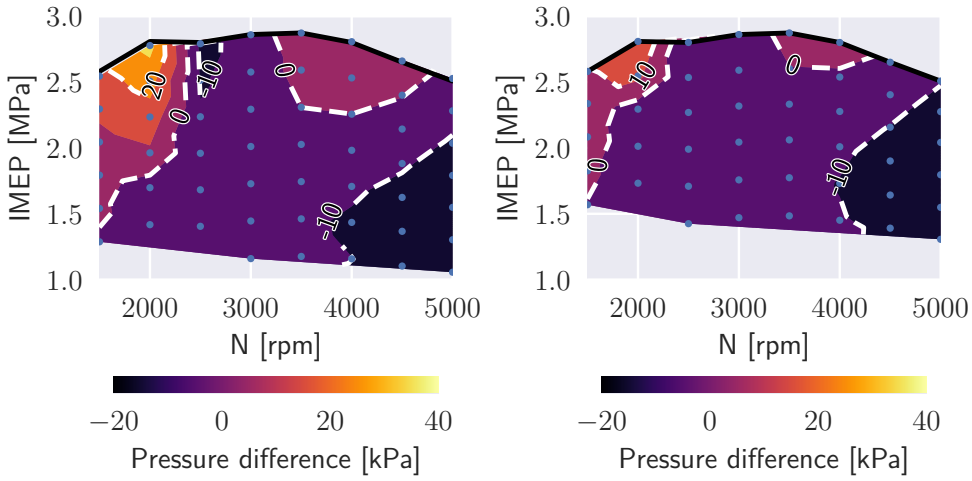

(a) CR 9.6 (b) CR 20

Figure 6.23: Map of pressure difference between intake and exhaust manifolds at part-load using two different compression ratios

The improvement in volumetric efficiency values are better understood considering the mean difference between the engine's intake and exhaust manifold pressures, shown in Figure 6.23. Positive values indicate that the intake manifold has a higher pressure. A reduction in the engine load and an increment in the engine speed leads to a decrease in the pressure difference, reaching a maximum point at 2,000 rpm and full load in both cases. Higher values occur at CR9.6 due to higher energy availability in the exhaust gas turbine (element 22 in the layout, see Figure 6.1) due to higher temperatures at the exhaust gases, allowing better performance of the coupled compressor (element 17), increasing the intake pressure. Consequently, the volumetric efficiency is improved.

In this sense, Figure 6.24 displays the temperature of the exhaust manifold, which indicates how much energy is available to drive, not only the O_2/EGR turbocharger but the oxygen production. As expected, higher loads and speeds lead to an increment in the temperature. As mentioned, higher temperature levels are reached at CR9.6, achieving temperatures as high as 1,150 °C. On the other hand, a temperature higher than 1,000 °C is surpassed at CR20 by around 50 °C.

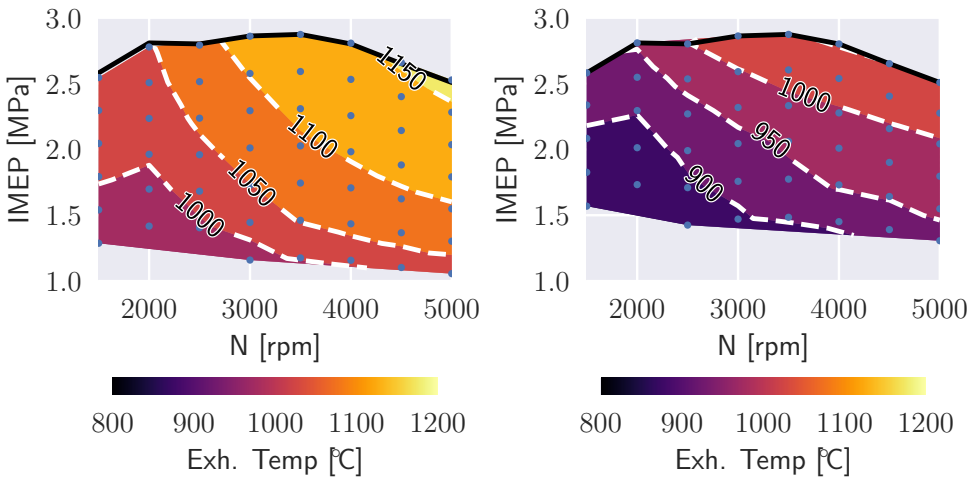

(a) CR 9.6

(b) CR 20

Figure 6.24: Exhaust temperature map at part-load using two different compression ratios

Consequently, more energy is available to drive the intake compressor and boost the oxygen production cycle in CR9.6. This is the main reason why a lower engine load of 40% can be achieved in CR9.6, while for CR20 the minimum load is 50 % of the reference full load. The latter will be fully explained later with the performance indicators previously described.

Nonetheless, the higher exhaust temperatures in CR9.6 bring a considerable

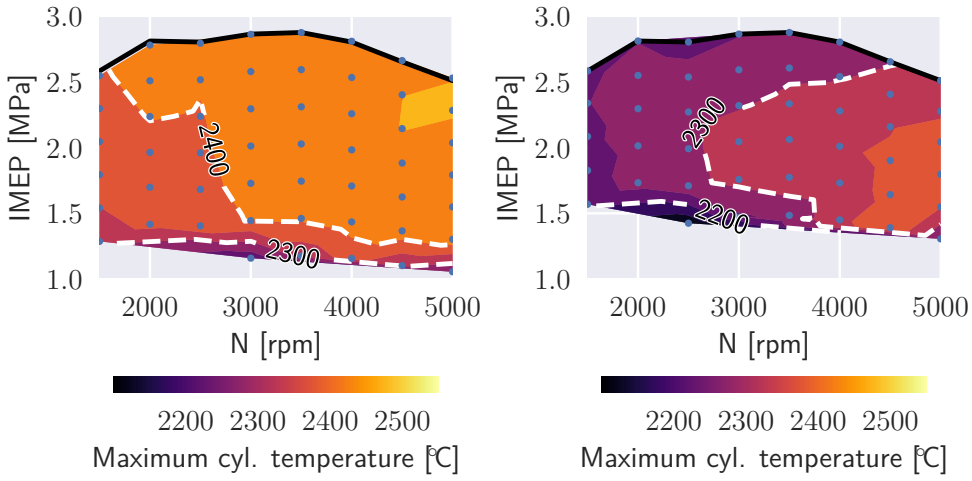

(a) CR 9.6 (b) CR 20

Figure 6.25: In-cylinder maximum temperature map at part-load using two different compression ratios

technological risk, where specialized materials that can withstand the high thermal stress must be used in the exhaust pipes in HE-10 (element 10 in Figure 6.2) and the turbines, which is avoided in CR20. Lower oxygen concentrations within the acceptable range can be implemented to reduce the temperatures, reducing the probability of jeopardizing the engine operation.

On the other hand, Figure 6.25 depicts the maximum in-cylinder temperatures for both cases. None of both cases surpasses the temperature limit (3,000 K, 2,700 °C) to avoid high thermomechanical stress in the cylinder. In CR9.6, higher values are obtained due to the higher fuel consumption, increasing with the engine speed and load. For CR20, it is observed that there is a maximum value of maximum in-cylinder temperature for each speed level. Load reduction leads to an advancement in the start of combustion, as explained. In this sense, a better centering of the combustion allows for reaching higher temperatures before the expansion stroke advances and the temperatures reduce. For higher load, as the combustion has to be delayed, heat release peaks are presented in moments where the expansion stroke has advanced, reducing the maximum in-cylinder temperature. Simultaneously, as the load keeps reducing, the amount of fuel decreases, and lower in-cylinder temperatures are reached, as observed.

6.7.2 Oxygen production cycle

Regarding the oxygen production cycle, Figure 6.26 shows the air mass flow driven for oxygen production. Larger air streams are found at higher loads and speeds, where the increasing power production demands more oxygen production. In this sense, CR9.6 can achieve air flows higher than 500 $kg\,h^{-1}$, while in CR20, the air mass flow surpasses 400 $kg\,h^{-1}$ at higher loads and speeds.

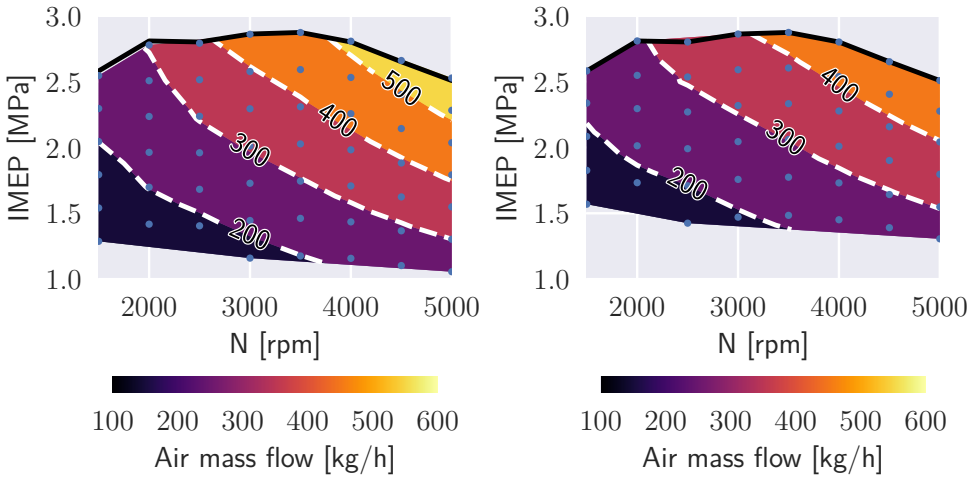

(a) CR 9.6 (b) CR 20

Figure 6.26: Map of air mass flow for oxygen production at part-load using two different compression ratios

Following this idea, Figure 6.27(a) and Figure 6.27(b) depict the air pressure at the inlet of the feed side of the membrane for both cases. Similar to the air mass flow behavior, the increments in the air feed pressure are found at increasing speed and load. Larger streams lead to more available enthalpy in the oxygen-depleted turbines, for which the air can be more pressurized, enhancing oxygen production. In CR9.6, air feed pressures higher than 0.5 MPa can be found, while the highest air feed pressure in CR20 is around 0.4 MPa. On the other hand, it is seen that feed pressures lower than 0.2 MPa are found at low loads and speeds, affecting oxygen production. Considering that the control strategy to regulate oxygen production (and consequently the power) is throttling the air inlet before the low-pressure compressor, modifying the control strategy to reduce oxygen production can benefit this region.

Finally, the air feed temperature of both cases is shown in Figure 6.27(c) and Figure 6.27(d). These values are highly dependent on the temperature of the exhaust manifold gases, which finally drive the whole oxygen production and impose the maximum air temperature limit at the membrane's feed side.

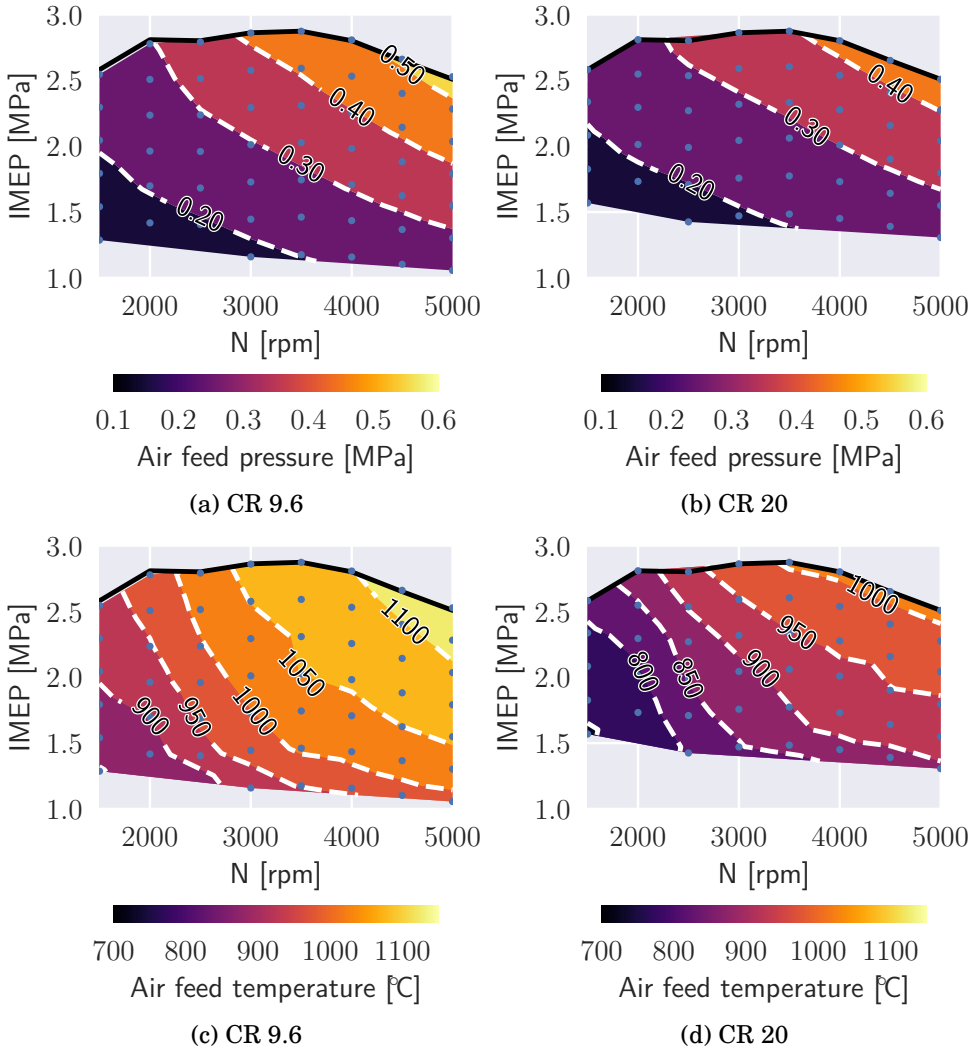

(a) CR 9.6

(b) CR 20

(c) CR 9.6

(d) CR 20

Figure 6.27: Map of air pressure and temperature at the inlet feed side of the membrane at part-load using two different compression ratios

In this sense, a similar trend in the air feed temperature is expected compared with the exhaust temperature. A considerable operation region operates at feed temperatures higher than 1,000 °C in CR9.6, a value that is slightly surpassed in CR20 only at engine speeds higher than 3,500 rpm at full load.

Being the latter said, Figure 6.28 shows the temperature of membrane operation for both cases. It is seen that similar values are obtained compared with the air feed temperature, which is different from Case 2 in chapter 5. For the engine, the sweeping gases come to the membrane after HE-10 (element 10 of the HEN), which is a high-temperature heat exchanger, where the exhaust gases do not reduce their temperature considerably due to a slight temperature difference with air. In this sense, sweeping gases are driven to the membrane with a similar temperature to the air, not affecting oxygen production due to a reduction in the temperature operation while reducing the oxygen partial pressure on the permeate side, promoting air separation.

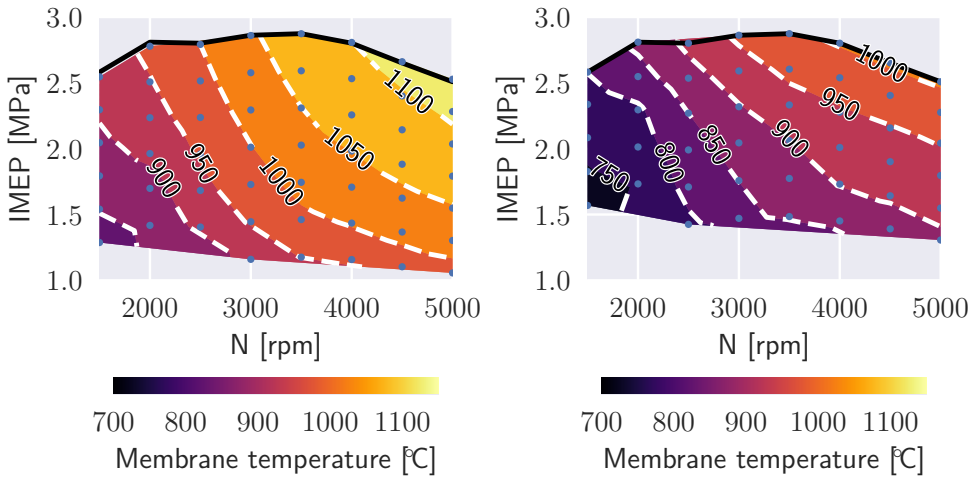

(a) CR 9.6 (b) CR 20

Figure 6.28: Map of membrane temperature at part-load using two different compression ratios

Considering the latter, Figure 6.29 shows the membrane efficiency for both cases. The conditions for oxygen production improve with the engine speed, where the best conditions regarding pressure and temperature are found. On the contrary, with the cases of chapter 5, the membrane efficiency behavior does not respond to the same reasons. In chapter 5, the same oxygen production is required, for which a modification in pressure and temperature conditions would change the membrane performance for a unique oxygen flow. For the engine in this chapter, higher efficiencies are associated with higher oxygen flows, while a reduction in membrane efficiency comes with a lower oxygen requirement. If an improvement in membrane efficiency is needed, the position of the turbines can be adjusted to increase the feed pressure and enhance oxygen production. This strategy will also reduce the air stream, which contributes to increasing the temperature efficiently, thus creating an additional source for enhancing

membrane operation.

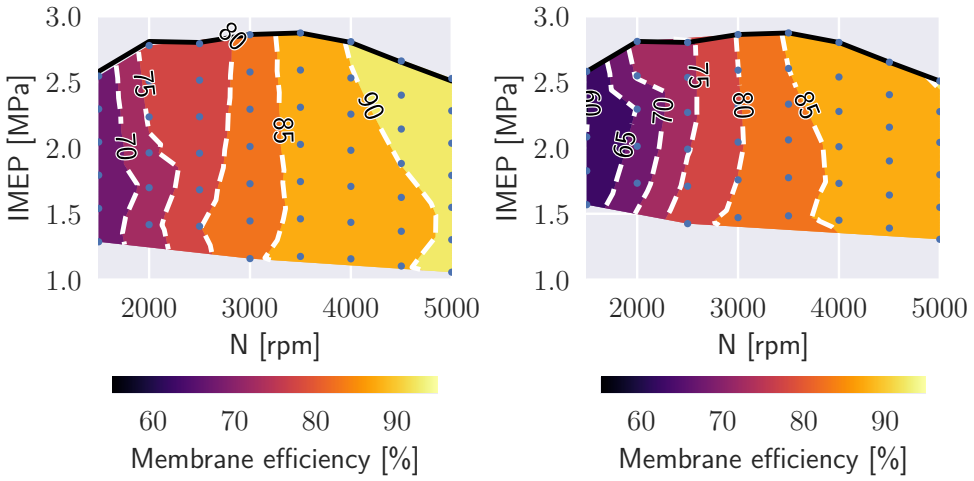

(a) CR 9.6

(b) CR 20

Figure 6.29: Map of membrane efficiency at part-load using two different compression ratios

Considering the latter, Figure 6.30 shows the membrane map for both cases, where different operation points of the engine are depicted. It is seen that increasing the engine load and speed leads to enhance the oxygen production, as expected, where higher partial pressures and temperatures are found in the membrane. Regarding engine speed, a similar trend is found. In CR9.6, the membrane performance increases linearly at a constant engine speed as the engine load increments. On the other hand, in CR20, this trend is not found where the points at 80 % load deviate from this behavior. The latter occurs considering that at this load, the combustion can be more advanced considering the pressure limit in the cylinder. In this sense, the membrane temperature reduces more than expected, affecting oxygen production and increasing the oxygen partial pressure at the feed side due to an increment in the oxygen concentration at the outlet of the feed side.

Figure 6.31 and Figure 6.32 shows the maps of the three implemented compressors for engine operation at both compression ratios. Most of the operation points in the air-driven compressors form a straight line in the high-efficiency zone, demonstrating that an appropriate selection has been made regarding the size of these turbomachines. When both engine scenarios are compared at the same speed and load, the compressors operate at higher compression ratios and air flows at CR9.6, resulting from the higher energy available. Special attention must be given when the engine works at low speeds under a load below 60 %, where the compressors operate at low speed, which can be harmful

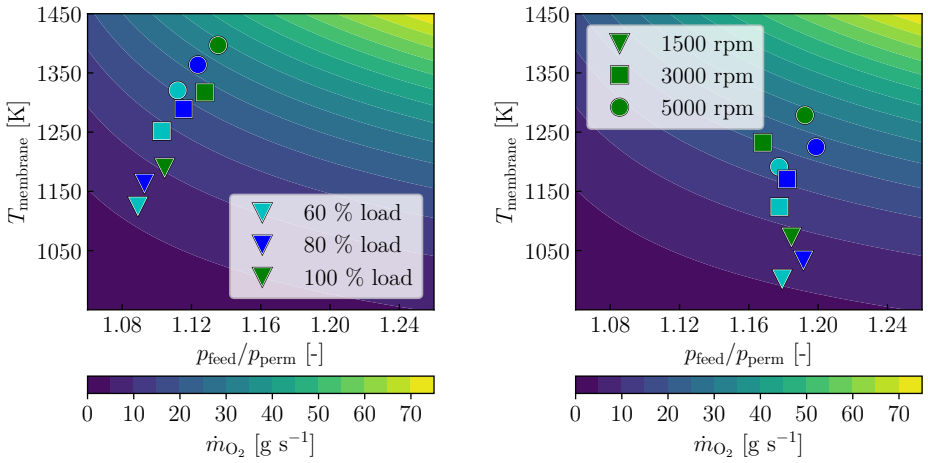

(a) CR 9.6

(b) CR 20

Figure 6.30: Map of membrane efficiency at part-load using two different compression ratios

considering possible transient conditions in real operation, leading to choke or surge conditions.

On the other hand, the O_2/EGR compressor works at low speeds independently of the engine's speed, load, or compression ratio. Compression ratios around 1.2 are found at maximum speed and load for both engine compression ratios while reducing speed, and load leads the turbomachine to barely compress the O_2/EGR to the engine intake. As explained before, for the full load cases, there is a considerable unbalance in the streams comparing the O_2/EGR compressor and the exhaust gases turbine, for which the available energy to boost the intake mixture is reduced. In this sense, the exhaust gas turbine mainly operates as a regulation valve, where a small portion of energy can be reused to increase the intake pressure of the engine.

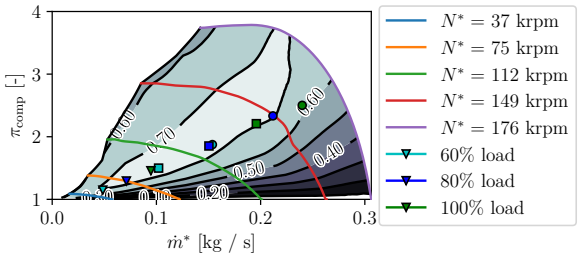

(a) Low pressure compressor

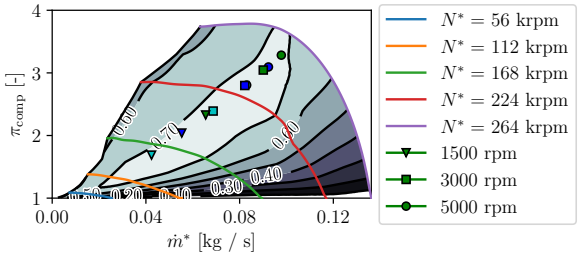

(b) High pressure compressor

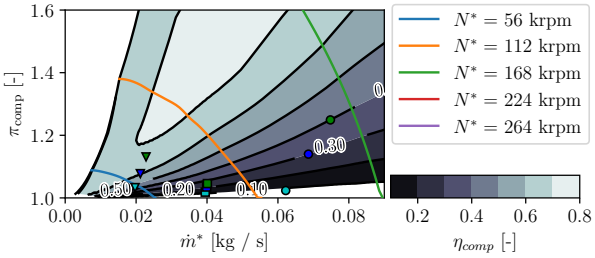

(c) O_2/EGR compressor

Figure 6.31: Compressor maps in CR9.6

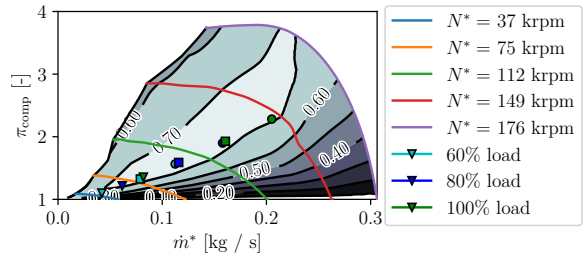

(a) Low pressure compressor

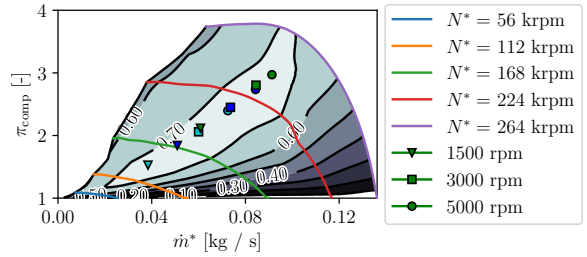

(b) High pressure compressor

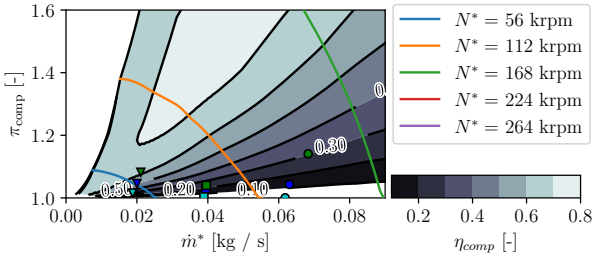

(c) O_2/EGR compressor

Figure 6.32: Compressor maps in CR20

6.7.3 Limits evaluation

The limits of the engine operation are presented, considering energy and operative limits. I_1 and I_2 are presented in Figure 6.33 for both studied compression ratios. I_1 increases with the engine load for both studied cases, while I_2 grows with the engine load and the engine speed reduction. Nonetheless, there is no uniformity regarding the value limiting oxygen production related to the available energy considering the whole speed range.

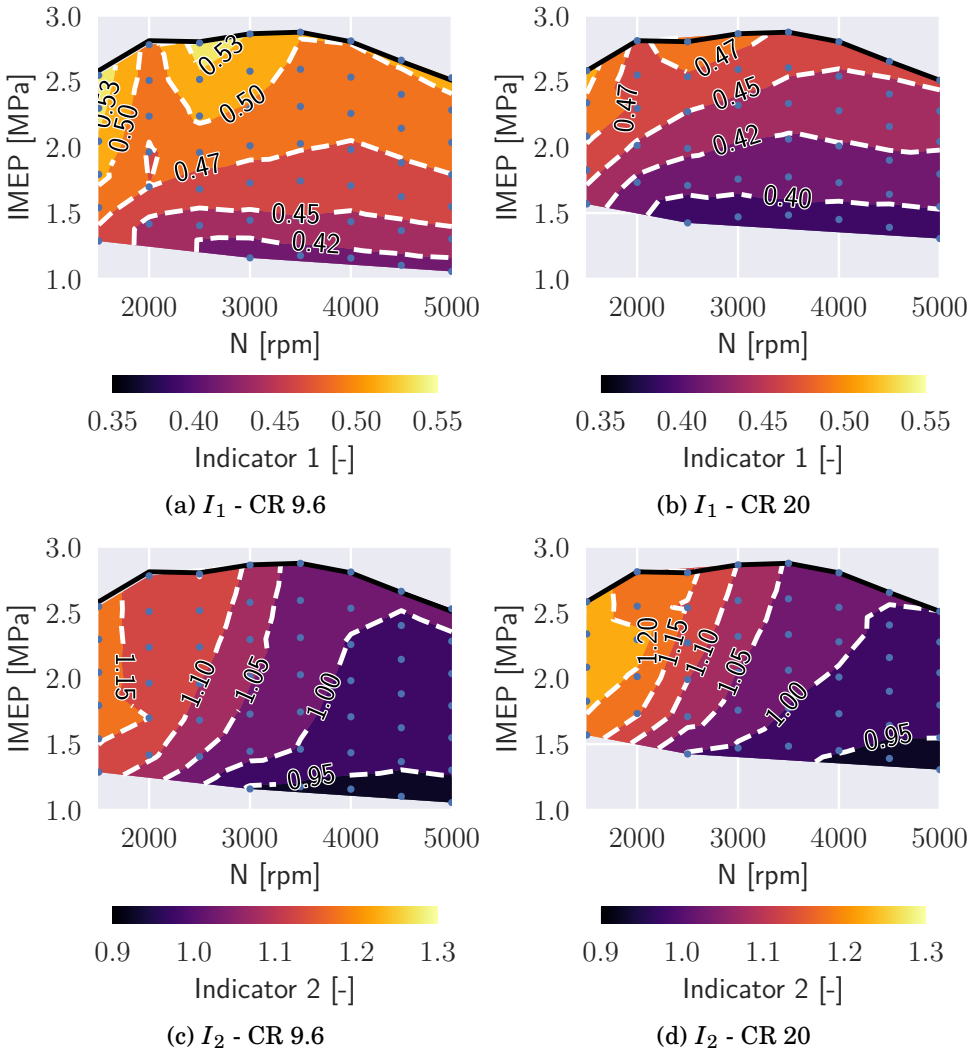

(a) I_1 - CR 9.6

(b) I_1 - CR 20

(c) I_2 - CR 9.6

(d) I_2 - CR 20

Figure 6.33: I_1 and I_2 at part-load using two different compression ratios

In this sense, I_1^* and I_2^* are presented in Figure 6.34. For CR9.6, it is seen that I_1^* values above 0.7 ensure a suitable engine operation, while for CR20,

this value grows to 0.8. These values can be interpreted as the minimum ratio between the heat released in the cylinders and the energy supplied to the air flow to produce 1 g of oxygen for each displaced liter of the engine. These values are different, considering that more heat losses are achieved in CR9.6 because this scenario has higher temperature levels.

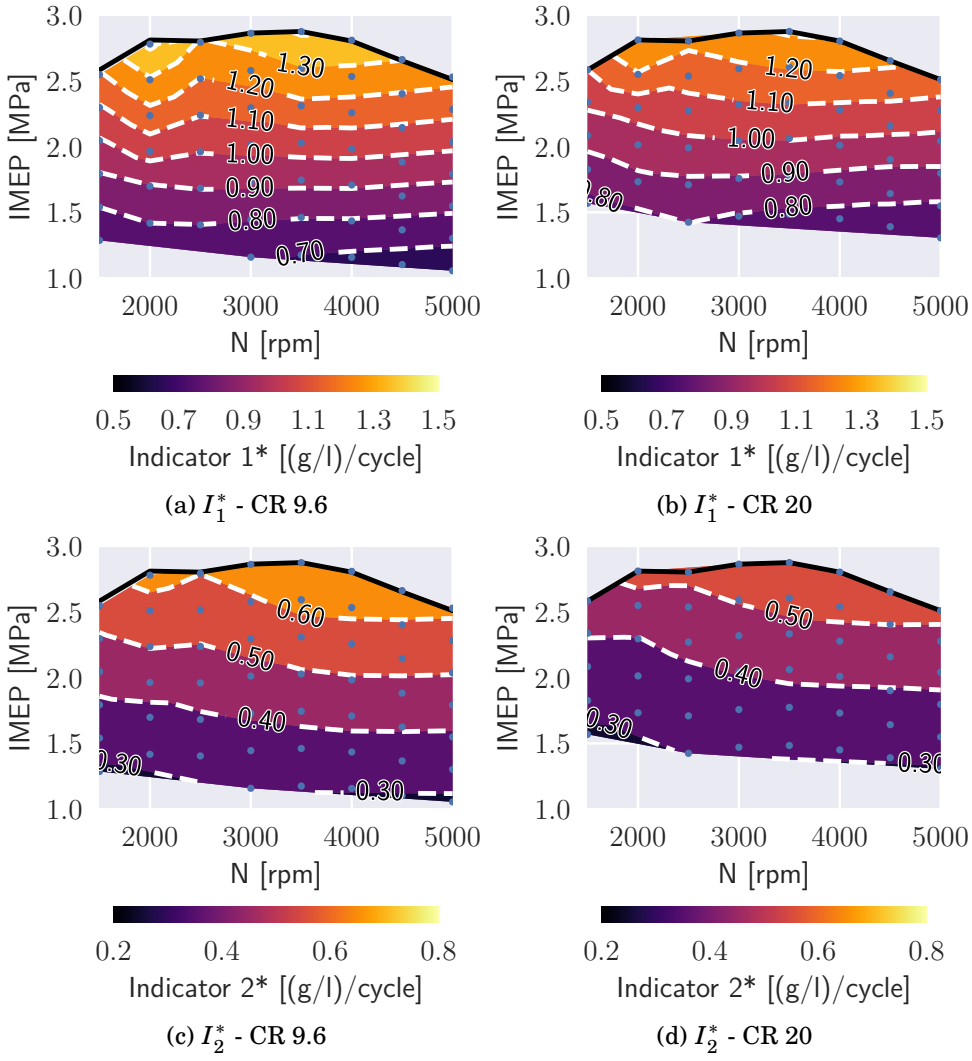

(a) I_1^* - CR 9.6

(b) I_1^* - CR 20

(c) I_2^* - CR 9.6

(d) I_2^* - CR 20

Figure 6.34: I_1^* and I_2* at part-load using two different compression ratios

Thus, I_2^* is considered for both cases. For this indicator, there is a clear limit for both compression ratios, meaning that the ratio of the available energy in the exhaust manifold to the energy supplied to the airflow to produce 1 g of oxygen for each displaced liter of the engine must be higher than 0.3 to ensure

proper operation.

For both I_1^* and I_2^*, operating below the obtained limits represent that the engine and oxygen production coupling is not self-sustaining and additional strategies can be applied to operate at lower conditions:

- Add an energy source, such as a heater or an electric compressor: This requires the addition of weight and volume to the system, as well as an increment in energy consumption.

- Increase the membrane area: The engine studies were made using a membrane area of $100\,m^2$, selected after a trade-off decision between membrane size and oxygen production enhancement. Increasing the membrane area forces the air separation while increasing the system size, which can be detrimental in the transport context.

- Varying the position of the turbines: This action increases the air pressure, promoting oxygen production.

- Delaying the combustion: This reduces the engine efficiency while increasing the exhaust temperature, thus, the available energy for oxygen production.

Further research must be performed on applying these strategies if the reduction of the engine load is the objective.

It also must be added that these indicators can be used for other engines that work under similar conditions. An example is the work performed by Arnau et al. [16], whose operation limits regarding the proposed indicators in this study are 0.223 and 0.454 for I_1^* and I_2^*, respectively. In this case, the authors work with an engine that is 70 % bigger than the one used in this study, using compression ignition and applying lean combustion in the cylinders, as well as the methods for energy usage are different.

On the other hand, Figure 6.35 shows the intake pressure for both engine compression ratios. In CR9.6, the engine intake operates below the atmospheric pressure for loads below 50 % while for CR20, the same scenario is observed below 60 %. Even if, in energy terms, the engine can operate at this load, there is a risk of atmospheric air entrance, which can produce the presence of nitrogen in the combustion process, promoting NOx generation. Because the studied points operate at a constant intake temperature, further research should be performed to keep the intake density while changing the temperature, elevate the intake pressure, and avoid nitrogen entrance to the system.

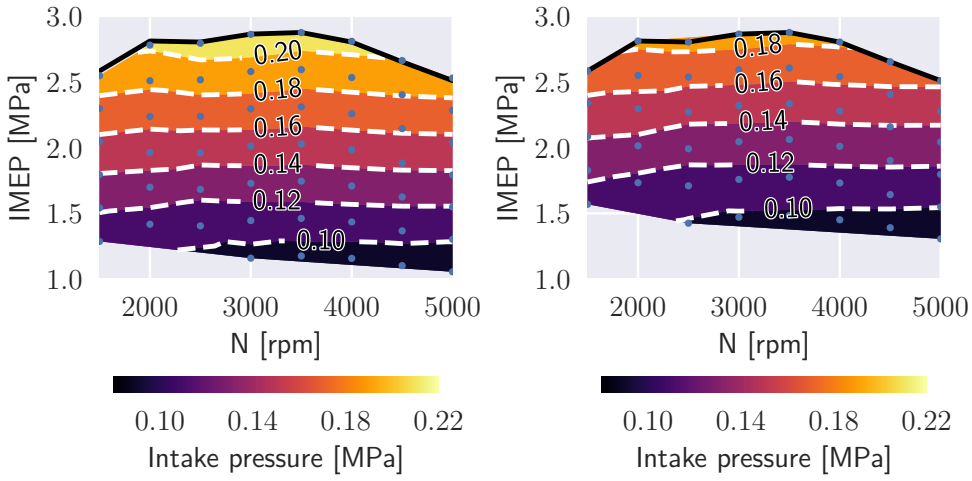

(a) CR 9.6 (b) CR 20

Figure 6.35: Map of engine intake pressure at part-load using two different compression ratios

6.8 Altitude

6.8.1 Engine

The behavior of the engine is studied at different altitudes by changing the boundary conditions (pressure and temperature in points 1, 15, and 23 of Figure 6.1), which are varied until a limitation in the engine working is found. CR9.6 and CR20 cases are used in the study, using an intake oxygen concentration of 30 %. The reference full load conditions are considered in this study, maintaining the power objective for each engine speed as the altitude increases. Additionally, the used atmosphere model in altitude is the international standard atmosphere ISO 2533:1975.

Considering the latter, Figure 6.36 shows the engine power at different altitudes in the studied engine speed range. It is seen that the system can provide the reference power for each case until an altitude of 5,000 m is reached for each engine compression ratio. At the mentioned altitude, the power starts to be reduced at high engine speeds for CR9.6, while for CR20 at low speeds (1,500 rpm), the power production is considerably diminished, thus, is not even depicted in the figure.

On the other hand, Figure 6.37 depicts the BSFC for both compression ratios. The fuel consumption slightly increases with the altitude, especially at low and medium speeds, which is not expected due to the pressure reduction in the boundary conditions.

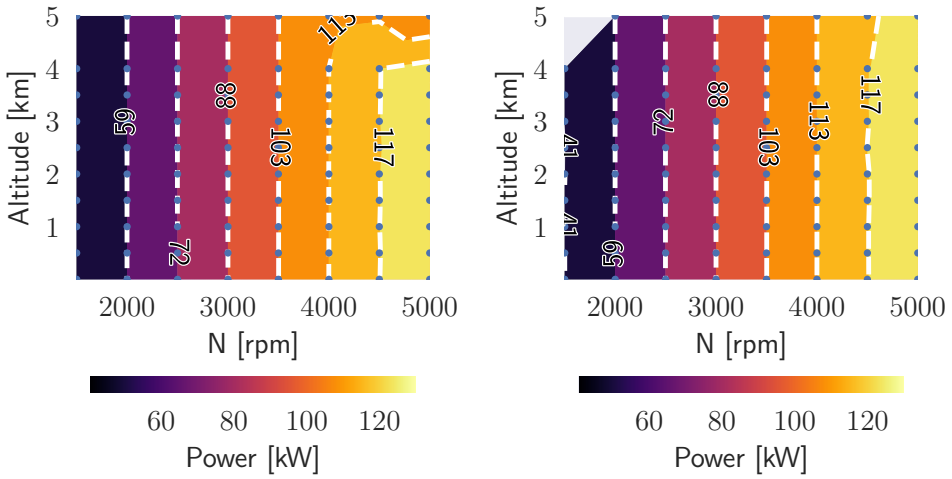

(a) CR 9.6 (b) CR 20

Figure 6.36: Engine power at different altitude conditions

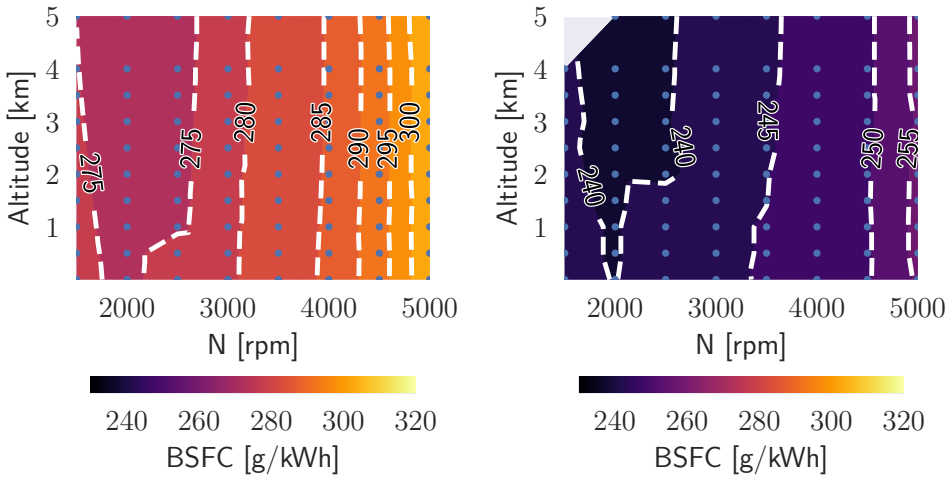

(a) CR 9.6 (b) CR 20

Figure 6.37: Engine brake specific fuel consumption at different altitude conditions

The improvement in the engine performance can be explained by considering a minor enhancement in mechanical efficiency, as seen in Figure 6.38. Similarly to fuel consumption, mechanical efficiency grows at low and medium speeds for both compression ratios. In this sense, it is seen in Figure 6.39 that the friction power does not show variation in any of the cases for which the mechanical efficiency varies due to changes in volumetric efficiency.

Thus, volumetric efficiency and PMEP are depicted in Figure 6.40 and Figure 6.41, respectively. The volumetric efficiency is higher at lower speeds and higher altitudes, reaching values higher than 98 % in CR9.6. Consequently, there is an improvement in the pumping loop performance, as depicted in Figure 6.41, where positive loop zones are generated, favoring the gas exchange process and improving the performance.

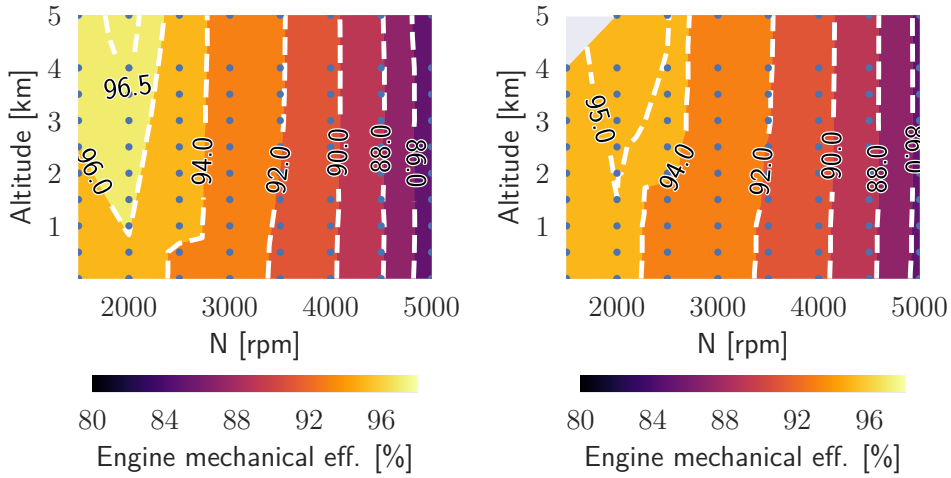

(a) CR 9.6

(b) CR 20

Figure 6.38: Engine mechanical efficiency at different altitude conditions

On the other hand, Figure 6.42 shows the exhaust manifold temperature for both engine compression cases. A slight reduction in the temperature value is seen, a consequence of the reduction in fuel consumption, without a significant effect on oxygen production.

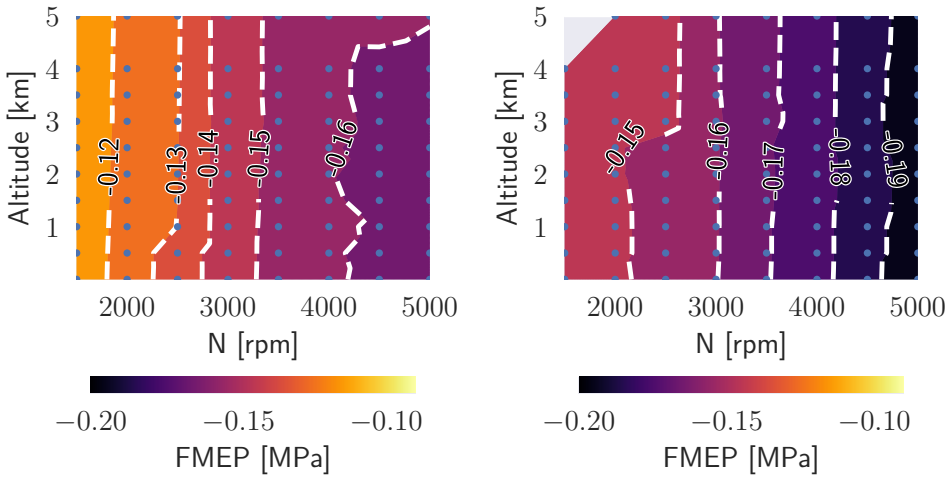

(a) CR 9.6 (b) CR 20

Figure 6.39: Engine FMEP at different altitude conditions

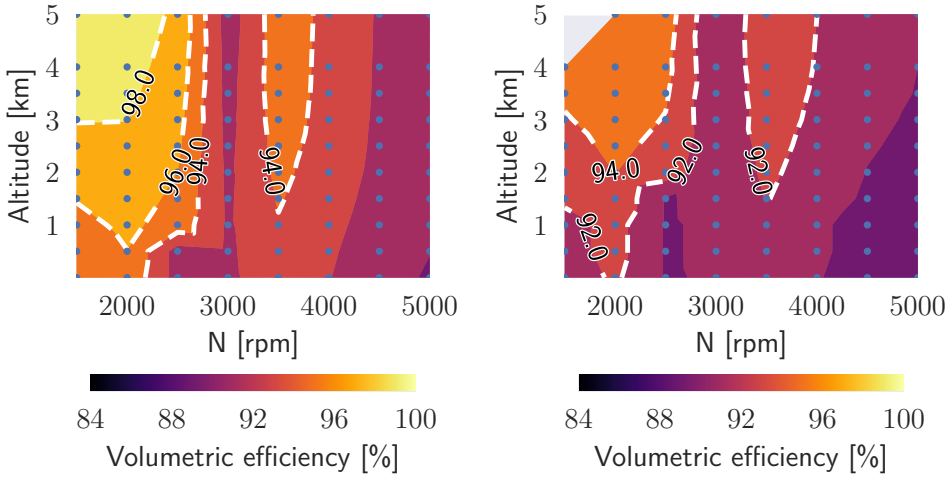

(a) CR 9.6 (b) CR 20

Figure 6.40: Engine volumetric efficiency at different altitude conditions

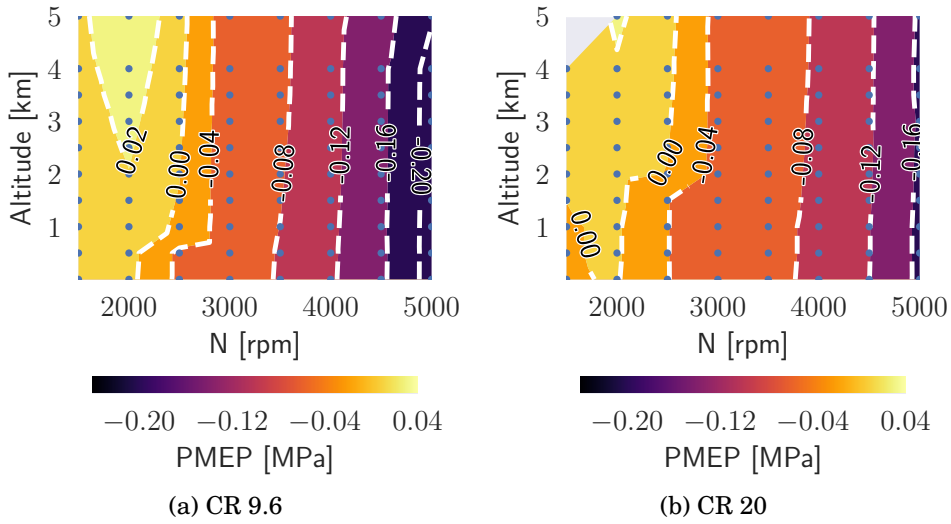

(a) CR 9.6 (b) CR 20

Figure 6.41: Engine PMEP at different altitude conditions

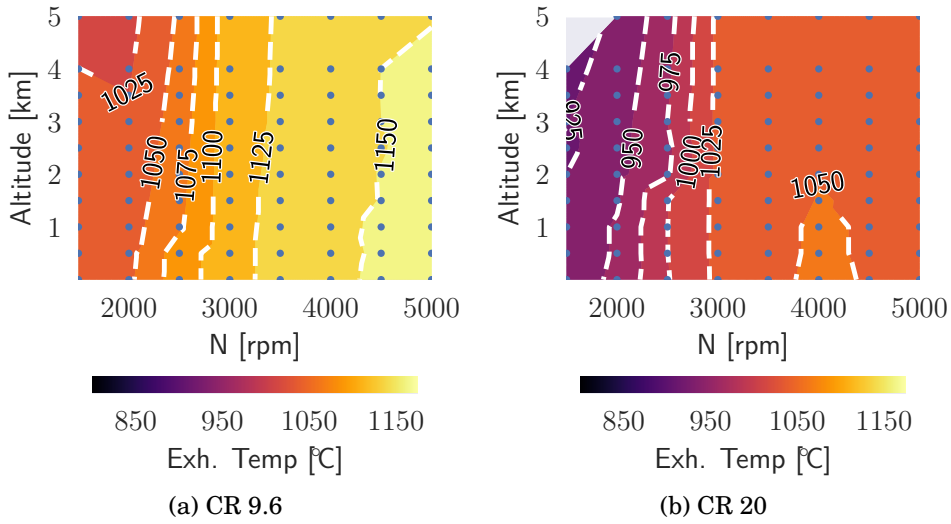

(a) CR 9.6 (b) CR 20

Figure 6.42: Exhaust manifold temperature at different altitude conditions

6.8.2 Oxygen production cycle

Thus, the air feed variables, such as mass flow, pressure, and temperature, also exhibit a small decrement, shown in Figure 6.43 and Figure 6.44, where the slight reduction of the available energy in the exhaust gases comes together with a proportional reduction in oxygen production requirements.

Considering the latter, Figure 6.45 shows the membrane map depicting different altitude and engine speed values for both engine compression ratios. At constant speed, it is seen that the membrane operation is performed almost at an isoline of oxygen production, where the points move to the top left direction as the altitude is decreased. This occurs due to the increase of the membrane temperature at lower altitudes, for which the oxygen partial pressure is decreased due to an improvement in the air separation. The latter reduces the oxygen concentration at the outlet of the feed side, decreasing the mean oxygen partial pressure in this side of the membrane.

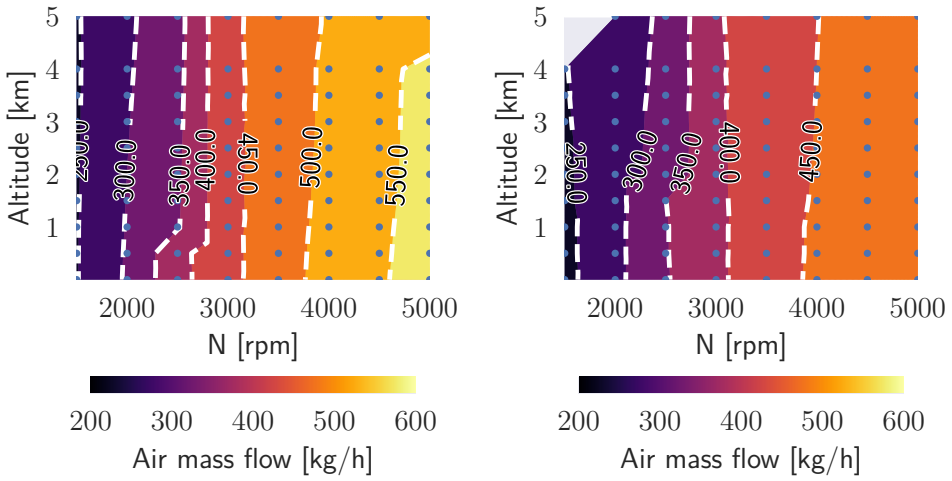

(a) CR 9.6 (b) CR 20

Figure 6.43: Air mass flow for oxygen production at different altitude conditions

This effect is less notorious as the engine speed increases, and in the CR9.6 case, there is more available energy to heat the membrane and increase the air pressure, for which the membrane almost operates in the same position in the map. Additionally, the effect of engine improvement is found mainly at low speeds, for which the higher variations in available energy are also found at these conditions, changing the operating point of the membrane.

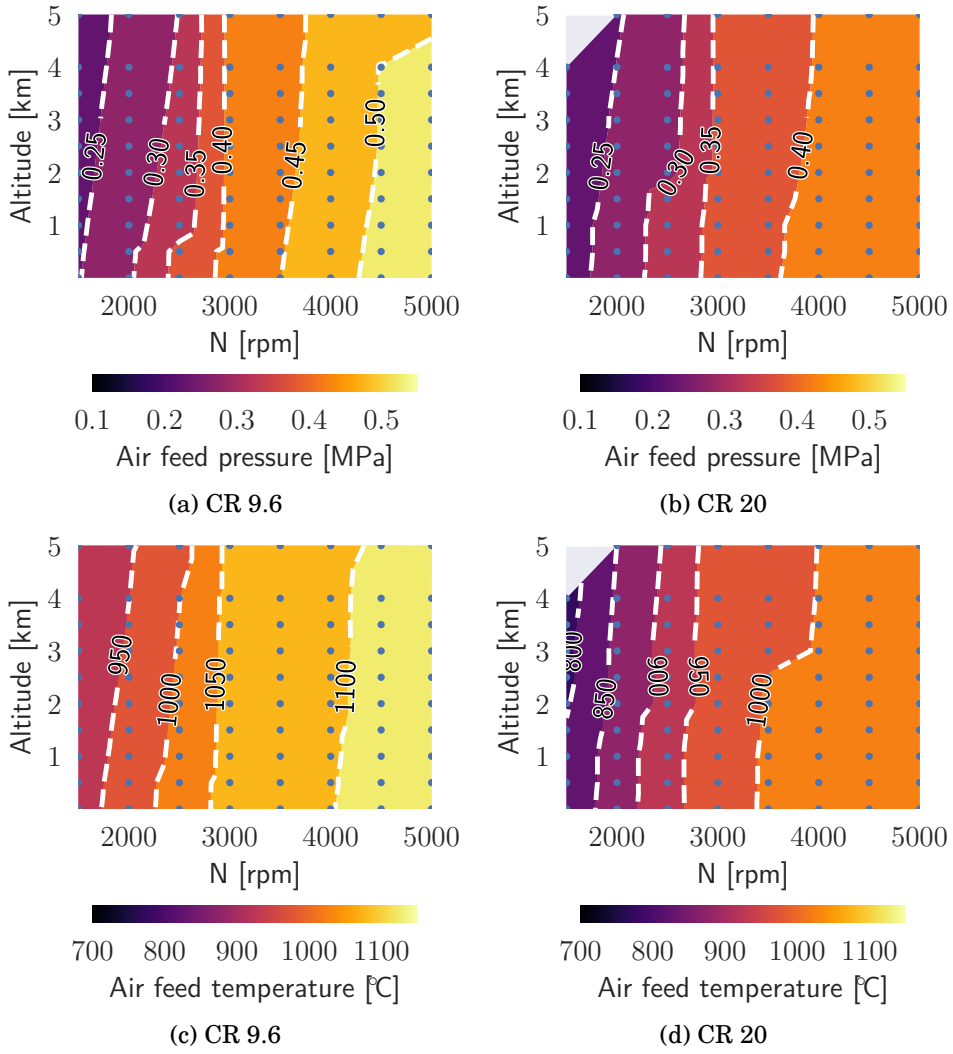

(a) CR 9.6

(b) CR 20

(c) CR 9.6

(d) CR 20

Figure 6.44: Air pressure and temperature at the inlet feed side of the membrane at different altitude conditions

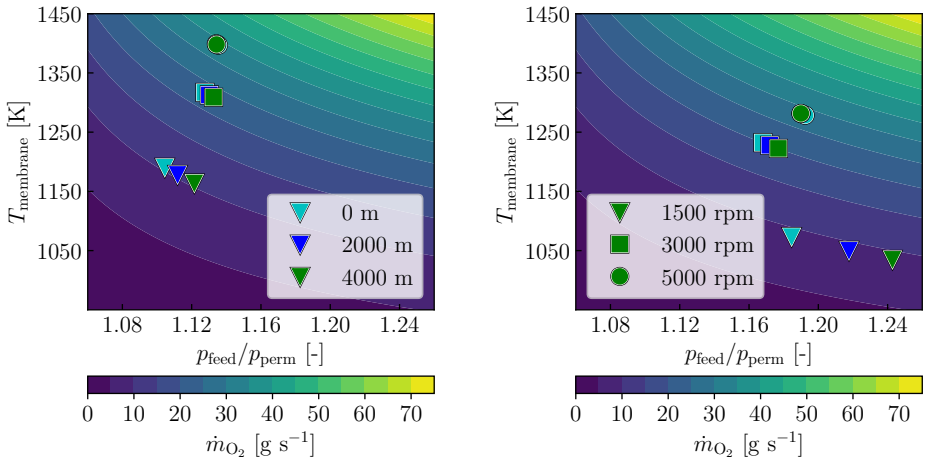

(a) CR 9.6

(b) CR 20

Figure 6.45: Map of membrane efficiency at different altitude conditions

On the other hand, Figure 6.46 and Figure 6.47 show the compressor maps for both studied cases at different altitude conditions and engine speeds. Similar to the partial load study, the operation points in the air-driven compressors work, generating a straight line in the central zone of the map, which is a suitable region for operation, with a considerable distance from the surge and choke regions.

For both compressors, it is seen that the altitude increment leads to increased speed, where the density reduction leads to an increasing corrected mass flow, while a higher compression ratio is required to achieve the membrane conditions for oxygen production. In this sense, special attention must be given at high engine speeds and altitude, where the operation is performed near overspeeding conditions. For example, operating the engine at 5,000 rpm at an altitude of 4,000 m leads the low-pressure compressor to run at the maximum speed of the reported map, for which the thermal loads in the component can jeopardize the performance.

Thus, it can be said that the reduction in power production as the altitude increases is due to an increase in the total compression ratio required for both compressors to meet the needed conditions for oxygen production in the membrane. In this sense, the available energy in the exhaust gases is insufficient to compress the air mass flow, and the power production decays. The turbine's position can be modified to increase the air pressure to improve the air compression and achieve the oxygen production required.

In contrast, it is seen that at higher altitudes, the performance of the O_2/EGR compressor is enhanced. The expansion ratio of the exhaust gases turbine

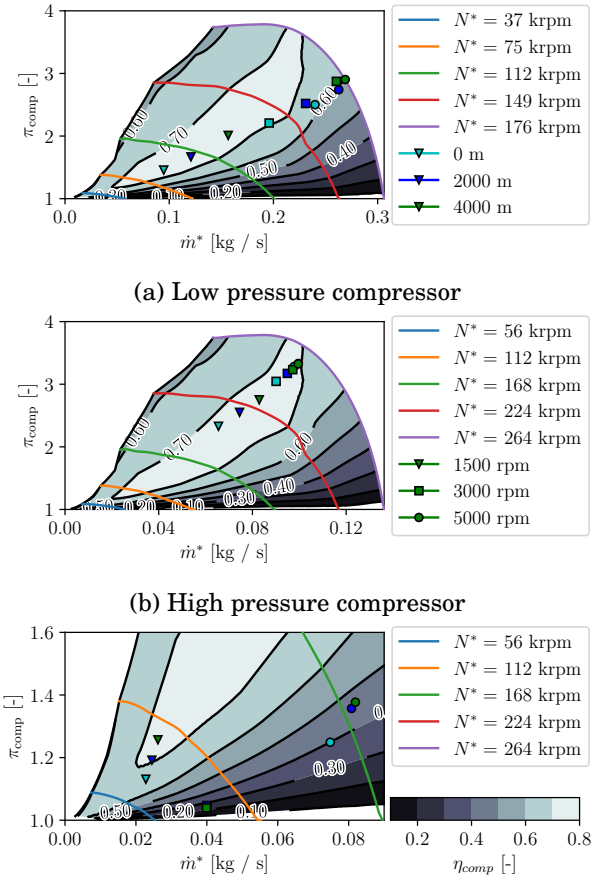

(a) Low pressure compressor

(b) High pressure compressor

(c) O_2/EGR compressor

Figure 6.46: Compressor maps in altitude conditions at CR9.6

increases due to the decrease in the outlet pressure of the turbine, for which the power to move the associated compressor increases. The latter leads to an increase in the intake pressure of the engine, being the primary reason for the volumetric efficiency improvement.

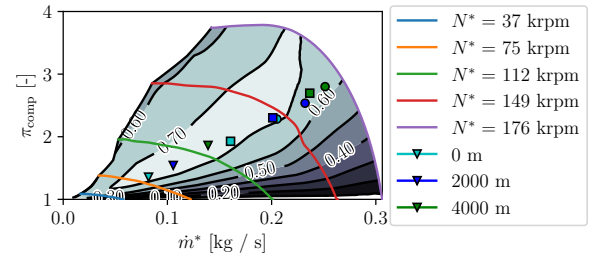

(a) Low pressure compressor

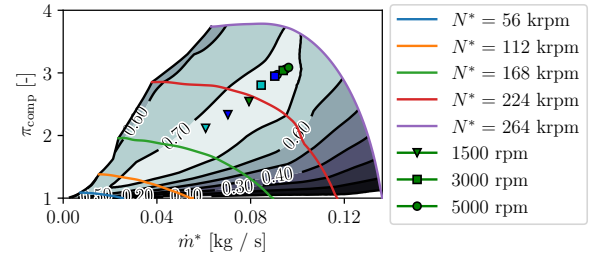

(b) High pressure compressor

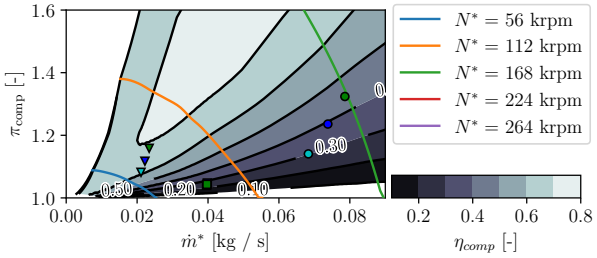

(c) O_2/EGR compressor

Figure 6.47: Compressor maps in altitude conditions at CR20

6.9 Summary

The coupling of a spark ignition engine working under oxycombustion with an oxygen production cycle is studied in this chapter. The engine's exhaust gases boost the oxygen production cycle, consisting of a set of turbochargers, a heat exchanger network, and a membrane, similar to the configurations found in chapter 4 and chapter 5.

Initially, the influence of the oxygen concentration and the engine compression ratio in the system performance is examined, being compared with the conventional operation. Higher compression ratios in oxycombustion enhance the fuel consumption of the engine. Nonetheless, the combustion must be delayed to maintain the maximum pressure limit, reducing the potential engine performance.

Additionally, higher oxygen concentrations promote the reactivity of the mixture in the cylinder, reducing the combustion duration. In contrast, the start of combustion must be delayed to avoid combustion issues affecting fuel consumption. The medium oxygen concentration (30 %) was found to be optimum, where a trade-off condition is identified that permits the engine compression ratio to increase up to 20, achieving the best engine performance in this study.

The physicochemical properties of the main bulk gases, CO_2 for oxycombustion and N_2 for conventional cases, are the leading cause of the differences between oxycombustion and conventional operation. In conventional cases, the presence of N_2 leads to more delayed combustion to avoid instabilities in conventional operation. In contrast, in oxycombustion cases, the CO_2 leads to worse compression and expansion strokes performance due to the in-cylinder mixture's lower specific heat capacities ratio. Additionally, a lower reactivity due to CO_2 presence leads to longer combustion processes, affecting performance.

On the other hand, increasing the compression ratio implies a reduction in the available energy for the oxygen production cycle and lower fuel consumption, for which less oxygen is required, compensating for the reduction in the available energy. Therefore, an autonomous coupled system was obtained, allowing changes in the working conditions and generating the demanded oxygen according to the power output needed.

Additionally, the system's behavior at full-load operation in a wide range of speeds is assessed, comparing its performance with the conventional operation. In this sense, the study was extended by considering a medium oxygen concentration (30 %) at the engine intake, implementing the original compression ratio (9.6) and 20 at a wide range of engine speeds (1,500 to 5,000 rpm). The engine working under oxycombustion achieved the reference full load values, showing a sustainable system from an energy point of view in the studied speed range. For CR9.6, the oxycombustion engine has similar fuel consumption values to the CS1 case, while CR20 has a similar fuel consumption to CS2.

Operative limits at part-load operation of the system were determined, considering indicators that help to identify those limits. For CR9.6, lower loads than 40 % cannot be achieved without additional energy sources or control strategies. On the other hand, for CR20, lower loads than 50 % cannot be achieved. Two primary indicators, I_1^* and I_2^*, are used to determine energy limits, finding similar limit values for both engine compression ratios. These indicators can be applied to engines with similar operation conditions and specifications, expecting comparable results. Increasing the membrane area, delaying the combustion, adding an energy source (a heater or an electric compressor), and varying the position of the turbines were identified as possible actions to reduce the engine load.

However, lower loads than 50 % for CR9.6 and 60 % for CR20 are also limits in terms of possible backflow presence due to an intake pressure lower than atmospheric conditions, which can lead to the presence of N_2 in the combustion process. Operating at higher intake temperatures can lead to an increase in the intake pressure. However, further research must be performed on this topic.

For the altitude operation, it is seen that the system exhibits a correct operation until an altitude of 4,000 m. A limitation is found regarding the increasing compression ratio required for the driven air to reach the needed membrane conditions, disposing of similar available energy as the altitude increases. Nonetheless, the engine's performance is improved due to an enhancement in the volumetric efficiency, the product of the increasing efficiency of O_2/EGR compressor because of a higher expansion ratio of the exhaust gases turbine, which increases its available energy.

That said, oxycombustion used in a spark-ignition engine coupled with a membrane-based oxygen production cycle exhibits a promising performance where different load and altitude conditions can be operated. In addition, high compression ratios and advanced spark timings can be performed, leading to significant benefits in fuel consumption. Also, an oxygen production cycle based on a MIEC membrane can be used in the engine operation to fulfill the oxygen requirements by taking advantage of the exhaust gases energy. This cycle has demonstrated to be capable of operating in different oxygen concentrations and compression ratios, as well as engine speeds and load conditions.

6.10 References

[12] J. Serrano, J. Martín, J. Gomez-Soriano, and R. Raggi. "Theoretical and experimental evaluation of the spark-ignition premixed oxy-fuel combustion concept for future CO2 captive powerplants". In: *Energy Conversion and Management* 244 (Sept. 2021), p. 114498. DOI: 10.1016/j.enconman.2021.114498 (cit. on pp. 2, 59, 151, 156, 161).

[13] J. R. Serrano, J. M. Díaz, J. Gomez-Soriano, and R. Raggi. "Exploring the Oxy-Fuel Combustion in Spark-Ignition Engines for Future Clean Powerplants". In: *ASME 2022 ICE Forward Conference*. American Society of Mechanical Engineers, Oct. 2022. DOI: 10.1115/icef2022-89167 (cit. on pp. 2, 33, 34, 42, 58, 59, 61, 62, 151, 156, 161).

[15] J. Serrano, F. Arnau, L. García-Cuevas, and V. Farias. "Oxy-fuel combustion feasibility of compression ignition engines using oxygen separation membranes for enabling carbon dioxide capture". In: *Energy Conversion and Management* 247 (Nov. 2021), p. 114732. DOI: 10.1016/j.enconman.2021.114732 (cit. on pp. 3, 56, 152, 153).

[16] F. Arnau, G. Bracho, L. García-Cuevas, and V. Farias. "A strategy to extend load operation map range in oxy-fuel compression ignition engines with oxygen separation membranes". In: *Applied Thermal Engineering* 226 (May 2023), p. 120268. DOI: 10.1016/j.applthermaleng.2023.120268 (cit. on pp. 3, 202).

[75] A. Mohammed, A. Elkhazraji, S. Jan, and B. Johansson. "A Study on the Performance and Emissions of HCCI Oxy-Fuel Combustion in a CFR Engine with Recirculated Carbon Dioxide". In: *SAE Technical Paper Series*. SAE International, Sept. 2020. DOI: 10.4271/2020-01-2065 (cit. on pp. 33, 161).

[137] J. R. Serrano, P. Piqueras, J. D. la Morena, A. Gómez-Vilanova, and S. Guilain. "Methodological analysis of variable geometry turbine technology impact on the performance of highly downsized spark-ignition engines". In: *Energy* 215 (Jan. 2021), p. 119122. DOI: 10.1016/j.energy.2020.119122 (cit. on pp. 151, 154).

[138] F. Arnau, J. Benajes, D. Catalán, J. Desantes, L. M. García-Cuevas, J. Serra, and J. R. Serrano. "Internal Combustion Engine and operating method of same". Spanish. WO 2020/193833 A1. 2020 (cit. on p. 151).

[139] N. Komninos and E. Rogdakis. "Design considerations for an Ericsson engine equipped with high-performance gas-to-gas compact heat exchanger: A numerical study". In: *Applied Thermal Engineering* 133 (Mar. 2018), pp. 749–763. DOI: 10.1016/j.applthermaleng.2018.01.078 (cit. on p. 155).

[140] X. Li, Y. Pei, T. Ajmal, K.-J. Rana, A. Aitouche, R. Mobasheri, and Z. Peng. "Numerical investigation on implementing Oxy-Fuel Combustion (OFC) in an ethanol-gasoline Dual-Fuel Spark Ignition (DFSI) engine". In: *Fuel* 302 (Oct. 2021), p. 121162. DOI: 10.1016/j.fuel.2021.121162 (cit. on pp. 161, 162).

[141] M. Ditaranto and J. Hals. "Combustion instabilities in sudden expansion oxy–fuel flames". In: *Combustion and Flame* 146.3 (Aug. 2006), pp. 493–512. DOI: 10.1016/j.combustflame.2006.04.015 (cit. on p. 161).

CHAPTER 7

Conclusions and future works

Contents

7.1 Introduction

THERE is increasing interest in mitigating pollutant and greenhouse emissions due to their effect on the atmospheric composition and properties, globally affecting the climate and locally reducing the air quality, creating health issues.

Therefore, global authorities are making an effort to control the effects from different human activities by creating regulations that set emission limits for the different industrial sectors, as well as promoting the research and application of different strategies to reduce emissions.

In this context, oxycombustion appears as a promising alternative, showing benefits such as eliminating NOx emissions, an easy coupling within industrial contexts, and the possibility for carbon capture. Several studies have demonstrated the benefits of oxycombustion within industrial facilities.

Oxycombustion requires a high-purity oxygen source, which is usually an air separation system that operates within the facility where it is required. The most extended method for air separation, cryogenic air separation (CAS), usually performs with high power requirements, reducing the efficiency of the system where it operates.

In this context, membrane-based air separation appears as an attractive alternative for oxygen production, displaying better energy consumption than CAS.

The current thesis has studied three systems demonstrating the feasibility of oxygen production cycles and oxycombustion in industrial contexts. Initially, the study of an oxygen production cycle within a ceramic plant revealed its competitive behavior compared with other air separation systems.

Then, this oxygen production cycle is adapted to operate coupled within an oxycombustion power plant, where two different membrane configurations are studied. Compared with the base case, which operates with CAS, a performance improvement was achieved.

Finally, the oxygen production cycle coupling within a spark-ignition engine was explored. Firstly, the operation under oxycombustion is compared with the conventional operation, showing promising results because of oxycombustion operation. The oxygen production cycle is also examined, showing good operation under the studied cases. Then, different loads and atmospheric conditions were studied, finding limits regarding energy availability and operative limitation.

Thus, this chapter presents the primary conclusion of the mentioned studies, showing the increasing complexity level of the thesis. Finally, some limitations of the thesis results are presented, and possible future works are proposed.

7.2 Oxygen production cycle for an industrial application

A system with a high-temperature source for oxygen production in an industrial context was studied to assess the feasibility of membrane-based oxygen production compared with current oxygen market prices and other oxygen production cycles. The initial idea is a configuration capable of producing around $0.12\,\mathrm{kg\,s^{-1}}$ ($10.4\,\mathrm{t\,d^{-1}}$), a typical production for a ceramic plant in the Spanish context. This study was performed to demonstrate the feasibility of membrane-based oxygen production in terms of energy and economic costs, to later be applied in power production contexts.

In this sense, two cases of the cycle are proposed: Case 1 uses an electric compressor for vacuum generation in the oxygen line, without any additional heat source besides the recycling gases from the other process of the plant. Case 2 uses a turbocharger for vacuum generation, where the turbine uses the available energy between two air-driven turbocharger stages to move the compressor in the oxygen line while using an additional heat source that ensures 1,000 °C in the membrane operation. For both cases, off-design conditions are studied, considering the initial objective of oxygen production for component sizing but assessing a wide range of controllable cycle parameters.

Both cases differ in behavior, exhibiting different oxygen production levels and costs. Case 1 maximum production point achieved the initial objective goal of $0.12\,\mathrm{kg\,s^{-1}}$ with an operative cost 38 % lower than the wholesale market prices. Moreover, an optimum cost point was also found, with a production of $0.060\,\mathrm{kg\,s^{-1}}$, and operating costs are $23.7\,€\,\mathrm{t^{-1}}$, 53 % lower than the reference market price.

In contrast, Case 2 optimum production point doubles the initial design objective ($0.227\,\mathrm{kg\,s^{-1}}$), although with a $61\,€\,\mathrm{t^{-1}}$ cost is achieved. This value is 22 % higher than the reference market price of oxygen, achieved due to the constant membrane feed temperature of 1,000 °C that elevates the feed temperature.

Moreover, there is no optimum cost point in this case; however, if the reference production is considered, a minimum operating cost of $36\,€\,\mathrm{t^{-1}}$ was achieved, 28 % lower than the reference price.

The results also conclude that both cases can be implemented in industrial facilities with similar oxygen demand to those obtained in the study, considering the availability of high-temperature energy sources, such as recycling gases, for energy exploitation to drive the cycle properly. The reference oxygen production goal was achieved, accounting for good profitability in a wide range of the studied points compared to wholesale market prices.

Additionally, applying one of both cases depends on the context, considering

the energy availability, the economic resources, and oxygen demand, where higher oxygen productions are found in Case 2, while a more profitable scenario is found for Case 2.

Specifically, Case 1 exhibits a comfortable controllability, where different oxygen demands can be achieved depending on the requirement variations of the facility where the cycle is installed. For a particular oxygen demand, the best option can be selected, considering the energy consumption and costs to select the values of the controllable parameters.

Additionally, membrane-based oxygen production has been demonstrated to be an energy-competitive alternative compared with other oxygen production methods, reaching higher oxygen purities due to the exclusive selectivity of oxygen of the MIEC membranes.

On the other hand, additional conclusions were obtained, applicable to the two following case studies. For example, it was found that the external addition of heat, as for Case 2, increases the oxygen production cost. In this sense, correctly using heat sources within the facilities is the most efficient option. The oxygen partial pressure reduction in the permeate side is preferable using an uncoupled mechanism independent of air driving to avoid inefficient energy use.

Finally, implementing four-end membranes that add a sweeping gas for oxygen partial pressure can improve oxygen production performance, avoiding energy consumption for vacuum generation. However, an appropriate sweeping has to be selected, as the cost for separating it from oxygen has to be low enough to not offset the reduction in energy consumption, if high-purity is required while using four-end membranes.

7.3 Coupling of an oxygen production cycle and a power production cycle under oxycombustion

The second case study of this thesis was the coupling of membrane-based oxygen production with a power plant using a medium-temperature source within the process to drive the air separation process. The Graz cycle is the studied power plant, a high-efficiency configuration developed at the Graz University of Technology that operates with oxycombustion, whose primary oxygen source is a cryogenic air separation process.

This study was performed to further push the limits of the oxygen production cycle, using a lower quality energy source compared with the previous case study. There is an advance in understanding these cycles' behavior by increasing the complexity by adding a membrane configuration in the study (four-end membranes). The study also provides a step in the membrane-based oxygen production research, where the effect of coupling the cycle within an industrial

context is studied regarding performance variations, comparing the obtained results with typical oxygen production (CAS).

Two different membrane-based configurations were considered, using three-end and four-end membranes; thus, the mechanisms for oxygen partial pressure reduction in the permeate side differ, changing the interactions with the power cycle. The operation of these configurations is compared with the base case that operates with CAS.

The first membrane-based case (Case 1) uses a three-end membrane with a set of electric compressors for vacuum generation to reduce the oxygen partial pressure on the permeate side. The second membrane-based case (Case 2) has a four-end membrane, which is swept with the outlet stream from the first stage of recycling gases compression (C1), commonly at conditions near 1.5 MPa and 480 °C. The latter stream transports oxygen production. For both cases, the primary energy source is the stream between the second and the third stages of the high-temperature turbine (HTT).

Case 1 has an optimum operating point that leads to net power production of the Graz cycle of 404.67 MW with a thermal efficiency of 54.08 %. These results improved the delivered power of the base case in 4.67 MW and the thermal efficiency in 0.61 %. The membrane of this optimum point operates at 0.4 MPa at feed pressure, 0.02 MPa at permeate pressure, and 825 °C of feed temperature.

On the other hand, the system performance is enhanced using the Case 2 configuration. This case has an optimum net power production of 417.24 MW, providing a thermal efficiency of 55.76 %, higher in 17.24 MW of power and 2.30 % points of thermal efficiency compared with the base case.

7.4 A spark-ignition engine under oxycombustion with oxygen production in situ

The third case study of this thesis was the coupling of membrane-based oxygen production with a spark-ignition engine using a high-temperature source (exhaust gases) to drive the air separation process. The base design of the system comes from a patent developed within the institute in which this thesis was performed.

This is the final step in this succession of studies, where a power production unit with pulsating flow works at different conditions, assessing the system's performance regarding fuel consumption and energy conditions for oxygen production. This section's complexity increases because different combustion conditions are assessed, and the available energy to drive oxygen production varies considerably. In this case, the effect of the coupling working between both

systems is more pronounced compared with the power plant case. Additionally, a comparison with conventional combustion operation is also made.

In general, promising system performance was found in the different studied conditions, where a membrane-based oxygen production cycle exhibited the potential to provide the oxygen needs of the engine by using the exhaust gases energy.

7.4.1 Oxycombustion and conventional modes comparison

The first step in this case study was the examination of different oxygen concentrations, compression ratios, and speeds, considering their effect on the engine and oxygen production performance while establishing the differences with the conventional operation.

A study at medium speed (3,000 rpm) and full load was performed, assessing the influence of the oxygen concentration and compression ratio. Increasing the compression ratio enhances the fuel consumption, as naturally excepted, but requires a combustion delay to avoid surpassing the maximum pressure limit. The latter limits the potential for performance enhancement.

A trade-off condition at medium oxygen concentration was found, where a balance between combustion duration, the start of combustion, and intake conditions is achieved, permitting the increment of the engine compression ratio up to 20, which leads to the system's best performance.

Regarding the oxygen production operation, higher compression ratios reduce the exhaust gases' temperature, affecting the available energy for oxygen production. Nonetheless, the performance enhancement reduces the oxygen demand, compensating for the enthalpy flow reduction. In this sense, it is seen that a system that allows for different working conditions was obtained.

A comparison of the properties of CO_2 and N_2 explains the main differences between oxycombustion and conventional operation. The conventional case is limited by the high reactivity of air combustion, requiring more delayed combustion and lower engine compression ratios. On the other hand, CO_2 presence as the primary bulk gas leads to a less efficient process in the compression and expansion strokes due to a higher lower specific heat ratio. Additionally, the high CO_2 concentration increases the combustion duration due to reduced reactivity.

On the other hand, the system was studied at full-load operation in a wide range of engine speeds, comparing the performance with the conventional operation. This part of the study considered the mentioned optimum conditions regarding oxygen concentrations found in the medium speed study while implementing the original and the maximum possible engine compression ratios. The engine working under oxycombustion achieved the reference full load values, showing a sustainable system from an energy view in the studied speed range,

considering oxygen production. Due to the possibility of engine compression ratio increment, the benefits of both conventional cases can be obtained in oxycombustion, where high power production and reduced fuel consumption are achieved in the oxycombustion best case.

7.4.2 System operative limitations (Part-load and altitude)

The second step in this case study is assessing the engine working at different loads and altitude conditions to find the operative limits of the system.

The original (CR9.6) and highest possible (CR20) engine compression ratios with a medium oxygen concentration were used to perform this part of the study. Different load limits were found for both compression ratios. For CR9.6, the lower possible load was found at 40 %, while for CR20 the limit is 50 %. The indicators used to evaluate energy limits achieved similar values for both compression ratios. They can be applied to engines with similar operation conditions and specifications, expecting comparable results.

On the other hand, lower loads than 50 % for CR9.6 and 60 % for 20 are also limits due to the possible backflow presence, a product of an intake pressure lower than atmospheric conditions. The latter can lead to having N_2 in the combustion process. Operating at higher intake temperatures can lead to an increase in the intake pressure. However, further research must be performed on this topic.

Regarding energy limits, membrane area increment, combustion delaying, an energy source addition (a heater or an electric compressor), and turbine position variation were identified as possible actions to reduce the engine load if required.

Similarly, operative limits at altitude conditions were found. An appropriate operation was observed until an altitude of 4,000 m. The primary limitation for altitude increment was that the compression ratio required for the driven air increases with the altitude while the available energy in the exhaust gases stays almost constant. In this sense, the membrane operation conditions for the required oxygen production cannot be achieved, and power production declines. However, the volumetric efficiency is enhanced due to a better performance of the O_2/EGR compressor, a product of an expansion ratio increment of the exhaust gases turbine, which enhances the compressor boosting.

7.5 Main conclusions

The analysis of a membrane-based oxygen production cycle working within different oxycombustion contexts has been performed. The cycle has shown flexibility to work in a wide range of available energy, displaying a suitable

performance according to the requirements. Additionally, possible advantages in energy consumption and operative costs have been found.

The coupling between the air separation process and power production is a central issue to be addressed when applying this type of system. The characteristics of the energy source (location, mass flow, and thermodynamic properties), the membrane configuration (three or four-end), the quality of the sweeping gases (in the case of a four-end membrane used), and the oxygen production requirement are some parameters to consider for complete design.

On the other hand, oxycombustion exhibits particular advantages regarding NOx emissions and the possibility of carbon capture; thus, it is a promising alternative to reduce pollutant emissions. Nonetheless, it can affect the system performance due to the combustion process's characteristics, like extending the combustion duration or changing the in-cylinder processes in the particular case of an engine.

However, at the same time, these oxycombustion characteristics open the possibility of compensating for the performance worsening by optimizing specific parameters, such as an increment of the compression ratio or the combustion advancement.

In this sense, applying oxycombustion systems with oxygen production using membranes must be carefully designed, considering the particular characteristics of the systems to be coupled. The latter allows the obtention of a system with near-zero emissions and reasonable performance, such as those obtained in the present thesis.

7.6 Limitations and future works

The three main objectives in chapter 1 have been accomplished. Nonetheless, the performed studies in the present thesis have particular limitations to be addressed. The performance of an oxygen production cycle has properly been evaluated under different contexts, coupled in two power production systems with promising results.

Nonetheless, at first sight, one can see a gap regarding experimental data of these types of facilities, especially regarding the coupling of an oxygen production cycle within a power production facility. It is necessary to examine the operation of an oxygen production cycle based on membranes driven by the available energy of high-energy streams. Moreover, coupling the mentioned systems with a power production device working under oxycombustion is still to be made. Some advances are being performed in the facilities of CMT - Motores Térmicos, where the installation of a set of turbochargers and a heat exchanger network fed with exhaust gases from an engine to reach optimum conditions for

oxygen production with membranes have been made, and the initial results are currently expected.

In this sense, the primary bottleneck for the complete operation of the system is an operative MIEC membrane with the required size to generate the needed oxygen to feed an engine.

On the other hand, the current thesis was developed with the Wagner model for membrane calculations. Wagner's model helped determine tendencies regarding the required energy for oxygen production and the coupling behavior with the studied systems. Nonetheless, this model is only valid when considering thick membranes because it assumes that bulk resistance is the main restriction for oxygen permeation. However, this may vary depending on the membrane thickness and operation conditions, for which more precise models are needed.

In this sense, researchers of CMT - Motores Térmicos and ITQ, institutes of Universitat Politècnica de Valencia, are working on the implementation of a consistent model that considers the superficial resistance of the membrane on both sides, which acquires importance for thinner membranes and taking into account the effect of operative conditions of pressure and temperature.

The presented studies were performed from a preliminary stage perspective, where some components were modeled considering reasonable values of their properties as the effectiveness of the heat exchangers. In this sense, more detail is required for these components to increase the presented results' precision. The heat exchangers' type, geometry, and materials are required, as well as the power control valve's lifting law, to mention a pair of the components whose detailed design is needed.

Additionally, extended experimental and CFD studies regarding the heat release under oxycombustion are required to further understand oxycombustion at different speeds, loads, and compression ratios. This would improve the obtained results while new phenomena could be studied.

The Graz cycle coupled with the membrane-based oxygen production cycle was only evaluated at one load condition (400 MW). Thus, part-load conditions can be evaluated to study the response of the coupled cycles at different operative conditions.

Oxycombustion is implemented to reduce pollutant emissions, especially by avoiding NOx formation by eliminating N_2 from the combustion process. Nonetheless, the whole process completeness lies in applying carbon capture to achieve a near-zero emissions system. In the moment of the present thesis writing, the coupling of a carbon capture system that initially eliminates water excess through condensation while compressing the CO_2 using an engine cylinder and an additional reciprocating compressor is under study. The system uses water injection at the intake manifold to enhance performance while controlling the intake temperature. Preliminary results indicate that the carbon capture process demands nearly 11 % of the net power production.

The bulk gas shifting within the cylinders from N_2 to CO_2 leads to different characteristics regarding the in-cylinder processes. Changes in the specific heat ratios lead to differences in the compression and expansion processes and the admission and exhaust of gases. In this sense, the valve timing can be optimized, considering its effect on the engine performance and available energy for oxygen production.

Finally, the study of different fuels can be performed. Different fuel compositions lead to different reaction processes, changing the stoichiometry, thus, the EGR composition and the available energy in the exhaust manifold. In this sense, new-generation fuels can be studied in the oxycombustion framework.

References

[1] **Arnau, F., Novella, R., García-Cuevas, L. M., and Gutiérrez, F.**
"Adapting an Internal Combustion Engine to Oxy-Fuel Combustion With In-Situ Oxygen Production"
in: *ASME 2021 Internal Combustion Engine Division Fall Technical Conference*. American Society of Mechanical Engineers Oct. 2021. DOI: 10.1115/icef2021-67707 (cit. on pp. vii, 2)

[2] **Serrano, J. R., Arnau, F. J., García-Cuevas, L. M., and Gutiérrez, F. A.**
"Thermo-economic analysis of an oxygen production plant powered by an innovative energy recovery system"
in: *Energy* 255 (Sept. 2022), p. 124419. DOI: 10.1016/j.energy.2022.124419 (cit. on pp. vii, 56)

[3] **Gutiérrez, F. A., Garcıa-Cuevas, L. M., and Sanz, W.**
"Comparison of cryogenic and membrane oxygen production implemented in the Graz cycle"
in: *Energy Conversion and Management* 271 (Nov. 2022), p. 116325. DOI: 10.1016/j.enconman.2022.116325 (cit. on p. vii)

[4] **Serrano, J. R., Arnau, F. J., Garcıa-Cuevas, L. M., and Gutiérrez, F. A.**
"Coupling an oxygen generation cycle with an oxy-fuel combustion spark ignition engine for zero NOx emissions and carbon capture: A feasibility study"
in: *Energy Conversion and Management* 284 (May 2023), p. 116973. DOI: 10.1016/j.enconman.2023.116973 (cit. on p. vii)

[5] **Huang, X., Guo, J., Liu, Z., and Zheng, C.**
"Opportunities and Challenges of Oxy-fuel Combustion"
in: *Oxy-Fuel Combustion*. Elsevier 2018, pp. 1–12. DOI: 10.1016/b978-0-12-812145-0.00001-3 (cit. on pp. 2, 31, 32)

[6] **Koohestanian, E. and Shahraki, F.**
"Review on principles, recent progress, and future challenges for oxy-fuel combustion CO2 capture using compression and purification unit"
in: *Journal of Environmental Chemical Engineering* 9.4 (Aug. 2021), p. 105777. DOI: 10.1016/j.jece.2021.105777 (cit. on pp. 2, 32)

[7] **Wu, F., Argyle, M. D., Dellenback, P. A., and Fan, M.**
"Progress in O2 separation for oxy-fuel combustion–A promising way for cost-effective CO2 capture: A review"
in: *Progress in Energy and Combustion Science* 67 (July 2018), pp. 188–205. DOI: 10.1016/j.pecs.2018.01.004 (cit. on pp. 2, 35–38)

[8] **Zhu, X. and Yang, W.**
"Introduction to Mixed Ionic–Electronic Conducting Membranes"
in: *Green Chemistry and Sustainable Technology*. Springer Berlin Heidelberg Nov. 2016, pp. 1–10. DOI: 10.1007/978-3-662-53534-9_1 (cit. on pp. 2, 35, 38, 39, 112, 135, 140)

[9] **Castillo, R.**
"Thermodynamic analysis of a hard coal oxyfuel power plant with high temperature three-end membrane for air separation"
in: *Applied Energy* 88.5 (May 2011), pp. 1480–1493. DOI: 10.1016/j.apenergy.2010.10.044 (cit. on pp. 2, 39, 141)

[10] **Skorek-Osikowska, A., Bartela, Ł., and Kotowicz, J.**
"A comparative thermodynamic, economic and risk analysis concerning implementation of oxy-combustion power plants integrated with cryogenic and hybrid air separation units"
in: *Energy Conversion and Management* 92 (Mar. 2015), pp. 421–430. DOI: 10.1016/j.enconman.2014.12.079 (cit. on pp. 2, 39)

[11] **Portillo, E., Fernández, L. M. G., Vega, F., Alonso-Fariñas, B., and Navarrete, B.**
"Oxygen transport membrane unit applied to oxy-combustion coal power plants: A thermodynamic assessment"
in: *Journal of Environmental Chemical Engineering* 9.4 (Aug. 2021), p. 105266. DOI: 10.1016/j.jece.2021.105266 (cit. on pp. 2, 38, 39, 141)

[12] **Serrano, J., Martín, J., Gomez-Soriano, J., and Raggi, R.**
"Theoretical and experimental evaluation of the spark-ignition premixed oxy-fuel combustion concept for future CO2 captive powerplants"
in: *Energy Conversion and Management* 244 (Sept. 2021), p. 114498. DOI: 10.1016/j.enconman.2021.114498 (cit. on pp. 2, 59, 151, 156, 161)

[13] **Serrano, J. R., Díaz, J. M., Gomez-Soriano, J., and Raggi, R.**
"Exploring the Oxy-Fuel Combustion in Spark-Ignition Engines for Future Clean Powerplants"
in: *ASME 2022 ICE Forward Conference*. American Society of Mechanical Engineers Oct. 2022. DOI: 10.1115/icef2022-89167
(cit. on pp. 2, 33, 34, 42, 58, 59, 61, 62, 151, 156, 161)

[14] **Serrano, J. R., Bracho, G., Gomez-Soriano, J., and Fernandes, C.**
"Development of an Oxy-Fuel Combustion System in a Compression-Ignition Engine for Ultra-Low Emissions Powerplants Using CFD and Evolutionary Algorithms"
in: *Applied Sciences* 12.14 (July 2022), p. 7104. DOI: 10.3390/app12147104 (cit. on p. 2)

[15] **Serrano, J., Arnau, F., García-Cuevas, L., and Farias, V.**
"Oxy-fuel combustion feasibility of compression ignition engines using oxygen separation membranes for enabling carbon dioxide capture"
in: *Energy Conversion and Management* 247 (Nov. 2021), p. 114732. DOI: 10.1016/j.enconman.2021.114732 (cit. on pp. 3, 56, 152, 153)

[16] **Arnau, F., Bracho, G., García-Cuevas, L., and Farias, V.**
"A strategy to extend load operation map range in oxy-fuel compression ignition engines with oxygen separation membranes"
in: *Applied Thermal Engineering* 226 (May 2023), p. 120268. DOI: 10.1016/j.applthermaleng.2023.120268 (cit. on pp. 3, 202)

[17] *Internal Combustion Engine Handbook. Basics, Components, Systems, and Perspectives*
SAE International 2004, p. 868. ISBN: 9780768011395
(cit. on pp. 10–14, 17, 20, 21)

[18] **Baumbach, G. and Kobayashi, M.**
Air Quality Control Formation and Sources, Dispersion, Characteristics and Impact of Air Pollutants - Measuring Methods, Techniques for Reduction of ... Formation and Sources, Dispersion, Characteristics and Impact of Air Pollutants - Measuring Methods, Techniques for Reduction of ...
Brand: Springer, p. 508. ISBN: 9783642790034 (cit. on pp. 10–14)

[19] **Fernández, J. M. D. and González, F. P.**
MOTORES DE COMBUSTIÓN INTERNA ALTERNATIVOS
Universitat Politècnica de València, p. 1024. ISBN: 9788483637050
(cit. on pp. 11–15, 17–20, 23, 25–31)

[20] **Heywood, J.**
Internal combustion engine fundamentals
McGraw-Hill Education 2018. ISBN: 9781260116106
(cit. on pp. 12–15, 17, 18, 26–28, 31)

[21] **Zhao, L., Yu, X., Qian, D., Dong, W., Sun, P., He, L., and Yang, S.**
"The effects of EGR and ignition timing on emissions of GDI engine"
in: *Science China Technological Sciences* 56.12 (Dec. 2013), pp. 3144–3150. DOI: 10.1007/s11431-013-5379-y (cit. on pp. 12, 15, 18)

[22] **Saw, O. P. and Mallikarjuna, J. M.**
"Effect of spark plug and fuel injector location on mixture stratification in a GDI engine - A CFD analysis"
in: *IOP Conference Series: Materials Science and Engineering* 243 (Sept. 2017), p. 012025. DOI: 10.1088/1757-899x/243/1/012025 (cit. on pp. 12, 15, 20)

[23] **Jiang, C., Li, Z., Qian, Y., Wang, X., Zhang, Y., and Lu, X.**
"Experimental studies on the co-effects of engine operating parameters and fuel functional groups on the performance and emissions of a GDI engine"
in: *Applied Thermal Engineering* 140 (July 2018), pp. 707–715. DOI: 10.1016/j.applthermaleng.2018.05.095 (cit. on pp. 12, 16, 18, 21)

[24] **Deng, B., Li, Q., Chen, Y., Li, M., Liu, A., Ran, J., Xu, Y., Liu, X., Fu, J., and Feng, R.**
"The effect of air/fuel ratio on the CO and NOx emissions for a twin-spark motorcycle gasoline engine under wide range of operating conditions"
in: *Energy* 169 (Feb. 2019), pp. 1202–1213. DOI: 10.1016/j.energy.2018.12.113 (cit. on pp. 13, 16)

[25] **Duronio, F., Vita, A. D., Montanaro, A., and Villante, C.**
"Gasoline direct injection engines – A review of latest technologies and trends. Part 2"
in: *Fuel* 265 (Apr. 2020), p. 116947. DOI: 10.1016/j.fuel.2019.116947 (cit. on p. 13)

[26] **Zhu, G., Liu, J., Fu, J., Xu, Z., Guo, Q., and Zhao, H.**
"Experimental study on combustion and emission characteristics of turbocharged gasoline direct injection (GDI) engine under cold start new European driving cycle (NEDC)"
in: *Fuel* 215 (Mar. 2018), pp. 272–284. DOI: 10.1016/j.fuel.2017.10.048 (cit. on pp. 13, 17, 19)

[27] **Reşitoğlu, İ. A., Altinişik, K., and Keskin, A.**
"The pollutant emissions from diesel-engine vehicles and exhaust aftertreatment systems"
in: *Clean Technologies and Environmental Policy* 17.1 (June 2014), pp. 15–27. DOI: 10.1007/s10098-014-0793-9 (cit. on pp. 13, 18, 19)

[28] **Pan, W., Yao, C., Han, G., Wei, H., and Wang, Q.**
"The impact of intake air temperature on performance and exhaust emissions of a diesel methanol dual fuel engine"
in: *Fuel* 162 (Dec. 2015), pp. 101–110. DOI: 10.1016/j.fuel.2015.08.073 (cit. on pp. 13, 16, 19)

[29] **Hasan, A. O., Osman, A. I., Al-Muhtaseb, A. H., Al-Rawashdeh, H., Abu-jrai, A., Ahmad, R., Gomaa, M. R., Deka, T. J., and Rooney, D. W.**
"An experimental study of engine characteristics and tailpipe emissions from modern DI diesel engine fuelled with methanol/diesel blends"
in: *Fuel Processing Technology* 220 (Sept. 2021), p. 106901. DOI: 10.1016/j.fuproc.2021.106901 (cit. on pp. 13, 17, 19)

[30] **Selvan, B. K., Das, S., Chandrasekar, M., Girija, R., Vennison, S. J., Jaya, N., Saravanan, P., Rajasimman, M., Vasseghian, Y., and Rajamohan, N.**
"Utilization of biodiesel blended fuel in a diesel engine – Combustion engine performance and emission characteristics study"
in: *Fuel* 311 (Mar. 2022), p. 122621. DOI: 10.1016/j.fuel.2021.122621 (cit. on pp. 13, 17, 19, 20)

[31] **Lattimore, T., Wang, C., Xu, H., Wyszynski, M. L., and Shuai, S.**
"Investigation of EGR Effect on Combustion and PM Emissions in a DISI Engine"
in: *Applied Energy* 161 (Jan. 2016), pp. 256–267. DOI: 10.1016/j.apenergy.2015.09.080 (cit. on pp. 15, 18)

[32] **Polat, S., Uyumaz, A., Solmaz, H., Yilmaz, E., Topgül, T., and Yücesu, H. S.**
"A numerical study on the effects of EGR and spark timing to combustion characteristics and NOx emission of a GDI engine"
in: *International Journal of Green Energy* 13.1 (May 2014), pp. 63–70. DOI: 10.1080/15435075.2014.909361 (cit. on p. 15)

[33] **Rakopoulos, C. D., Rakopoulos, D. C., Mavropoulos, G. C., and Kosmadakis, G. M.**
"Investigating the EGR rate and temperature impact on diesel engine combustion and emissions under various injection timings and loads by comprehensive two-zone modeling"
in: *Energy* 157 (Aug. 2018), pp. 990–1014. DOI: 10.1016/j.energy.2018.05.178 (cit. on pp. 16, 20, 28)

[34] **Sindhu, R., Rao, G. A. P., and Murthy, K. M.**
"Effective reduction of NOx emissions from diesel engine using split injections"

in: *Alexandria Engineering Journal* 57.3 (Sept. 2018), pp. 1379–1392. DOI: 10.1016/j.aej.2017.06.009 (cit. on pp. 16, 20)

[35] **Drake, M. C., French, D. T., and Fansler, T. D.**
"Advanced diagnostics for minimizing hydrocarbon emissions from a direct-injection gasoline engine"
in: *Symposium (International) on Combustion* 26.2 (1996), pp. 2581–2587. DOI: 10.1016/s0082-0784(96)80091-9 (cit. on p. 18)

[36] **Zhang, M., Hong, W., Xie, F., Su, Y., Liu, H., and Zhou, S.**
"Combustion, performance and particulate matter emissions analysis of operating parameters on a GDI engine by traditional experimental investigation and Taguchi method"
in: *Energy Conversion and Management* 164 (May 2018), pp. 344–352. DOI: 10.1016/j.enconman.2018.03.017 (cit. on pp. 18, 19)

[37] **Überall, A., Otte, R., Eilts, P., and Krahl, J.**
"A literature research about particle emissions from engines with direct gasoline injection and the potential to reduce these emissions"
in: *Fuel* 147 (May 2015), pp. 203–207. DOI: 10.1016/j.fuel.2015.01.012 (cit. on p. 20)

[38] **Buysse, C. and Miller, J.**
TRANSPORT COULD BURN UP THE EU'S ENTIRE CARBON BUDGET
Web page Apr. 2021. URL: https://theicct.org/transport-could-burn-up-the-eus-entire-carbon-budget/ (cit. on p. 21)

[39] **EPA**
Inventory of U.S. Greenhouse Gas Emissions and Sinks
Web page Apr. 2023. URL: https://www.epa.gov/ghgemissions/inventory-us-greenhouse-gas-emissions-and-sinks (cit. on p. 21)

[40] **ONU**
The Paris Agreement
Web page. URL: https://www.un.org/en/climatechange/paris-agreement (cit. on p. 21)

[41] **Ribeiro, C. B., Rodella, F. H. C., and Hoinaski, L.**
"Regulating light-duty vehicle emissions: an overview of US, EU, China and Brazil programs and its effect on air quality"
in: *Clean Technologies and Environmental Policy* 24.3 (Nov. 2021), pp. 851–862. DOI: 10.1007/s10098-021-02238-1 (cit. on pp. 21, 22, 24)

[42] **Dieselnet**
United States: Cars and Light-Duty Trucks
Webpage July 2021. URL: https://dieselnet.com/standards/us/ld.php (cit. on p. 22)

[43] **Dieselnet**
United States: Cars and Light-Duty Trucks: Tier 2
Webpage Dec. 2006. URL: https://dieselnet.com/standards/us/ld_t2.php (cit. on pp. 22, 23)

[44] **Dieselnet**
United States: Cars and Light-Duty Trucks: Tier 3
Webpage Aug. 2016. URL: https://dieselnet.com/standards/us/ld_t3.php (cit. on pp. 22, 23)

[45] **Dieselnet**
United States: Cars and Light-Duty Trucks: Tier 1
Webpage Apr. 2007. URL: https://dieselnet.com/standards/us/ld_t1.php (cit. on p. 23)

[46] **EPA**
EPA Sets Tier 3 Motor VehicleEmission and Fuel Standards
Regulatory Announcement. EPA 2014. URL: https://nepis.epa.gov/Exe/ZyPDF.cgi/P100HW00.PDF?Dockey=P100HW00.PDF (cit. on p. 23)

[47] **Bharj, R. S., Kumar, R., and Singh, G. N.**
"On-Board Post-Combustion Emission Control Strategies for Diesel Engine in India to Meet Bharat Stage VI Norms"
in: *Advanced Engine Diagnostics*. Springer Singapore Nov. 2018, pp. 105–125. DOI: 10.1007/978-981-13-3275-3_6 (cit. on pp. 24, 25)

[48] **EU**
Commission proposes new Euro 7 standards to reduce pollutant emissions from vehicles and improve air quality
Webpage Nov. 2022. URL: https://ec.europa.eu/commission/presscorner/detail/en/ip_22_6495 (cit. on pp. 24, 25)

[49] **UE**
Annexes to the Proposal for a Regulation of the European Parliament and the Councilon type-approval of motor vehicles and engines and of systems, components andseparate technical units intended for such vehicles, with respect to their emissions andbattery durability (Euro 7) and repealing Regulations (EC) No 715/2007 and (EC) No595/2009
tech. rep. UE 2022. URL: https://single-market-economy.ec.europa.eu/publications/euro-7-standard-proposal_en (cit. on p. 25)

[50] **EU**
Questions and Answers: Commission proposal on the new Euro 7 standards
Webpage Nov. 2022. URL: https://ec.europa.eu/commission/presscorner/detail/en/QANDA_22_6496 (cit. on p. 26)

[51] **Lyu, M., Bao, X., Zhu, R., and Matthews, R.**
"State-of-the-art outlook for light-duty vehicle emission control standards and technologies in China"
in: *Clean Technologies and Environmental Policy* 22.4 (Mar. 2020), pp. 757–771. DOI: 10.1007/s10098-020-01834-x (cit. on p. 26)

[52] **ICCT**
INDIA BHARAT STAGE VI EMISSION STANDARDS
Policy update. International Council on Clean Transportation Apr. 2016. URL: https://theicct.org/sites/default/files/publications/India%20BS%20VI%20Policy%20Update%20vF.pdf (cit. on p. 26)

[53] **Leach, F., Kalghatgi, G., Stone, R., and Miles, P.**
"The scope for improving the efficiency and environmental impact of internal combustion engines"
in: *Transportation Engineering* 1 (June 2020), p. 100005. DOI: 10.1016/j.treng.2020.100005 (cit. on pp. 26, 31)

[54] **Piqueras, P., Morena, J. D. la, Sanchis, E. J., and Pitarch, R.**
"Impact of Exhaust Gas Recirculation on Gaseous Emissions of Turbocharged Spark-Ignition Engines"
in: *Applied Sciences* 10.21 (Oct. 2020), p. 7634. DOI: 10.3390/app10217634 (cit. on p. 27)

[55] **Shen, K., Li, F., Zhang, Z., Sun, Y., and Yin, C.**
"Effects of LP and HP cooled EGR on performance and emissions in turbocharged GDI engine"
in: *Applied Thermal Engineering* 125 (Oct. 2017), pp. 746–755. DOI: 10.1016/j.applthermaleng.2017.07.064 (cit. on p. 27)

[56] **Mahmoudi, A. R., Khazaee, I., and Ghazikhani, M.**
"Simulating the effects of turbocharging on the emission levels of a gasoline engine"
in: *Alexandria Engineering Journal* 56.4 (Dec. 2017), pp. 737–748. DOI: 10.1016/j.aej.2017.03.005 (cit. on p. 28)

[57] **Silva, L. S., Silva, J. A., Henrıquez, J. R., and Lira Junior, J. C. de**
"Numerical Analysis of Effects of Engine Downsizing and Turbocharging on the Parameters of Performance and Emissions of an Internal Combustion Engine"

in: *Arabian Journal for Science and Engineering* 48.3 (June 2022), pp. 2795–2805. DOI: 10.1007/s13369-022-06947-7 (cit. on p. 28)

[58] **Lou, D., Ren, Y., Li, X., Zhang, Y., and Sun, X.**
"Effect of Operating Conditions and TWC Parameters on Emissions Characteristics of a Stoichiometric Natural Gas Engine"
in: *Energies* 13.18 (Sept. 2020), p. 4905. DOI: 10.3390/en13184905 (cit. on p. 29)

[59] **Bae, W. B., Kim, D. Y., Byun, S. W., Hazlett, M., Yoon, D. Y., Jung, C., Kim, C. H., and Kang, S. B.**
"Emission of NH3 and N2O during NO reduction over commercial aged three-way catalyst (TWC): Role of individual reductants in simulated exhausts"
in: *Chemical Engineering Journal Advances* 9 (Mar. 2022), p. 100222. DOI: 10.1016/j.ceja.2021.100222 (cit. on p. 29)

[60] **Hu, S., Deng, B., Wu, D., and Hou, K.**
"Energy flow behavior and emission reduction of a turbo-charging and EGR non-road diesel engine equipped with DOC and DPF under NRTC (non-road transient cycle)"
in: *Fuel* 305 (Dec. 2021), p. 121571. DOI: 10.1016/j.fuel.2021.121571 (cit. on pp. 30, 31)

[61] **Resitoglu, I. A., Altinisik, K., Keskin, A., and Ocakoglu, K.**
"The effects of Fe2O3 based DOC and SCR catalyst on the exhaust emissions of diesel engines"
in: *Fuel* 262 (Feb. 2020), p. 116501. DOI: 10.1016/j.fuel.2019.116501 (cit. on p. 30)

[62] **Tan, L., Guo, Y., Liu, Z., Feng, P., and Li, Z.**
"An investigation on the catalytic characteristic of NO reduction in SCR systems"
in: *Journal of the Taiwan Institute of Chemical Engineers* 99 (June 2019), pp. 53–59. DOI: 10.1016/j.jtice.2019.02.020 (cit. on p. 30)

[63] **Ko, J., Kim, K., Chung, W., Myung, C.-L., and Park, S.**
"Characteristics of on-road particle number (PN) emissions from a GDI vehicle depending on a catalytic stripper (CS) and a metal-foam gasoline particulate filter (GPF)"
in: *Fuel* 238 (Feb. 2019), pp. 363–374. DOI: 10.1016/j.fuel.2018.10.091 (cit. on p. 31)

[64] **Wilberforce, T., Olabi, A., Sayed, E. T., Elsaid, K., and Abdelkareem, M. A.**
"Progress in carbon capture technologies"

in: *Science of The Total Environment* 761 (Mar. 2021), p. 143203. DOI: 10.1016/j.scitotenv.2020.143203 (cit. on p. 31)

[65] **Koytsoumpa, E. I., Bergins, C., and Kakaras, E.**
"The CO2 economy: Review of CO2 capture and reuse technologies"
in: *The Journal of Supercritical Fluids* 132 (Feb. 2018), pp. 3–16. DOI: 10.1016/j.supflu.2017.07.029 (cit. on p. 31)

[66] **Ozsari, I., Ust, Y., and Kayadelen, H. K.**
"Comparative Energy and Emission Analysis of Oxy-Combustion and Conventional Air Combustion"
in: *Arabian Journal for Science and Engineering* 46.3 (Jan. 2021), pp. 2477–2492. DOI: 10.1007/s13369-020-05130-0 (cit. on p. 32)

[67] **Chen, S.**
"Fundamentals of Oxy-fuel Combustion"
in: *Oxy-Fuel Combustion*. Elsevier 2018, pp. 13–30. DOI: 10.1016/b978-0-12-812145-0.00002-5 (cit. on pp. 32, 33)

[68] **Shi, Y., Liu, Q., Shao, Y., and Zhong, W.**
"Energy and exergy analysis of oxy-fuel combustion based on circulating fluidized bed power plant firing coal, lignite and biomass"
in: *Fuel* 269 (June 2020), p. 117424. DOI: 10.1016/j.fuel.2020.117424 (cit. on p. 32)

[69] **Liang, Y., Cai, L., Guan, Y., Liu, W., Xiang, Y., Li, J., and He, T.**
"Numerical study on an original oxy-fuel combustion power plant with efficient utilization of flue gas waste heat"
in: *Energy* 193 (Feb. 2020), p. 116854. DOI: 10.1016/j.energy.2019.116854 (cit. on p. 32)

[70] **Cai, L., Tan, L., Liang, Y., Yin, X., Liu, C., and Guan, Y.**
"Numerical study on sulfur-bearing natural gas oxy-fuel combustion power plant"
in: *Applied Thermal Engineering* 196 (Sept. 2021), p. 117292. DOI: 10.1016/j.applthermaleng.2021.117292 (cit. on p. 32)

[71] **Park, S. K., Kim, T. S., Sohn, J. L., and Lee, Y. D.**
"An integrated power generation system combining solid oxide fuel cell and oxy-fuel combustion for high performance and CO2 capture"
in: *Applied Energy* 88.4 (Apr. 2011), pp. 1187–1196. DOI: 10.1016/j.apenergy.2010.10.037 (cit. on p. 32)

[72] **Thorbergsson, E. and Grönstedt, T.**
"A Thermodynamic Analysis of Two Competing Mid-Sized Oxyfuel Combustion Combined Cycles"

in: *Journal of Energy* 2016 (2016), pp. 1–14. DOI: 10.1155/2016/2438431 (cit. on pp. 32, 35)

[73] **Hanak, D. P., Powell, D., and Manovic, V.**
"Techno-economic analysis of oxy-combustion coal-fired power plant with cryogenic oxygen storage"
in: *Applied Energy* 191 (Apr. 2017), pp. 193–203. DOI: 10.1016/j.apenergy.2017.01.049 (cit. on p. 32)

[74] **Blarigan, A. V., Kozarac, D., Seiser, R., Chen, J., Cattolica, R., and Dibble, R.**
"Spark-ignited engine NOx emissions in a low-nitrogen oxycombustion environment"
in: *Applied Energy* 118 (Apr. 2014), pp. 22–31. DOI: 10.1016/j.apenergy.2013.12.007 (cit. on p. 33)

[75] **Mohammed, A., Elkhazraji, A., Jan, S., and Johansson, B.**
"A Study on the Performance and Emissions of HCCI Oxy-Fuel Combustion in a CFR Engine with Recirculated Carbon Dioxide"
in: *SAE Technical Paper Series*. SAE International Sept. 2020. DOI: 10.4271/2020-01-2065 (cit. on pp. 33, 161)

[76] **Wu, Z.-J., Yu, X., Fu, L.-Z., Deng, J., Hu, Z.-J., and Li, L.-G.**
"A high efficiency oxyfuel internal combustion engine cycle with water direct injection for waste heat recovery"
in: *Energy* 70 (June 2014), pp. 110–120. DOI: 10.1016/j.energy.2014.03.095 (cit. on p. 33)

[77] **Kang, Z., Wu, Z., Zhang, Z., Deng, J., Hu, Z., and Li, L.**
"Study of the Combustion Characteristics of a HCCI Engine Coupled with Oxy-Fuel Combustion Mode"
in: *SAE International Journal of Engines* 10.3 (Mar. 2017), pp. 908–916. DOI: 10.4271/2017-01-0649 (cit. on p. 33)

[78] **Tan, Q. and Hu, Y.**
"A study on the combustion and emission performance of diesel engines under different proportions of O2 &amp N2 &amp CO2"
in: *Applied Thermal Engineering* 108 (Sept. 2016), pp. 508–515. DOI: 10.1016/j.applthermaleng.2016.07.151 (cit. on p. 33)

[79] **Gao, Y., Li, L., Yu, X., Deng, J., and Wu, Z.**
"Effect of Compression Ratio on Internal Combustion Rankine Cycle Based on Simulations"
in: *Lecture Notes in Electrical Engineering*. Springer Berlin Heidelberg Dec. 2014, pp. 129–138. DOI: 10.1007/978-3-662-45043-7_14 (cit. on p. 33)

[80] **Li, C., Chew, J. J., Mahmoud, A., Liu, S., and Sunarso, J.**
"Modelling of oxygen transport through mixed ionic-electronic conducting (MIEC) ceramic-based membranes: An overview"
in: *Journal of Membrane Science* 567 (Dec. 2018), pp. 228–260. DOI: 10.1016/j.memsci.2018.09.016 (cit. on p. 35)

[81] **Escudero, A. I., Espatolero, S., and Romeo, L. M.**
"Oxy-combustion power plant integration in an oil refinery to reduce CO 2 emissions"
in: *International Journal of Greenhouse Gas Control* 45 (Feb. 2016), pp. 118–129. DOI: 10.1016/j.ijggc.2015.12.018 (cit. on pp. 35, 36)

[82] **Cau, G., Tola, V., Ferrara, F., Porcu, A., and Pettinau, A.**
"CO2-free coal-fired power generation by partial oxy-fuel and post-combustion CO2 capture: Techno-economic analysis"
in: *Fuel* 214 (Feb. 2018), pp. 423–435. DOI: 10.1016/j.fuel.2017.10.023 (cit. on pp. 35, 36)

[83] **Xiong, J., Zhao, H., and Zheng, C.**
"Exergy Analysis of a 600 MWe Oxy-combustion Pulverized-Coal-Fired Power Plant"
in: *Energy Fuels* 25.8 (July 2011), pp. 3854–3864. DOI: 10.1021/ef200702k (cit. on pp. 35, 36)

[84] **Habib, M. A., Nemitallah, M., and Ben-Mansour, R.**
"Recent Development in Oxy-Combustion Technology and Its Applications to Gas Turbine Combustors and ITM Reactors"
in: *Energy &amp Fuels* 27.1 (Dec. 2012), pp. 2–19. DOI: 10.1021/ef301266j (cit. on p. 35)

[85] **Yang, R. T.**
Gas separation by adsorption processes
World Scientific 1997, p. 352. ISBN: 1860940471 (cit. on p. 36)

[86] **Smith, A. and Klosek, J.**
"A review of air separation technologies and their integration with energy conversion processes"
in: *Fuel Processing Technology* 70.2 (May 2001), pp. 115–134. DOI: 10.1016/s0378-3820(01)00131-x (cit. on pp. 36, 37)

[87] **Alipour, M., Pudasainee, D., Nychka, J. A., and Gupta, R.**
"ZrO_2–CuO Sorbents for High-Temperature Air Separation"
in: *Industrial Engineering Chemistry Research* 53.27 (June 2014), pp. 10990–10999. DOI: 10.1021/ie501068d (cit. on p. 36)

[88] **Institute of Chemistry, N. Z.**
Production of Chemicals
2018. URL: https://nzic.org.nz/chemical-processes-new-zealand/production-ofchemicals (cit. on p. 36)

[89] **Liu, Y., Zhang, Q., Cao, Y., Yang, X., Li, Z., Liu, W., Habyarimana, J. B., Cui, Y., Wang, H., and Yang, R. T.**
"Effect of intermittent purge on O2 production with rapid pressure swing adsorption technology"
in: *Adsorption* 27.2 (Nov. 2020), pp. 181–189. DOI: 10.1007/s10450-020-00284-7 (cit. on p. 36)

[90] **Chang, C.-S., Ni, S.-H., Yang, H.-S., and Chou, C.-T.**
"Simulation study of separating oxygen from air by pressure swing adsorption process with semicylindrical adsorber"
in: *Journal of the Taiwan Institute of Chemical Engineers* 120 (Mar. 2021), pp. 67–76. DOI: 10.1016/j.jtice.2021.03.027 (cit. on p. 36)

[91] **Zhu, X., Sun, Y., Liu, Y., Sun, X., and Shi, J.**
"Experimental performance analysis of vacuum pressure swing adsorption air separation process under plateau special conditions"
in: *Separation Science and Technology* 57.18 (June 2022), pp. 2885–2893. DOI: 10.1080/01496395.2022.2085115 (cit. on p. 36)

[92] **Zhou, C., Shah, K., and Moghtaderi, B.**
"Techno-Economic Assessment of Integrated Chemical Looping Air Separation for Oxy-Fuel Combustion: An Australian Case Study"
in: *Energy &amp Fuels* 29.4 (Mar. 2015), pp. 2074–2088. DOI: 10.1021/ef5022076 (cit. on p. 37)

[93] **Zhou, C., Shah, K., Song, H., Zanganeh, J., Doroodchi, E., and Moghtaderi, B.**
"Integration Options and Economic Analysis of an Integrated Chemical Looping Air Separation Process for Oxy-fuel Combustion"
in: *Energy &amp Fuels* 30.3 (Dec. 2015), pp. 1741–1755. DOI: 10.1021/acs.energyfuels.5b02209 (cit. on p. 37)

[94] **Shi, B., Wu, E., and Wu, W.**
"Novel design of chemical looping air separation process for generating electricity and oxygen"
in: *Energy* 134 (Sept. 2017), pp. 449–457. DOI: 10.1016/j.energy.2017.05.080 (cit. on p. 37)

[95] **Zhu, L., Wang, F., and Zhang, Z.**
"Thermodynamic evaluation of a conceptual process for coal gasification coupled with chemical looping air separation"
in: *Chemical Engineering and Processing: Process Intensification* 106 (Aug. 2016), pp. 33–41. DOI: 10.1016/j.cep.2016.05.002 (cit. on p. 37)

[96] **Plazaola, A. A., Labella, A. C., Liu, Y., Porras, N. B., Tanaka, D. P., Annaland, M. S., and Gallucci, F.**
"Mixed Ionic-Electronic Conducting Membranes (MIEC) for Their Application in Membrane Reactors: A Review"
in: *Processes* 7.3 (Mar. 2019), p. 128. DOI: 10.3390/pr7030128 (cit. on p. 38)

[97] **Anderson, L. L. et al.**
"Advances in ion transport membrane technology for oxygen and syngas production"
in: *Solid State Ionics* 288 (May 2016), pp. 331–337. DOI: 10.1016/j.ssi.2015.11.010 (cit. on p. 39)

[98] **Maxwell Christie, G. and Lane, J.**
"COMPOSITE OXYGEN TRANSPORT MEMBRANE"
English. US 2013/0156978 A1 2013 (cit. on p. 39)

[99] **Prasad, R., Schwartz, J. M., Robinson, E. T., and Gottzmann, C. F.**
"Syngas production metjod utilizing an oxygen transport membrane"
English. US 6,695,983 B2 Feb. 2004 (cit. on p. 39)

[100] **Kelly, S., Chakravarti, S., and Li, J.**
"Oxygen transport membrane reactor based method and system for generating electric power"
English. US 9,562.472 B2 Feb. 2017 (cit. on p. 39)

[101] **Bai, W., Feng, J., Luo, C., Zhang, P., Wang, H., Yang, Y., Zhao, Y., and Fan, H.**
"A comprehensive review on oxygen transport membranes: Development history, current status, and future directions"
in: *International Journal of Hydrogen Energy* 46.73 (Oct. 2021), pp. 36257–36290. DOI: 10.1016/j.ijhydene.2021.08.177 (cit. on pp. 39, 140)

[102] **Martin, J., Arnau, F., Piqueras, P., and Auñon, A.**
"Development of an Integrated Virtual Engine Model to Simulate New Standard Testing Cycles"
in: *SAE Technical Paper Series*. SAE International Apr. 2018. DOI: 10.4271/2018-01-1413 (cit. on p. 56)

[103] **Olmeda, P., Martın, J., Arnau, F. J., and Artham, S.**
"Analysis of the energy balance during World harmonized Light vehicles Test Cycle in warmed and cold conditions using a Virtual Engine"
in: *International Journal of Engine Research* 21.6 (Oct. 2019), pp. 1037–1054. DOI: 10.1177/1468087419878593 (cit. on p. 56)

[104] **Arnau, F. J., Martın, J., Piqueras, P., and Auñón, Á.**
"Effect of the exhaust thermal insulation on the engine efficiency and the exhaust temperature under transient conditions"
in: *International Journal of Engine Research* 22.9 (Oct. 2020), pp. 2869–2883. DOI: 10.1177/1468087420961206 (cit. on p. 56)

[105] **GmbH, S.**
Introducing IPSEpro Simulation Environment
May 2023. URL: https://www.simtechnology.com/cms/ipsepro-menu/ipse-pro (cit. on p. 57)

[106] **Catalán-Martınez, D., Santafé-Moros, A., Gozálvez-Zafrilla, J., Garcıa-Fayos, J., and Serra, J.**
"Characterization of oxygen transport phenomena on BSCF membranes assisted by fluid dynamic simulations including surface exchange"
in: *Chemical Engineering Journal* 387 (May 2020), p. 124069. DOI: 10.1016/j.cej.2020.124069 (cit. on p. 57)

[107] **Shubnikova, E., Popov, M., Bychkov, S., Chizhik, S., and Nemudry, A.**
"The modeling of oxygen transport in MIEC oxide hollow fiber membranes"
in: *Chemical Engineering Journal* 372 (Sept. 2019), pp. 251–259. DOI: 10.1016/j.cej.2019.04.126 (cit. on p. 57)

[108] **Li, C., Li, W., Chew, J. J., Liu, S., Zhu, X., and Sunarso, J.**
"Oxygen permeation through single-phase perovskite membrane: Modeling study and comparison with the dual-phase membrane"
in: *Separation and Purification Technology* 235 (Mar. 2020), p. 116224. DOI: 10.1016/j.seppur.2019.116224 (cit. on p. 57)

[109] **Payri, F., Olmeda, P., Martin, J., and Carreño, R.**
"A New Tool to Perform Global Energy Balances in DI Diesel Engines"
in: *SAE International Journal of Engines* 7.1 (Apr. 2014), pp. 43–59. DOI: 10.4271/2014-01-0665 (cit. on p. 58)

[110] **Benajes, J., Olmeda, P., Martın, J., and Carreño, R.**
"A new methodology for uncertainties characterization in combustion diagnosis and thermodynamic modelling"
in: *Applied Thermal Engineering* 71.1 (Oct. 2014), pp. 389–399. DOI: 10.1016/j.applthermaleng.2014.07.010 (cit. on p. 58)

[111] **Liu, Y.-D., Jia, M., Xie, M.-Z., and Pang, B.**
"Enhancement on a Skeletal Kinetic Model for Primary Reference Fuel Oxidation by Using a Semidecoupling Methodology"
in: *Energy &amp Fuels* 26.12 (Nov. 2012), pp. 7069–7083. DOI: 10.1021/ef301242b (cit. on p. 59)

[112] **Serrano, J. R., Olmeda, P., Tiseira, A., Garcıa-Cuevas, L. M., and Lefebvre, A.**
"Theoretical and experimental study of mechanical losses in automotive turbochargers"
in: *Energy* 55 (June 2013), pp. 888–898. DOI: 10.1016/j.energy.2013.04.042 (cit. on p. 64)

[113] **Serrano, J. R., Olmeda, P., Arnau, F. J., Reyes-Belmonte, M. A., and Tartoussi, H.**
"A study on the internal convection in small turbochargers. Proposal of heat transfer convective coefficients"
in: *Applied Thermal Engineering* 89 (Oct. 2015), pp. 587–599. DOI: 10.1016/j.applthermaleng.2015.06.053 (cit. on p. 64)

[114] **Serrano, J., Olmeda, P., Arnau, F., and Dombrovsky, A.**
"General Procedure for the Determination of Heat Transfer Properties in Small Automotive Turbochargers"
in: *SAE International Journal of Engines* 8.1 (Oct. 2014), pp. 30–41. DOI: 10.4271/2014-01-2857 (cit. on p. 64)

[115] **Serrano, J. R., Olmeda, P., Arnau, F. J., Dombrovsky, A., and Smith, L.**
"Methodology to Characterize Heat Transfer Phenomena in Small Automotive Turbochargers: Experiments and Modelling Based Analysis"
in: *Volume 1B: Marine; Microturbines, Turbochargers and Small Turbomachines; Steam Turbines*. American Society of Mechanical Engineers June 2014. DOI: 10.1115/gt2014-25179 (cit. on p. 64)

[116] **Serrano, J., Arnau, F., Dolz, V., Tiseira, A., and Cervelló, C.**
"A model of turbocharger radial turbines appropriate to be used in zero- and one-dimensional gas dynamics codes for internal combustion engines modelling"
in: *Energy Conversion and Management* 49.12 (Dec. 2008), pp. 3729–3745. DOI: 10.1016/j.enconman.2008.06.031 (cit. on p. 64)

[117] **Payri, F., Serrano, J., Fajardo, P., Reyes-Belmonte, M., and Gozalbo-Belles, R.**
"A physically based methodology to extrapolate performance maps of radial turbines"

in: *Energy Conversion and Management* 55 (Mar. 2012), pp. 149–163. DOI: 10.1016/j.enconman.2011.11.003 (cit. on p. 64)

[118] **Galindo, J., Navarro, R., Garcıa-Cuevas, L. M., Tarı, D., Tartoussi, H., and Guilain, S.**
"A zonal approach for estimating pressure ratio at compressor extreme off-design conditions"
in: *International Journal of Engine Research* 20.4 (Feb. 2018), pp. 393–404. DOI: 10.1177/1468087418754899 (cit. on p. 64)

[119] **Sanz, W., Jericha, H., Luckel, F., Göttlich, E., and Heitmeir, F.**
"A Further Step Towards a Graz Cycle Power Plant for CO2 Capture"
in: *Volume 5: Turbo Expo 2005*. ASMEDC Jan. 2005. DOI: 10.1115/gt2005-68456 (cit. on pp. 65, 104, 107)

[120] **Aneke, M. and Wang, M.**
"Potential for improving the energy efficiency of cryogenic air separation unit (ASU) using binary heat recovery cycles"
in: *Applied Thermal Engineering* 81 (Apr. 2015), pp. 223–231. DOI: 10.1016/j.applthermaleng.2015.02.034 (cit. on p. 97)

[121] **Xu, J., Wang, T., Chen, Q., Zhang, S., and Tan, J.**
"Performance design of a cryogenic air separation unit for variable working conditions using the lumped parameter model"
in: *Frontiers of Mechanical Engineering* 15.1 (Nov. 2019), pp. 24–42. DOI: 10.1007/s11465-019-0558-6 (cit. on p. 97)

[122] **Cormos, C.-C.**
"Energy and cost efficient manganese chemical looping air separation cycle for decarbonized power generation based on oxy-fuel combustion and gasification"
in: *Energy* 191 (Jan. 2020), p. 116579. DOI: 10.1016/j.energy.2019.116579 (cit. on p. 97)

[123] **Qing, M., Jin, B., Ma, J., Zou, X., Wang, X., Zheng, C., and Zhao, H.**
"Thermodynamic and economic performance of oxy-combustion power plants integrating chemical looping air separation"
in: *Energy* 206 (Sept. 2020), p. 118136. DOI: 10.1016/j.energy.2020.118136 (cit. on p. 97)

[124] **Zhang, D., Duan, R., Li, H., Yang, Q., and Zhou, H.**
"Optimal design, thermodynamic, cost and CO2 emission analyses of coal-to-methanol process integrated with chemical looping air separation and hydrogen technology"
in: *Energy* 203 (July 2020), p. 117876. DOI: 10.1016/j.energy.2020.117876 (cit. on p. 97)

[125] **Banaszkiewicz, T. and Chorowski, M.**
"Energy Consumption of Air Separation Adsorption Methods"
in: *Entropy* 20.4 (Mar. 2018), p. 232. DOI: 10.3390/e20040232
(cit. on p. 97)

[126] **Radek, S. and Pavel, D.**
"The Potential of Energy Savings in Oxygen Production by Pressure Swing Adsorption"
in: *Chemical Engineering Transactions* 86 (2021), pp. 313–318. DOI: 10.3303/CET2186053 (cit. on p. 97)

[127] **Sanz, W., Jericha, H., Moser, M., and Heitmeir, F.**
"Thermodynamic and Economic Investigation of an Improved Graz Cycle Power Plant for CO2 Capture"
in: *Journal of Engineering for Gas Turbines and Power* 127.4 (Sept. 2005), pp. 765–772. DOI: 10.1115/1.1850944 (cit. on p. 104)

[128] **Jericha, H., Sanz, W., and Go¨ttlich, E.**
"Design Concept for Large Output Graz Cycle Gas Turbines"
in: *Volume 4: Cycle Innovations Electric Power Industrial and Cogeneration Manufacturing Materials and Metallurgy*. ASMEDC Jan. 2006. DOI: 10.1115/gt2006-90032 (cit. on pp. 104, 105)

[129] **Jericha, H., Sanz, W., Go¨ttlich, E., and Neumayer, F.**
"Design Details of a 600 MW Graz Cycle Thermal Power Plant for CO2 Capture"
in: *Volume 2: Controls, Diagnostics and Instrumentation Cycle Innovations Electric Power*. ASMEDC Jan. 2008. DOI: 10.1115/gt2008-50515
(cit. on p. 104)

[130] **Sanz, W., Mayr, M., and Jericha, H.**
"Thermodynamic and Economic Evaluation of an IGCC Plant Based on the Graz Cycle for CO2 Capture"
in: *Volume 3: Controls, Diagnostics and Instrumentation Cycle Innovations Marine*. ASMEDC Oct. 2010. DOI: 10.1115/gt2010-22189
(cit. on p. 104)

[131] **Sanz, W., Hustad, C.-W., and Jericha, H.**
"First Generation Graz Cycle Power Plant for Near-Term Deployment"
in: *Volume 4: Cycle Innovations Fans and Blowers Industrial and Cogeneration Manufacturing Materials and Metallurgy Marine Oil and Gas Applications*. ASMEDC Jan. 2011. DOI: 10.1115/gt2011-45135
(cit. on p. 104)

[132] **Sanz, W., Braun, M., Jericha, H., and Platzer, M. F.**
"Adapting the Zero-Emission Graz Cycle for Hydrogen Combustion and Investigation of Its Part Load Behaviour"
in: *Volume 3: Coal, Biomass and Alternative Fuels Cycle Innovations Electric Power Industrial and Cogeneration Organic Rankine Cycle Power Systems*. American Society of Mechanical Engineers June 2016. DOI: 10.1115/gt2016-57988 (cit. on pp. 104, 105)

[133] **Wimmer, K. and Sanz, W.**
"Optimization and comparison of the two promising oxy-combustion cycles NET Power cycle and Graz Cycle"
in: *International Journal of Greenhouse Gas Control* 99 (Aug. 2020), p. 103055. DOI: 10.1016/j.ijggc.2020.103055
(cit. on pp. 104–107, 111, 112, 139)

[134] **Mitterrutzner, B., Sanz, W., and Nord, L. O.**
"A part-load analysis and control strategies for the Graz Cycle"
in: *International Journal of Greenhouse Gas Control* 113 (Jan. 2022), p. 103521. DOI: 10.1016/j.ijggc.2021.103521
(cit. on pp. 104, 105)

[135] **Chen, W., Ham, L. van der, Nijmeijer, A., and Winnubst, L.**
"Membrane-integrated oxy-fuel combustion of coal: Process design and simulation"
in: *Journal of Membrane Science* 492 (Oct. 2015), pp. 461–470. DOI: 10.1016/j.memsci.2015.05.062 (cit. on p. 141)

[136] **BailianCompressors**
What is an oxygen compressor?
May 2023. URL: https://www.oxygen-compressors.com/oxygen-compressor.html (cit. on p. 140)

[137] **Serrano, J. R., Piqueras, P., Morena, J. D. la, Gómez-Vilanova, A., and Guilain, S.**
"Methodological analysis of variable geometry turbine technology impact on the performance of highly downsized spark-ignition engines"
in: *Energy* 215 (Jan. 2021), p. 119122. DOI: 10.1016/j.energy.2020.119122 (cit. on pp. 151, 154)

[138] **Arnau, F., Benajes, J., Catalán, D., Desantes, J., García-Cuevas, L. M., Serra, J., and Serrano, J. R.**
"Internal Combustion Engine and operating method of same"
Spanish. WO 2020/193833 A1 2020 (cit. on p. 151)

[139] **Komninos, N. and Rogdakis, E.**
"Design considerations for an Ericsson engine equipped with high-performance gas-to-gas compact heat exchanger: A numerical study"
in: *Applied Thermal Engineering* 133 (Mar. 2018), pp. 749–763. DOI: 10.1016/j.applthermaleng.2018.01.078 (cit. on p. 155)

[140] **Li, X., Pei, Y., Ajmal, T., Rana, K.-J., Aitouche, A., Mobasheri, R., and Peng, Z.**
"Numerical investigation on implementing Oxy-Fuel Combustion (OFC) in an ethanol-gasoline Dual-Fuel Spark Ignition (DFSI) engine"
in: *Fuel* 302 (Oct. 2021), p. 121162. DOI: 10.1016/j.fuel.2021.121162 (cit. on pp. 161, 162)

[141] **Ditaranto, M. and Hals, J.**
"Combustion instabilities in sudden expansion oxy–fuel flames"
in: *Combustion and Flame* 146.3 (Aug. 2006), pp. 493–512. DOI: 10.1016/j.combustflame.2006.04.015 (cit. on p. 161)